Development of Multiple-Breath-Helium-Washout System for Lung Function Studies

Jau-Yi Wang, BSc

Thesis submitted to the University of Nottingham
for the degree of Doctor of Philosophy
June 2009

Acknowledgements

My first thank must go to my supervisor, Prof. John Owers-Bradley who provides me such a great opportunity working on this project. With his brilliant tuition, encouragement and his kindness, I have learnt not only how to do research but also giving more concern about the human health. John, thank you for not just being a good teacher but also a father always so thoughtful and understandable. Too many thanks that I can only do all my best contributing my skills to human beings.

The second one I would like to thank is Dr. Matt Suddards who shares his experience and always makes good suggestions on my project. This project would not have been achieved without his great help. Also I would like to thank Dr. Chris Mellor who provides the easyPLL detector for this project.

I would like to thank my colleagues Arianna, Adam, Marius, Jason, Jacqueline, Elliot, Iain, Emmanuel, Ananth, Mark, Kuldeep, Antonia, James, and Daniel who always give me their hands whenever I need. Ari, thank you for always being so sweet and thoughtful and being with me especially through the very difficult time. Daphne and Jac, thank you for the encouragement and being so supportive. Marius, thank you for all the help no matter on experiments or life. Mark, thank you for being so nice to me as your younger sister. Toni, thank you for the cakes, cards, and surprise. Adam, thank you for all the concern and being so thoughtful. James, Dan, Robin, and Mu, thanks for the after-work drinks and concern especially during the writing-up period.

Many thanks to all my volunteers.

Many thanks to Iain for the proofreading.

Mom, Dad, Alan, Jensen and my lovely dog, thank you for all the support.

Abstract

This thesis discusses the development of the multiple-breath-helium washout (MBHW) measurement for lung-function study.

Multiple-breath washout (MBW) has been regarded as a sensitive technique to study the ventilation inhomogeneity in conducting or acinar airways. The tracer gas washed out from the lungs breath by breath is monitored. By analysing the concentration of the tracer gas versus the expired tidal volumes, the washout results provide two indices S_{cond} and S_{acin} which reflect the degree of ventilation inhomogeneity. S_{cond} is the increasing rate of the noramlised phase III slopes breath by breath while the S_{acin} is the nomralised phase III slope from the first breath with the subtraction of S_{cond}. The higher S_{cond} value the greater ventilation inhomogeneity in the conductive airways while the higher S_{acin} value the greater ventilation inhomogeneity in the acinar airways.

Traditionally, nitrogen is used as the tracer gas, washed out by the pure oxygen in a multiple-breath-nitrogen washout (MBNW) measurement. It is usually chosen because it is the gas we normally breathe and has no direct influence on physiology unlike oxygen. In this study, ^{4}He gas is used as the tracer gas instead. Since helium is less dense and has higher diffusivity than nitrogen, it is believed that it will be able to reach deeper into our lungs in a given time. Therefore, helium washout may provide more ventilation information especially in the small airways.

In our MBHW system, a quartz tuning fork with a resonant frequency 32768Hz is used as the gas density sensor. The resonant frequency of the tuning fork is linearly related to the surrounding gas density. The helium concentration is given by eliminating all other gas components and calculating it from the tuning fork signal. Considering other components of our expiration, the carbon dioxide is detected by the infrared sensor, and the water is filtered out by a trap.

We have performed the washout measurements on 11 volunteers, three of them have been diagnosed having mild lung diseases (asthma), two are smokers, and the other five are normal healthy people. The peak expiratory flow is also measured for each subject. The single breath MBHW curves from asthmatic people have higher normalised phase III slopes and higher S_{cond} or S_{acin} values. This shows a greater conductive or acinar ventilation inhomogeneity in asthmatics' lungs. The lung clearance washout curves are fitted with a summation of two exponential curves which represent two compartments with different ventilation rates. The compartment with higher decay rate represents the better-ventilated compartment and the other one is the poorly-ventilated compartment. Subjects with larger proportion of poorly-ventilated compartments have a lower peak expiratory flow rate compared to the predicted values.

A 2.2-litre lung model has been built. A loud speaker has been used to simulate the movement of the diaphragm. MBHW measurements have been performed on the lung model which has a 0- to 4-generation dichromatic structure. The washout results from the lung models is compared to the results from the real lungs.

List of Figures

List of Tables

Contents

3 MBHW System 46

Chapter 1

Introduction

1.1 Human Respiratory System

The respiratory system works with the blood circulation system to deliver oxygen to the cells and remove carbon dioxide. It consists of the airways, the lungs, and the respiratory muscles (the diaphragm) that mediate the movement of air in and out of the body. Figure 1.1 shows the human respiratory system.

The human respiratory system can be subdivided into the upper respiratory tract and the lower respiratory tract. The upper tract starts with the nostrils which open into the nasal cavity. The nasal cavity and the mouth meet at the pharynx, or the throat, at the back of the nose and mouth. The pharynx, a part of the digestive system as well as the respiratory system, leads to the larynx (voice box). The trachea extending downward from the larynx leads to the thoracic cavity. The lower respiratory tract starts with the trachea. At the bottom end of the trachea, it divides into the right and left main bronchi which connect to the lungs. Within the lungs, the main bronchi branch into smaller bronchi and into even smaller tubes called the bronchioles. The bronchioles lead to the terminals of the airway, the alveolar sacs, in which most of the gas exchange occurs [12, pp. 59].

The diaphragm is responsible for pumping the air in and out of the lungs. It is a sheet of muscles that lies across the bottom of the chest cavity. When it descends, the

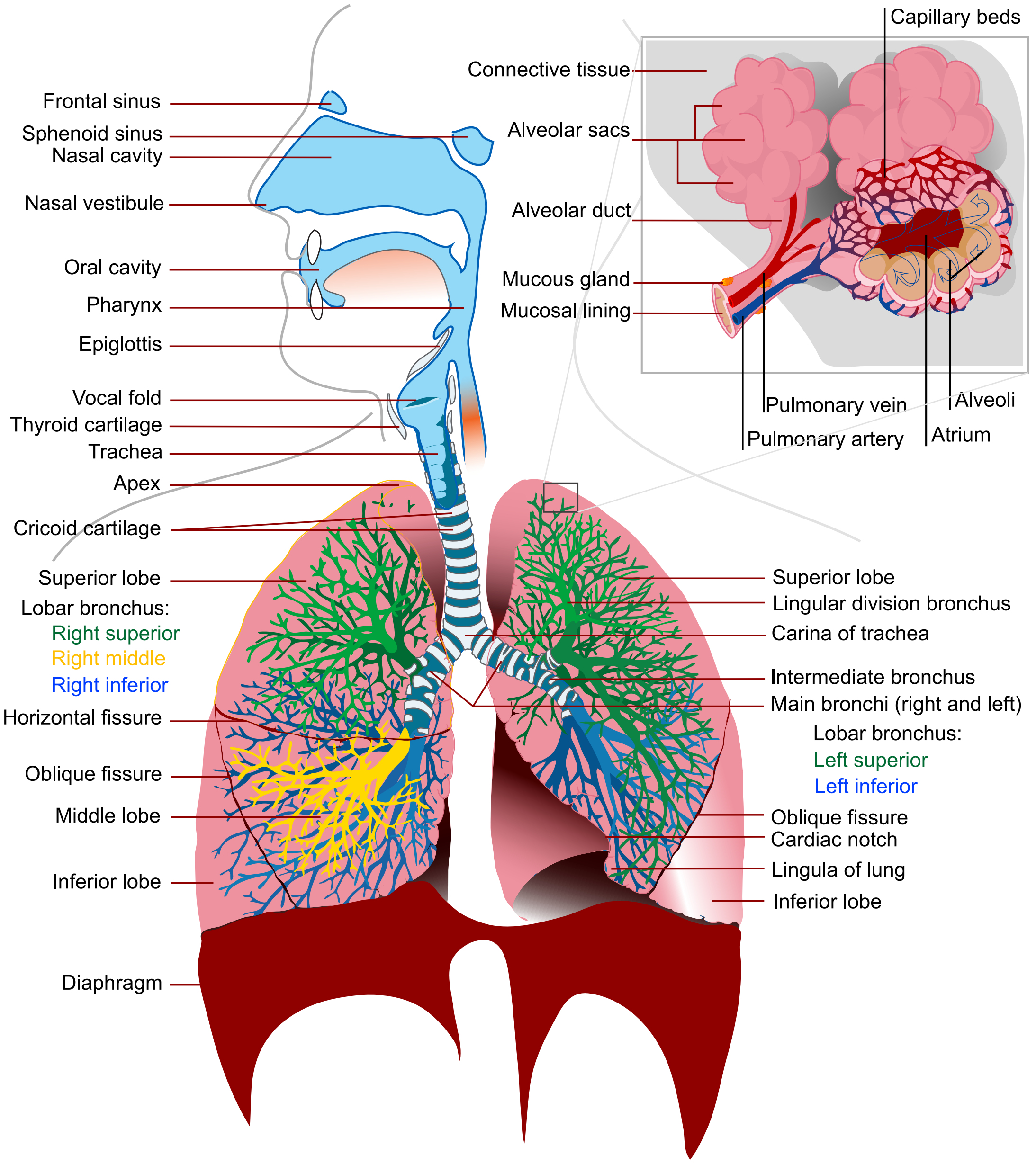

Figure 1.1: The Human Respiratory System. (Reproduced with permission from LadyofHats on Wikimedia, 2008)

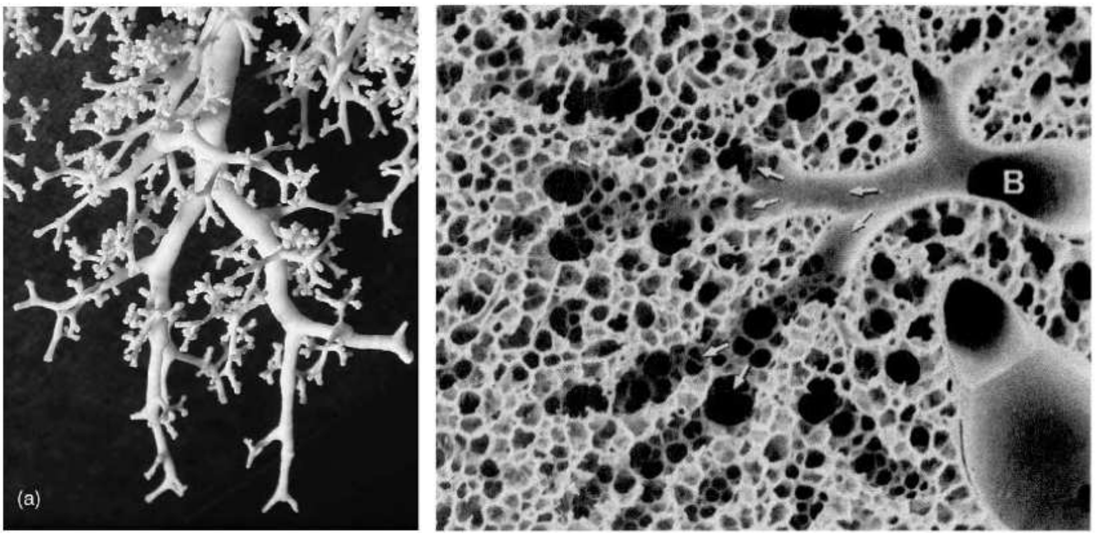

(a) (b)

Figure 1.2: (a) The cast of the human lungs [82]. (b) Scanning electron micrographs of end branches of smooth walled bronchioles (B) is the entrance of the pulmonary acinus. [81]

lungs expand and air is pulled into the alveoli. When it rises, the lungs deflate and carbon dioxide, oxygen, nitrogen and water vapour gas mixture is pumped out of the body [12, pp. 66].

1.2 Human Lung Anatomy

The human lungs are a pair of sponge-like organs in the ribcage which are built as dichotomous trees (Figure 1.2). The right lung is divided into the upper, middle and lower lobes which are supplied by a division of the right main bronchus. The left lung is divided into the upper and lower lobes; the later is supplied by the lower division of the left upper lobe bronchus and is analog to the middle lobe of the right lung. The lobes are divided into ten segments in the right lung and nine in the left.

The proximal subdivisions are two main bronchi which subdivide into secondary bronchi. The right main bronchus is wider, shorter, and more vertical than the left main bronchus. The main bronchi subdivide into two and three segmental bronchi that each serve the left and right lungs, respectively. The distal subdivisions are bronchioles which differ from bronchi in having no cartilage or mucus glands.

The portion of lung distal to one terminal bronchiole is called acinus. An acinus contains 2 to 3 orders of respiratory bronchioles each of which leads to approximately 2 to 11 alveolar ducts(alveoli). The alveolus is a hollow cavity with 5 or 6 even smaller alveolar sacs inside, and has radii of about 0.2 mm and wall thicknesses of about 0.1 μm. Figure 1.3 shows the model of human lower airway generations of branching system from trachea to acinar way (alveoli) modified by Weibel [82] [42, pp. 8].

Within the lungs, each broncus goes on for 18 to 30 generations, 23 generations on average. Since the number of branches doubles with each generation, there will be 2^{23} or about 8 million end branches, generally called alveolar sacs. The airways within a given generation are of identical length and diameter; however, the dimensions are different among the generations [42, pp. 10].

1.3 Human Lung Function and Gas Exchange

The lungs are an essential link in our respiratory airway for gas exchange between blood and air. The inhaled gas transports from upper respiratory tract into the lungs, and then mixes in the terminal respiratory units of acinus which are the basic units of the gas exchanger in our lungs. Upon inspiration, oxygen-rich air flows into the lung driven by the pump action of respiratory muscles, while during expiration O_2-depleted but CO_2-rich air is blown out.

In the first 14 generations, the gas transports via convection and there is no gas exchange. In the following 8 generations of acinar airways where convection diminishes and O_2 now diffuses through the alveolar membrane into blood. Conversely, carbon dioxide is released from the blood to the alveolar gas via diffusion across the membrane. The driving force for gas exchange is the partial pressure difference between the alveoli, air and capillary blood determined by Fick's first law of diffusion in biological perspective [42, pp. 33]:

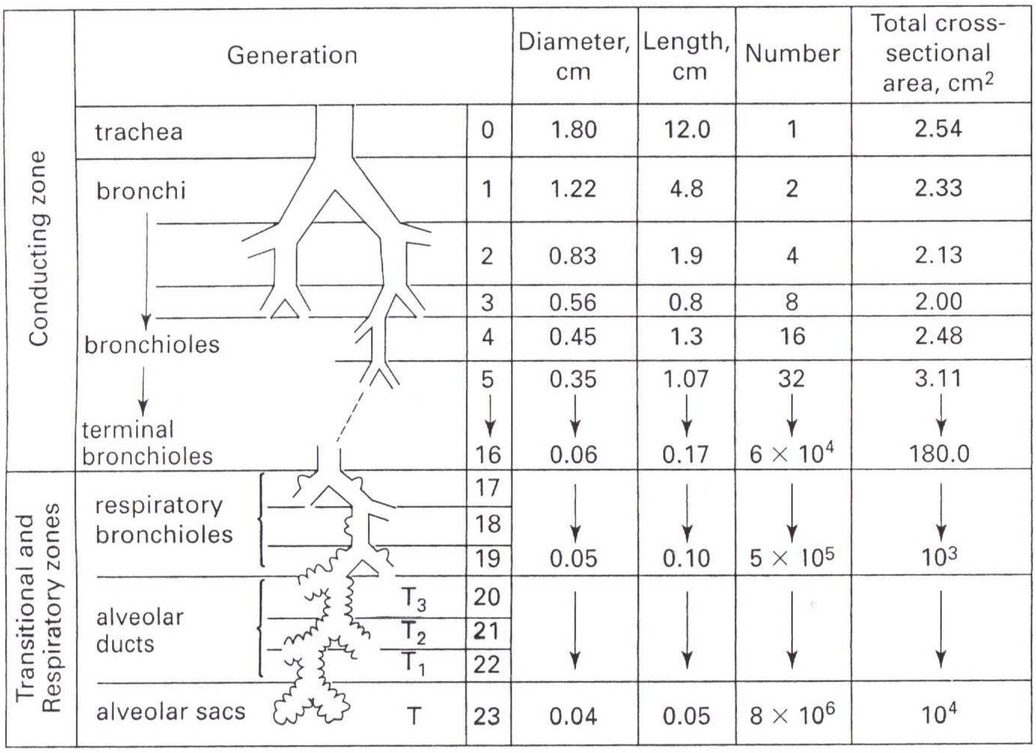

	Generation			Diameter, cm	Length, cm	Number	Total cross-sectional area, cm^2
Conducting zone	trachea		0	1.80	12.0	1	2.54
	bronchi		1	1.22	4.8	2	2.33
	↓		2	0.83	1.9	4	2.13
			3	0.56	0.8	8	2.00
	bronchioles		4	0.45	1.3	16	2.48
	↓		5	0.35	1.07	32	3.11
			↓	↓	↓	↓	↓
	terminal bronchioles		16	0.06	0.17	6×10^4	180.0
Transitional and Respiratory zones	respiratory bronchioles		17	↓	↓	↓	↓
			18				
			19	0.05	0.10	5×10^5	10^3
	alveolar ducts	T_3	20	↓	↓	↓	↓
		T_2	21				
		T_1	22				
	alveolar sacs	T	23	0.04	0.05	8×10^6	10^4

Figure 1.3: Model of human airway system assigned to generations of symmetric branching from trachea (generation 0) to acinar airways (generations 17-23), ending in alveolar sacs. Modified after Weibel (1963) [82] [42, pp. 8].

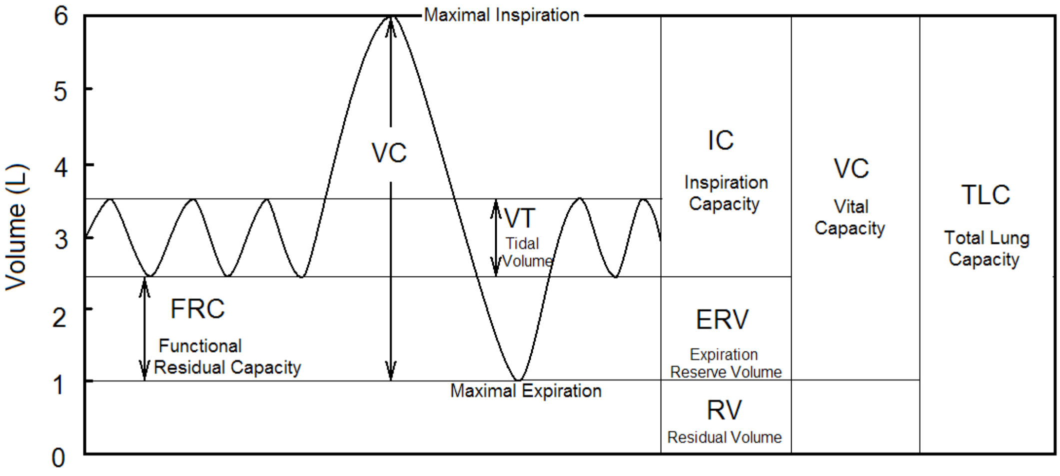

Figure 1.4: Lung Volumes and Capacities [12, pp. 76].

$$\dot{V} = -D\frac{A \times (P_a - P_b)}{d_m} \tag{1.1}$$

where $\dot{V}$ is the gas volume diffusing through the membrane per time, D is the diffusion coefficient, A is the surface area of the membrane, $P_a - P_b$ is the gas pressure difference between the alveoli the blood, and d_m is the thickness of the membrane.

1.4 Lung Capacities and Function Measurements

1.4.1 Lung Capacities and Spirometry

Lung capacities are different combinations of lung volumes related to inhalation and exhalation. Figure 1.4 shows the lung volumes and capacities. Traditionally, spirometers are used for measuring lung volumes by monitoring the normal and forced expiration and inspiration at the mouth. The spirometer is a device for measuring gas volumes and flow rate. The tidal volumes, expiratory reserve volume, inspiratory capacity, and vital capacity can be measured with the spirometer. Figure 1.5 shows the spirometry trace which has the forced inspiratory and expiratory flow with the gas volumes.

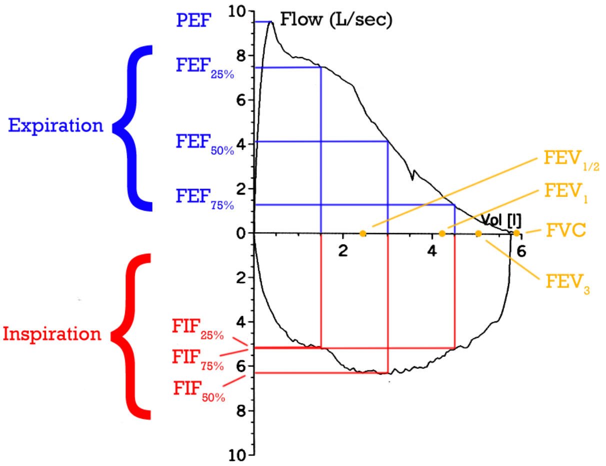

FVC (Forced Vital Capacity)	The total amount of air that can forcibly be blown out after full inspiration.
FEV_1 (Forced Expiratory Volume in 1 Second)	The amount of air that you can forcibly blow out in one second.
FEV_1 / FVC ($FEV_{1\%}$)	The ratio of FEV 1 to FVC. In healthy adults this is around 75 - 80%.
PEF (Peak Expiratory Flow)	The speed of the air moving out of your lungs at the beginning of the expiration.
$FEF_{25-75\% \text{ or } 25-50\%}$ (Forced Expiratory Flow 25-75% or 25-50%)	The average flow rate of air coming out of the lung during the middle portion of the expiration.
FIF $_{25-75\% \text{ or } 25-50\%}$ (Forced Inspiratory Flow 25%-75% or 25%-50%)	This is similar to FEF 25%-75% or 25%-50% except the measurement is taken during inspiration.
FET (Forced Expiratory Time)	The length of the expiration in seconds.
VT (Tidal Volume)	The specific volume of air is drawn into and then expired out of the lungs during respiratory cycle.
MVV (Maximum Voluntary Ventilation)	The maximum amount of air that can be inhaled and exhaled in one minute.

Figure 1.5: Spirometry and the measured lung capacities (Reproduced from Carnildo on Wikimedia, 2005. *http://en.wikipedia.org/wiki/Image:Flow-volume-loop.png*).

The forced vital capacity (FVC) is a useful index for assessing expiratory airways resistance. The most sensitive part to the airways resistance is the first second of expiration (FEV_1). In a normal subject, the FEV_1/FVC is greater than 0.75. A patient with airway obstruction or restriction would be expected to have a FEV_1/FVC far below 0.75. Obstructive diseases can interfere with airflow and restrictive diseases restrict the expansion of the lungs which results in a decrease in the maximal flow rate that the patient can achieve [42, pp. 42].

The functional residual capacity (FRC) and the residual volume (RV) are not measurable with the spirometer but can be determined by the body plethysmography, the helium-dilution technique, and the nitrogen washout technique.

1.4.2 Body Plethysmography

The body plethysmograph consists of a body-sized chamber, a flow meter, two pressure transducers, and an electrically-controlled shutter as shown in figure 1.6. Subjects are asked to sit inside a closed chamber breathing through tubing connected to a flow meter and a pressure transducer. The pressure nearby the mouth is monitored (P_M) as well as the inner-chamber pressure (P_{box}). The shutter is closed at the end of an expiration followed by a quick inspiration against the closed airway. As a forced inspiration is made against the closed airway, the chamber pressure (P_{box}) increases because of the lung expansion while the mouth pressure (P_M) decreases. According to Boyle's law, the product of the initial pressure and initial volume of a closed system is equal to the product of the final pressure and the final volume, *i.e.*, $P_i \cdot V_i = P_f \cdot V_f$ [42, pp. 65];

$$P_{boxi} \cdot V_{Ci} = P_{boxf} \cdot (V_{Ci} - \Delta V) \tag{1.2}$$

$$P_{Mi} \cdot FRC = P_{Mf} \cdot (FRC + \Delta V) \tag{1.3}$$

where V_{Ci} is the chamber volume before the shutter closed and ΔV is the volume change of the lungs. The functional residual capacity can be determined by the above equations as [42, pp. 65]:

$$FRC = V_{Ci} \cdot (\frac{P_{Mf}}{P_{boxf}}) \frac{P_{boxf} - P_{boxi}}{P_{Mi} - P_{Mf}}. \tag{1.4}$$

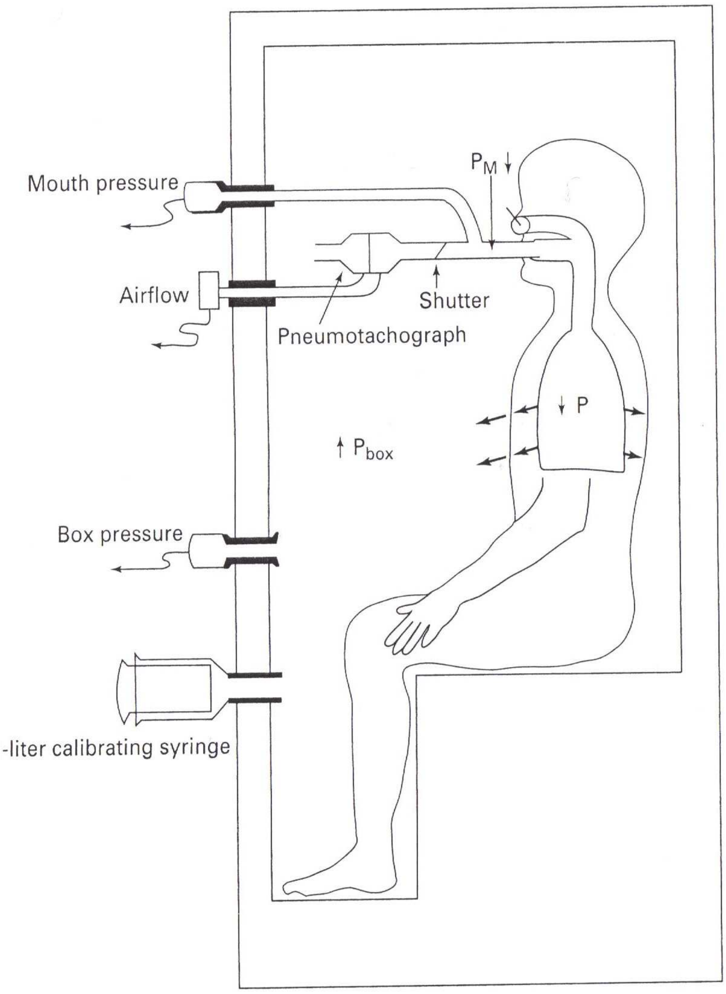

Figure 1.6: The body plethysmograph [42, pp. 64].

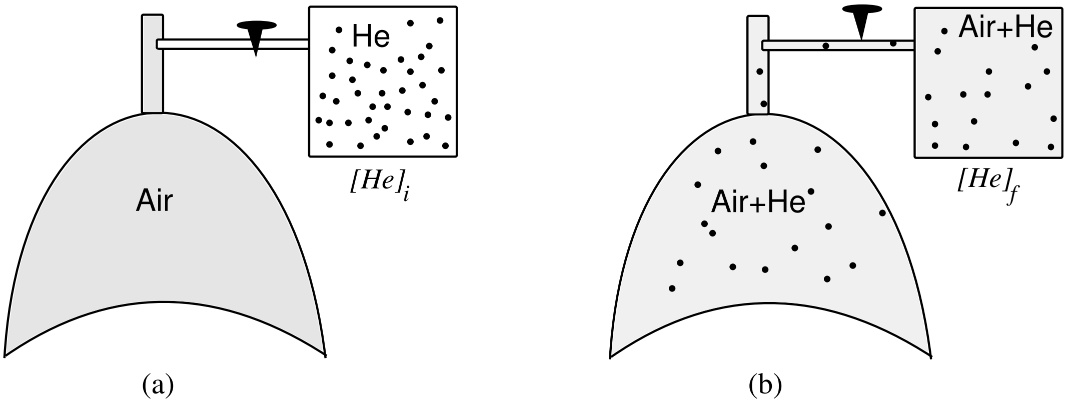

Figure 1.7: The helium-dilution technique diagram.

1.4.3 Helium-dilution Technique

The helium-dilution technique is based on monitoring the concentration of helium in a closed system before and after a few breaths until the concentration stops decreasing as shown in figure 1.7. The total amount of helium molecules in the system initially is equal to its final quantity. After starting inhaling helium at the end of the expiration, the system volume is equal to the FRC plus the volume of helium container V$_{He}$ [42, pp. 61], *i.e.*,

$$[He]_i \cdot V_{He} = [He]_f \cdot (FRC + V_{He}) \tag{1.5}$$

$$FRC = V_{He} \cdot (\frac{[He]_i}{[He]_f} - 1) \tag{1.6}$$

1.4.4 Multibreath-Nitrogen Washout Technique

In a multibreath-nitrogen-washout measurement, the nitrogen concentration of the expiration gas is monitored while the subject inspires 100% oxygen over several breaths until the nitrogen concentration is lower then 2%. The nitrogen concentration decreases breath by breath during the washed out process by oxygen gas (Figure 1.8). The expired gas volume is also measured with a flow meter. FRC can be determined by comparing the total amount of initial nitrogen gas in the lungs and the total expired

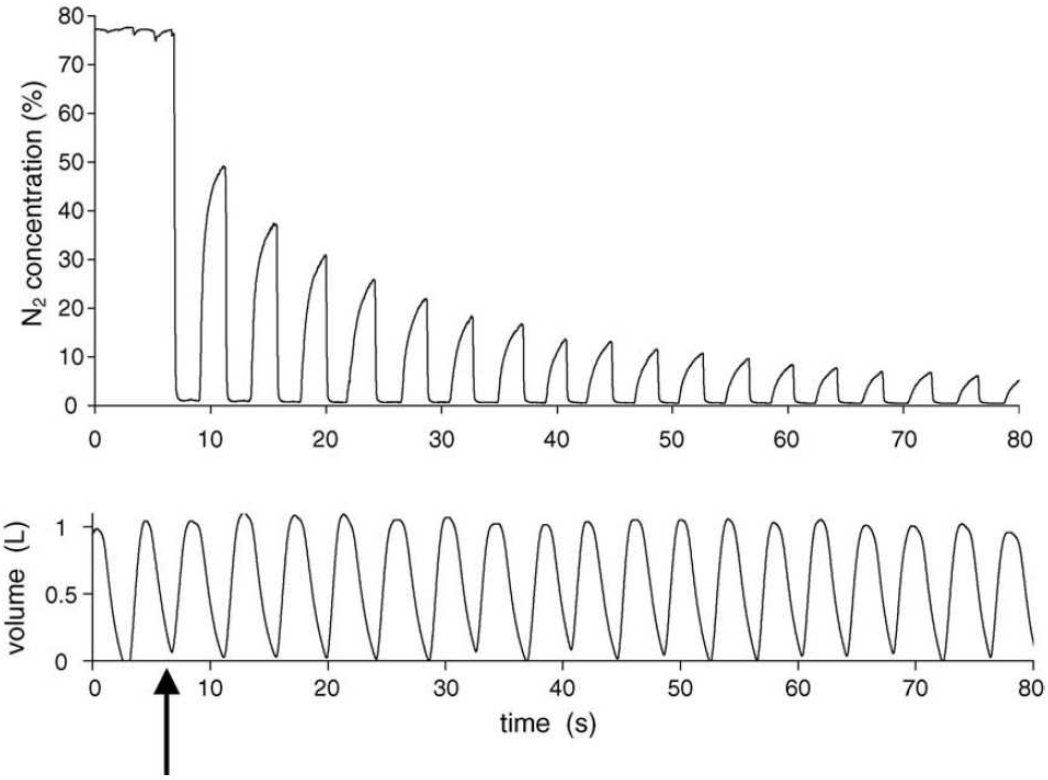

Figure 1.8: The typical nitrogen washout curve. The upper graph shows the concentration of nitrogen and the lower graph shows the respiratory tidal volumes during the washout process. The arrow indicates the start of inspiring pure oxygen [49].

nitrogen gas volume [86]:

$$\sum_n \int [N_2]_n dV_n = FRC \cdot [N_2]_{initial}, \tag{1.7}$$

$$FRC = \frac{\sum_n \int [N_2]_n dV_n}{[N_2]_{initial}}. \tag{1.8}$$

where $[N_2]_n$ and V_n are the nitrogen concentration and expired gas volume of the nth breath respectively.

1.5 Common Lung Diseases

There are three major physiologic categories of lung diseases: obstructive, restrictive and defect in gas exchange type. The obstructive lung diseases such as asthma, chronic bronchitis, and emphysema are caused by the widespread airway narrowing. This narrowing can reduce the forced expiratory flow and thus can be diagnosed on the basis of a low forced expiratory volume together with small forced vital capacity in one second (FEV_1). The restrictive lung diseases are the result of the restriction of lung or the chest wall expansion. These types of disease reduce the vital capacity and total lung capacity. The restriction can also limit the forced expiratory volume and flow rate [12, pp. 398]. Figure 1.9 shows the spirometry of the normal lungs along with obstructed and restricted lungs.

The defective gas exchange is due to the thickening walls of the alveoli, respiratory bronchioles, and pulmonary airfoil. The defect in gas exchange also gives rise to a ventilatory defect which results in lung restriction. This abnormal gas exchange lowers the rate of oxygen absorption from the alveoli to the pulmonary capillaries [12, pp. 398].

1.5.1 Asthma

Asthma is an obstructive disease due to widespread narrowing of the bronchial tube. During the attack, the lining of the airways swell and the muscles surrounding the bronchi contract. These can slow the air movement and this makes breathing difficult. The clinical characteristics are wheezing, coughing, and abnormal shortness of breath.

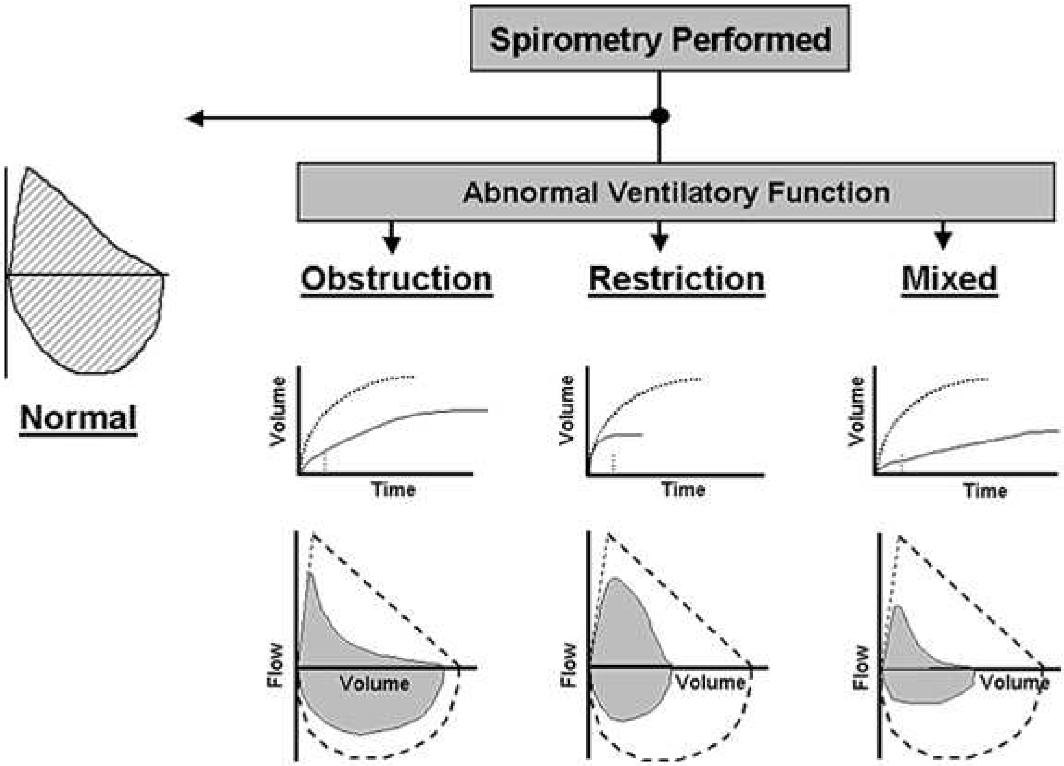

Figure 1.9: The spirometry of normal lungs, with obstructive diseases, and with restrictive diseases [37].

The narrowing increases the airway resistance and cause an uneven distribution of the inspired gas [12, pp. 412].

1.5.2 COPD

COPD (chronic obstructive pulmonary disease) is a disease that includes both chronic bronchitis and emphysema. Patients may have one or the other, but often a combination of both which leads to a decrease in blood oxygen levels and shortness of breath. In the emphysema type of COPD, the walls between the alveoli are damaged which results to larger alveolar sacs. It reduces the surface area of the alveoli and thus lowers the exchange of oxygen and carbon dioxide. In chronic bronchitis, the airways are inflamed and thickened which increases the number of mucus-producing cells and thus more mucus is produced. The clinical characteristics are coughing and difficulty in breathing [12, pp. 414].

1.5.3 Cystic Fibrosis

Cystic fibrosis is a genetic disorder caused by mutations in a pair of genes which are responsible for the protein production (chromosome 7). It causes abnormal electrolyte and water movements through the epithelial cells and thus thick and sticky mucus is accumulated in the lungs. Patients with cystic fibrosis are not only have abnormal oxygen absorption but also at risk of getting bacterial chest infections [12, pp. 412].

1.6 Overview of thesis

This thesis introduces the multiple-breath-helium washout system for lung function measurement with the quartz tuning fork applied as the helium gas sensor. The structure of the thesis is as follows: Chapter 2 gives an overview the washout measurement and the related mechanism of gas mixing and distribution in the lungs. The development of helium-washout system is introduced in Chapter 3. The MBHW system control programmes and the anaysis programme are introduced in Chapter 4. MBHW results from 11 volunteers and a lung model with its MBHW results are discussed in Chapter 5. Chapter 6 introduces three methods for helium gas detection which have been tried and found unsuitable for MBHW measurement. Chapter 7 contains a brief summary and suggestions for future work.

Chapter 2

Multiple-Breath Washout Measurements

This chapter is based on the theoretical study of M. Paiva and L. Engel of the respiratory gas mixing mechanism [22, 58] and their review of previous pioneering work. The mechanism of how pulmonary gas exchange and gas distribution is related to multiple-breath washout (MBW) tests will be introduced in section 2.1. The traditional single-breath washouts (SBW) and multiple-breath-nitrogen washouts (MBNW) will be introduced in section 2.2. The multiple-breath washouts (MBW) and the related analysis will be discussed in section 2.3.

Multiple-breath washout measurements have been regarded as a sensitive technique for respiratory ventilation study. The concentration of tracer gas is monitored while washed out of the lungs breath by breath. The respiratory gas volume is also measured by monitoring the flow rate of breathing. In single-breath washout (SBW) measurements, subjects expire near the whole vital capacity, while in MBW subjects take about 1 litre tidal breaths. Each breath can be regarded as a single washout curve while the sequential emptying and filling in MBW tests can reflect the ventilation inhomogeneity in conductive or acinar airways that is unable to be differentiated in SBW tests. As briefly described in section 1.4, nitrogen is normally used as the tracer gas washed out by 100% oxygen in multiple-breath-nitrogen washout measurements. Figure 2.1(a) shows the pneumotachograph of MBNW and figure 2.1(b) shows the washout curve and the expired volume from a single breath.

2.1 Pulmonary Gas Exchange and Distribution

As mentioned in section 1.2, the human respiratory system can be divided into 23 generations on average due to Weibel's dichotomous model [82]. In the first 16 generations, gas is transported by bulk flow, called the conduction zone (or conducting airways). The following 17th to 23rd generations are the alveolar airways (or acinar airways) where the gas exchange occurs. In this area, the bulk flow speed is nearly zero and the gas transport is dominated by diffusion. The diffusive mechanism is driven by the partial pressure difference of the gases and determined by the Fick's first law of diffusion as mentioned in section 1.3. In reality, the uneven distribution of the alveoli and asymmetric dichotomy of bronchial structure complicate these two mechanisms.

Convective Gas Transport

In conductive airways where the gas transport is dominated by convection, there is no gas (O_2-CO_2) exchange thus it is also referred to the anatomic dead space. The mechanism of the bulk flow is determined by Fick's second law of diffusion [22, pp. 15]:

$$\frac{\partial c}{\partial t} = -\nabla(DA\nabla c) \tag{2.1}$$

where c, A, D and ∇c are the gas concentration, airway cross section, gas diffusion coefficient, and gas concentration gradient along the longitudinal airways, respectively. This can be derived from the mass conservation and the Fick's first law of diffusion considering the time-dependent concentration of gas molecules.

Baker et al. [1] described how Fick's law applied to the gas mixing along the longitudinal airway including the accumulation, bulk transport, and longitudinal mixing terms, *i.e.*,

$$\frac{\partial c}{\partial t} = \dot{V}\nabla c - \nabla\left[A(\kappa + D)\nabla c\right] \tag{2.2}$$

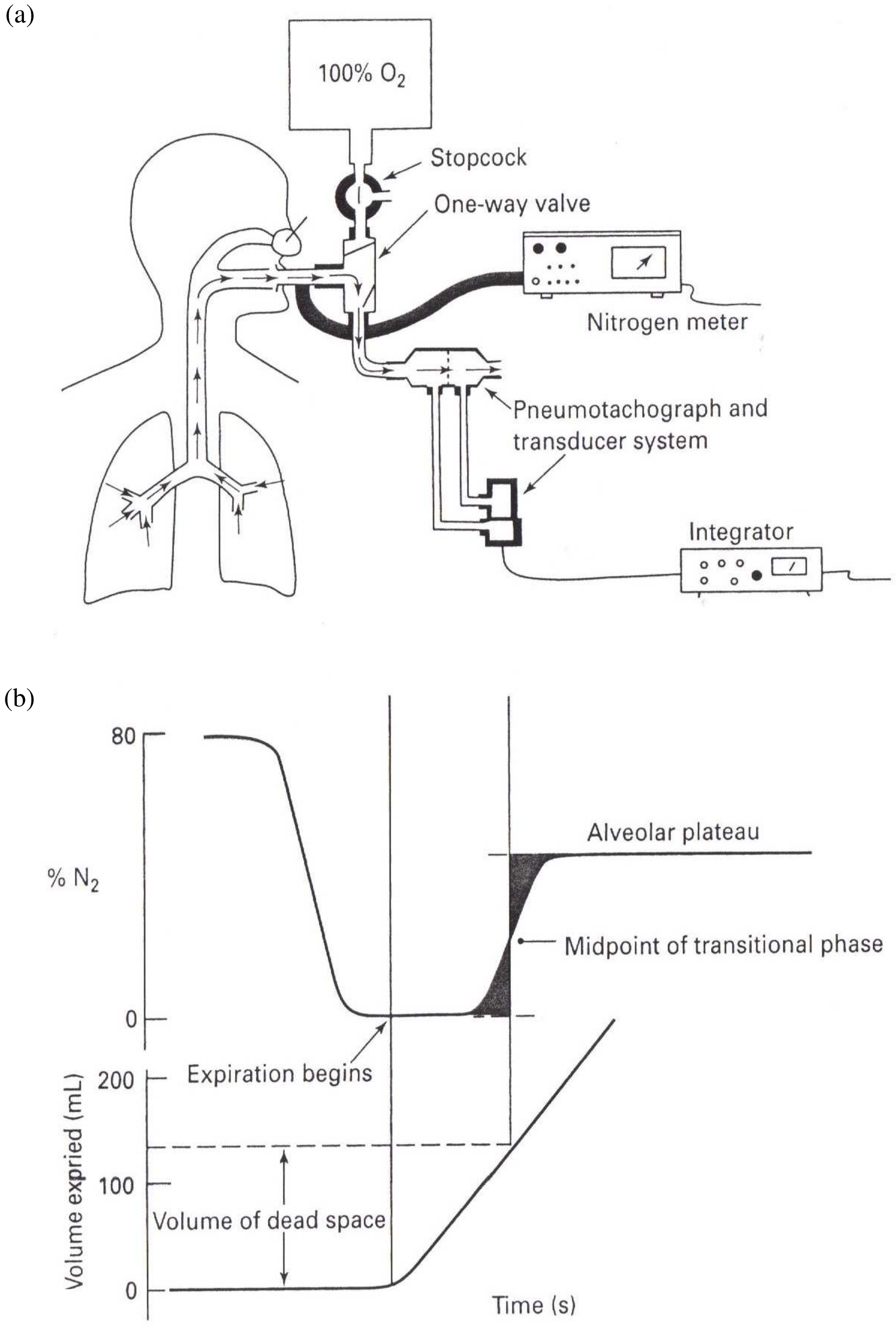

Figure 2.1: (a) Pneumotachograph of MBNW. (b) The washout curve from a single breath [42, pp. 68].

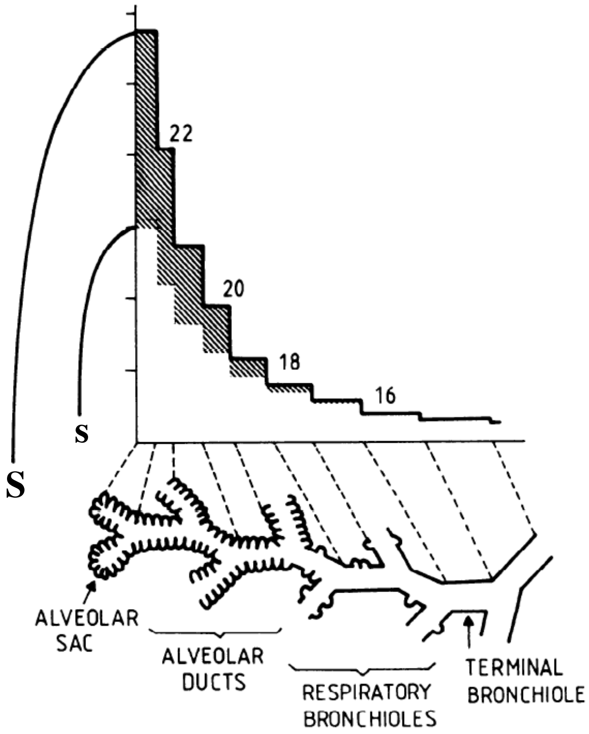

Figure 2.2: Schematic representation of airway cross sections based on Paiva's two trumpet model and Weibel's acinar model. **S** and **s** are the total cross sections of airways inclusive and exclusive of the alveoli. The shaded area represents the alveolar cross sections [58].

where $\dot{V}$ is the volumetric flow and κ is the longitudinal dispersion or mixing coefficient [22, pp. 91]. The first term on the right-hand side corresponds to the bulk mixing while the second term corresponds to the longitudinal mixing.

Diffusive Gas Transport

In alveolar airways, alveoli distribute unevenly along the bronchial tree. Approaching the terminals of the lung, the bulk flow speed is nearly zero, thus gas transport is dominated by diffusion. For oxygen and carbon dioxide, the partial pressure difference between alveolar sacs and the capillary blood is around 40 mmHg for CO_2 and 60 mmHg for O_2, which drives those two gases across the alveoli membrane [42, pp. 73]. For other insoluble gases such as nitrogen or helium, the gas diffusion is caused by the partial pressure difference between the inspired gas and within the alveoli. Paiva [59] has described the gas mixing in our lungs considering the second Fick's law of diffusion with a source term as:

$$\frac{\partial c}{\partial t} = D\frac{\mathbf{s}}{\mathbf{S}}\nabla^2 c + \frac{D}{\mathbf{S}}\nabla\mathbf{s}\nabla c - \vec{u}\cdot\nabla c + Q_a \tag{2.3}$$

where $\mathbf{S}$ and $\mathbf{s}$ are the airway cross section inclusive and exclusive of alveoli, $\vec{u}$ is the bulk flow velocity and Q_a is the source term corresponding to the gas molecule produced or consumed in alveoli. The cross-sectional area of the airway is shown in figure 2.2. This transport equation is based on a few assumptions including the incompressibility of the gas mixture, constant temperature along the airways, only generation 11th to 23rd taken into account, gas exchange mechanism across the alveoli membrane can not be described with this equation, and the volume change of alveoli is not considered.

Diffusion Coefficient D

The diffusion coefficient D mentioned above has been regarded as the binary diffusion coefficient for a gas mixture with two kinds of molecules `A` and `B`. According to Chapman-Enskog theory [9] [22, pp. 10],

$$D = \frac{1.86\cdot 10^{-3}T^{3/2}\sqrt{\frac{1}{M_{\mathtt{A}}}+\frac{1}{M_{\mathtt{B}}}}}{P\sigma_{\mathtt{AB}}^2\Omega} \tag{2.4}$$

where T is the temperature (K), M_A and M_B are the molecular weights of gases `A` and `B`, P is the ambient pressure (atm), $\sigma_{\mathtt{AB}}$ is the Lennard-Jones force constant for the binary mixture (Å), and Ω is the dimensionless integral corresponding to molecules collision (usually in the order of 1). For helium and air mixture, the binary diffusion coefficient is 0.708 cm^2/sec at 20^{o}C, 1 atm [22, pp. 11].

Interaction Between Diffusion and Convection

In Paiva's simulation work of single-breath washouts, the fractional concentration of nitrogen gas was plotted as a function of the longitudinal depth along the airways with different gas binaries [22, pp. 242]. He also pointed out the transition from the

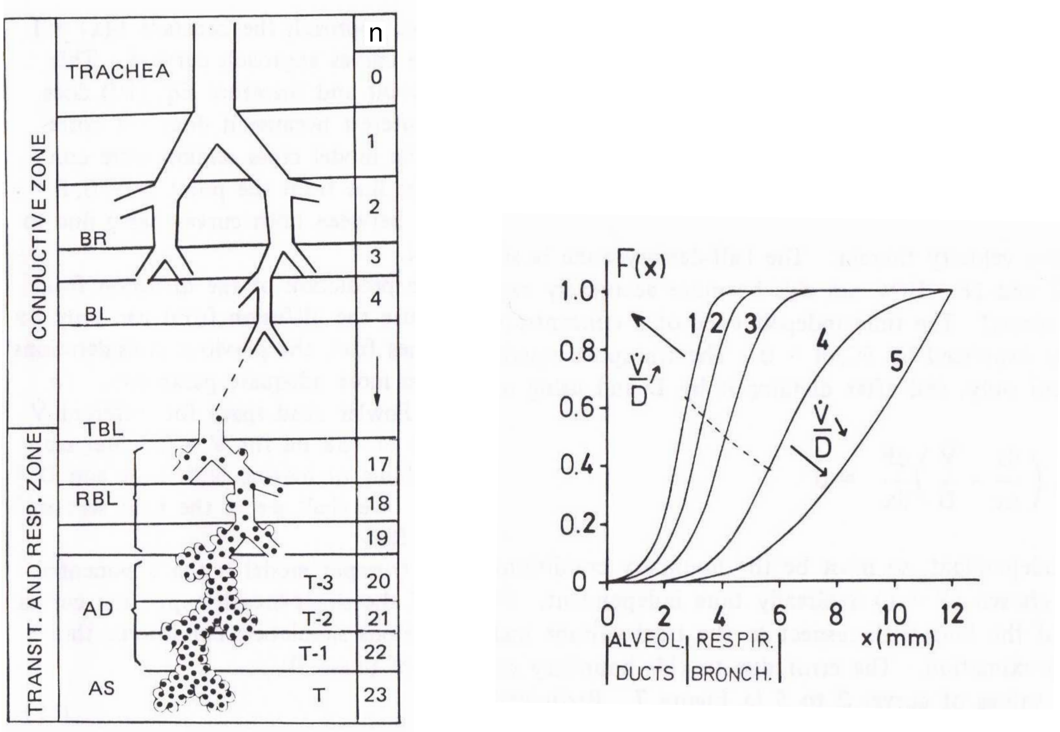

(a) (b)

Figure 2.3: (a) Schematic of the gas mixing in the lungs from Paiva which is based on Weibel's model. (b) The solutions of Eq.(2.5) with the boundary conditions of $c(z = 0) = 0$ and $c(z = 12) = 1$. Curves 1, 2, and 3 correspond to $D = 0.1$ (SF_6-air), 0.225 (N_2-O_2), 0.6 (He-air) cm^2/sec, respectively and $\dot{V} = 500$ mL/sec. Curves 4 and 5 corresponds to $\dot{V} = 125$ and 0 mL/sec with $D = 0.6$ cm^2/sec [58] [22, pp. 242].

convection to the diffusion mechanism was located at the 16th and 17th generations. The solution to the Eq.(2.3) regardless of the time-dependent gas concentration, *i.e.*, $\partial c/\partial t = 0$, at this transition point is where ∇c reached the maximum value while $\nabla^2 c = 0$. Replacing the bulk flow velocity $\vec{u}$ to the bulk flow rate across the total cross section $\mathbf{S}$, *i.e.*, $\vec{u} = \dot{V}/\mathbf{S}$, Eq.(2.3) can be re-written as [22, pp. 241-242]

$$\frac{D}{\mathbf{S}}\nabla \mathbf{s} \nabla c - \vec{u} \cdot \nabla c = 0 \tag{2.5}$$

$$\nabla \mathbf{s} = \frac{\dot{V}}{D}. \tag{2.6}$$

This transition point happens to be the Fowler dead space which will be introduced in the following section. The solutions of Eq.(2.5) with the boundary conditions of $c(z = 0) = 0$ and $c(z = 12\ mm) = 1$, different diffusion coefficients and flow rates are plotted in figure 2.3(b) [58] [22, pp. 242]. For a given bulk flow rate, the diffusion front (or the diffusion-convection interaction front) is more peripheral for a heavier gas (smaller D). Curve 5 corresponds to the pure diffusive transport in which the bulk flow $\dot{V}$ is zero.

2.2 Single-Breath Washouts (SBW)

Single-breath washout measurement is based on mixing the inhaled gas with the gas remaining in the lung. Normally, oxygen is used for diluting the nitrogen in the lung. In single-breath-nitrogen washouts, the concentration of nitrogen from a deep expiration is monitored after a deep inhalation of pure oxygen is taken. The exhaled nitrogen concentration is plotted versus the expired gas volume as a single washout curve in figure 2.4. It can be divided into four phases. Phase I corresponds to the pure inspiratory gas and there is no tracer gas. Phase II, with a sharp increase of gas concentration, is the transition between the inspiration and the gas remaining in the lung. Phase III corresponds to the alveolar plateau with a positive slope due to the structural asymmetry of alveoli and inequality of gas emptying. Phase IV is caused by the airway closure at the end of expiration and the sudden change to inspiratory gas, especially when the expiration is larger than a normal tidal volume.

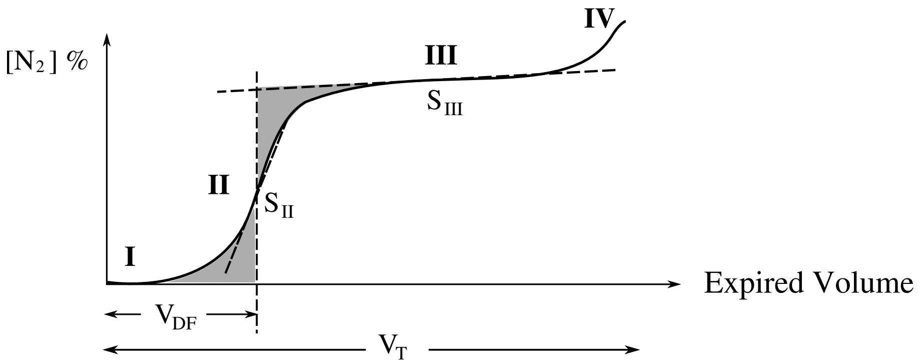

Figure 2.4: Single-breath-nitrogen washout curve. Phase I corresponds to the pure inspiratory gas followed by phase II which is the rapid transition between the inspired and the remaining gas in the lung. Alveolar plateau occurs in phase III with a positive slope due to uneven gas distribution in alveoli. Phase IV is caused by the airway closure at the end of expiration and suddenly change to inspiration. Two shadowed area in phase II are equal and the middle point of the phase II is defined as the Fowler dead space [22, pp. 296].

Phase II and Fowler Dead Space

The method used to measure the respiratory dead space is based on the pioneering work of Fowler [23]. According to Fowler's definition, the dead space is the volume of the conducting airways down to the location at which a large change in gas composition occurs' [22, pp. 326]. He solved Bohr's equation of the respiratory dead space [4] [22, pp. 326], V_{DB},

$$\frac{V_{DB}}{V_T} = \frac{c_E - c_A}{c_I - c_A} \tag{2.7}$$

where V_T is the tidal volume, c_E, c_I are the mixed expired concentration of expired and inspired gas, and c_A is the mean gas concentration in alveoli. The volume of the dead space is located near the middle point of phase II. As shown in figure 2.4, two shaded areas in phase II are equal and the inflection point of the phase II is defined as the Fowler dead space V_{DF} [23]. It is a functional dead space and its volume also reflects where the diffusion and convection boundary occurs.

Recent studies on single-breath test of CO_2 tracing have shown that patients with lung disease normally have larger Fowler dead space and smaller normalised phase II slopes than normal persons [39, 77]. It is caused by the restriction in the airways that

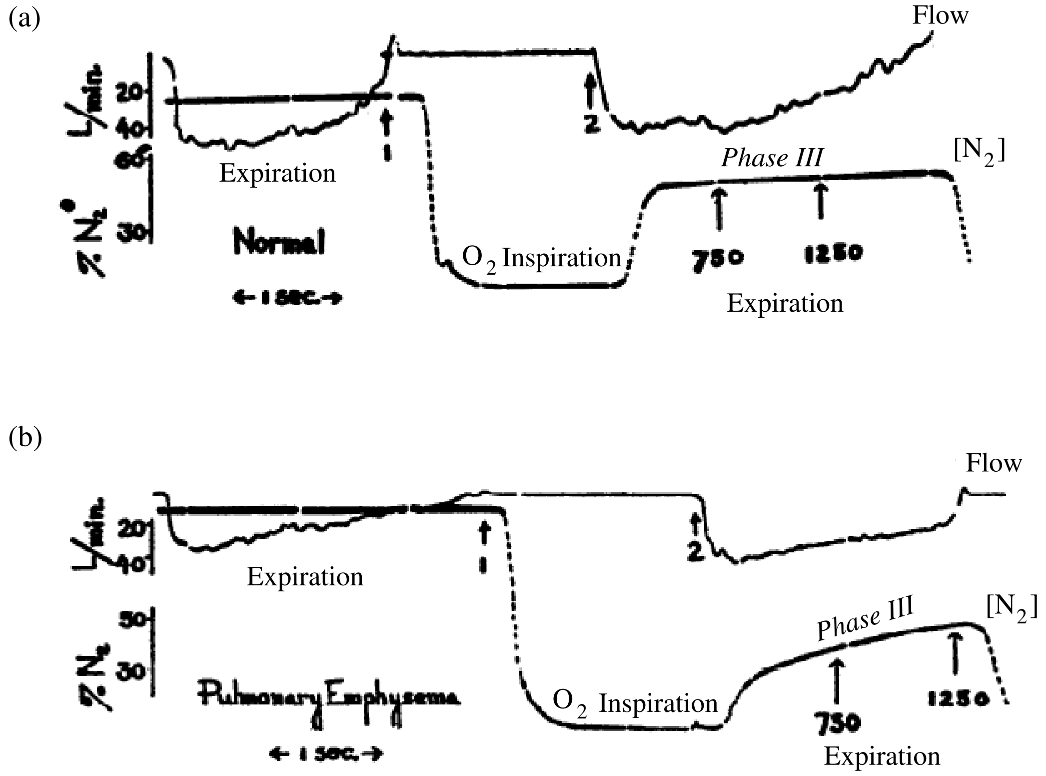

Figure 2.5: The single-breath-nitrogen washout curves from a normal subject (a) and a pulmonary emphysematic patient (b). The upper curve is the expiratory volume flow and the bottom one is the nitrogen concentration. A single expiration is followed by an O_2 inspiration (`1-2`). The phase III (`750-1250 (mL)`) slope from the patient is steeper than the normal subject [24].

the poor ventilation in deeper lungs requires more bulk flow into diseased airways. The normalised phase II slope (S_{NII}) is the slope of the tangent line at the V_{DF} (S_{II}) as shown in figure 2.4 divided by the mean concentration. Also, this functional dead space for helium is smaller than for a heavier (or less diffusible) gas such as SF_6 [71] which is consistent as Paiva's work as mentioned in the previous section. The anatomic dead space is about 150 mL for adults while the Fowler dead space ranges from 130 mL to 200 mL depending on the tracer gases and expiratory flow rate [42, pp. 68] [23].

Phase III and Alveolar Ventilation

Phase III represents the alveolar portion of the washout curve. The plateau normally has a slightly positive slope which is the phase III slope, S_{III}. The main mechanism of this positive slope is believed as a result of the asymmetrical structure of alveolar airways and the uneven distribution of alveoli and thus the ventilation. The pulmonary ventilation is defined as the bulk flow rate ($\dot{V}$) at which gas enters or leaves the lung and can be given by the sum of the alveolar ventilation ($\dot{V}_A$) and the dead space ventilation ($\dot{V}_D$) [58]

$$\dot{V} = \dot{V}_A + \dot{V}_D. \tag{2.8}$$

The inspired gas with lower concentration is mixed with the gas remaining in alveolar sacs and is distributed unevenly to different units of the lungs [24]. After an inspiration, the gas mixture in those respiratory units with less ventilation (*i.e.*, more difficult for the inspired gas to diffuse into) has higher concentration of N_2 and is flushed out less easily. The gas mixture in the better-ventilated units relatively has lower concentration of N_2 since the gas is diluted well and contributes to the early part of the alveolar expiration. Less-ventilated regions contribute to the later part of the phase III. It thus causes the positive phase III slopes. Patients with lung diseases normally have steeper phase III than normal people because of the greater inhomogeneity of their airways as well as the respiratory ventilation [24]. Other minor effects such as body posture or inspiration and expiration flow rates can also increase the phase III slopes [63].

Phase IV and Closing Volume

Phase IV corresponds to the closing volume in alveolar airways. The main mechanism causing phase IV is believed as a result of even poorer ventilation in small units related to airway closure. It can only be measured in vital capacity breathing test or sometimes in very diseased patients as part of steep phase III [22, pp. 304] [8, 46]. In multiple-breath washouts, phase IV can hardly be measured since the subjects are breathing normal tidal volumes and there is no closure. Therefore, the main analysis will be focused on phase II and phase III.

2.3 Multiple-Breath Washouts (MBW)

In contrast to the single-breath washouts, subjects are taking about 1L normal tidal volumes in traditional MBW technique [49, 51, 79]. The tracer gas is washed out of the lungs breath by breath. The concentration as well as the flow rate is monitored during the test. Each breath from MBW is almost identical to the curve from SBW test but shorter and without phase IV, either. The sequential emptying reflects the ventilation inhomogeneity from different units in the normalised phase III slopes and the mean concentration from each breath which can not be measured in one single breath.

2.3.1 Lung Clearance and Two Compartment Model

For a perfect ventilated lung, the phase III is flat and S_{III} is near zero. For unevenly ventilated lungs, the resulting alveolar gas concentration becomes unequal from unit to unit and the first breath should be weighted by the better-ventilated units. The degree of ventilated inhomogeneity arises progressively less from those better-ventilated units and more from the poorly-ventilated units in the second and the following breaths. This is because the alveolar gas is washed out more quickly from the better-ventilated units than from poorly-ventilated units.

For an ideal container with a perfect ventilation (which means the inspired diluting gas mixes perfectly well with the tracer gas remaining in it), the mean concentration of expiration is exponentially related to the breath number in the MBW test with constant tidal volumes. The relation can be given by as [51, 55]

$$c_n = c_0 \left(\frac{FRC}{FRC + V_T} \right)^n \tag{2.9}$$

where n is the breath number, c_n and c_0 are the tracer gas concentration from the nth breath and from the lungs before washout starts, and FRC is the residual capacity (or the volume of the container before inspiration). By taking the logarithm from each sides, the equation can be written down as

$$log\ c_n = log\ c_0 + nlog\ \frac{FRC}{FRC + V_T}. \tag{2.10}$$

The logarithm of the mean concentration is linearly related to the breath number. However, for real lungs, the uneven distribution of inspired gas is washed out asynchronously and it results in a nonlinear relation of log c_n and n. The interpretation of the washout curve from MBNW was first studied by Robertson et al. [65] [22, pp. 312]. The washout curve corresponds to the sum of two (or more) exponential functions representing two (or more) compartments independently ventilated at different rates as shown in figure 2.6(b).

For patients with airway diseases, the respiratory ventilation inhomogeneity reflects in a more curved line as shown in figure 2.7 [45]. Considering the non-constant tidal volumes, Cumming [15] described an alternative handling for these washout curves. The logarithm of concentration was plotted as a function of the turnover, which is the accumulative expired gas volumes (ΣV_T) divided by the residual volume (FRC). The resulting washout curve is almost identical to the original one with breath number and is more well-accepted in recent studies [80].

A simple related index, LCI (lung clearance index), has been introduced for studying the efficiency of tracer gas washed out of lungs [6, 16, 17, 25]. It is defined as the expirations (ΣV_T) required to wash out N_2 down to 2-1.5% divided by lung residual volume (FRC) during nitrogen washouts. Cutillo *et al* performed the washouts on normal subjects and COPD patients [16, 17]. The LCI for normal subjects (8.5-10) are lower than the patients (>13) [22, pp. 314] which means the diseased lungs are so inhomogeneously ventilated that it requires more expirations to flush out the tracer gas compared to the normal-healthy lungs.

Another useful index is the curve linearity (C_{urv}). It is a measure of how much the straight line is curved. Since the clearance washout curve is more straight for better-ventilated lungs. By fitting the first and second half of the clearance washout data with two straight lines, the C_{urv} is the ratio of those two straight lines' slopes. Thus for an

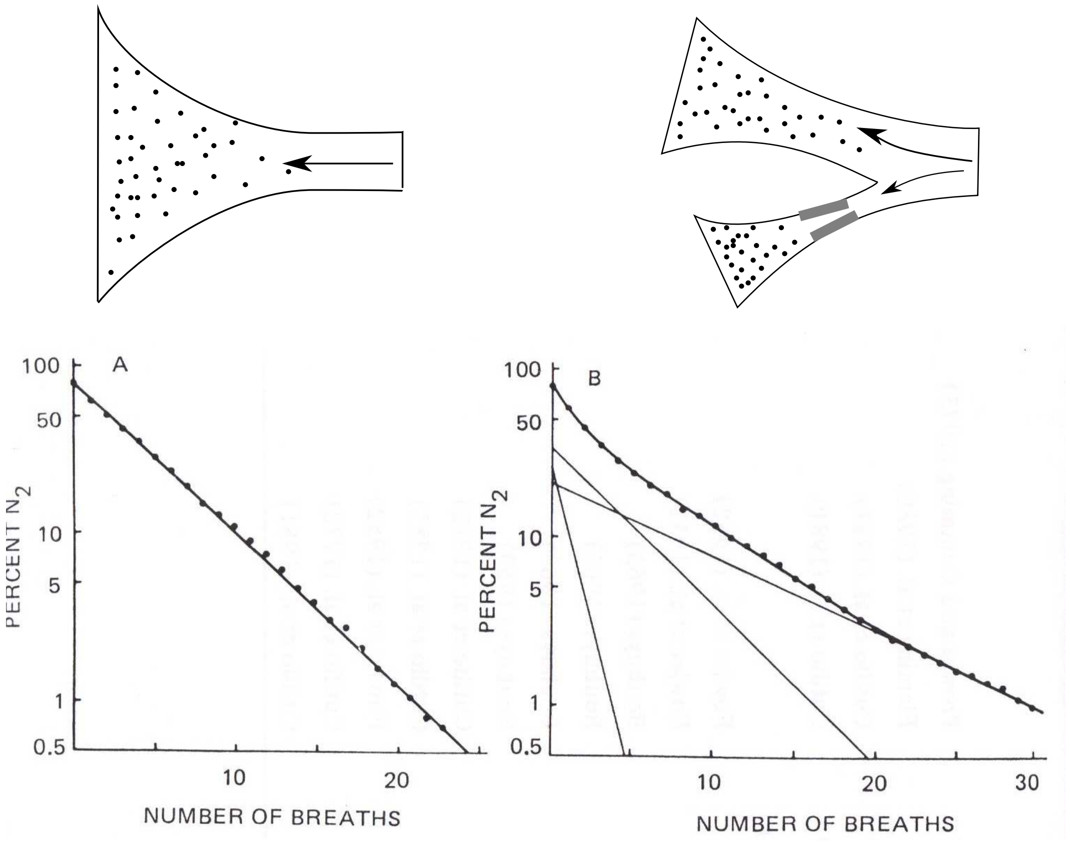

(a) (b)

Figure 2.6: (a) The perfect lung model as a well-ventilated container with perfect gas mixing. The multiple-breath nitrogen washout curve is a straight line. (b) Two (or more) compartment model with two different ventilated rates. The nitrogen washout curve is a sum of two (or more) exponential curves [5] [22, pp. 312].

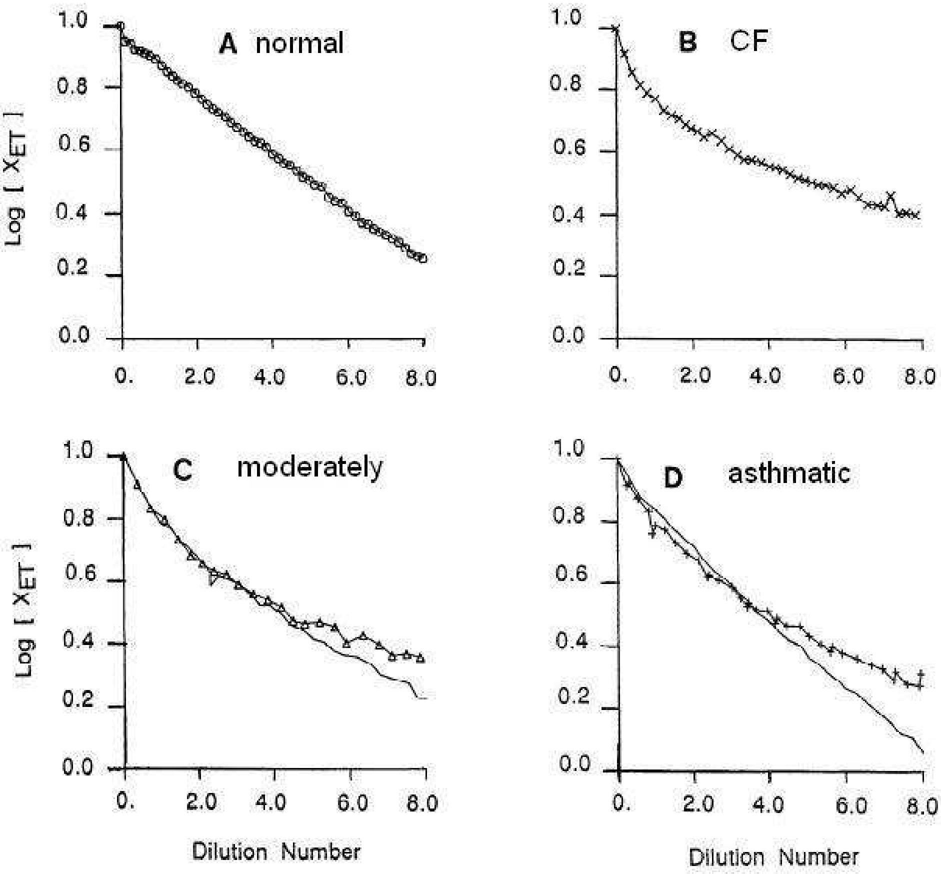

Figure 2.7: The washout curve from A. a normal subject, B. a cystic fibrosis patient, C. a moderately obstructed asthmatic patient, and D. a mildly obstructed asthmatic patient. Washout curves from patients with airway diseases are more curved than the straight line from the normal subject [45].

ideal ventilated unit, C$_{urv}$=1; for more inhomogeneously-ventilated lungs the C$_{urv}$ are less than 1 [80].

2.3.2 Washout Dead space and Phase II

As mentioned in previous section, for single-breath washout measurements, Fowler has solved Bohr's [4] equation for defining a functional dead space (V_{DB}) using a mass conservative principle, *i.e.*,

$$c_E V_T = c_I V_{DB} + c_A V_A \tag{2.11}$$

which can be rearranged as

$$\frac{V_{DB}}{V_T} = \frac{c_E - c_A}{c_I - c_A} \tag{2.12}$$

where c_E, c_I, c_A, V_T, and V_A are the mean expired gas concentration, inspired gas concentration, alveolar gas concentration, expired tidal volume (in this case is the lung vital capacity), and alveolar volume. In SBW, subjects breathe the whole vital capacity, such that V_{DB} approximates the real anatomic dead space. Since in multiple-breath washouts, the tidal volume is far below the vital capacity, a washout dead space (V_{DW}) is defined by the equation

$$\bar{c_n} = c_0 \left(\frac{FRC}{FRC + V_T} \right) \tag{2.13}$$

and

$$FRC = V_{DW} + V_A, \tag{2.14}$$

where $\bar{c_n}$ is the mean tracer gas concentration from the nth expired breath and c_0 is the initial tracer gas concentration in the lungs just before the washout starts. The magnitude of the washout dead space is progressively increasing breath by breath since the inspired gas front is pushed more deeply into the lungs due to the diffusion and the decreasing tracer gas concentration [22]. The effective dead space also depends on the diffusivity of the tracer gas, the tidal volume, and the flow rate from each breath.

Figure 2.8 shows the logarithmic plot of N$_2$ concentration at different points of the expired breath during MBW measurements [66]. Point B represents the Fowler dead space from each breath which is also the washout dead space. The washout curve

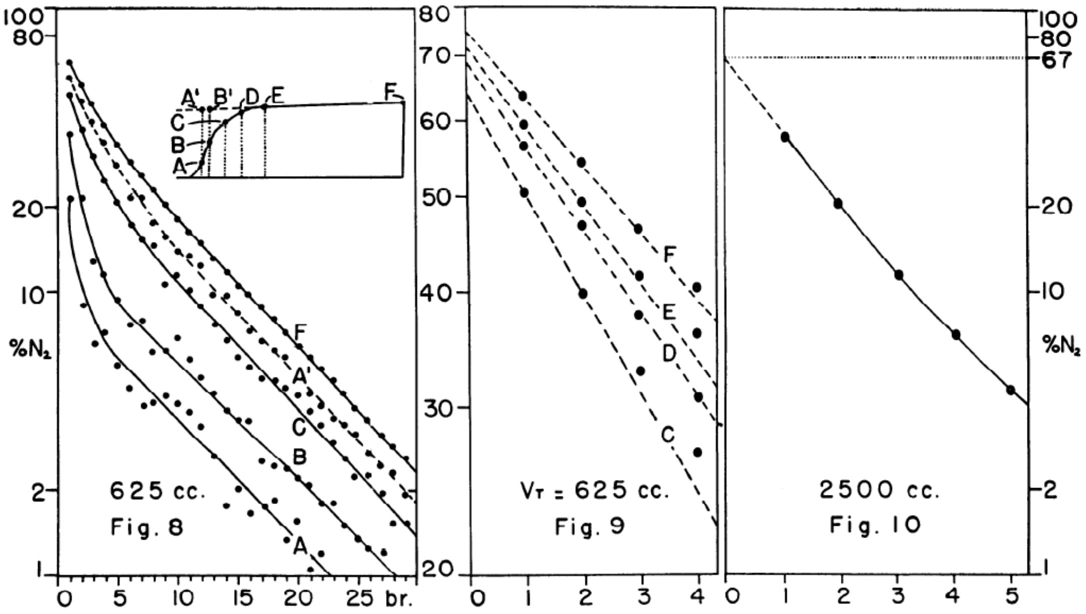

(a) (b) (c)

Figure 2.8: (a) and (b) The logarithmic plot of N_2 concentration at different points of expired breath during MBW measurements with tidal volumes of 625 mL. (c) The N_2 concentration at end-expiration with 2.5-L tidal volumes in MBW [66].

drops sharply in the first few breaths and then decreases steadily which means the dead space front is increasing more for the first few breaths and then reaches a steady value gradually. Approaching the end-expiration (point F), the washout curves are more straight. Figure 2.9(a) shows the washout dead space taken from the mid-point of phase II plotted versus the breath number. In Figure 2.9(b), the phase II slope is decreasing with the breath number in MBNW tests.

2.3.3 Gas Mixing Mechanism and Phase III Slopes

As mentioned in the SBW section, the positive phase III slopes (S_{III}) result from the uneven ventilation among the parallel airway units. The units with less ventilation (less bulk flow enters) contribute more in the later part of phase III while the better-ventilated units contribute more in the early part. The degree of ventilation

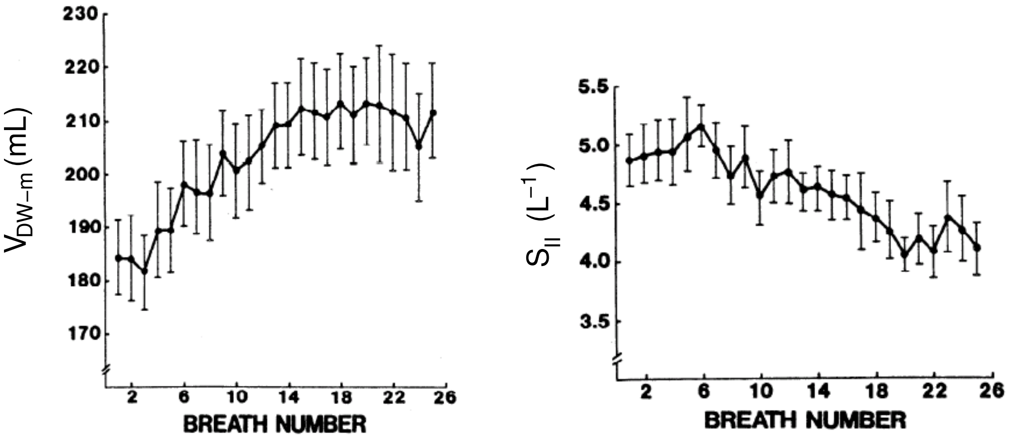

(a) (b)

Figure 2.9: (a) The midpoints of phase II (V_{DW-m}) from the MBNW results. The magnitudes of these midpoints are close to the functional Fowler dead space from each breath. (b) The phase II slopes from each breath. It decreases progressively while the dead space increases breath by breath [14].

inhomogeneity results in the steepness of SBW phase III slope [25]. The slope also depends on the dominant convective mechanism in the conducting airways and the interaction between convection and diffusion near the terminals of the acinar airways. Thus the SBW test can only reflect the overall result but is unable to differentiate between the two mechanisms. However, the series of emptying and filling in MBW tests, the inhomogeneities caused by diffusive-convective interaction or convention result in the first normalised phase III slope (S_{NIII}) value and the increasing rate of S_{NIII} [13, 14, 54, 56, 80].

Each breath from MBW tests has an identical shape to the SBW curve. However, the initial conditions for each breath are not all the same but depend on the previous breath. The mean concentration of tracer gas ($\overline{c_n}$) and the phase III slopes (S_{III}) decrease breath by breath. The normalised phase III slopes (S_{NIII}), which is S_{III} divided by $\bar{c_n}$, increase progressively. The mathematical model followed by the two-compartment model has been developed by Paiva [55]. The nitrogen washout curve of normalised phase III slopes from the real MBNW data and the simulated result is

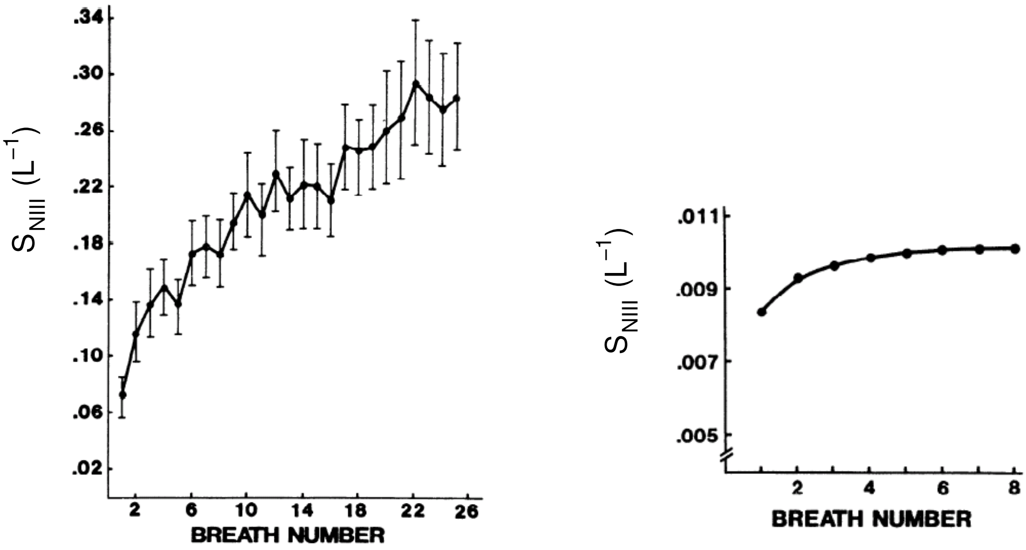

(a) (b)

Figure 2.10: (a) The washout curve of mean normalised phase III slopes from six subjects [14]. (b) The simulated normalised phase III slopes for first eight breaths [57].

shown in figure 2.10. S_{NIII} increases sharply for the first few breaths which is caused by the diffusion- and convection-dependent inhomogeneity (DCDI). It then increases progressively. This progressive increase of S_{NIII} is caused by the convection-dependent inhomogeneity (CDI) [13, 14].

Diffusion- and Convection-Dependent Inhomogeneity (DCDI)

Both the structural and gas distribution asymmetry cause the uneven ventilation among the airways. Near the terminals where the diffusive mechanism dominates the gas transport, the interaction between the bulk flow and the molecular diffusion more likely contributes to an unequal gas concentrations in the parallel units than the diffusion alone [13, 14]. This interaction gives rise to an alveolar slope that is especially high for the first breath as the new dilution gas is transported and starts mixing with the alveolar gas. After a few breaths, this interaction becomes weaker and reaches a steady state since the gas has been mixed well in the small airways. This diffusion and convection interaction is reflected in a sharp increase in the first few breaths of the S$_{NIII}$ washout curve and then remain the same in the rest of the breaths [54, 56, 60, 80].

Convection-Dependent Inhomogeneity (CDI)

The convection-dependent inhomogeneity exists on every single breath since the gas transport is dominated by convection all the way down to the acinar airways. It is caused by the uneven gas distribution and the unequal ventilation from the parallel unit which also results in a positive alveolar plateau. As mentioned previously, the better-ventilated units contribute more in the early part of the expiration while the poorly-ventilated units contribute more in the later part during one single breath. It is also revealed in the consecutive emptying and filling in a clearance MBW model based on the two-compartment model [5] [22, pp. 312]. If this convective ventilation pattern remains the same for all single breath in MBW, by eliminating the variable of the gas concentration, the normalised phase III slopes should remain the same for all breaths. However, in real washout results, there is a progressive increase in S$_{NIII}$ after the first few breaths. This increasing rate can reflect the inhomogeneity of the convective mechanism pattern especially between the better- and poorly-ventilated units [13, 14, 54, 56, 80].

Two Simple Indices: S_{cond} and S_{acin}

Based on the two-compartment model, Paiva pointed out two simple indices for describing the convection-dependent and diffusion-convection-interaction dependent inhomogeneities [55]. Since the increasing rate on the normalised phase III slopes can reflect the degree of the CDI, an index S_{cond}, is thus defined as the increasing rate of S$_{NIII}$ as a function of turnover after the first few breaths. It is found by taking a linear fit to the S$_{NIII}$ washout curve. The slope of that linear fitting curve is defined as S_{cond} [19, 20, 79].

The other index, S_{acin}, is for describing the degree of DCDI which normally takes place in acinar airways. Since the first breath can reflect the most about how the new

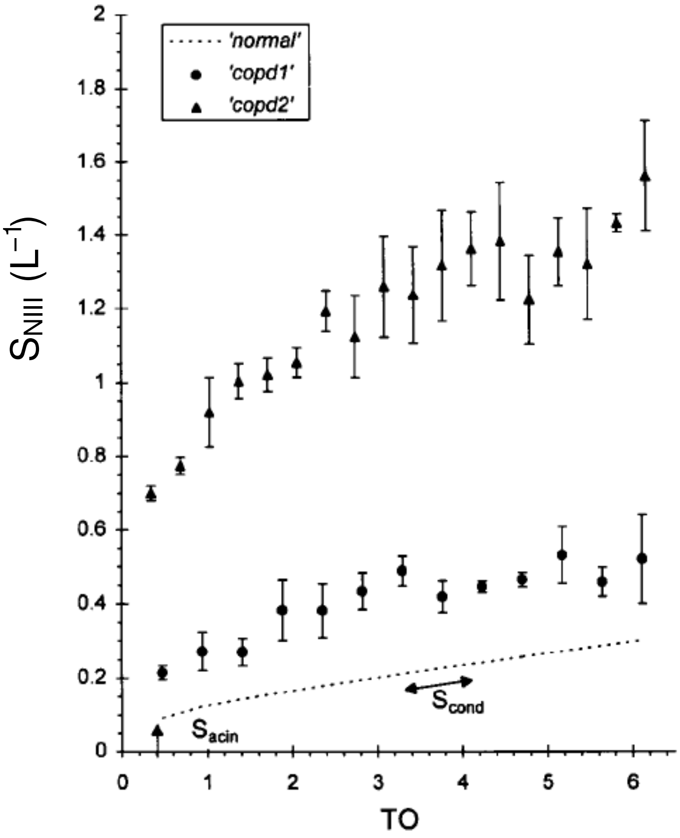

Figure 2.11: The washout curve of normalised phase III slopes versus turnover from a normal subject and two COPD patients [79].

dilution gas interacts with the alveolar gas by convection and diffusion, S_{acin} is given by the first S_{NIII} value eliminating the convection inhomogeneity. Thus, it is defined as

$$S_{acin} = S_{NIII}(1) - S_{cond} \cdot TO(1) \tag{2.15}$$

where $\mathrm{S}_{NIII}(1)$ is the normalised phase III slope of the first breath and $TO(1)$ is the turnover value from the first breath [79]. The turnover is defined as the ratio of the accumulative expired tidal volumes and the lung residual volume FRC.

$$TO(n) = \frac{\sum_1^n V_T(n)}{FRC} \tag{2.16}$$

The magnitudes of S_{cond} and S_{acin} for patients with lung diseases are normally higher than normal persons in MBNW tests as shown in figure 2.11 [79].

Paiva's Mathematical Model

These two indices, S_{cond} and S_{acin}, have been adapted from Paiva's original mathematical model and the following derivation is based on his original paper [55]. The model is based on a few assumptions summarized as follows:

1. The lung consists of two compartments (1 and 2) in parallel which have different ventilation rates $\dot{V}_1(t)$ and $\dot{V}_2(t)$.
2. The inspired gas mixes well instantly in these two compartments and thus the gas concentration from each breath is constant during expiration.
3. The expired flow rate is higher from the better-ventilated compartment, *i.e.*, $\dot{V}_1(t) > \dot{V}_2(t)$.
4. The flow rate from the better-ventilated compartment decreases steadily during expiration ($\ddot{V}_1(t) < 0$) while from the poor-ventilated compartment increases steadily ($\ddot{V}_2(t) > 0$). And the overall flow rate is constant ($\ddot{V}_1(t) + \ddot{V}_2(t) = 0$)[1].

As shown in figure 2.12, consider that these two compartments with gas concentrations $c_{1,n}$, $c_{2,n}$ from the nth expired breath each has an exponential form as a function

---

[1] In real cases, the flow rate is hardly constant.

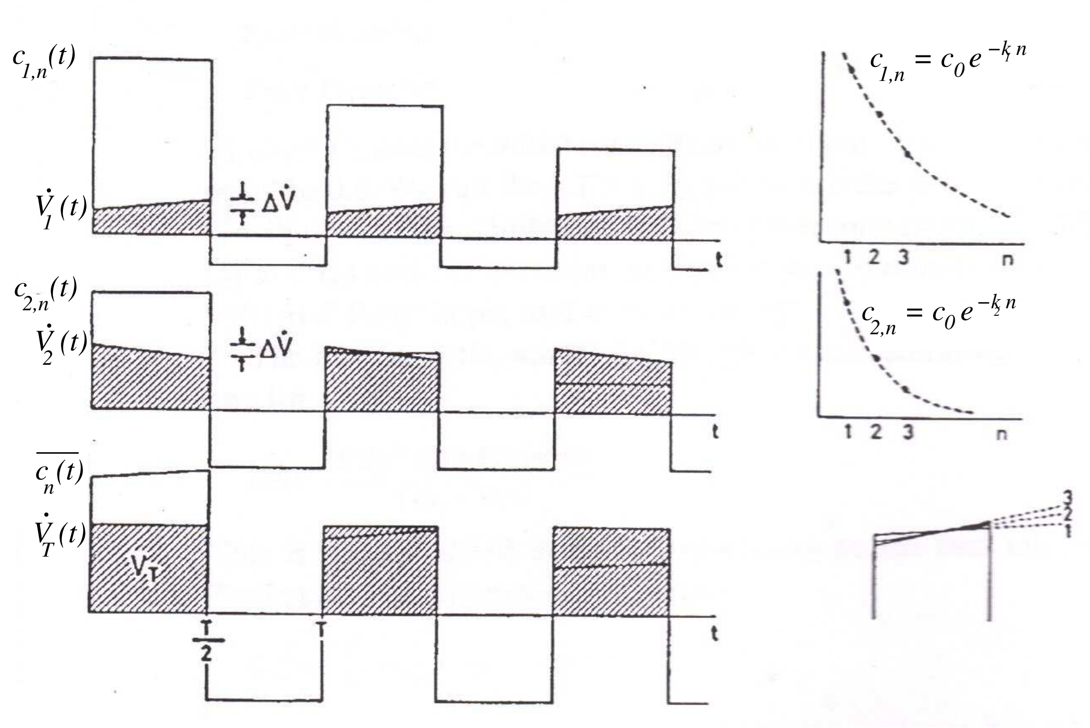

Figure 2.12: The schematic flow and concentration diagram of Paiva's model based on two-compartment model with different ventilation rate. The upper one $c_{1,n}$ is the poorly-ventilated units. The middle one the the better-ventilated units. The bottom one is the overall ventilation. The hashed area is the expired volume. Both of the volume changing rate and the concentration are plotted as a function of time [55].

of breath number with the clearance coefficient k_1 and k_2, *i.e.*,

$$c_{1,n} = c_{1,0}e^{-k_1 n}, \tag{2.17}$$

$$c_{2,n} = c_{2,0}e^{-k_2 n}. \tag{2.18}$$

Both of the initial gas concentration in each compartment $c_{1,0}$ and $c_{2,0}$ are equal to the initial alveolar concentration c_{a0}. The instant expired gas concentration $\overline{c_n(t)}$ can be expressed as

$$\begin{aligned} \overline{c_n(t)} &= \frac{c_{1,n}\dot{V}_1(t) + c_{2,n}\dot{V}_2(t)}{\dot{V}_1(t) + \dot{V}_2(t)} \\ &= \frac{c_{1,n}\dot{V}_1(t) + c_{2,n}(t)\dot{V}_2(t)}{\dot{V}_T} \end{aligned} \tag{2.19}$$

where

$$\dot{V}_T = \dot{V}_1(t) + \dot{V}_2(t) \tag{2.20}$$

is the overall time-dependent expiration flow rate from the lungs.

The phase III slope from the nth breath $d\overline{c_n}/dV$ is the increasing rate of the gas concentration as a function of expired gas volume (V_T) which can be given by

$$\begin{aligned}
\frac{dc_n(t)}{dV} &= \frac{\overline{c_n(\frac{T}{2})} - \overline{c_n(0)}}{V_T} \\
&= \frac{[c_{1,n}\dot{V}_1(\frac{T}{2}) + c_{2,n}\dot{V}_2(\frac{T}{2})] - [c_{1,n}\dot{V}_1(0) + c_{2,n}\dot{V}_2(0)]}{V_T\dot{V}_T(t)} \\
&= \frac{[c_{1,0}e^{-k_1 n}\dot{V}_1(\frac{T}{2}) + c_{2,0}e^{-k_2 n}\dot{V}_2(\frac{T}{2})] - [c_{1,0}e^{-k_1 n}\dot{V}_1(0) + c_{2,0}e^{-k_2 n}\dot{V}_2(0)]}{V_T\dot{V}_T(t)} \\
&= \frac{c_{a0}e^{-k_1 n}[\dot{V}_1(\frac{T}{2}) - \dot{V}_1(0)] + e^{-k_2 n}[\dot{V}_2(\frac{T}{2}) - \dot{V}_2(0)]}{V_T\dot{V}_T(t)} \\
&= \frac{c_{a0}\Delta\dot{V}[e^{-k_1 n} - e^{-k_2 n}]}{V_T\dot{V}_T(t)}
\end{aligned} \tag{2.21}$$

where $\frac{T}{2}$ is the expiration duration time and $\Delta\dot{V}$ is the flow rate change as shown in figure 2.12. The mean concentration from the nth breath is

$$\begin{aligned}
\overline{c_n} &= \frac{[c_{1,n}\dot{V}_1(\frac{T}{2}) + c_{1,n}\dot{V}_1(0)]\frac{T}{2} + [c_{2,n}\dot{V}_2(\frac{T}{2}) + c_{2,n}\dot{V}_2(0)]\frac{T}{2}}{2V_T} \\
&= \frac{Tc_{a0}[e^{-k_1 n}\overline{\dot{V}_1} + e^{-k_2 n}\overline{\dot{V}_2}]}{2V_T}.
\end{aligned} \tag{2.22}$$

The normalised phase III slopes can thus be written as

$$\begin{aligned}
S_{nIII} &= \frac{\frac{d\overline{c_n}}{dV}}{\overline{c_n}} \\
&= \frac{c_{a0}\Delta\dot{V}[e^{-k_1 n} - e^{-k_2 n}]}{\dot{V}_T\frac{T}{2}[e^{-k_1 n}\overline{\dot{V}_1} + e^{-k_2 n}\overline{\dot{V}_2}]} \\
&= \frac{c_{a0}\Delta\dot{V}[e^{-k_1 n} - e^{-k_2 n}]}{V_T[e^{-k_1 n}\overline{\dot{V}_1} + e^{-k_2 n}\overline{\dot{V}_2}]}.
\end{aligned} \tag{2.23}$$

In Paiva's paper [55], two clearance coefficients k_1 and k_2 have been mistakenly regarded as

$$k_1 + k_2 = \frac{V_1 + V_2}{FRC} = \frac{V_T}{FRC}. \tag{2.24}$$

However, in practice the gas concentration from two compartments should be given by

$$\begin{aligned} c_{1,n} &= c_{a0}\left(\frac{FRC_1}{FRC_1+V_1}\right)^n \\ c_{2,n} &= c_{a0}\left(\frac{FRC_2}{FRC_2+V_2}\right)^n, \end{aligned} \tag{2.25}$$

where

$$FRC = FRC_1 + FRC_2, \tag{2.26}$$

$$V_T = V_1 + V_2. \tag{2.27}$$

Thus k_1 and k_2 is more accurately given separately by

$$e^{-k_1} = \frac{FRC_1}{FRC_1+V_1}, \tag{2.28}$$

$$e^{-k_2} = \frac{FRC_2}{FRC_2+V_2}. \tag{2.29}$$

The normalised phase III slope can thus be re-written down as

$$S_{NIII} = \frac{c_{a0}\Delta\dot{V}\left[\left(\frac{FRC_1}{FRC_1+V_1}\right)^n - \left(\frac{FRC_2}{FRC_2+V_2}\right)^n\right]}{\dot{V}_T\frac{T}{2}\left[\left(\frac{FRC_1}{FRC_1+V_1}\right)^n\overline{\dot{V}_1} + \left(\frac{FRC_2}{FRC_2+V_2}\right)^n\overline{\dot{V}_2}\right]}. \tag{2.30}$$

If we re-define the clearance coefficients CL_1 and CL_2 as

$$CL_1 = \frac{FRC_1}{FRC_1+V_1} \tag{2.31}$$

$$CL_2 = \frac{FRC_2}{FRC_2+V_2}, \tag{2.32}$$

S_{NIII} can be re-written down as

$$S_{NIII} = \frac{c_{a0}\Delta\dot{V}\left[{CL_1}^n - {CL_2}^n\right]}{\dot{V}_T\frac{T}{2}\left[{CL_1}^n\overline{\dot{V}_1} + {CL_2}^n\overline{\dot{V}_2}\right]}. \tag{2.33}$$

The changing rate of S_{NIII} as a function of n can be given by

$$\frac{dS_{NIII}}{dn} = \frac{c_{a0}\Delta\dot{V}}{\dot{V}_T\frac{T}{2}} \cdot \frac{\left[{CL_1}^n \cdot {CL_2}^n \cdot ln\frac{CL_1}{CL_2} \cdot \left(\overline{\dot{V}_1} + \overline{\dot{V}_2}\right)\right]}{\left[{CL_1}^n\overline{\dot{V}_1} + {CL_2}^n\overline{\dot{V}_2}\right]^2} \tag{2.34}$$

$$= \frac{c_{a0}\Delta\dot{V} ln\frac{CL_1}{CL_2}}{\frac{T}{2}} \cdot \frac{\left[{CL_1}^n \cdot {CL_2}^n\right]}{\left[{CL_1}^n\overline{\dot{V}_1} + {CL_2}^n\overline{\dot{V}_2}\right]^2}. \tag{2.35}$$

Thus, $\frac{dS_{NIII}}{dn}$ is always positive as long as the clearance coefficient from the poorly-ventilated compartment is higher than from the better-ventilated compartment, *i.e.*, $CL_1 > CL_2$ or $\frac{V_1}{FRC_1} < \frac{V_2}{FRC_2}$. As mentioned previously, S_{cond} is the increasing rate of $\frac{dS_{NIII}}{dn}$ after the first few breaths, and S_{acin} is given in Eq. 2.15 as the S_{NIII} from the first breath with the subtraction of S_{cond}. Thus, two indices can be given by

$$S_{cond} = \frac{dS_{NIII}}{dn}_{n\rightarrow\infty} \tag{2.36}$$

$$= \frac{c_{a0}\Delta\dot{V}}{\frac{T}{2}} \cdot ln\frac{CL_1}{CL_2} \cdot \frac{CL_2{}^n}{CL_1{}^n\overline{\dot{V}_1}^2}, \tag{2.37}$$

$$S_{acin} = \frac{c_{a0}\Delta\dot{V}\,[CL_1 - CL_2]}{\dot{V}_T\frac{T}{2}\left[CL_1\overline{\dot{V}_1} + CL_2\overline{\dot{V}_2}\right]} - \frac{c_{a0}\Delta\dot{V}}{\frac{T}{2}} \cdot ln\frac{CL_1}{CL_2} \cdot \frac{CL_2{}^n}{CL_1{}^n\overline{\dot{V}_1}^2}. \tag{2.38}$$

Figure 2.13 shows six S_{NIII} curves as a function of n with the same residual capacity ($FRC = 3.6$ L), expiration duration ($\frac{T}{2} = 2.5$ sec), initial alveolar concentration ($c_{a0} = 0.8$) but different FRC_1 and FRC_2, V_1 and V_2, tidal volume V_T, and flow rate change $\Delta\dot{V}$. The S_{cond} and S_{acin} values from each curve are also displayed. Since Paiva's model has idealised the expiration pattern by assuming instantly well-mixed gas and constant flow rate, it is hard to correlate the S_{cond} value to the ventilation inhomogeneity in the conduction airways or the S_{acin} value to the inhomogeneity in the acinar airways. It can only be roughly summarised that the higher ratio of two clearance coefficients (CL_1/CL_2) or the higher flow rate change ($\Delta\dot{V}$) gives the higher values of S_{cond} and S_{acin}. It means when the flow or the expansion from the less-ventilated compartment is badly restricted compared to the better-ventilated compartment, the resulting S_{cond} and S_{acin} values are relatively high. However, the definition of S_{acin} in Paiva's mathematical model is contradictory in physiological model. S_{acin} is defined as an index to tell the degree of inhomogeneity in the acinar airways. It comes from the first breath with the subtraction of the conductive inhomogeneity since the interaction between oxygen and nitrogen is weighted the most for the first breath. The existence of the interaction between two gases is contradictory to the well-mixed assumption which Paiva's model is based on. Therefore, the model is unable to reveal the real washout results.

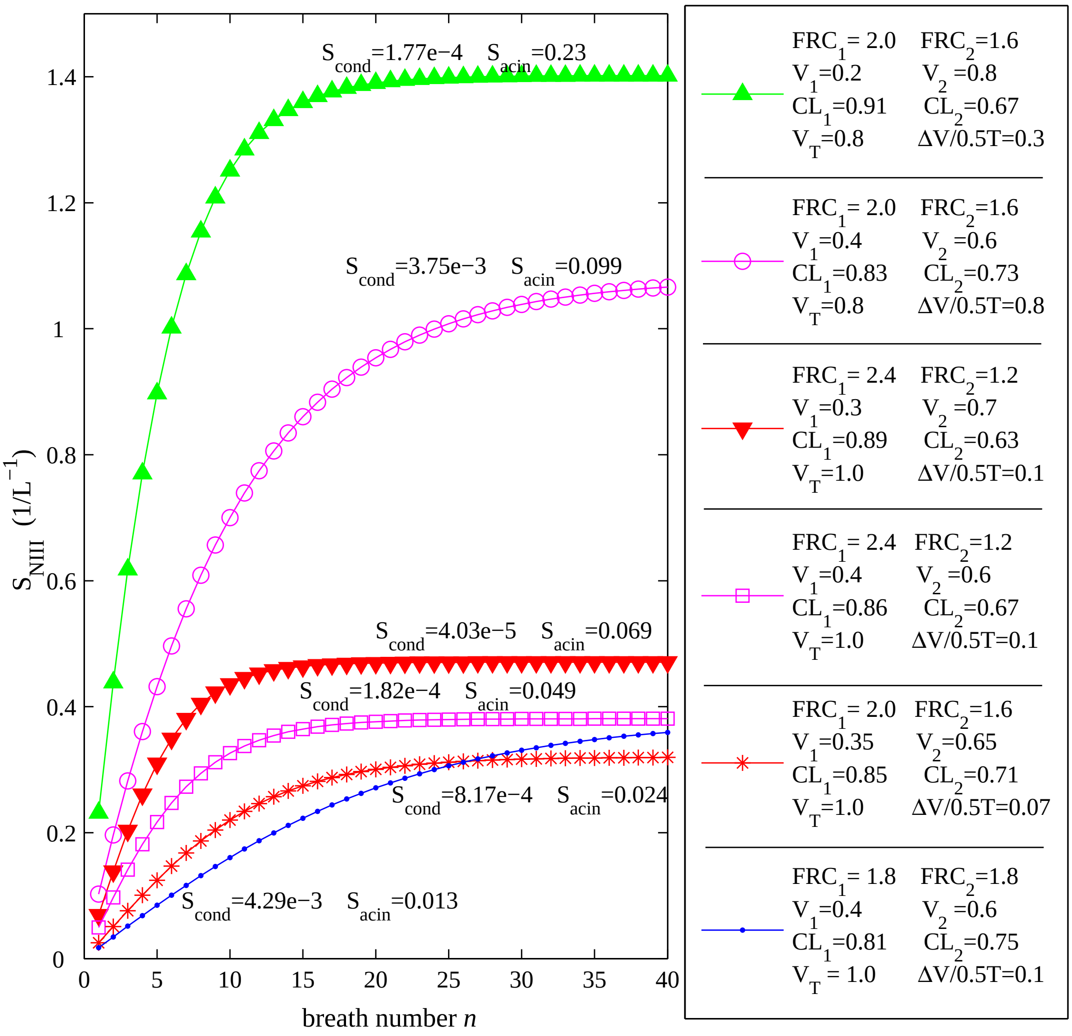

Figure 2.13: The simulation results from the Paiva's two-compartment mathematic model. The normalised phase III slope S_{NIII} as a function of breath number n with initial alveolar concentration $c_{a0} = 0.8$, $FRC = 3.6(L)$ and $T/2 = 2.5(sec)$. Six different curves represent different FRC_1 and FRC_2 (in L), V_1 and V_2 (in L), CL_1 and CL_2 (dimensionless),V_T (in L), and $\Delta\dot{V}(=\Delta V/0.5T$, in L/sec).

The comparison of the normalised phase III slopes S_{NIII} and the clearance washout results has rarely been shown in recent studies of MBW measurements. Therefore, it will be a key part in the analysis on MBHW measurements.

2.3.4 Continuous Emptying Pattern on 50-Compartment Model

Unlike the simple two-compartment model, S. Lewis has developed a more complex model that the human lungs are consisted of 50 parallel compartments with different ventilations [43, 44]. Each compartment i is specified by the ventilation $V_T \cdot \dot{V}(i)$ and its tidal ventilation $S(i)(= V_T \cdot \dot{V}(i)/V_0(i))$, where V_T is the overall tidal volume, $\dot{V}(i)$ is the fraction of the ventilation from ith compartment, and $V_0(i)$ is the volume of the compartment at end expiration. The mean concentration of the jth breath (C_j) is given by the summation of all compartments

$$\frac{C_j}{C_0} = \sum_{i=1}^{50} \dot{V}(i) \cdot \left(\frac{1}{1+S(i)}\right)^j \equiv M(j, \vec{V}) \tag{2.39}$$

where C_0 is the initial nitrogen concentration before the washout started and $\vec{V}$ indicates the collection of $\dot{V}(i)$. The washout data were analysed by minimising the expression

$$\sum_j \left[W(j) \cdot \left(\frac{C_j}{C_0} - M(j, \vec{V})\right)\right]^2 + 0.001 \cdot \sum_i \left[WC(i) \cdot \dot{V}(i)\right] \tag{2.40}$$

where $W(j)$ is a weighting constant (which has been set as unity), and $WC(i)$ is the weighting function given by $1/C_1 \cdot (1 - C_n)$ where C_1 and C_n are concentrations in a given compartment on the first and last breaths from the washout data, respectively. Two assumptions have been made in this model. The tidal ventilation $S(i)$ is fixed for each specified compartment from each breath during the washout measurement. The specified compartments were equally spaced on a log scale from a specific ventilation of 0.005 to 10 [44]. The washout results from 15 obstructive patients show a wide unimodal distribution in poorly ventilated units or bimodal distribution in very poorly- and very well-ventilated units. However, for the normal young subjects, the results show a narrow unimodal distribution at the well-ventilated units [43] as shown in figure 2.14.

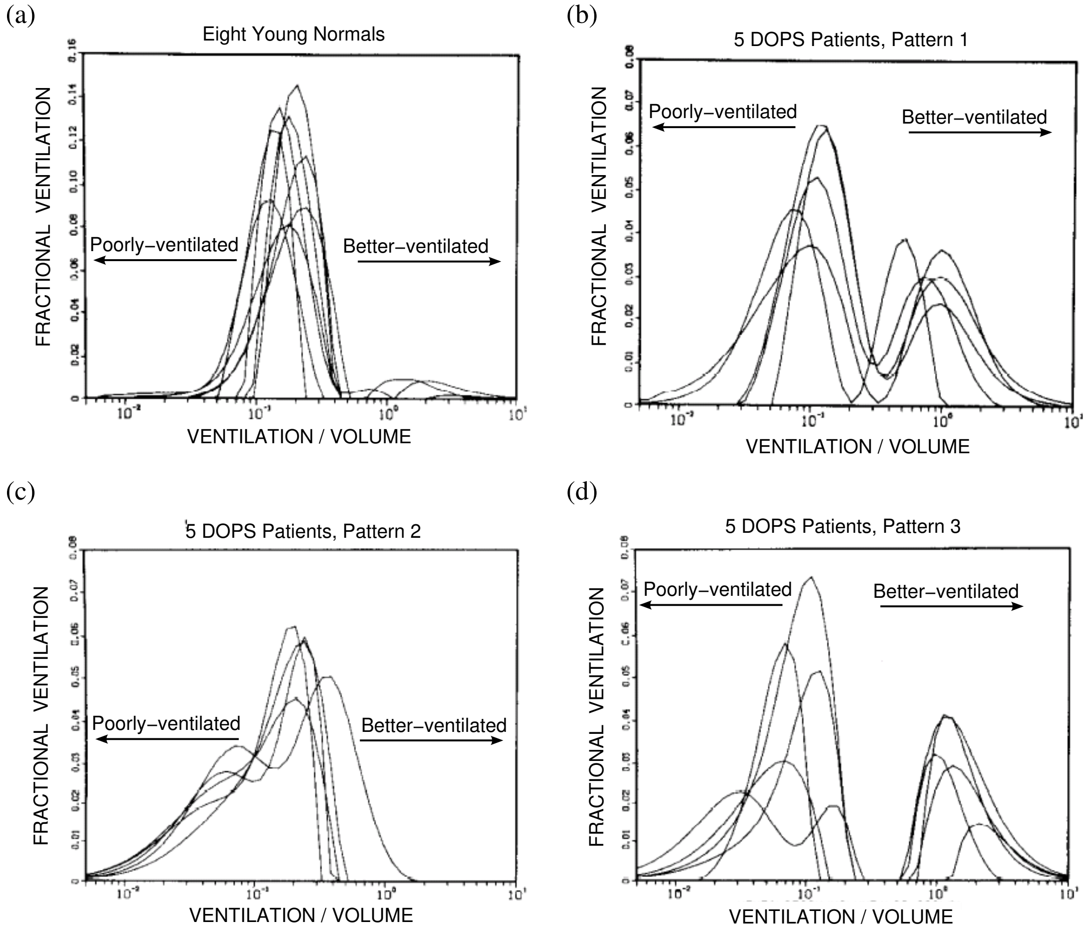

Figure 2.14: The washout results based on the analysis of 50-compartment model. The fractional ventilation is plotted as a function of relative tidal ventilations (tidal ventilation/lung volume). (a) shows the results from 8 young normal people. All show a narrow unimodal distribution located at around 0.2 relative ventilations. Occasionally another small peak appears at better- ventilated units with the value of 1 to 2 relative ventilations. (b), (c) and (d) show three different patterns from 15 subjects (5 for each graph) with diffuse obstructive pulmonary syndromes (DOPS). Pattern 1 and 3 show bimodal distribution with very poorly- and well-ventilated units. Pattern 2 shows a wide unimodal distribution lacking of very well-ventilated units [44].

The new model of tidal emptying pattern has been developed in a few modern studies with the consideration of gas re-breathing from the dead space [26, 84]. The mathematical model based on the one- and 50-compartment model are described and compared with the results from the inert gas elimination technique. Unlike the MBW technique, the tracer gas is inserted into the blood and the concentration of the tracer gas is sampled by taking the blood sample. From the inert gas elimination results, the breathing pattern is more likely tidal emptying instead of continuous which means the gas re-breathing from the dead space is unable to be ignored.

Chapter 3

MBHW System

3.1 Overview

The multi-breath-helium-washout (MBHW) system built in Nottingham is introduced in this chapter. Helium gas is used as the tracer gas instead of nitrogen and washed out by room air in the MBHW measurements. First, the heliox gas (21% O_2+79%^{4}He) is inhaled until the air is flushed out of lungs which is the helium wash-in (or the nitrogen washout) process. The helium washout measurement is followed by the wash-in process by switching the inhaled gas supply from the heliox to room air. All the measurements are made at room temperature(18±2 ^{o}C) under atmosphere (100±3 kPa) in a lab with windows open. Calibrations have been made for sensors and linear fitting curves have been applied to some of the data. All the fittings have been done by the MatLab curve fitting tool box (v7.0.4) and the goodness of those fittings are represented by SSE (the sum of squares due to error), R-square (the coefficient of multiple determination which represents how successful the fit is, a value closer to 1 indicates a better fit), and RMSE (the root mean square error, a value closer to 0 indicates a better fit)[1].

The whole system can be divided into two main parts, the gas volume measuring and the gas analysing system as shown in figure 3.1. The gas volume measuring system

---

[1] More details about the meaning of those three values can be referred to the user guide of MatLab (v7.0.4).

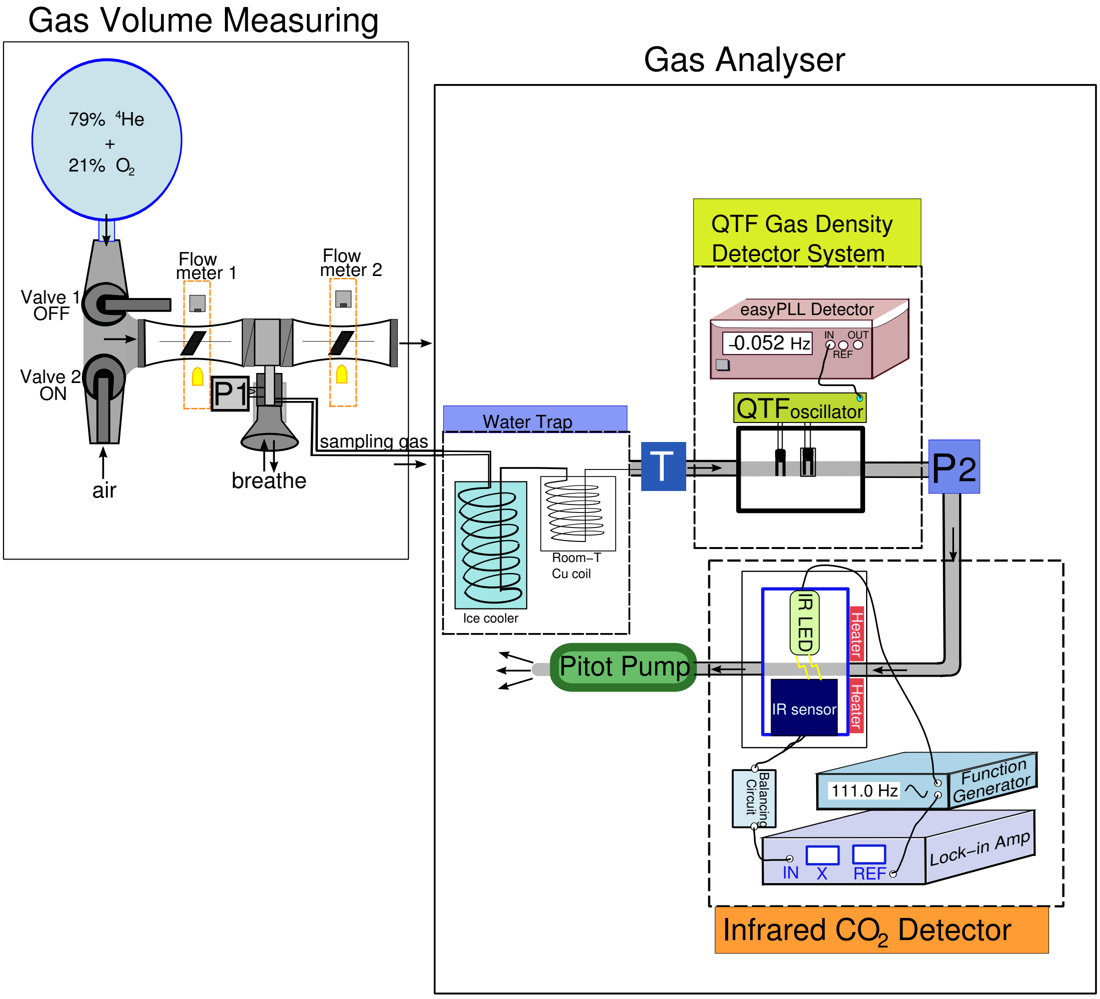

Figure 3.1: MBHW System.

uses turbine and a pressure sensor to monitor the pressure at the mouth and two flow meters to measure the inspired and expired gas volumes. The gas analysing system consists of a quartz-tuning-fork (QTF) gas density detector, and an infrared (IR) CO_2 detector. Since the expired gas mixture from our lungs is saturated with water vapour which interferes with the QTF and IR detector signal, a water trap has been used to filter out the water vapour. A quartz tuning fork, with a resonant frequency (f_c) 32768 Hz, is used as a gas density detector. Its resonant frequency is linearly related to the surrounding gas density and gives a big response to helium gas (with about 4 Hz frequency shift for heliox). The concentration of carbon dioxide is monitored by an infrared absorption detector. The temperature and the pressure are monitored by a filament-type thermistor and a silicon-diaphragm differential pressure sensor. The sampling gas is pumped by a Pitot-type air pump.

3.2 Gas Volume Measuring System

The system diagram is shown in Figure 3.2. The mouth-piece is connected to two flow meters for measuring the inspired and expired gas volume. A pressure sensor (26PCCFA1D, Honeywell, UK) connected nearby the mouth-piece is for detecting the direction of the flow. Its signal (P1) is coupled through a break out box to the PC and is used in LabView (DAQboth.vi) to reset the volume measurement when changing the breathing direction.

Each flow meter consists of a one-way valve, a LED emitter (Op290A GaAlAs Plastic infrared emitting diode, Optek Technology, US) and receiver (OPB917 Photologic slotted optical switch, Optek Technology, US), and a turbine (Medical turbine, MicroMedical, UK) with a light, black turbine fan inside. Each receiver is connected to a circuit which consists of a counter, a digital-to-analog converter and an operational amplifier. The LED emitter and receiver are fixed close to the turbine and opposite to each other with the fan blade in between. When there is no gas flowing through, the LED light is blocked out by the fan (figure 3.3(a)). When the gas passes through the turbine, the fan starts rotating, the LED light is unblocked and received by the LED

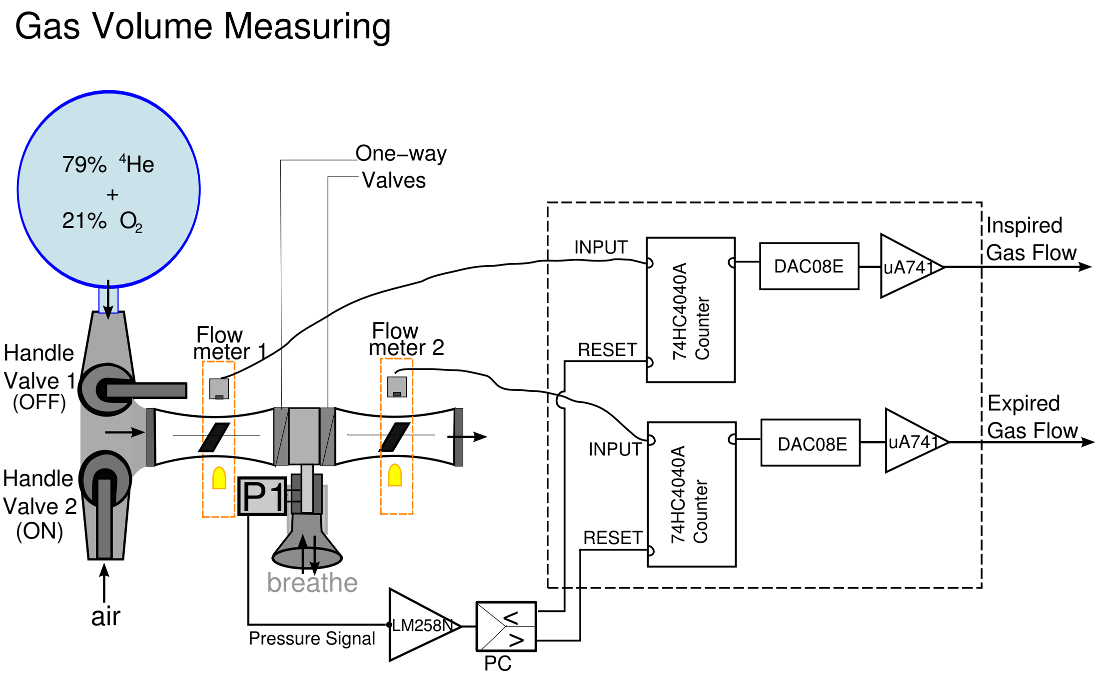

Figure 3.2: The Gas Volume Measuring System. Two handle valves control the inspired gas (heliox or air). Two turbines for measuring the number of rotations of the fan which is proportional to the gas volume. The signal of two LED receivers goes into a circuit for converting the digital signal to the analog signal. The pressure sensor is for defining the flow direction and tells the PC to send a pulse signal resetting the counters. The system dead space (between the mouth-piece and two one-way valves) is 10.4±0.05 mL.

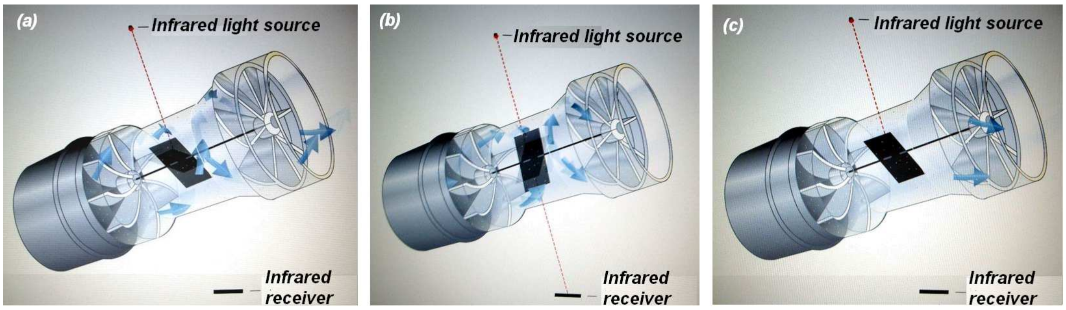

Figure 3.3: Turbine and LED detecting diagram. (a) The gas flowing through and the fan starts rotating. (b) The light is unblocked and received twice per cycle. (c) No gas flowing through the fan stops rotating and light is blocked again. (*http://www.micromedical.co.uk/products/animatedturbine2.swf*)

receiver twice per rotation which sends a pulsed signal to the counter (figure 3.3(b)). During expiration, the pressure signal (P1) is higher than the non-flowing signal which tells the computer to send a pulse, resetting the inspiration counter to zero. On the other hand, during inspiration a pulse signal is sent to reset the expiration counter. Since the fan is very light, the inertial force from its mass can be ignored. Therefore, the gas volume passing through can be assumed to be proportional to the number of rotations. The whole system is controlled by a LabView programme (DAQboth.vi) which will be described in the following chapter.

Commercial medical pneumotac flow meters applied to spirometry are not suitable for this experiment. They detect the pressure difference across a fine mesh which is dependent on the gas viscosity. According to the Poiseuille law, the pressure drop (ΔP) in a laminar, incompressible, viscous fluid flowing through a long cylindrical pipe can be given by

$$\Delta P = -\frac{8\mu l Q}{\pi r^4} \tag{3.1}$$

where μ is the dynamic viscosity of the fluid which is different from air (188.5 mP) to helium (209.5 mP) [29], l is the length of the pipe, Q is volumetric flow rate, and r is the radius of the pipe. Thus they cannot be applied to a gas mixture with an unknown concentration of multiple constituents. The other end of the inspiration turbine is connected to two full-way manual handle valves with 1 cm inner diameter. One of them is open to room air and the other is connected to a 80 litre foil balloon full of heliox gas at room temperature. During the washout measurement, the composition of the inspired gas is controlled manually by switching on and off the manual valves.

3.3 Gas Analysing System

The system consists of a water trap, a quartz-tuning-fork (QTF) gas density detector, an infrared (IR) absorption CO_2 detector, a thermistor (T), and a pressure sensor (P2) as shown in Figure 3.1. The sampling gas is taken from nearby the mouth and flows through the water trap first to filter out the water vapour. The water trap is made of a stainless steel coil dipped in an ice bath joined to a copper coil at room temperature which is introduced in section 3.4. The QTF gas density detector system is the key sensor for this multiple gas analyser system and is introduced in section 3.5. The infrared CO_2 detection cell is the other main sensor in this system since the exhalation consists of about 4% carbon dioxide. To reduce the water vapour condensed on the wall which would block the IR signal, two heaters are attached to the infrared cell with a temperature control circuit. More details are introduced in section 3.6.

A thermistor is connected near the water trap for monitoring the temperature of the gas entering the QTF cell. It is described in section 3.7. The other end of the QTF cell is connected to a pressure sensor for detecting the pressure nearby the tuning fork. It is described in section 3.8 The thermistor and pressure sensor need to be connected together close to the QTF cell because the density of gas depends on pressure and temperature which should be taken into account when calculating the concentrations of the gases. The sampling gas is pumped with a Pitot-type air pump which is more stable than other mechanical diaphragm pumps and will be described in section 3.9.

The washout measurement block diagram is shown in figure 3.4. Before the washout measurements start, subjects are asked to do several normal breaths. This is to de-

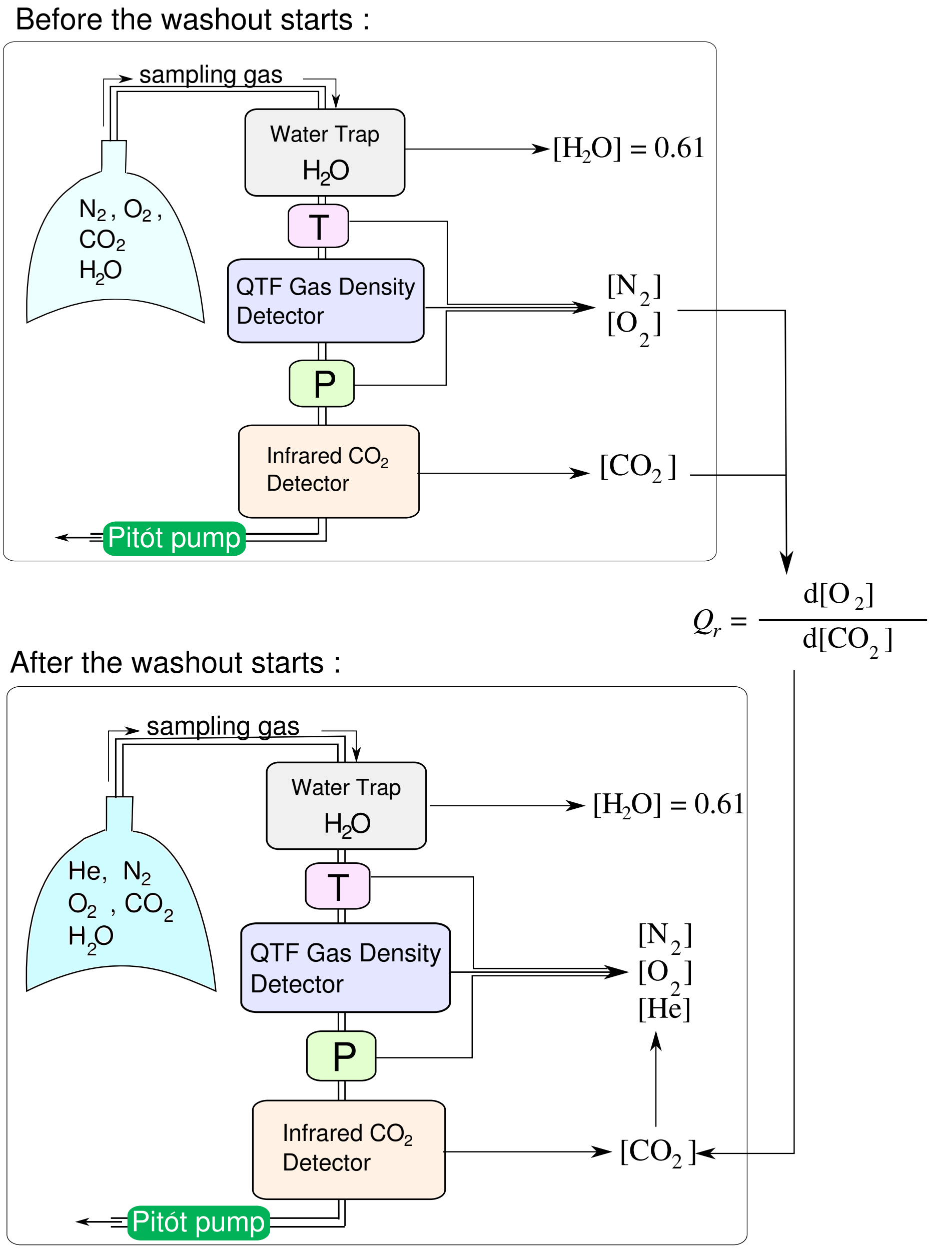

Figure 3.4: Washout Measurement Block Diagram

termine the concentration changing rate of oxygen consumption (d[O_2]) versus carbon dioxide production (d[CO_2]), Q_r, from each subject. The reason for this pre-washout CO_2 measurement is because of the difficulty of detecting oxygen or nitrogen. Mass spectrometers are normally used for detecting nitrogen concentration but have slow response for the washout measurement. Commercial oxygen sensors such as electro-galvanic fuel cells have even slower response (more than 3 seconds) or in high price such as phosphorenscense life time method (response time 0.1 seconds). Therefore, the combination of QTF density and CO_2 measurement can be regarded as an indirect method of oxygen sensing by getting the Q_r value for each subject which we assume it is constant during the washout measurements.

3.4 Water Trap

The water trap (Figure 3.5) consists of a coil (inner diameter 3.5 mm) made of stainless steel dipped in an ice bath followed by a copper coil (inner diameter 1.5 mm) at room temperature. Water vapour is condensed on the wall of the stainless steel coil which has slightly lager inner diameter than other tubes in case the gas is blocked by water droplets. The temperature, pressure, and the flow rate of the sampling gas is stabilised by the narrow copper coil.

The efficiency of the water trap cannot be quantified accurately in this work. The main reason is that the sampling gas is always pumped under a high speed (dynamic pressure is about 0.9 atm) through the sensors while normal commercial humidity detectors have a slow response. A humidity measurement has been made with a moisture meter (The Shaw Automatic Dewpoint Meter, Shaw, UK) which gives the same response to room air as to the gas filtered by the water trap. Without the water trap, water droplets can be condensed on the QTF which causes QTF signal to drift out of the detectable range during the washout measurement (less than two minutes). This takes more than two hours to dry up. With the water trap, the QTF signal is detectable for longer than half an hour. According to the Goff-Gratch equation, which describes the partial pressure of the water vapour saturated in air varying with temperature,

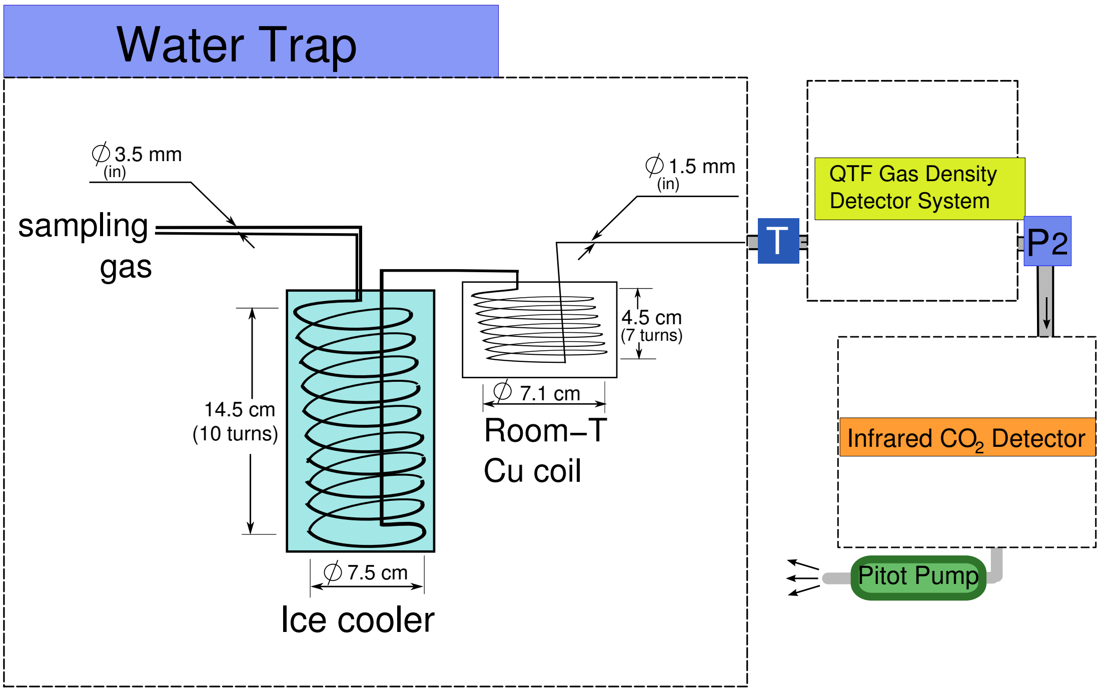

Figure 3.5: Water Trap

$$\begin{aligned}
Log_{10}P_{H_2O} \quad = \quad & -7.90298\left(\frac{373.15}{T}-1\right)+5.02808\times Log_{10}\left(\frac{373.15}{T}\right) \\
& -1.3816\times 10^{-7}\left(10^{11.344\left(1-\frac{373.15}{T}\right)}-1\right) \\
& +8.1328\times 10^{-3}\left(10^{-3.49149\left(\frac{373.15}{T}-1\right)}-1\right) \\
& +Log_{10}1013.25 \qquad (3.2)
\end{aligned}$$

$$P_{H_2O}(T=0^oC) \quad = \quad 0.61 \qquad (3.3)$$

$$P_{H_2O}(T=38^oC) \quad = \quad 6.62 \qquad (3.4)$$

where $P_{H_2O}(T)$ is the saturated water vapour in kPa in the air at temperature T (in Kelvin). We simply assume the expiration is saturated with water vapour (6.54 % at 38 ^{o}C) passes through the 0 ^{o}C water trap leaving only 0.60 % of water vapour remaining in the gas. A more accurate saturated water vapour pressure can be determined by measuring the temperature of the sampled gas mixture flowing through the water trap with a quick-response thermistor.

3.5 QTF Gas Density Detecting System

To detect helium gas accurately and efficiently is always a challenge because of its small density and high mobility. Traditionally, mass spectrometers are used as helium leak detectors especially in vacuum systems. However, their slow response prevents application to the washout measurement. Other sensors for helium leak detectors such as ultrasonic transducers can only detect small amount of helium because of the high acoustic attenuation in mixtures or low signal-to-noise ratio. In helium washout measurements, high accuracy and quick response (less than 0.01 sec) is required. Thus, instead of the traditional methods mentioned above, a quartz tuning fork with a phase-lock-loop frequency detector is used as the gas density detector which gives quick response to the helium gas. The response-time measurement is described in section 3.10.4.

Piezoelectric quartz tuning forks are normally used as frequency standards in digital watches. Because of their high stability and quality factor (10,000 in air), quartz tuning

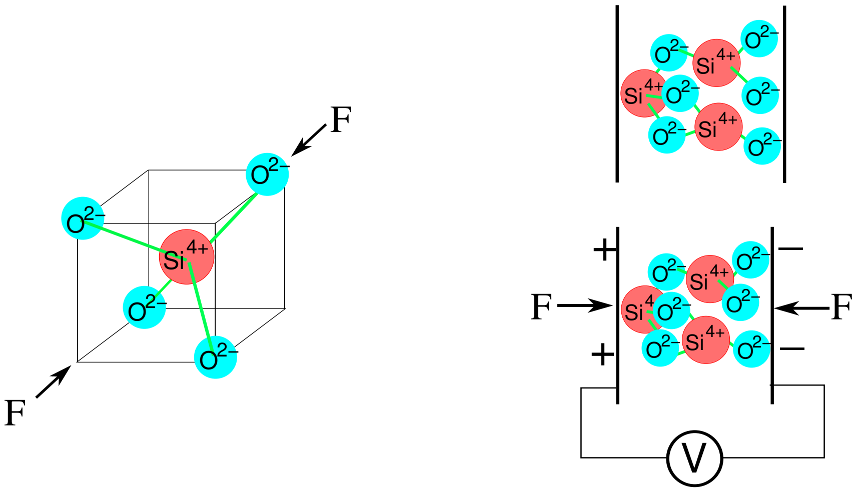

(a) (b)

Figure 3.6: (a) Crystal structure of quartz SiO_2. (b) Piezoelectricity of the quartz. When an external mechanical force applied on it which causes the crystal deformation, there exists an electric potential of the crystal.

forks have been used in various sensor applications; for example, measuring the thermal properties of liquid helium [3], as force sensors for atomic force microscopy [28], as SF_6-gas density sensors [89], and as mass sensitive sensors in liquid [90].

3.5.1 Theory

Piezoelectricity

Quartz (SiO_2) crystals have been known to have a piezoelectric property, *i.e.*, they generate the electric potential when an external mechanical stress is applied. The piezoelectricity is the ability to convert the mechanical deformed potential to the electric potential. Figure 3.6 shows the piezoelectricity of the quartz crystal. The inverse piezoelectric effect converts the external electric potential to a mechanical deformation. This effect explains the quartz tuning fork oscillation.

The typical tuning fork has two tines (with length L=3.98 mm in this work) and a rectangular cross-section (of thickness h=0.40 mm and width b=0.60 mm). The mechanical resonance of the tuning fork geometry is coupled electrically to the metal

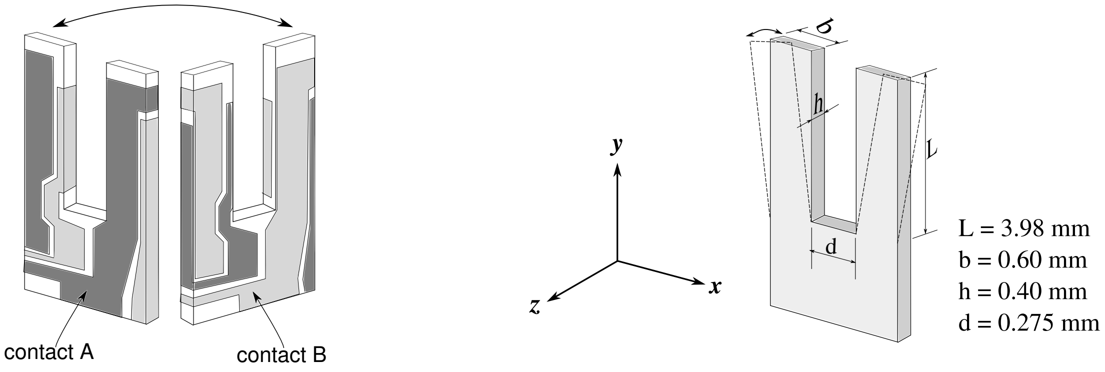

(a) (b)

Figure 3.7: Sketch of the quartz tuning fork

contacts on the surface of the quartz. The electrical metal contacts are made of silver, patterned on the surface of the tines (Figure 3.7(a)) to excite a flexural mode of oscillation as shown in Figure 3.7(b) dashed lines.

Damping Oscillator

When a tuning fork is placed in a fluid medium, each tine can be regarded as a damped oscillating cantilever. The equation of motion can be given by the form of harmonic oscillator for the fundamental mode with a driving force F at angular frequency ω, *i.e.*,

$$Fe^{i\omega t} = m_e \frac{\partial^2 x}{\partial t^2} + m_e \gamma \frac{\partial x}{\partial t} + kx, \tag{3.5}$$

where m_e is the effective mass of the cantilever, x is the relevant vibrating displacement, γ is the drag force constant caused by the viscosity of the fluid, and k is the elastic constant of the cantilever. For a uniform cantilever beam with rectangular cross section, k can also be expressed in terms of the Young's modulus E [11]

$$k = E\frac{h^3 b}{4L}, \tag{3.6}$$

where h, L, and b are the dimensions of the cantilever beam as shown in Figure 3.7 [11]. The related fundamental resonant frequency f can be expressed in a general form of

$$\begin{aligned} f = \frac{\omega}{2\pi} &= \frac{1}{2\pi}\sqrt{\frac{k}{m_e}} \\ &= \frac{1}{2\pi}\sqrt{\frac{Eh^3b}{4Lm_e}} \\ &= \frac{C_q}{2\pi}\sqrt{\frac{E}{\rho_q+\rho_g}}, \end{aligned} \tag{3.7}$$

where C_q is the geometry factor of the cantilever, ρ_q and ρ_g are the density of the cantilever (quartz) and the surrounding medium (gas), respectively. For small gas density ρ_g compared to the density of quartz ρ_q, the frequency shift (Δf_g), can be expressed as

$$\begin{aligned} \frac{\Delta f_g}{f_v} &= \frac{f_v - f_g}{f_v} \\ &= 1 - \sqrt{\frac{\rho_q}{\rho_q+\rho_g}} \\ &\cong \frac{1}{2}\left(\frac{\rho_g}{\rho_q}\right), \end{aligned} \tag{3.8}$$

where the resonant frequency in vacuum (f_v) and in gas (f_g) are given by

$$f_v = f(\rho_g = 0) = \frac{C_q}{2\pi}\sqrt{\frac{E}{\rho_q}}, \tag{3.9}$$

$$f_g = f(\rho_g > 0) = \frac{C_q}{2\pi}\sqrt{\frac{E}{\rho_q+\rho_g}}. \tag{3.10}$$

The resonant frequency in heliox-air mixture (f_{He}) can be related to the resonant frequency in nitrogen (f_{N_2}) and carbon dioxide (f_{CO_2}) as

$$\frac{\Delta f_{He} - \Delta f_{N_2}}{f_v} \cong \frac{1}{2}\left(\frac{\rho_{He} - \rho_{N_2}}{\rho_q}\right), \tag{3.11}$$

$$\frac{\Delta f_{He} - \Delta f_{N_2}}{\Delta f_{CO_2} - \Delta f_{N_2}} \cong \left(\frac{\rho_{He} - \rho_{N_2}}{\rho_{CO_2} - \rho_{N_2}}\right), \tag{3.12}$$

where $\rho_{He}, \rho_{N_2}, \rho_{CO_2}$ are the densities of heliox-air mixture, nitrogen, and carbon dioxide, respectively.

Therefore, the net effect of the surrounding medium will cause a change in the effective mass of the cantilever which depends on fluid density and viscosity. For a QTF

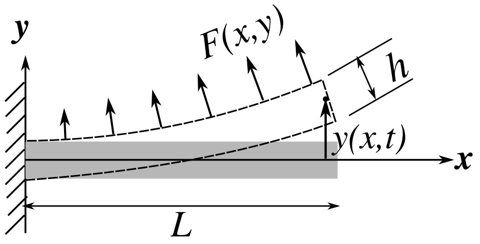

Figure 3.8: The vibration of a cantilever beam with small deflection *y(x,t)* in a flexural mode. The beam is fixed at $x = 0$ with length L and rectangular cross-sectional area $A = b \times h$.

oscillator, the patterned silver contacts should also be included in the effective mass. When exposed to air, silver will be oxidised gradually, increasing the effective mass, and thus decreasing the resonant frequency (about 1 Hz per three month in Nottingham). In this work, instead of measuring the frequency in vacuum (f_v), the resonant frequency in pure nitrogen f_{N_2} and in pure carbon dioxide f_{CO_2} are measured as the reference frequencies before every the washout measurement to allow accurate calculation of expiratory gas density. Since the density of helium is much lower than of nitrogen ($(\rho_{He} - \rho_{N_2})/\rho_{N_2} = -86\%$) compared to the viscosity ($(\mu_{He} - \mu_{N_2})/\mu_{N_2} = 5.6\%$), only the density effect is taken into account in the frequency shift.

Elastic Equation of a Cantilever Beam in Fluid

Another theory extended by J. E. Sader is to consider the cantilever as an elastic beam immersed in a fluid [78]. He pointed out an unpublished experimental result from Chu [10] which gave an expression for a flexural angular resonant frequency of a cantilever in fluid ω_f

$$\omega_f = \omega_v \left(1 + \frac{\pi \rho_f b}{4 \rho_q h}\right)^{-1/2} . \tag{3.13}$$

where ρ_f and ρ_q are the density of surrounding fluid and the cantilever, b and h are the width and thickness of the cantilever, respectively. For small ρ_f, this formula gives the similar form of the frequency shift to the damped oscillator theory mentioned in the previous section.

To derive the resonant frequency from an elastic equation, first of all consider a cantilever beam vibrating in a flexural mode with the small deflection $y(x,t)$ which is a function of x and time t (Figure 3.)[1]. The strain φ, which is the displacement of $y(x,t)$ along x, due to the bending component is

$$\frac{\partial y(x,t)}{\partial x} = \varphi(x,t). \tag{3.14}$$

The kinetic energy $K(t)$ of the whole beam and the potential energy $V(t)$ due to the deformation can be written as

$$K(t) = \frac{1}{2}\int_0^L \rho_q A \left[\frac{\partial y}{\partial t}\right]^2 dx, \tag{3.15}$$

$$V(t) = \frac{1}{2}\int_0^L EI_A \left(\frac{\partial \varphi}{\partial x}\right)^2 dx. \tag{3.16}$$

where E is the elastic modulus, and I_A is the area moment of inertia of the cross section A about the neutral axis x

$$\begin{aligned} I_A &= \int_{\frac{-h}{2}}^{\frac{h}{2}} y^2 dA \\ &= \int_{\frac{-h}{2}}^{\frac{h}{2}} y^2 dx dy \\ &= \frac{bh^3}{12}. \end{aligned} \tag{3.17}$$

The work $W_F(t)$ done by an external force per unit length $F(x,t)$ is

$$W_F(t) = \int_0^L F(x,t) y(x,t) dx. \tag{3.18}$$

The Lagrangian of the cantilever beam can be given by

$$\mathbf{L} = \int_{t_1}^{t_2} \left[K(t) + V(t) + W_F(t)\right] dt. \tag{3.19}$$

According to the Hamilton's principle,

$$\frac{\partial \mathbf{L}}{\partial q} - \frac{d}{dt}\frac{\partial \mathbf{L}}{\partial \dot{q}} = 0, \tag{3.20}$$

---

[1] The shear mode and rotary mode are not taken into account in this case. The further derivation of the full modes can see the reference [30].

by taking the second derivative of x on both sides, we can get

$$\rho A\frac{\partial^2 y(x,t)}{\partial t^2} + EI_A\frac{\partial^4 y(x,t)}{\partial x^4} = F(x,t) \tag{3.21}$$

which is the so-called Euler-Bernoulli beam equation [30].

Solving Eq. 3.18 by separating $y(x,t)$ as a form of a spatial function $Y(x)$ times a time function $\Im(t)$, *i.e.*, $y(x,t) = Y(x)\Im(t)$, it leads to two differential equation [30]

$$\frac{d^2\Im(t)}{dt^2} + \omega_v^2\Im(t) = 0, \tag{3.22}$$

$$\frac{d^4Y(x)}{dx^4} - C^4Y(x) = 0, \tag{3.23}$$

where C is the root of

$$1 + \texttt{cos}C\texttt{cosh}C = 0. \tag{3.24}$$

The vacuum angular frequency ω_v thus can be given by [30]

$$\omega_v = \frac{C^2}{L^2}\sqrt{\frac{EI_A}{\rho_q A}}. \tag{3.25}$$

Now consider an external load applied by the surrounding fluid. By taking the Fourier transform of Eq. 3.18, the solution leads to the hydrodynamic load per unit length [78]

$$\tilde{F}(x|\omega) = \frac{\pi}{4}\rho_f\omega_f^2 b^2\Gamma(Re)y(x|\omega) \tag{3.26}$$

where $\Gamma(Re)$ is the normalised hydrodynamic load depending on the Reynolds number Re which is the ratio of the inertial force to the viscous force of the fluid under a certain circumstance. Hence the resonant angular frequency in the fluid ω_g thus can be written as

$$\omega_f = \omega_v\left[1 + \frac{\pi\rho_f b}{4\rho_q h}\Gamma(Re)\right]^{-1/2}, \tag{3.27}$$

where $\Gamma(Re)$ is given by

$$\Gamma(Re) = \left(1 + \frac{4iK_1(-i\sqrt{iRe})}{\sqrt{iRe}K_0(-i\sqrt{iRe})}\right)\left[\frac{0.91 - \Xi_0(Log_{10}Re)}{1 - \Xi_1(Log_{10}Re)}\right], \tag{3.28}$$

K_0 and K_1 are the modified Bessel functions, Ξ_0 and Ξ_1 are 6th-order power functions of Re [67]. For a cantilever with small thickness h compared to its length L vibrating in an incompressible flow, $\Gamma \to 1$.

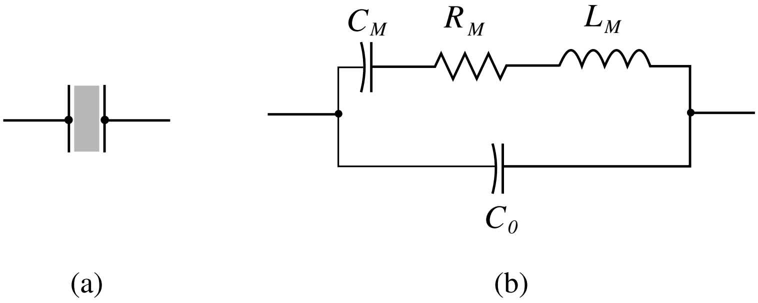

Figure 3.9: (a) The electronic symbol of a crystal oscillator. (b) The equivalent circuit of a crystal oscillator. C$_M$, L$_M$, and R$_M$ represent the capacitor, inductor, and resistor due to the crystal mechanical vibration.

3.5.2 System Diagram and Working Principle

The quartz tuning forks (Watch Crystal NC26, Fox Electronics, USA) are commercially supplied in a sealed can within a small amount of helium gas. Its dimensions have been shown in Figure 3.7. A resonant frequency (32,768 Hz) under such flexural excitation depends on the surface applied force. In this work, the quartz tuning fork is used as an actuator driven by a Pierce oscillator. Its resonant frequency is measured when it is exposed in the expired gas mixtures with the vacuum can removed.

Quartz Crystal Equivalent Circuit

When considering the quartz tuning fork as a damped harmonic oscillator, its equation of motion mentioned in previous section can be given by

$$m_e \frac{\partial^2 x}{\partial t^2} + m_e \gamma \frac{\partial x}{\partial t} + kx = F e^{i\omega t}. \tag{3.29}$$

The analog is a series-RLC circuit paralleled with a capacitor C_0 as shown in Figure 3.9. C_M, R_M and L_M represent the intrinsic property of the crystal. C_0 represents the coupled effect from the crystal leads and the circuit board. This operation can be expressed as

$$L_M \frac{d^2 \mathtt{Q}}{dt^2} + R_M \frac{d\mathtt{Q}}{dt} + \frac{\mathtt{Q}}{C} = V_q e^{i\omega t} \tag{3.30}$$

where $\mathtt{Q}$ is the charge and V_q is the driving electric potential at angular frequency ω. The RLC circuit is characterized by a large inductance L_M (hundreds of Henrys) the analog to the effective mass, a very small capacitance C_M (less than a milli pF) the analog to the elasticity, and a very small resistance R_M represents the damping factor. Capacitor C_0 represents the electrostatic capacitance and normally is as high as a few pF ($C_0 >> C_M$). The impedance of this circuit (Z_q) is [70]

$$\begin{aligned} Z_q &= \left(Z_{C_M} + Z_{L_M} + Z_{R_M}\right) // Z_{C_0} \\ &= \left(\frac{1}{j\omega C_M} + j\omega L_M + R_M\right) // \left(\frac{1}{j\omega C_0}\right) \\ &= \frac{s^2 + s\frac{R_M}{L_M} + \omega_s^2}{s\left[s^2 + s\frac{R_M}{L_M} + \omega_a^2\right]} \end{aligned} \tag{3.31}$$

where $j = \sqrt{-1}$, $s = j\omega$, ω_s and ω_a are the series- and anti-resonant angular frequency, respectively. When the crystal is excited at the series-resonance, it looks resistive in the circuit. At this point, $|Z_{L_M}| = |Z_{C_M}|$, and ω_s solely depends on series capacitor C_M and L_M, *i.e.*,

$$\omega_s = \sqrt{\frac{1}{L_M \cdot C_M}}. \tag{3.32}$$

When it is operating at anti-resonance mode, the $L_M \cdot C_M$ looks inductive and resonates with C_0, *i.e.*,

$$\omega_a = \sqrt{L_M \cdot \frac{C_M + C_0}{C_M \cdot C_0}} = \omega_s \left(\sqrt{1 + \frac{C_0}{C_M}}\right). \tag{3.33}$$

For a crystal with high Q factor ($Q = \omega L_M / R_M \cong 5000$ for a QTF in air) , the damping factor (R_M) is very small and normally can be neglected. Thus the impedance can be written as [70]

$$Z(j\omega) = -j\frac{1}{\omega C_0}\left(\frac{\omega^2 - \omega_s^2}{\omega^2 - \omega_a^2}\right). \tag{3.34}$$

The crystal reactance characteristic curve versus frequency is plotted in Figure 3.10. The reactance is the imaginary part of the impedance. Since the impedance of a capacitor ($1/j\omega C_M$) or inductor ($j\omega L_M$) is purely imaginary, they can also be regarded as the reactance. The series-resonant frequency f_s and anti-resonant frequency f_a are also marked.

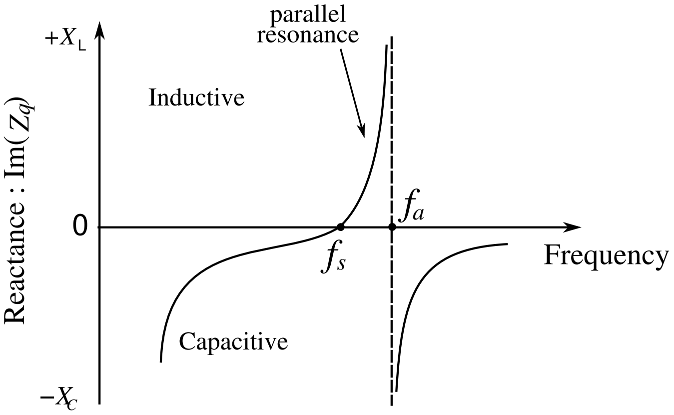

Figure 3.10: The frequency characteristic curve of a crystal reactance. Two special frequencies, series-resonant frequency $f_s = \omega_s/2\pi$ and anti-resonant frequency $f_a = \omega_a/2\pi$ are marked above. X_c and X_L are the reactance of the capacitor C_M and the inductor L_M, respectively. Modified from *http://www.fairchildsemi.com/an/AN/AN-340.pdf.*

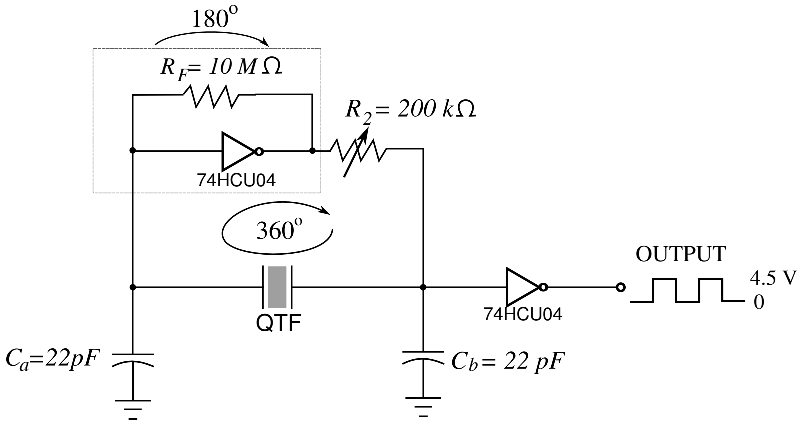

Figure 3.11: Pierce oscillator circuit diagram.
Modified from *http://www.fairchildsemi.com/an/AN/AN-340.pdf.*

Pierce Oscillator

A Pierce oscillator is one of the most common crystal oscillators. The circuit diagram is shown in Figure 3.11. The crystal (QTF in this work) works as an inductor since it is operating in its parallel mode. The inverting amplifier (inverter and a feedback resistor R_F) is phase shifted 180^o (negative feedback). In conjunction with C$_a$ and C$_b$, it forms a π-network band-pass filter which generates another 180^o phase and results in 360^o closed loop phase (positive feedback). A second resistor R_2 is to reduce the output of the inverter such that the crystal is not over driven. It also provides extra phase to cancel out the inherent delay shift from the inverter. The load capacitance C_L is the capacitance other than crystal itself, *i.e.*, $C_L = C_1//C_2 + C_{stray}$ where C_{stray} is from the leads and circuit board. C_L is chosen such that their series impedance is equal to 0. The values of R_F, R_2, C_1 and C_2 are given in Figure 3.11 for this work with an output signal through another inverter which gives the square wave of around 32757 Hz in air.

System Diagram

The QTF gas density detecting system diagram is shown in Figure 3.12. Two QTFs are mounted in a plastic cell where gas passes through, one is exposed to the gas and the other one is left with its vacuum can in place. The one within its vacuum can is for compensating any change due to the temperature variation. Since the temperature variation is very small during the washout measurement (less than 1^oC), in practice the temperature effect is simply ignored and the QTF exposed to the gas is the only that is used. Two Pierce oscillator circuits have been built for each QTF and fixed on a circuit board attached to the QTF cell and sealed with two rubber o-rings. A commercial frequency detector (easyPLL plus 3.0 Detector, NanoSurf, Switzerland) with an inner phase lock loop (PLL) is for detecting the frequency shift from the QTF. Its block diagram is shown in Figure 3.13.

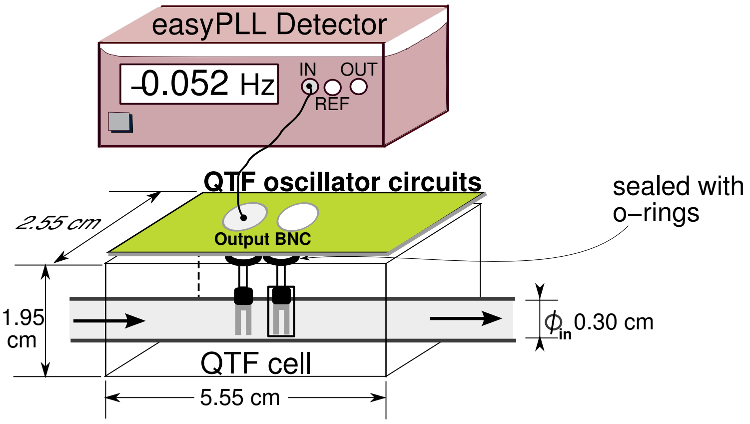

Figure 3.12: QTF gas density detecting diagram

easyPLL Detector Working Principle

The easyPLL Detector working with a easyPLL Controller is normally applied to the AFM (atomic force microscopy) [32, 40, 62, 68, 74]. The excitation signal from the Controller drives a piezo actuator to oscillate with a tip attached on it. The vibration detected by the Detector depends on the surface geometry of the sample. In this project, the Controller is replaced by a Pierce oscillator (excitation signal) for driving the QTF (piezo actuator). Figure 3.14 shows the block diagram of the easyPLL Detector modified from the diagram in its operation manual with all the parameters used in washout measurements. It consists of an input amplifier, a phase lock loop (PLL), an output filter and amplifier, and a parallel port connected to a PC. The driver has been installed and the front panel of the control software is shown in Figure 3.14. The PLL consists of three main parts put in a negative feedback loop: a phase detector which is a multiplier combined with a low-pass filter, a voltage controlled digital oscillator (VCDO), and a PI (proportional-integral) controller.

The VCDO produces a reference signal V_{ref} with the reference frequency f_{ref} and an internal signal which has a digitally set phase shift ($\delta = 192.3^o$) with respect to the reference signal $V_{ref+\delta}$. The internal signal goes into the multiplier combined with the amplified input signal V_{input} from the QTF oscillator which has a frequency f_{input}. Its

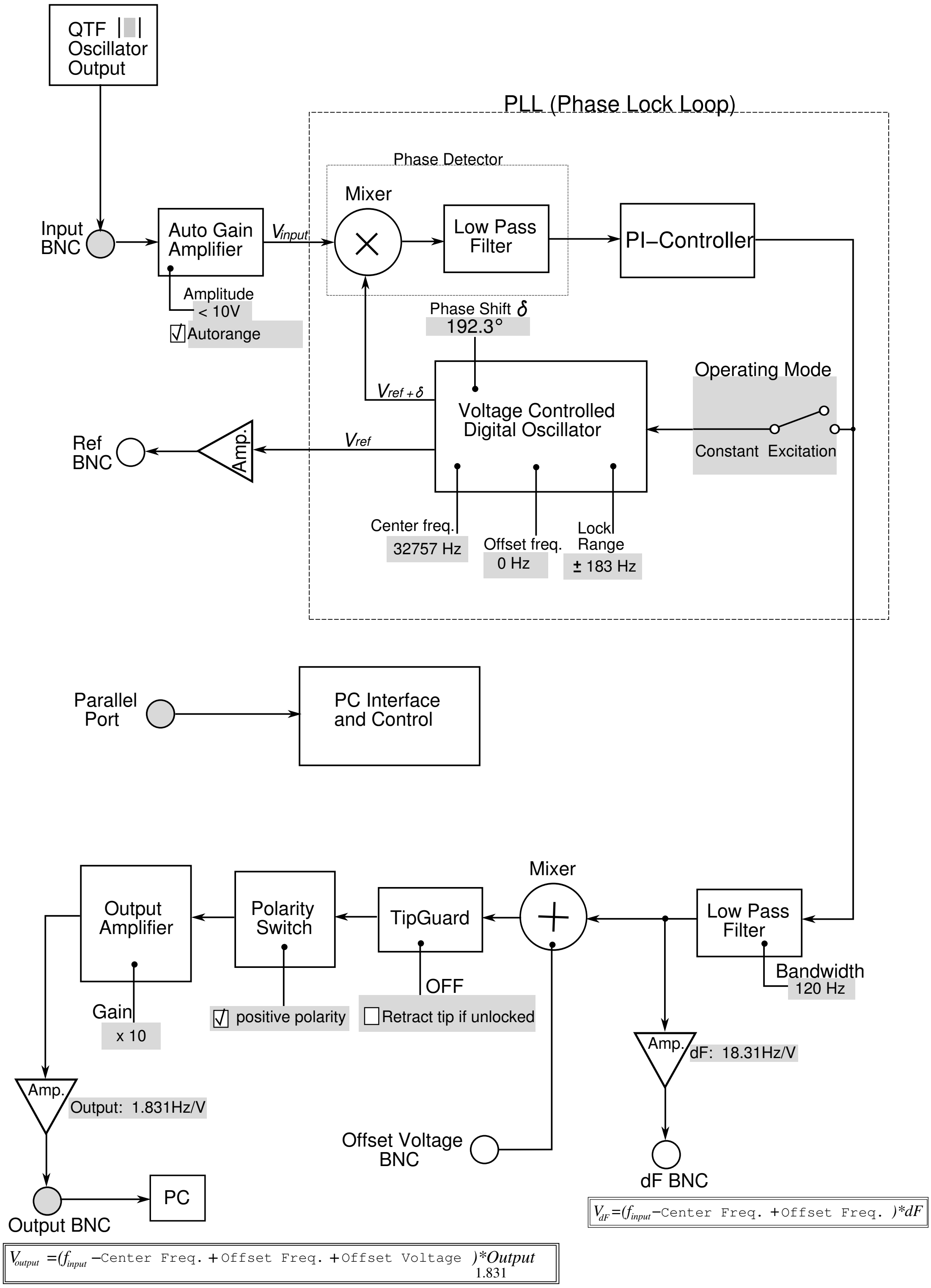

Figure 3.13: The easyPLL Detector block diagram modified from its operating manual

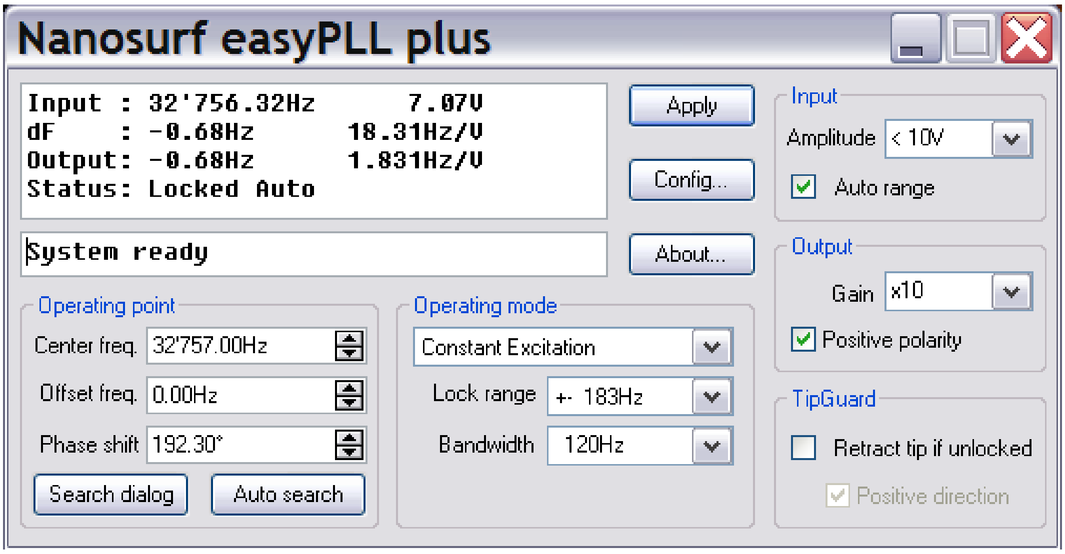

```
Input : 32'756.32Hz      7.07V
dF    : -0.68Hz       18.31Hz/V
Output: -0.68Hz       1.831Hz/V
Status: Locked Auto
```

```
System ready
```

Input
Amplitude: < 10V
☑ Auto range

Output
Gain: x10
☑ Positive polarity

Operating point
Center freq.: 32'757.00Hz
Offset freq.: 0.00Hz
Phase shift: 192.30°

Operating mode
Constant Excitation
Lock range: +- 183Hz
Bandwidth: 120Hz

TipGuard
☐ Retract tip if unlocked
☑ Positive direction

Figure 3.14: The easyPLL Detector driver front panel

operation can be represented as

$$
\begin{aligned}
V_{input} \otimes V_{ref} &= a_1 sin\left(2\pi f_{input} t + \phi_{input}\right) \cdot b_1 cos\left(2\pi f_{ref} t + \delta\right) \\
&= \frac{a_1 b_1}{2} sin\left(2\pi (f_{input} - f_{ref}) t + \phi_{input} - \delta\right) \\
&\quad + \frac{a_1 b_1}{2} sin\left(2\pi (f_{input} + f_{ref}) t + \phi_{input} + \delta\right) \qquad (3.35)
\end{aligned}
$$

where ϕ_{input} is the input phase relative to the reference signal, a_1 and b_1 are the amplification factors. The resulting signal contains sinusoidal waves with the sum and difference of f_{input} and f_{ref}. The low-pass filter filters out the sum, and the resulting signal V$_d$ is

$$
V_d = \frac{a_1 b_1}{2} sin\left(2\pi (f_{input} - f_{ref}) t + \phi_{input} - \delta\right). \qquad (3.36)
$$

A PI controller is a PID controller without the derivative part. It is a feedback control loop for stabilising a variable until it reaches the set point. The block diagram is given in Figure 3.15. It takes the summation of a proportional (**P**), integral (**I**) and derivative (**D**) of an error function ($e(t)$) which is the difference of the process variable (PV) and the set point (SP). In the easyPLL detector, the error function $e(t) = sin(2\pi(f_{input} - f_{ref})t + \phi_{input} - \delta)$. When the error function is small, the

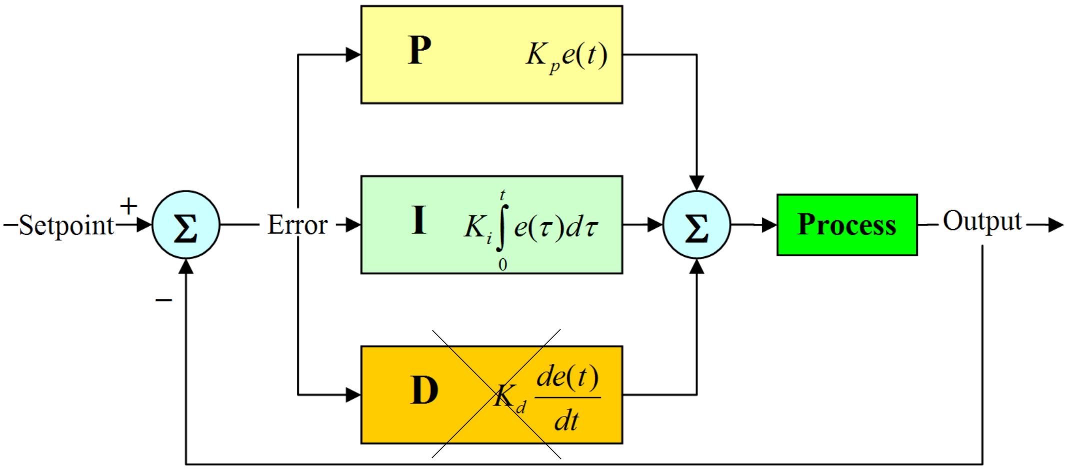

Figure 3.15: The block diagram of the PID (proportional-integral-derivative) controller. The differential part is not inclusive in a PI controller. Reproduced from *http://en.wikipedia.org/wiki/PID_controller* with the permission from Silverstar.

summation of the proportional and integral terms can be expressed as

$$\begin{aligned}
\mathbf{P} \oplus \mathbf{I} &= K_p e(t) + K_i \int_0^t e(\tau)d\tau \\
&= K_p sin(2\pi(f_{input} - f_{ref})t + \phi_{input} - \delta) \\
&\quad + K_i \int_0^t sin(2\pi(f_{input} - f_{ref})\tau + \phi_{input} - \delta)d\tau \\
&\cong K_P(2\pi(f_{input} - f_{ref})t + \phi_{input} - \delta) \\
&\quad + K_I(\pi(f_{input} - f_{ref})t^2 + \phi_{input} - \delta)t \qquad (3.37)
\end{aligned}$$

where K_p and K_i are the proportional and integral gain, respectively. The negative feedback signal from the PI controller tells the VCDO to change the reference frequency f_{ref} until the error function approaches zero, *i.e.*, the reference signal and the input signal have the same frequency and 0^o phase shift. In this case, the loop is ”locked”. Assume at first $f_{ref} \cong f_{input}$ and the time interval t is very small, thus two terms of $2\pi(f_{input} - f_{ref})t$ can be simply ignored. The feedback signal, which is proportional to $(\phi_{input} - \delta)$, becomes negative and the controller tells the VCDO to change the reference frequency until V_{ref} and V_{input} are in phase.

The signal from the PLL goes through another low-pass filter with the bandwidth 120 Hz to filter out unwanted frequencies outside this range. The filtered signal mixed with an external offset voltage is then amplified with the output gain of 1.831 Hz/V which gives the output signal to the PC, *i.e.*,

$$V_{output} = (f_{input} - \texttt{Center freq.} + \texttt{Offset freq.} + \texttt{OffsetVoltage}) \times 1.831. \quad (3.38)$$

Another output signal from the dF-BNC cable is the amplified signal without the external offset voltage and with the gain of 18.31 Hz/V. Both output gains are displayed in the control software panel. The operating mode "Constant Excitation" is chosen because the QTF is driven by an oscillator other than the eaPLL Controller. The other two modes, "Self Exciting Oscillation" and "Constant Amplitude", are useful when the amplitude dissipation or the amplitude of the oscillation needs to be measured with the easyPLL Controller. In this work only the Detector is used to detect the frequency shift. The TipGuard is turned off since the QTF is used as an actuator without any tip on it. The Polarity Switch controls the positive/negative sign of the output gain.

3.6 Infrared CO_2 Absorption Detector

The absorption of infrared (IR) radiation by carbon dioxide gas has been observed at several near IR bands inclusive of 2.7, 4.3, and 14.7 μm [47, 52]. The infrared absorption spectra of water and carbon dioxide is shown in Figure 3.16. Since the expired gas from our breath contains around 4% of CO_2, a lead selenide (PbSe) photoconductor (P9696 series, Hamamatsu, Japan) sensitive to 4.2-μm IR has been used for detecting the concentration of carbon dioxide [85, 88]. This is not sensitive to the abosrption from water vapour. The infrared absorption by carbon dioxide follows the Beer-Lambert law which is exponentially related to the concentration of carbon dioxide. The photoconductive PbSe film converts the optical energy into the electrical current.

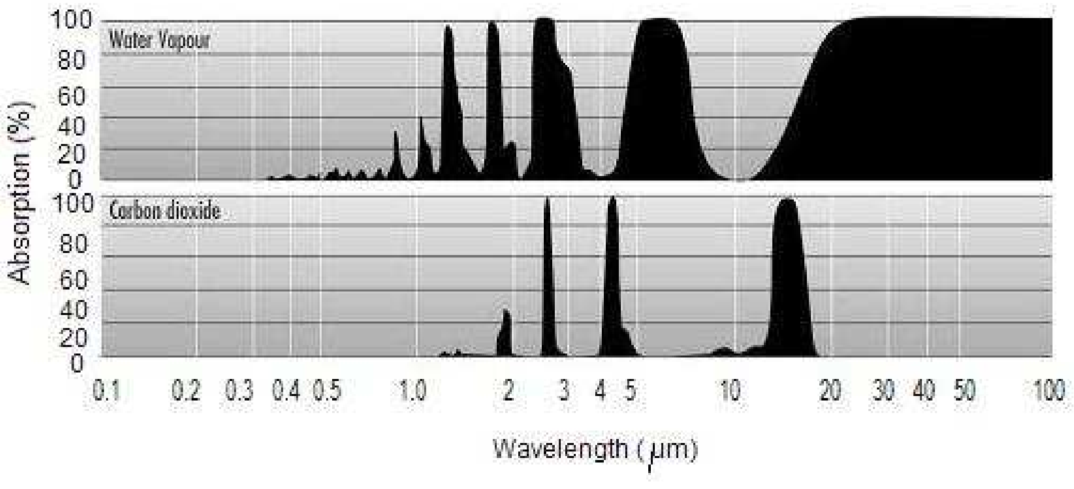

Figure 3.16: Infrared absorption spectra for water vapour (top) and carbon dioxide (bottom). Mdified from *http://www.bom.gov.au/info/climate/change/gallery/4.shtml*

3.6.1 Theory

Beer-Lambert's Law of Light Absorption

The Beer-Lambert's law in optics describes that the absorption of light by a material and is dependent on the concentration and the thickness of the material, *i.e.* [52],

$$I_{out} = I_0 e^{-\kappa l} \tag{3.39}$$

where I_0 and I_{out} are the initial and output light intensity, κ is the absorption coefficient of the material, and l is the thickness of the material travelled by the light. For multiple materials, the absorption coefficient κ is a linear combination of all compositions, *i.e.*

$$\kappa = c_1\epsilon_1 + c_2\epsilon_2 + c_3\epsilon_3 + \cdots = \sum_i c_i\epsilon_i \tag{3.40}$$

where c_i and ϵ_i are the concentrations and extinction coefficients of the materials, respectively. The diagram is shown in Figure 3.17. The derivation of the Beer-Lambert law can be simplified by considering a material composed of small particles with absorbing cross-section σ. Suppose the particle number of density is N and the beam

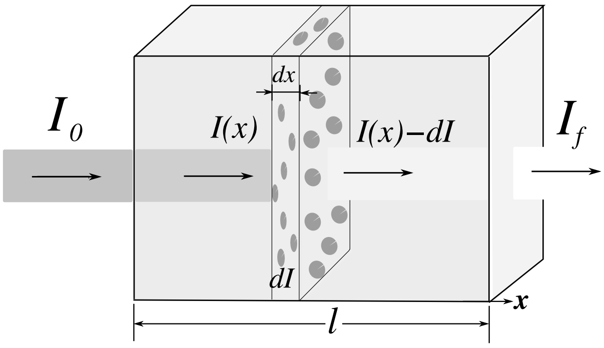

Figure 3.17: Beer-Lambert law of light absorption. A light with initial intensity I_0 passes through a material with thickness l. The output intensity can be expressed as $I_f = I_0 e^{-kl}$ where k is the absorption coefficient of the material.

light with cross-section A is traveling along $\boldsymbol{x}$ direction. Considering a thin slab of the material at x with the thickness dx, the light intensity is absorbed by a fraction of $\sigma \cdot N \cdot Adx$, *i.e.*,

$$\frac{dI(x)}{I(x)} = \frac{-\sigma \cdot N \cdot Adx}{A} \tag{3.41}$$

$$\int dI(x)I(x) = \int_0^l -\sigma \cdot N \cdot dx \tag{3.42}$$

$$I_{out} = I_0 e^{-\sigma \cdot N \cdot l} \tag{3.43}$$

where $\sigma \cdot N$ is the concentration of the absorbing particles.

Photoconductivity of PbSe Semiconductor

Photoconductivity is a physical property existing in some materials that their conductance increases due to the absorption of the photons with certain wavelength such as visible light, infrared, and ultra violet. It is produced by the interaction between photons and imperfect crystals. For semiconductors, there are additional energy levels in the forbidden gap associated with the defects which disturb the periodicity of the crystalline structure for a perfect crystal. Therefore, it is possible for electrons to take on those energy levels between the conduction and valence band. The electrons thus can be excited by absorbing the photon energy from valence band or from those additional energy levels to the conduction band, or from the conduction band to those

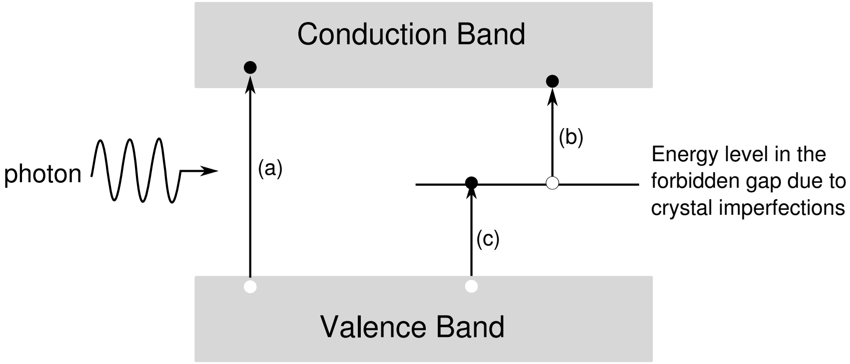

Figure 3.18: The electron excitation diagram. They can be freed (a) from valence band to the conduction band, or (b) from the energy level in the forbidden gap to the conduction band, or (c) from the valence band to those extra energy levels [7].

energy levels, as shown in figure 3.18 [7].

Following the excitation, the recombination of electron-hole pairs takes place which is the reverse of the excitation process. The lifetime τ of the carriers is defined as the time period between the generation and recombination. The conductance will increase as long as those photon-generated carriers remain free and contribute to the electrical current. Therefore, the longer carrier lifetime will cause the higher photoconductivity [87]. The lifetime of electrons τ_n (or holes τ_p) can thus be defined by $\tau_n g_p = \delta n$ (or $\tau_p g_p = \delta p$), where g_p is the photo-generated rate of carriers, δn (or δp) is the densities of additional free electrons (or holes) maintained by the radiation in the steady state. And the associated extra conductivity $\delta\sigma$ can be expressed as $\delta\sigma = \delta n e \mu_e + \delta p e \mu_p$, where μ_e and μ_p are the mobility of electrons and holes, and e is the electron charge [61, 87].

Considering the recombination process other than the main transition (conduction band to valence band), electron-hole pairs can recombine at those energy levels in the forbidden gap which are so called the recombination centres. However, if the cross-section of some recombination centres for capturing the majority carriers is much smaller than for capturing the minority carriers, there will be an extended period for the majority carriers to be freed before the recombination takes place. Those centres are called trapping centres (or traps) in which the trapped carriers may also be thermally excited back to the conduction band. The existence of trapping centres increases the lifetime of carriers and thus the photoconductivity [61, 87].

Photoconductivity of PbSe films was first observed at liquid nitrogen temperature. However, at room temperature no photoconductivity was observed. The highest response was made by baking in the presence of oxygen gas [34–36]. The PbSe films initially have low *n*-type resistivity and poor photoconductivity. The existence of oxygen converts these films into *p*-type semiconductor, and the maximum photoconductance relative to the dark conductance is obtained at slightly *p*-type region. The same treatment with sulphur, selenium or halogens can only produce photoconductivity below -195^{o}C. All those agents (O_2, S, Se, halogens) act as acceptors converting lead selenide films from *n*-type into *p*-type. However, only oxygen sensitises the photoconductivity of PbSe films at room temperature.

In the impurity sensitization model developed by Humphrey [35], oxygen introduces minority carrier(electron) traps, $(PbO)^{++}$, which increases the majority carrier(hole) lifetime and thus enhances the photoconductivity. An $(PbO)^{++}$ ion could trap an electron and become $(PbO)^{+}$ which repels holes, thus reduces the probability of recombination. Sulphur introduces shallow electron traps which can only increase the majority lifetime effectively at low temperature. The energy levels of shallow traps are very close to the conduction band such that electrons can be thermally re-excited back to the conduction band and the effect is negligible under thermal equilibrium [31]. Oxygen has much higher electronegativity (3.44) than sulphur (2.58) such that electrons can be trapped more easily by oxygen. The trap energy levels with the existence of oxygen lie much below the conduction band thus the thermal re-excitation will not easily take place. For halogens such as fluorine with even higher electronegativity (3.98), after trapping an electron the (PbF)+ ion becomes (PbF) which can not repel holes efficiently.

3.6.2 System Diagram and Working Principle

The system (Figure 3.19) consists of an optical cell, an On-Off temperature control circuit, a low-pass filter, a function generator and a lock-in amplifier. The optical cell

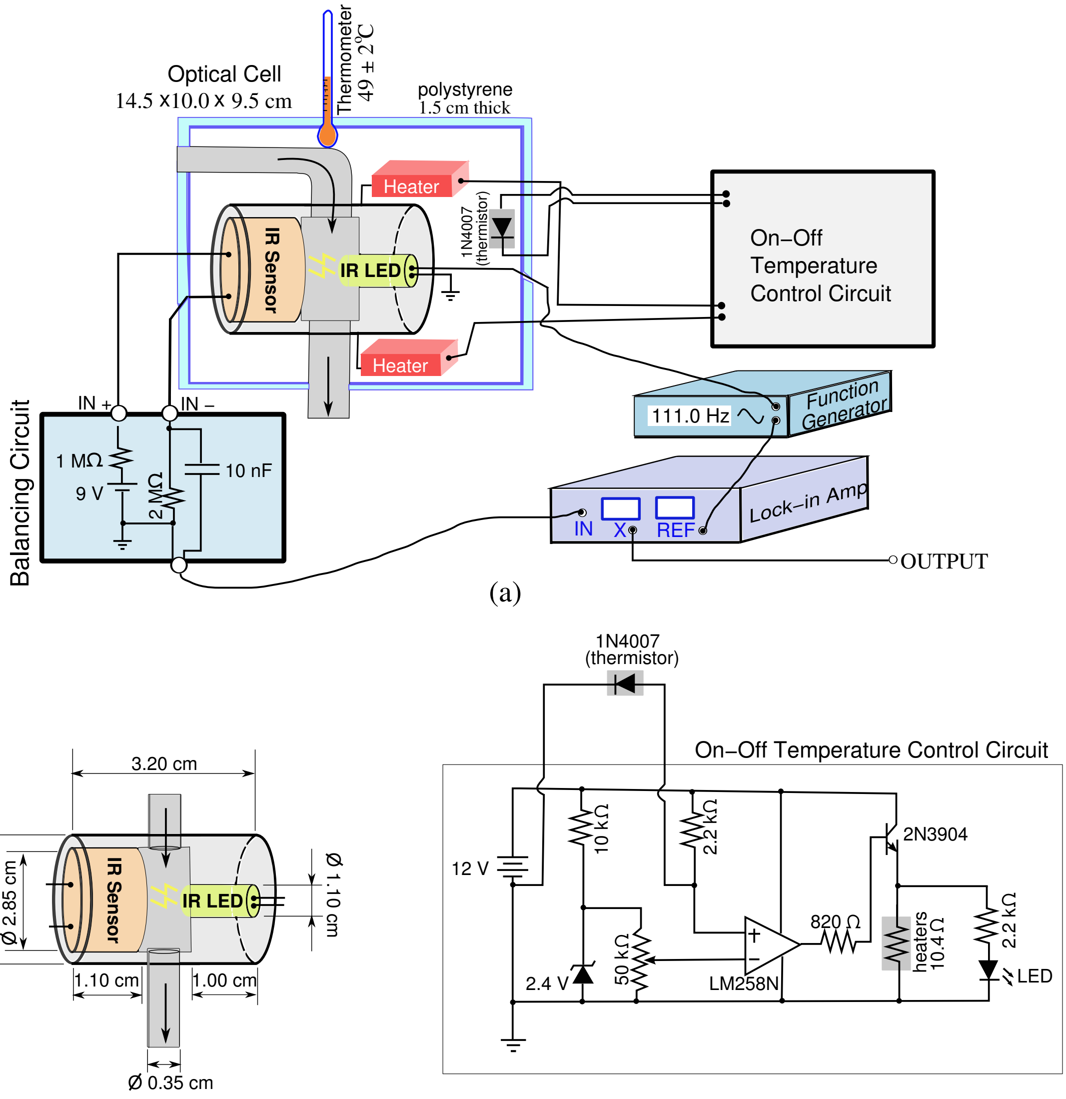

(a)

(b)

(c)

Figure 3.19: (a) The infrared CO_2 detecting system. It consists of an optical cell, a function generator, a balancing circuit, a lock-in amplifier, and a temperature-control circuit. (b) The dimensions of the optical cell. (c) The On-off temperature control circuit modified from *http : //www.electronics − lab.com/projects/motor$_l$ight/011/.*

consists of a 4.2 μm infrared LED (LED42SC, Scitec,UK) and a PbSe photoconductive detector (P9696 series, Hamamatsu, Japan) mounted in a metal box which is wrapped by 1.5 cm-thickness of polystyrene sheets. The function generator (DS335, Stanford Research Systems, US) gives 111.0 Hz[2], 4.0 V_{pp} sinusoidal signal to the LED. The PbSe photonconductive sensor contains a PbSe film and an optical chopper with 600 Hz chopping frequency. It is connected to a balancing circuit with a 9-V_{DC} battery for filtering out the DC signal and supplying the chopper. The output signal from the filter is amplified by the lock-in amplifier (SR510, Stanford Research Systems, US). Two heater resistors (2.2 Ω, 8.2 Ω) are put in the box connected to the temperature-control circuit for warming up the cell and reducing the water vapour condensed on the cell wall. A thermometer is attached to the cell for monitoring the inner temperature of the box.

Optical Cell Operation Setting

The output frequency from the function generator to the infrared LED should be higher than the main-power frequency 50 Hz. However, the signal to noise ratio will decrease with the increase of the frequency. In this work, 111.0 Hz with 4.0 V_{pp} sine wave is chosen with the parameters of the lock-in amplifier shown in the following table, it gives 8.0 mV noise which is relative to 0.1% of CO_2.

Figure 3.20(a) shows the output amplitude signal from the lock-in amplifier of which 0% and 100% carbon dioxide flowing through. Figure 3.20(b) shows the CO_2 concentraion versus the output voltage with a dual-exponential curve. The concentration of carbon dioxide is calibrated with the QTF system which will be described in a later section.

---

[2] Frequency lower than 600 Hz chopping frequency can be chosen due to the Nyquist-Shannon sampling theorem. 111 Hz input LED signal has been chosen to avoid the noise from the main power 50 Hz. The lock-in amplifier is to filter out the noise and give higher response. DC input LED signal can ideally be used while the output signal from the PbSe receiver will be small and noisy. Frequencies higher than 111 Hz can also be chosen but the signal-to-noise ratio will be relatively reduced.

Lock-In Amplifier Parameters : Optical Cell

SIGNAL FILTERS	OUT (all)	EXPAND	× 1
SIGNAL INPUT	A	REL	OFF
SENSITIVITY	2 mV	TIME CONSTANT PRE	100 ms
DYN RES	Low	TIME CONSTANT POST	0.1 s
DISPLAY	X	REFERENCE	f, SINE

Table 3.1: Lock-in Amplifier Parameters - Optical Cell

On-Off Temperature Control Circuit

This circuit (Figure 3.21(a)) controls two heater resistors (10.4 Ω in total, ceramic) based on comparing a set-point of the temperature. A silicon diode (1N4007GP) is used as the temperature sensor since its forward voltage drop (V_f) has linear negative dependence of temperature [50]. It is caused by the reduction of the band gap across the p-n junction where the electrons are thermally excited. An op-amp (LM258N) is working as a comparator in the open-loop mode. The simplification of the comparator diagram is shown in Figure 3.21(b) which gives the output voltage V_{OUT} as

$$V_{OUT} = V_{REF} + \frac{R_{12}}{R_{11}}(V_{REF} - V_{IN}) \tag{3.44}$$

as shown in Figure 3.21(c). Its inverting input is connected to a reference voltage adjusted by a 50Ω variable resistor. The paralleled zener diode gives a precise voltage limit of -2.4 volts, *i.e.*, $-2.4 \leq V_{REF} \leq 0$. Its non-inverting input is connected to the temperature-sensing diode. Since the forward voltage drop of the sensing diode has linear-negative-temperature dependence, the correspondence voltage V_{IN} can be written as $V_{IN}(T) = V_{IN}(0) - \alpha T$ where α is a positive constant. The output voltage of the comparator can be rewritten as

$$V_{OUT} = -\left|V_{REF}\right| + \frac{R_{12}}{R_{11}}(-\left|V_{REF}\right| - V(0) + \alpha T). \tag{3.45}$$

When the temperature is higher than a set-point, the forward voltage drop of the sensing diode cancels out the reference voltage, and the output voltage of the comparator is

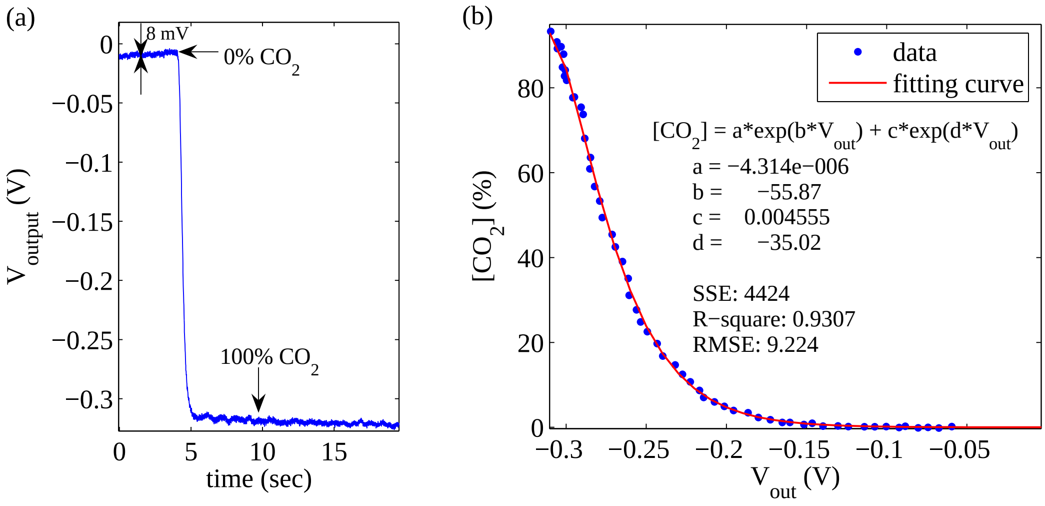

Figure 3.20: (a) The output signal from the lock-in amplifier of which are 0% and 100% of CO_2. (b) The concentration of carbon dioxide versus the output signal.

turning off the transistor thus the heaters. The the voltage across the heater is thus zero and the LED is off. In this work, the temperature set-point is about 51±2 ^{o}C measured by the thermometer. The voltage across the heaters is -6.63 volts when it is on which gives 4.22 Watt power.

3.7 Glass-Encapsulated Thermistor

The thermistor (G540, 10 kΩ, Glass-Encapsulated Sensor, EPCOS, Germany) is made of a tiny fuse encapsulated in a small glass bead. It has about 10-kΩ resistance at room temperature and 3-sec thermal cooling time constant in air. It is fixed within a plastic tube and connected to a circuit with a 8.7V battery-supplied voltage and a 1.005 MΩ resistor in series (Figure 3.22). Two output voltages (V_{therm} and V_{batte}) are connected to a second BNC box. The serial resistor is chosen higher than 1 MΩ to reduce the current and the self-heating effect. A battery is chosen as the power supply since it has low noise and steady DC voltage. To monitor two output voltages is necessary because

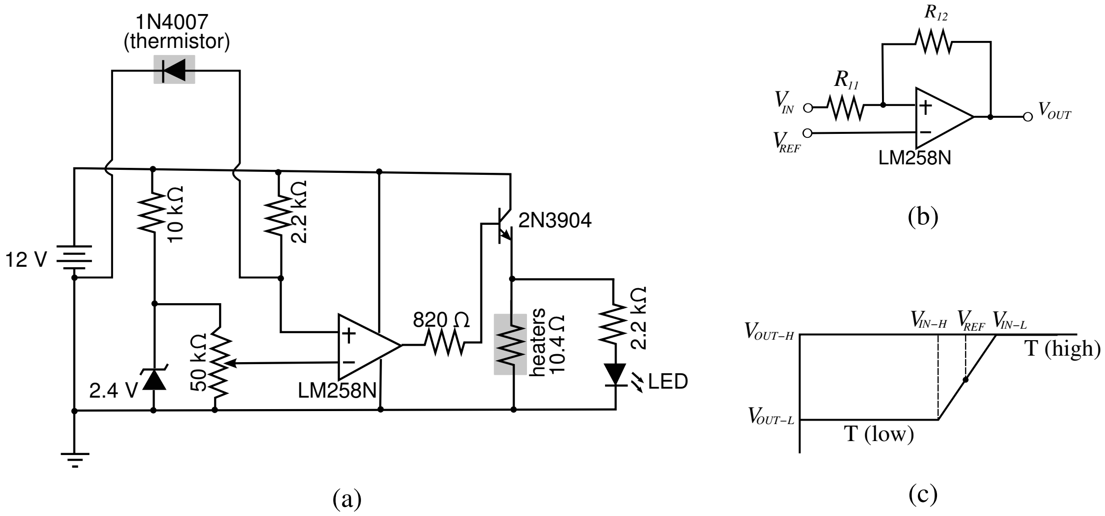

(a) (b) (c)

Figure 3.21: (a) The On-off temperature control circuit modified from $http : //www.electronics - lab.com/projects/motor_light/011/$. (b) The OP amplifier LM258N works as a comparator. (c) The highest and lowest output voltage (V_{OUT-H}, V_{OUT-L}) correspond to the lowest and highest input voltage (V_{IN-L}, V_{IN-H}.)

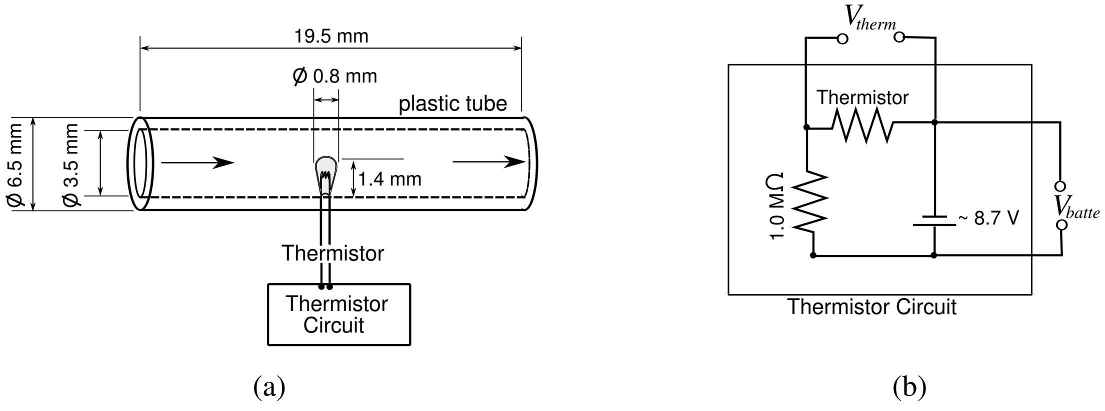

(a) (b)

Figure 3.22: (a) The thermistor system diagram. (b) The circuit of the thermistor.

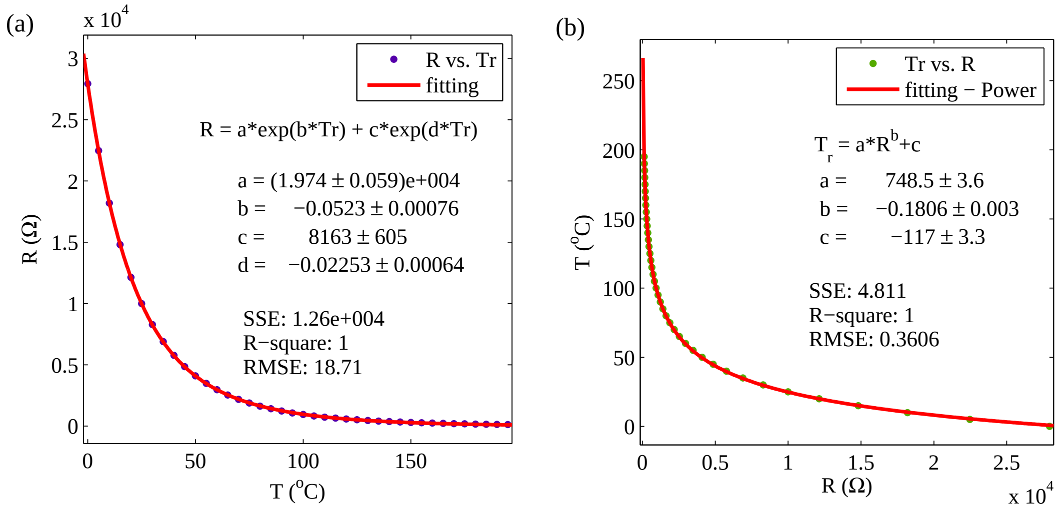

Figure 3.23: The characteristic curve of thermistor from its data sheet. (a) is the resistance as a function of temperature with an dual-exponential curve fitting. (b) is the inverse function of (a) fitting with a power function.

the battery is running out gradually. The resistance of the thermistor R_T (kΩ) can be given by

$$R_T = \frac{V_{therm} \times 1005}{V_{batte} - V_{therm}} \tag{3.46}$$

Figure 3.23 shows its characteristic curve of resistance versus temperature from its data sheet and a fitting curve fitted by MatLab (v7.0.4) curve fitting tool. Its resistance as a function of temperature from the fitting curve can be written as

$$R_T = 1.974 \times 10^4 e^{-0.0523T} + 8163 \times e^{-0.0225T} \tag{3.47}$$

while the inverse relation is

$$T = 748.5 * R_T^{-0.1806} - 117. \tag{3.48}$$

Thus, the resulting resistance can be converted into the corresponding temperature. The temperature from the thermistor is highly consistent with the temperature measured by a commercial thermometer (less than 0.1 ^{o}C error) in a non-flowing gas.

However, in this work, the gas is flowing and the concentration of gas mixture is varying which changes the thermal conductivity. The equation of energy dissipation due to heat transfer in an incompressible fluid is given by [2]

$$\frac{\partial T}{\partial t} + \vec{v} \cdot \nabla T = \chi \nabla^2 T \tag{3.49}$$

$$\chi = \frac{\kappa}{\rho_g C_p} \tag{3.50}$$

where T is the temperature, $\vec{v}$ is the flow velocity, χ is the thermometric conductivity related to the thermal conductivity κ, the density ρ_g, and the specific heat C_p of the fluid. For higher concentration of flowing helium gas, it will conduct more heat to or away from the thermistor. As helium gas passes through the water trap, it may thus cause a temperature drop compared to the air at the same flowing speed. Therefore, this thermistor is for monitoring the temperature stability of the gas passing through the tuning fork to ensure it is isothermal. This is important because the gas density is temperature dependent and thus the resonant frequency may be modified.

3.8 Pressure Sensor

3.8.1 Theory

Piezoresistivity

This type of pressure sensor is an application of the silicon piezoresistive effect. When a mechanical stress is applied to a silicon crystal, the electrical resistance of the silicon crystal changes. C. Smith (1954) had done a series of experiments on piezoresistance of silicon and germanium [73]. He cited J. Herring's [33] theory for explaining the piezoresistive effect of semiconductors that the constant energy surfaces of electrons can be presented as three ellipsoids in the momentum space which is related to the inner polarization. In the strained state, the deformation potential increases polarization in certain direction because of the distance reduction between carrier pairs, which causes more electrons with high mobility and fewer electrons with low mobility in the field

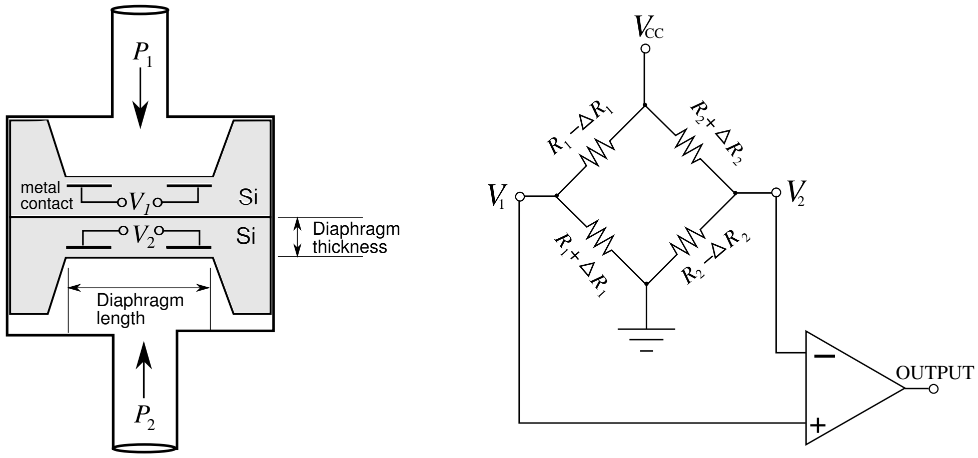

(a) (b)

Figure 3.24: (a) The differential silicon-diaphragm pressure sensor. (b) The circuit of the Wheatstone Bridge.

direction. Considering a single crystal of cubic silicon rod, its resistance R_ρ varies with the applied stress which can be expressed as

$$\frac{\Delta R_\rho}{R_{\rho 0}} = \pi_l \sigma_l + \pi_t \sigma_t \tag{3.51}$$

where $R_{\rho 0}$ is its unstrained resistance, π_l and π_t are the longitudinal and transverse piezoresistance coefficients, σ_l and σ_t are the longitudinal and transverse stress [76].

Dynamic Pressure

The gas mixture flowing through the pressure sensor produces the dynamic pressure P_d which is defined as

$$P_d = \frac{1}{2}\rho_g v^2 \tag{3.52}$$

where ρ_g and v are the fluid density and speed. The dynamic pressure of the fluid is related to the kinetic energy of a fluid particle and has the same unit as the static pressure. It is one of the terms of the Bernoulli's equation which will be described in the next section.

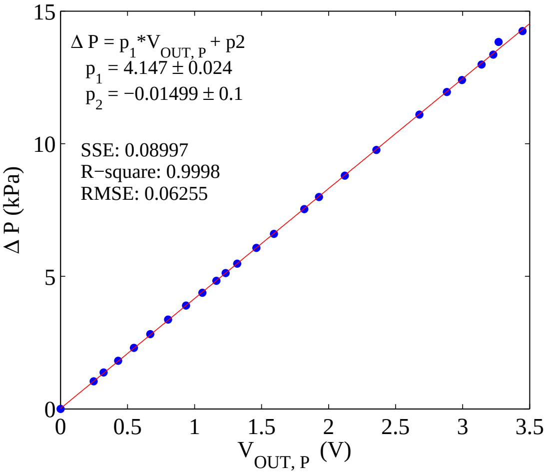

Figure 3.25: The amplified output signal from the pressure sensor as a function of the pressure at 18.5^o under 100.4 kPa room air.

3.8.2 Working Principle

This differential-type pressure sensor (26PCC type, Honeywell, Canada) is made of two silicon diaphragm wafers attached together as shown in Figure 3.24(a). Each diaphragm is open to a pressure inlet cavity and incorporates two piezoresistors in it. When the diaphragm is deformed caused by the pressure, two piezoresistors (R_{11}, R_{12}) subjected to the tangential and radial stress change. Two output voltages (V_1, V_2) from those resistors are then connected to a Wheatstone bridge (Figure 3.24(b)). The amplified output signal $V_{OUT,P}$ can thus be expressed as

$$\frac{V_{OUT,P}}{V_{CC}} = G_A \frac{\Delta R_\rho}{R_{\rho 0}} \tag{3.53}$$

where G_A is the gain of the amplifier. The calibration of the output signal ($V_{OUT,P}$ in volts) as a function of static pressure difference (P_1-P_2 in kPa) has been made at 18.5 ^{o}C under 100.4 kPa in the room air as shown in Figure 3.25. A linear curve is fitted with MatLab (v7.0.4) curve fitting toolbox and the relation can be expressed as

$$P_1 - P_2 = 4.147 \times V_{OUT,P} - 0.01499 \pm 0.10. \tag{3.54}$$

3.9 Pitot-Type Air Pump

3.9.1 Theory : Bernoulli's Equation

The Pitot tube was named after the inventor Henri Pitót (1732). It consists of two coaxial tubes as shown in figure 3.26(a). The interior is open to a steady flow with a higher pressure P_t while the exterior one with an opening paralleled to the streamlines registers the static pressure P_{static}. The pressure difference between the interior and exterior tube is the dynamic pressure of the flow. According to Bernoulli's equation under the gravitational circumstances, the kinetic energy of the flow caused by the dynamic pressure is converted to the potential energy, *i.e.*,

$$\frac{1}{2}v_f^2 + \frac{P_d}{\rho_f} + gh_f = constant, \tag{3.55}$$

where v_f, P_d, ρ_f, and h_f are the speed, dynamic pressure, density, and the height of the flow, respectively. Considering an incompressible fluid flowing at a steady speed along the streamlines, the Bernoulli's equation can be modified as

$$\frac{1}{2}v_{static}^2 + \frac{P_{static}}{\rho_f} = \frac{1}{2}v_t^2 + \frac{P_t}{\rho_f} \tag{3.56}$$

where v_{static} and P_{static}, v_t and P_t are the fluid velocity and fluid pressure in the exterior tube, the fluid velocity and fluid pressure in the interior tube, respectively. At $v_t = 0$, the interior pressure has the highest value where is called the stagnation point. The fluid velocity in the exterior tube can thus be given by

$$v_{static} = \sqrt{\frac{2(P_t - P_{static})}{\rho_f}} = \sqrt{2gh_f}. \tag{3.57}$$

Therefore, by applying a high-pressure air flow to the exterior tube, it produces a pressure difference thus pumps the gas into the interior tube.

3.9.2 Pump Diagram

The Pitot-type air pump (ZU07L, Vacuum Ejector Series, SMC, Japan) is a modified Pitot tube as shown in Figure 3.26(b). One end is connected to a air compressor which

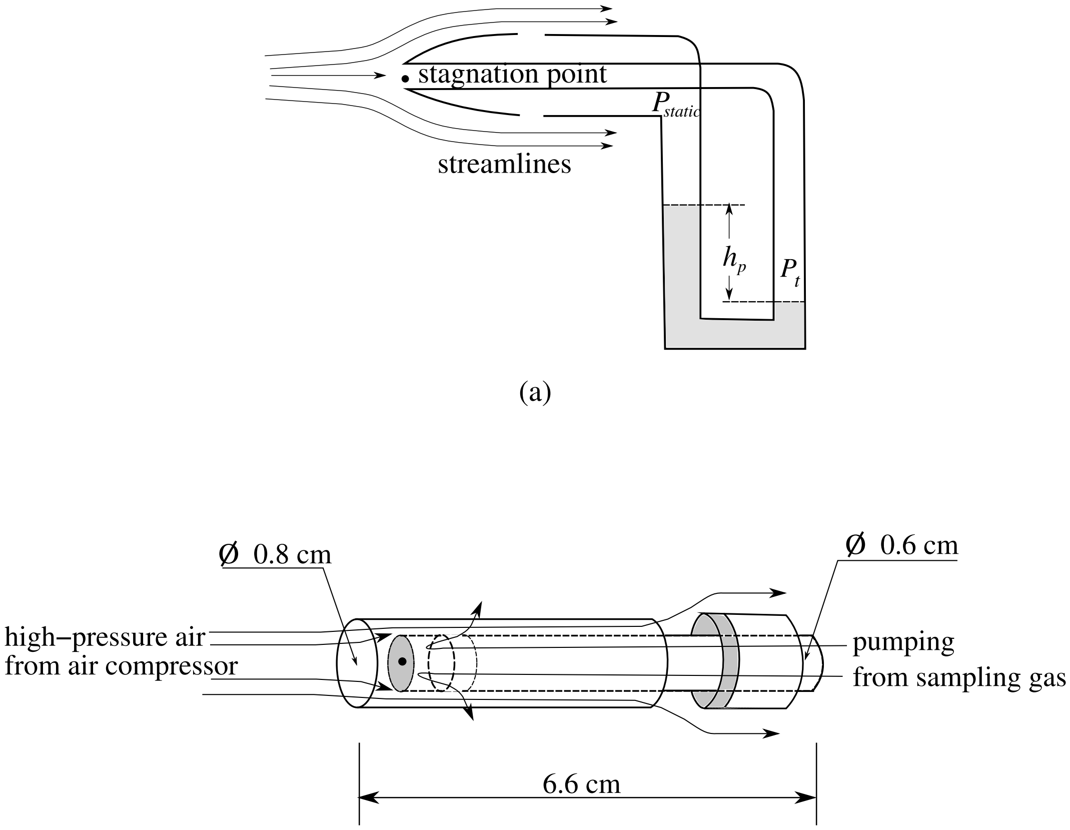

(a)

(b)

Figure 3.26: (a) The Pitot tube. (b) The Pitot-type air pump diagram.

can produce up to 15 kPa air pressure. The other end is connected to the sampling loop. Two identical copper tubes with outer diameter 6 mm are connected to the ends of the pump. The sampling gas pumping pressure is fixed at 8.95 kPa (-0.454 displaying on the pressure gauge).

3.10 Calibration for QTF in Gases

3.10.1 QTF in Non-flowing Gases

Considering the relation between the resonant frequency shift and the density of surrounding gas as described in Eq. 3.9, *i.e.*,

$$\frac{\Delta f_g - \Delta f_{N_2}}{\Delta f_{CO_2} - \Delta f_{N_2}} \cong \left(\frac{\rho_g - \rho_{N_2}}{\rho_{CO_2} - \rho_{N_2}} \right) \tag{3.58}$$

where f_{g,N_2,CO_2} and f_v are the resonant frequencies in different gases (gas mixture, nitrogen, carbon dioxide) and in vacuum, and $\rho_g, \rho_{N_2}, \rho_{CO_2}$ are the densities of gas mixture, nitrogen, and carbon dioxide, respectively. The density of the gas mixture ρ_g can be given by

$$\begin{aligned} \rho_g &\cong \rho_{N_2} + (\rho_{CO_2} - \rho_{N_2}) \cdot \frac{\Delta f_g - \Delta f_{N_2}}{\Delta f_{CO_2} - \Delta f_{N_2}} && (3.59) \\ &\cong \rho_{N_2} + \frac{\Delta f_g - \Delta f_{N_2}}{\zeta} && (3.60) \end{aligned}$$

where

$$\zeta = \frac{\Delta f_{CO_2} - \Delta f_{N_2}}{\rho_{CO_2} - \rho_{N_2}}. \tag{3.61}$$

Therefore, ρ_g can be given by measuring Δf_{N_2} and Δf_{CO_2}. The density of nitrogen ρ_{N_2} and carbon dioxide ρ_{CO_2} gas can be calculated according to the ideal gas law and the ratio of frequency shift to density shift ζ can also be obtained. The sensing QTF has been put in non-flowing pure dry nitrogen and carbon dioxide gas at room temperature under atmospheric pressure (Figure 3.27(b)). The pressure and temperature signals were also monitored (figure 3.27(a) and (d)). The infrared absorption signals from 100% and 0% of carbon dioxide (which is 100% nitrogen) were detected and the signal difference is -0.2560 V (figure 3.27(d)). The signal noise from those detectors are also marked in figure 3.27. The density of nitrogen is 1.1560 kg/m^3 (22.1 ^oC, 101.4152 kPa) and carbon dioxide gas is 1.8145 kg/m^3 (22.2 ^oC, 101.4576 kPa). The ratio ζ has been calculated as -4.5450 which can be regarded as a reference value for the flowing gas measurement.

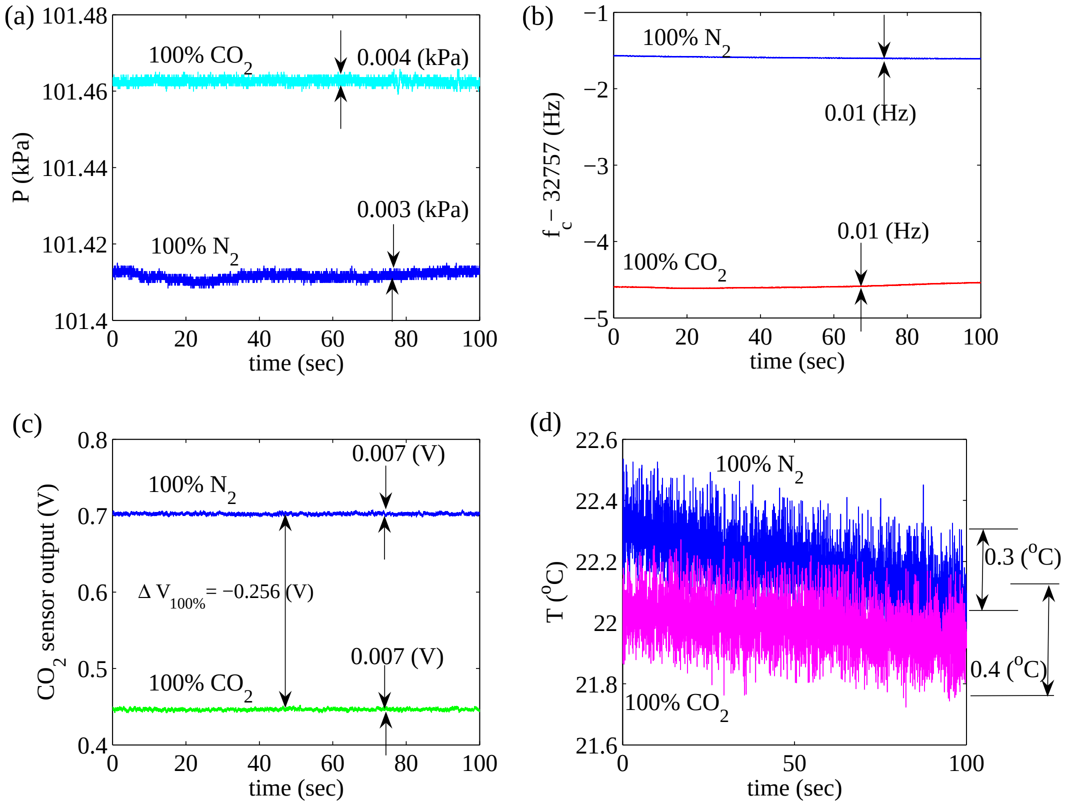

Figure 3.27: (a) Pressure monitored by the pressure sensor and the corresponding noise (0.004 kPa in CO_2 and 0.003 kPa in N_2). (b) Resonance frequencies of QTF in N_2 (32755.40 Hz) and in CO_2 (32752.40 Hz) and the related noise (0.01 Hz in both gases). (c) Output signals from the infrared detector and the related noise (0.007 V in both gases). The signal difference (ΔV) of 100% CO_2 from 0% CO_2 is -0.2560 V. (d) Temperature (22.3^oC in N_2 and 22.1^oC in CO_2) monitored by the thermistor and the related noise (0.3 ^oC in N_2 and 0.4 ^oC in CO_2).

3.10.2 QTF in Flowing Gases and Infrared CO_2 Detector Calibration

During the helium washout measurements, the flowing gas mixture passes through the cold water trap, the QTF cell, the thermistor and pressure sensor, and finally the optical cell. To get the density of the gas mixture in the flowing gas, a calibration has been performed by putting the flowing nitrogen and carbon dioxide gas through the gas analysing system before every washout measurement. Thus, the resonant frequency shifts $\Delta f_{N_2}, \Delta f_{CO_2}$, and Δf_g can be found, and the related temperature, pressure and signal from the carbon dioxide detector were also monitored. The pure nitrogen and carbon dioxide gas have been put in two foil balloons separately. Each balloon has been connected to a one-way Luer valve (Polycarbonate Luer Stopcocks, WZ-30600-06, Cole-Parmer, UK) for controlling the flow rate. Two valves from each gas are connected with a tee tube and then to the gas analysing system.

Figure 3.28 shows the results from those sensors with 100% N_2 and CO_2 gas flowing through including a value of the corresponding noise. Figure 3.28(e) and (f) display the output signal difference from the carbon dioxide detector, ΔV_{CO_2}, versus the concentration of the carbon dioxide. Figure 3.28(e) is fitted with a double-exponential curve from 0-100% CO_2. However, it gives a big error for lower concentration of CO_2 displyed in (f). It may result from the lower thermal conductivity of carbon dioxide compared to nitrogen such that the optical cell is warmed up when CO_2 flows through. Since the CO_2 detector is sensitive to temperature, when switching from the carbon dioxide to the nitrogen gas, the temperature effect can not be ignored for lower concenration of carbon dioxide signal. Therefore, a 5.6% of carbon dioxide mixed with nitrogen has been used instead, to calibrate the relationship between $[CO_2]$ and the CO_2 detector output signal as shown in figure 3.29. For lower concentration of CO_2, the output signal shows linear relation to $[CO_2]$ and it has been fitted with a linear polynomial curve.

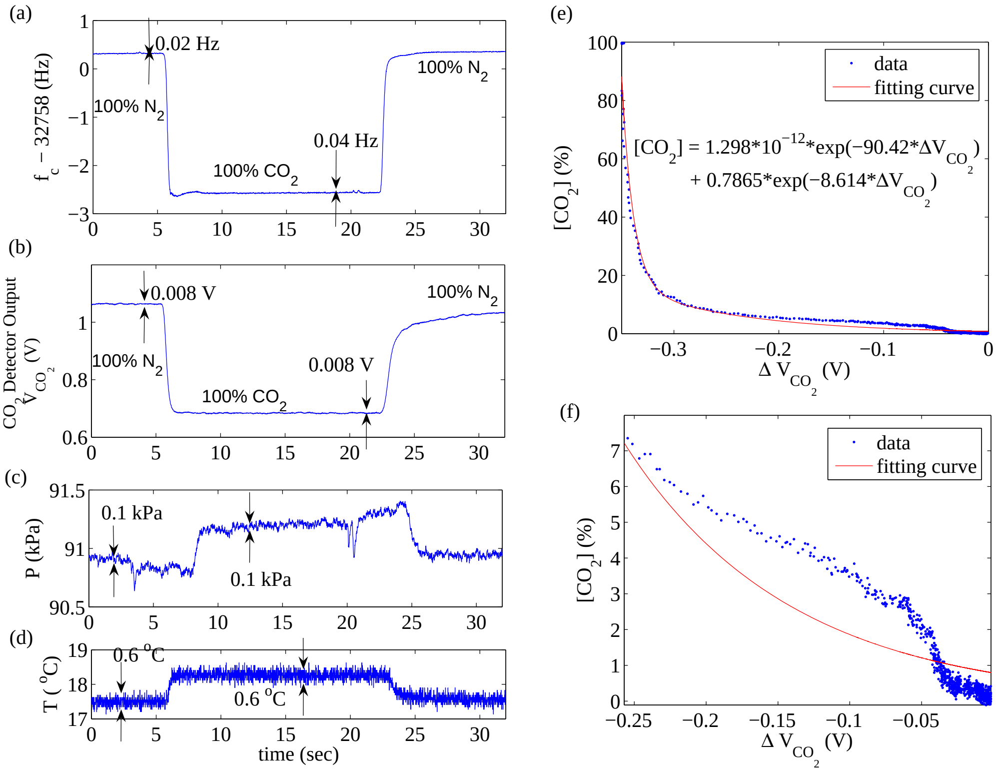

Figure 3.28: The four sub-graphs (a)-(d) display the results from the sense QTF, CO$_2$ detector, pressure sensor and thermistor when 100% N$_2$ and CO$_2$ gas flowing through. The corresponding noise has also been marked in each graphs. Two sub-graphs (e) and (f) on the right-hand side show the calibrated curve of CO$_2$ detector output signal versus the concentraion of carbon dioxide. The curve in (e) is fitted with a double-exponential curve from 0-100% of CO$_2$. (f) shows the fitting curve gives a big error for lower concentration of CO$_2$.

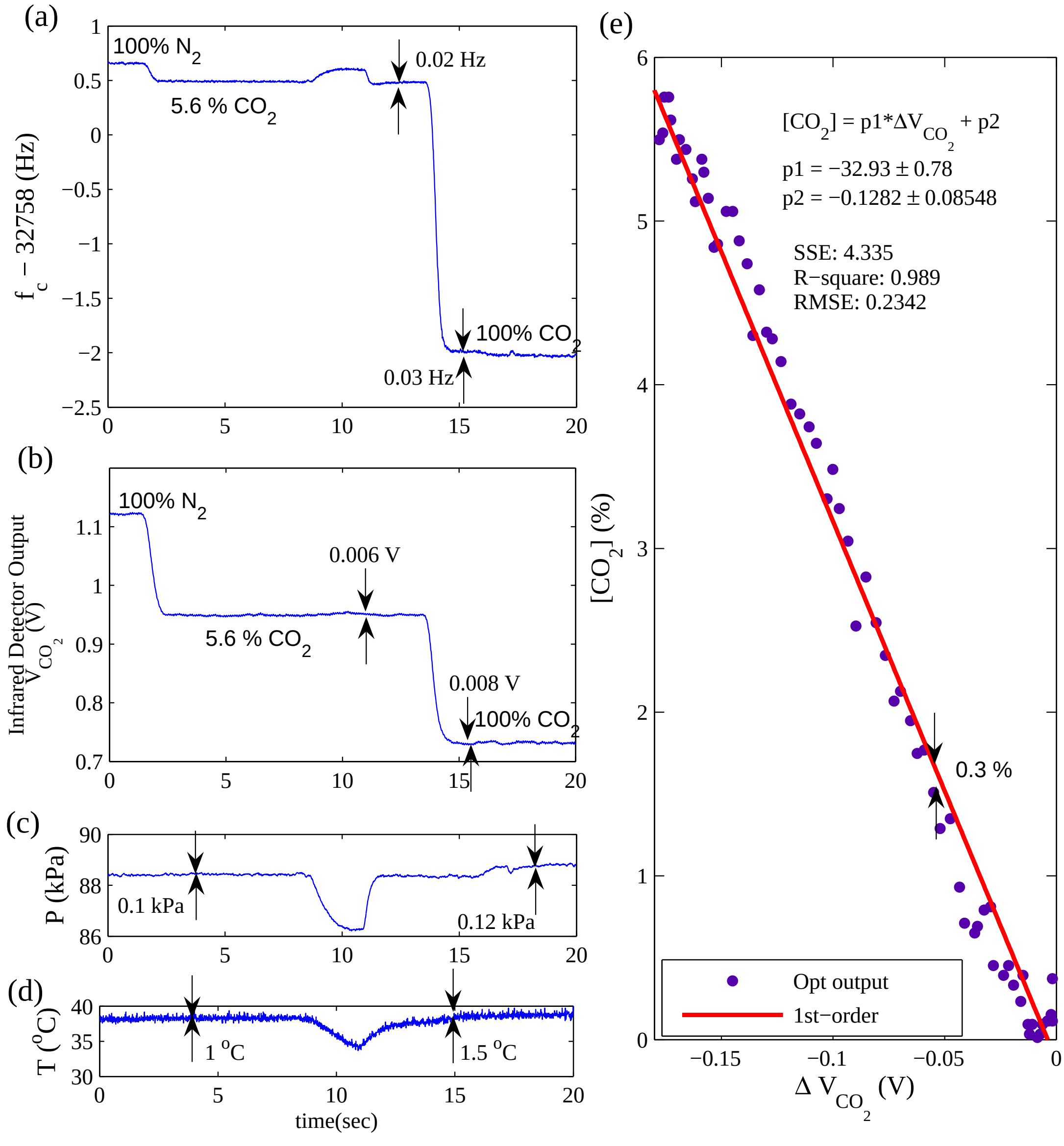

Figure 3.29: The calibration of CO$_2$ detector output signal versus concentration of carbon dioxide for low concentrations. The four graphs (a)-(d) show the results and the corresponding noise. Graph (e) shows the calibrated curve and a linear fitting curve and the fitting results.

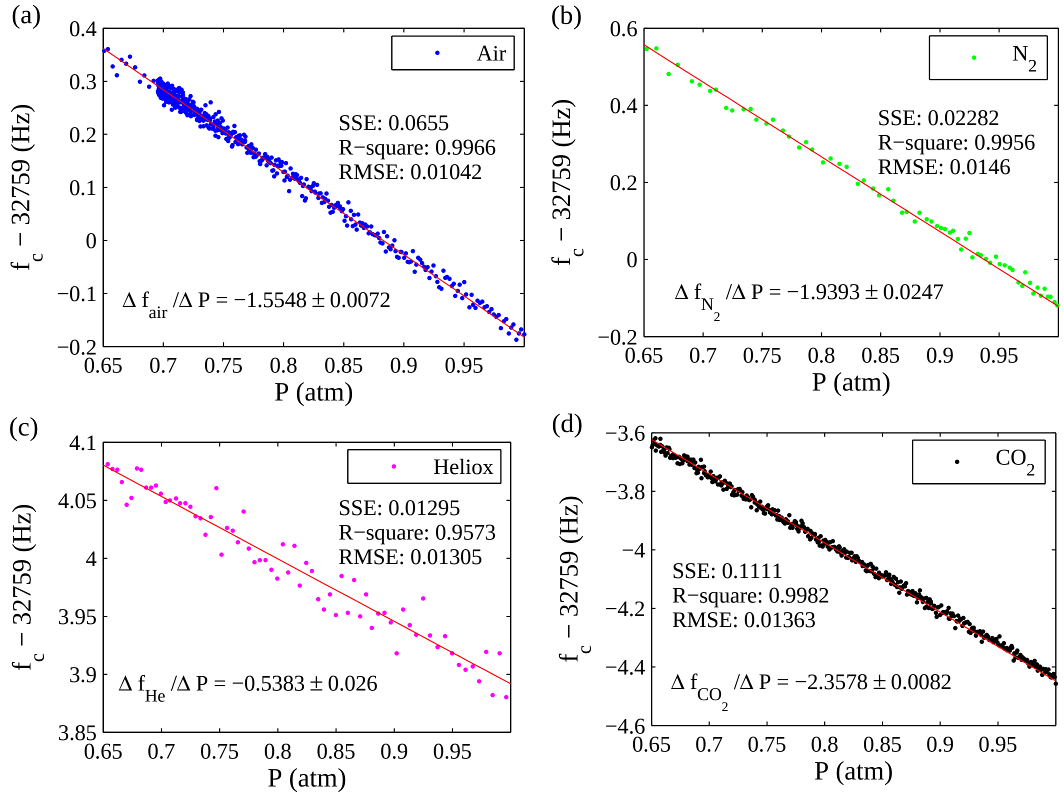

Figure 3.30: Dynamic pressure measurement for QTF resonant frequency shift in four different gases (air, pure nitrogen, heliox, pure carbon dioxide). A linear curve has been fitted for each data set. The ratio of the resonant frequency shift Δf_c and pressure difference is also displayed on each graph.

3.10.3 QTF under Different Pressure

The QTF sensor has been put in four different flowing gases (air, pure nitrogen, heliox, pure carbon dioxide) under 1 to 0.65 atm at room temperature. Each gas has been put in a 4L plastic bag pumping through the QTF cell with a one-way Luer valve (Polycarbonate Luer Stopcocks, WZ-30600-06, Cole-Parmer, UK) for controlling the flow and thus the pressure. The dynamic pressure is measured with a commercial pressure gauge (PDCR 4010, S/N 1635531, Druck, UK). Figure 3.30 shows the results of the resonant frequency f_c (in Hz) versus pressure (in atm) from four different gases.

A linear curve has been fitted for each data set and the ratio of frequency shift and pressure difference is also displayed on each graph.

The ratio of frequency shift versus the pressure change ($\frac{\Delta f}{\Delta P}$ in different gases under this calibrating method is not necessarily related to the gas density. The ratio is higher in nitrogen than in air. It may be caused by the gas viscosity since nitrogen has smaller viscosity (20.7430 $\mu Pa \cdot s$, at 300 K, 1 atm) compared to air (21.3241 $\mu Pa \cdot s$, at 300K, 1 atm) [41].

3.10.4 Response Time of QTF and Optical System

The response time of QTF system has been done by changing the dynamic pressure of flowing air at room temperature. A lower dynamic pressure was made manually by squeezing the sampling tube at the entrance of the QTF system. The sudden rise and drop of the QTF signal represents the tube being squeezed and loosed. The response time of the QTF system (<0.01 sec) has been taken as the time period of the pressure drop from low to high pressure (pressure difference is 0.88 atm) as shown in figure 3.31(a).

The real response time of the optical system is hard to be measured since it only has high response to the carbon dioxide gas and the time of gas diffusion and transportation needs to be considered [38, pp. 59]. Since the chopping frequency of the photoconductor is 600 Hz with the lock-in signal 110 Hz, the electronic response time is less than 0.01 sec. The response time of the optical system is not measured directly but the output signal has been compared to the QTF signal from a normal breathing measurement. Figure 3.31(b) shows the QTF signal and the modified optical signal[3] from a normal subject doing tidal breathing. Two sensors have identical response to the expirations although the QTF has higher digital noise. Optical signal has a lag in inspiration signal which is caused by the water vapour.

---

[3] It is modified by multiplying a constant to the original signal since at lower concentrations, the output optical signal has linear variation with the concentration of carbon dioxide.

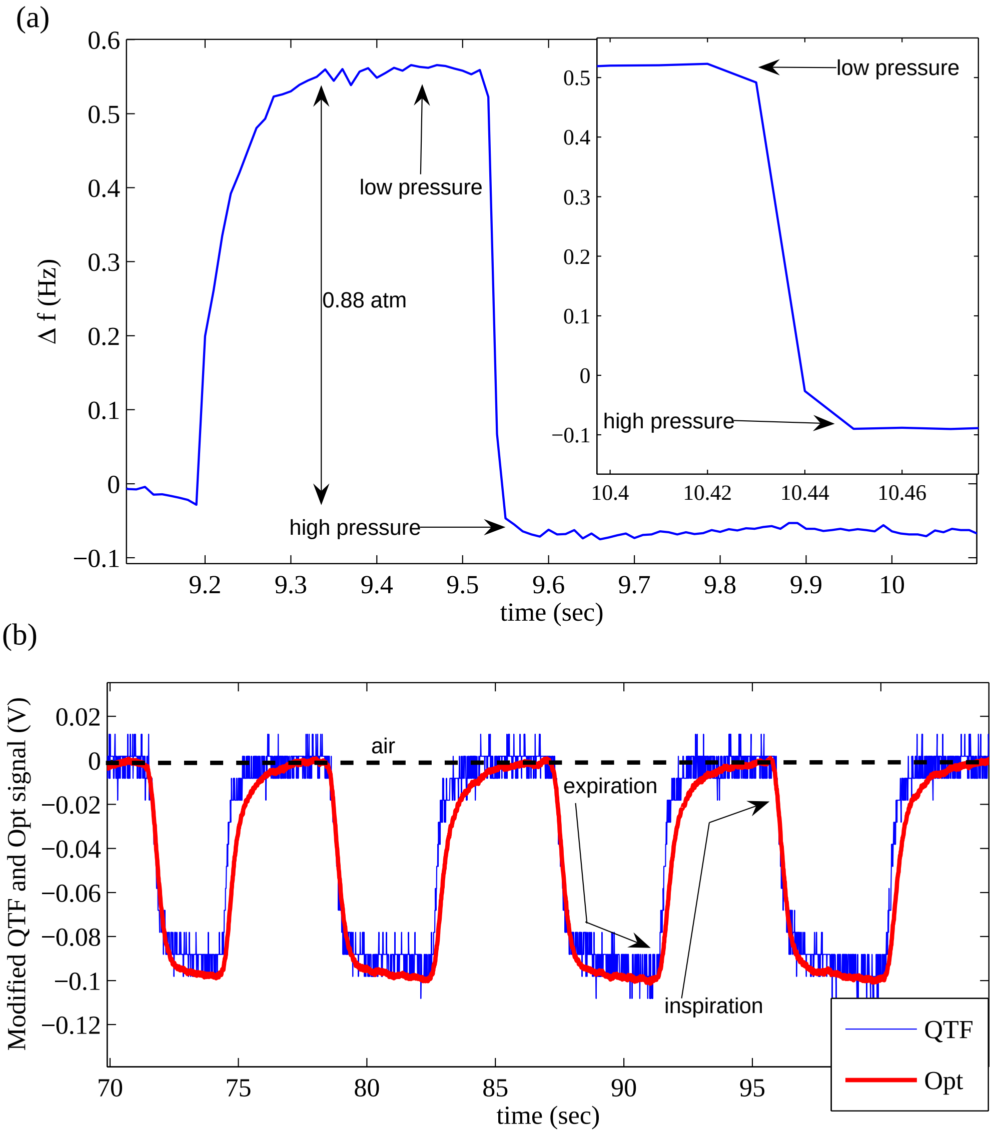

Figure 3.31: (a)The response time of QTF system (<0.01 sec) is taken as the sudden drop of the QTF signal from low to high pressure (pressure difference is 0.88 atm). (b)Modified output signal from the QTF and optical system during normal-tidal breathing measurement. Two sensors have identical response to the expirations, however, the optical signal has a lag in inspirations which is caused by the water vapour. The base line (dash) represents the air signal.

3.10.5 Temperature Effect on CO_2 Detector Output

Since the infrared photoconductor is very sensitive to the temperature, a measurement of the output voltage from the CO_2 detector has been done at various temperatures and CO_2 concentrations[4]. 100% nitrogen, 4.35% carbon dioxide, and 100% carbon dioxide gases have been put through the optical cell during the cooling from 36 ^oC to 15 and 8 ^oC. Each dataset has been fitted with a 4th-order polynomial curve as shown in Figure 3.32(a). Figure 3.32(b) shows inverse curves of (a) fitted with the Gaussian functions. The fitted polynomial and Gaussian functions are displayed in table 3.2 and table 3.3. The temperature of gas flowing through the optical cell is normally at 36 ± 2^oC where the difference of output optical signal between 100%, 5%, and 0% CO_2 are constants. Thus the linear realtion of $[CO_2]$ versus output optical signal in figure 3.29 is used for the calibration.

4-th order polynomial fitting $V_{CO_2} = p_1 \cdot T^4 + p_2 \cdot T^3 + p_3 \cdot T^2 + p_4 \cdot T + p_5$

Gases	p_1	p_2	p_3	p_4	p_5	SSE/R-Square
100 % N_2	$5.052 \cdot 10^{-6}$	$-3.026 \cdot 10^{-4}$	0.01109	-0.542	11.95	6.71/0.9998
4.35% CO_2 in N_2	$-2.377 \cdot 10^{-6}$	$4.322 \cdot 10^{-4}$	-0.01609	-0.06681	8.22	4.412/0.9989
100 % CO_2	$-1.38 \cdot 10^{-7}$	$1.249 \cdot 10^{-4}$	$-2.174 \cdot 10^{-3}$	-0.2944	8.679	1.507/0.9994

Table 3.2: Temperature versus Optical System Output Voltages Curve Fitting Parameters

---

[4] The temperature-dependence measurements of the PbSe photoconductive films from other groups can be found in [88]

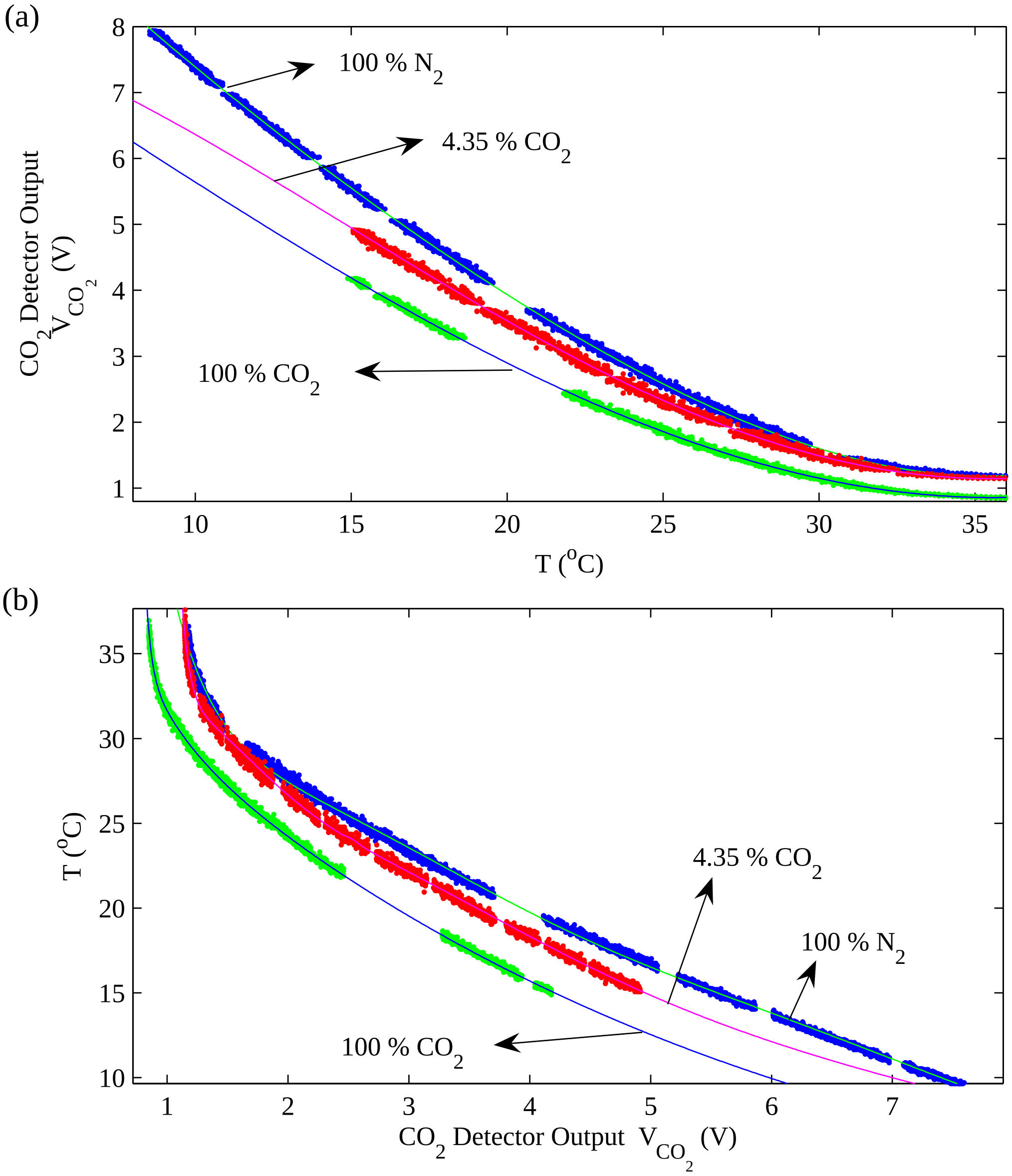

Figure 3.32: (a) Output voltage from the CO_2 detector when pure nitrogen, 4.35% carbon dioxide and pure carbon dioxide flowing through the optical cell under various temperature during cooling process. (b) Inverse curves of (a).

Gaussian fitting $T = \sum_{i=1}^{5} a_i \cdot e^{-(\frac{V_{CO_2}-b_i}{c_i})^2}$

Parameters	**100 % N_2**	**4.35 % CO_2**	**100 % CO_2**
a_1	$1.33752 \cdot 10^{12}$	7.086	$1.584 \cdot 10^{8}$
b_1	-16.03	0.8648	-0.7325
c_1	3.372	0.9934	0.3739
a_2	-1.837	15.67	$2.349 \cdot 10^{13}$
b_2	4.208	1.325	-19.23
c_2	1.916	8.262	3.686
a_3	29.92	$1.279 \cdot 10^{12}$	666.2
b_3	-0.1525	-2.263	-29.86
c_3	7.255	0.6635	17.49
a_4		0.102	
b_4		2.537	
c_4		0.06872	
a_5		9.632	
b_5		1.366	
c_5		2.899	
SSE/R-square	248.8/0.9995	180.4/0.9983	75.798/0.9992

Table 3.3: Optical System Output Voltages versus Temperature

Chapter 4

MBHW System Control, and Analysis Programme

This chapter is the user manual for the MBHW system. The MBHW system is described in section 4.1. The system-control Labview programme is described in section 4.2. The MBHW analysing programme is described in section 4.3. The systematic error and the error from the analysis is discussed in section 4.4.

4.1 MBHW Experiment Setup

4.1.1 Experiment Preparation

Before each washout measurement, the MBHW system needs to be prepared, which is described as follows:

Optical system warming up

To warm up the optical system to a steady temperature (47-50 ^oC) may take up to 2 hours from room temperature. Thus turning on a dc power supply to the heaters of the optical cell is the first thing to setup the system. In the mean time, the other detectors are powered up, and three LabView programmes *DAQmx01.vi*, *DAQmx02_both.vi* and

DAQmx_RESET.vi are loaded.

System Cooling down

When the temperature of the optical cell is nearly 47^oC, the MBHW system is ready to be connected to the ice water trap. Since in this project, an ice bath is used as the water trap, it will take about 5-10 minutes cooling down the whole system to a constant temperature (around 12^oC depending on the room temperature) by a flowing gas. To prepare for this step, an 80 litre balloon is filled with pure dry nitrogen gas. With the ice bath filled with ice, connecting the ice water trap to the system and to the nitrogen balloon, the dry nitrogen gas is flowing through the system. Nitrogen gas instead of room air is used in this step to avoid water droplets from the air condensing to the TF or other sensors or tubes joined between each sensors which will block the sampling loop. During this stage, signals from the TF detector, pressure sensor, thermistor, and the optical sensor need to be monitored (by the LabView Programme *DAQmx01.vi*) until they stop changing.

Flow Meter Calibration

Since the room temperature, inner room pressure, the room-air humidity, and the high pressure air supply can change from day by day, it is necessary to calibrate the output of the flow meter versus the real inspired and expired flow rate. Sometimes the turbine inside the expiration flow meter can stick due to the wet expired gas or it gets dirty. This can also cause the one-way valve to leak. Thus this step is also to check that the two flow meters work well.

3 litres of room air is put in a bag and connected to the inspired air inlet. A bung is put at the mouth piece to stop the air flowing. The other end of the expired turbine is connected to the air pump. The pressure ($P1$), inspired flow and expired flow signals are monitored at the same time. The pressure signal $P1$ indicates when the pumping starts and when it is ended. The calibrated inspired flow signal is 2.9947±0.0425 V/L (volts-per-litre) and the expired flow signal is 3.9596±0.0215 V/L at 24^oC, 103.0 kPa.

Sensor Checking

This step can be done while the optical cell is warming up or while the system is cooling down. The check list is as follows:

- **Flow Meters**: To make sure the resetting signals are input properly to the flow meter circuit, a LabView programme *DAQmx_RESET.vi* is loaded which will be introduced in the next section. This LabView programme sends a 5.0 V, 1.0 Hz pulse signal to reset the counter in the flow meter circuit. The two flow counters should go down to zero after resetting. Other checking, such as if the turbine is clean or if the valve is leaking should be done before doing the flow signal calibration. Sometimes the reset signal cannot be generated properly which may be caused by the bad connection of the DAQ card (on the main board and the external usb one) or the computer can not call the LabView programme properly.

- **Tuning Fork**: The supplied voltage of battery to the crystal oscillator should be remained at between 4.25V to 4.65V (figure 3.11). Voltages less than 4.25V will result in a smaller amplitude of square waves and an incorrect pulse trigger voltage and thus an incorrect frequency shift. The offset value of easyPLL control panel is normally set between 32756 Hz to 32759 Hz and the gain factor is normally set at 1.831 V/Hz for a best signal-to-noise ratio (better than 7.324 V/Hz). When nitrogen gas or air flows through, the frequency change is usually less than a hertz. If the frequency suddenly changes a lot or even shifts out of the detecting range, there could be a water droplet or dirt on the tuning fork. If this happens, the tuning fork should be dismounted and cleaned with ethanol or acetone liquid. The resonance frequency decreases while the temperature is increasing. To avoid the temperature change of the circuit board, a piece of polystyrene covers on the top of the tuning fork cell.

- **Thermistor**: The temperature is given by two signals- one is the voltage drop across the thermistor, the other one is the battery voltage. The voltage drop across the thermistor is normally around 0.2 V and the battery voltage is about

8.7 V which gives the resistance of the thermistor as about 13.1 kΩ at 18 ^{o}C.

- **Optical Sensor**: Optical sensor and infrared LED have been fixed in the optical cell. The setting of the lock-in amplifier and the function generator are the same as the table 3.1 in section 3.6.2. The sensitivity and the amplitude of the output signal depends on the setting. Also a calibration of the output signal versus the concentration of the carbon dioxide has been done at the same setting. A new calibration needs to be made if the setting is changed. The output signal of the lock-in amplifier goes down to around 1.8 V when the optical cell is warming up to 47 ^{o}C and changes from 0 to -0.15 V when the concentration of the carbon dioxide increases from 0 to 6 %.

- **Pressure Sensors**: Pressure $P2$ is recorded during the washout measurements. Its display value is normally adjusted at -0.477 (by controlling the air pump flow) which gives the output signal (P_2 =2.4 V) corresponding to a 10 kPa relative pressure to the atmosphere. A higher pressure (lower sampling flow rate) will cause a delay or slower response from the sensors while a lower pressure (higher sampling flow rate) will result in sucking the gas from our lungs involuntarily and affect the breathing.

Tuning Fork in Pure Nitrogen and Carbon Dioxide Gases

This measurement is required to get the ratio of resonance frequency shift and density change $\frac{\Delta f_{CO_2}-\Delta f_{N_2}}{\rho_{CO_2}-\rho_{N_2}}$. Signals from the pressure sensor ($P2$), two from thermistor cross voltages ($T1$ and $T2$), tuning fork detecting system, and optical detector are monitored while a pure nitrogen and pure carbon dioxide gas flows through the system separately. Each gas is put in a 80 litre balloon left at room temperature and controlled by a Luer valve. This calibration is necessary before each washout measurement because the tuning fork signal is sensitive to the surrounding air temperature. The ratio, $\frac{\Delta f_{CO_2}-\Delta f_{N_2}}{\rho_{CO_2}-\rho_{N_2}}$, will change slightly ($< 2\%$) depending on the room temperature variance. It may be caused by the heat conducted through the electrical board to the contact silver patterned on the surface of the tuning fork and thus modifies the tuning fork vibration.

4.1.2 LabView Control Programmes

The main washout control programme is a LabView programme *DAQmx02_both.vi* which will be described in this section. A general analog data-acquisition programme *DAQmx01.vi* is used for calibration measurements. It monitors the output signals connected to the 8-channel BNC box and input board with the continuous analog DAQ control vi. The sampling rate can be set up to 10^6 Hz (depending on the type of the DAQ card) but normally set as 100 to 1000 Hz. The flow meter reset programme *DAQmx_RESET.vi* is designed to give a 5 V, 1 Hz pulse signal to the counter of each flow circuit. The counter in the flow meter circuit should be set to zero after reset (all LED lights off).

DAQmx02_both.vi

This control programme is designed specially for MBHW measurements. Two DAQ cards along with two separate 8-channel BNC interfaces are used. One of them monitors the output signals from two flow meters (channel 0 and channel 1), pressure gauge $P2$ (channel 2), tuning fork detector (channel 3), voltage drop across the thermistor $T1$ (channel 4), optical detector (channel 5), and the battery voltage from the thermistor circuit $T2$ (channel 7). Channel 6 is also monitored because it used to be connected to the mass spectrometer which is not used any more in the washout measurements and will be described in next chapter. The eight analog signals are monitored at the sampling rate of 1000 Hz. The second DAQ card monitors the analog pressure signal $P1$ which indicates the breathing flow direction and thus the inspirations or the expirations. Two analog output channels are connected to the reset inputs of the flow meters.

Before a washout measurement, there are three settings on the front panel of the programme to key in as shown in figure 4.1.

- **Pressure Threshold**: The static pressure signal from pressure gauge $P1$ may change day by day. Thus the background value needs to be recorded as the thresholds of the breathing pressure change. By simply running this programme before washout measurements, the maximum (`max P`) and minimum (`min P`) of the static pressure signal $P1$ will be displayed. These two values tell the computer when to send a reset pulse to the flow meter counter.

- **Tunning Fork Setting**: The output signal from the easyPLL detector is the frequency shift divided by a gain factor. The central frequency (normally 32757 Hz) and the gain factor (normally 1.831 V/Hz) are set for the easyPLL control programme.

- **Tidal Volumes Setting**: `Vt` is the tidal volume setting for the measurement. Normally it is set at 0.99 litre. It can range from 0.7 to 1.6 litres depending on lung capacities. From the flow meter calibration measurement, the ratio of the output signal to the real gas volume flowing through and the background signal of the flow signal is found. When the tidal volume of gas is inspired or expired, a 'ding' sound from the speaker reminds the subject when to reverse the breathing. In this work, subjects are normally asked to breathe as normal and steady as possible. If the breathing is even, the speaker sometimes is turned off to make subjects as comfortable as possible.

After entering the settings, the subject is ready to prepare for the test as follows:

- **Sitting Posture**: In this work, MBHW tests are taken in the sitting posture. Subjects are asked to sit on an adjustable chair with their mouth and the mouth piece of the system at the same height.

- **Nose Clip**: In oder to avoid breathing through the nose, subjects are asked to put a nose clip on while doing the measurements.

- **Normal Breath**: In this work, subjects are asked to breathe as normally and steadily as possible. Instead of following the 1-litre tidal-volume in nitrogen-washout tests by other groups [79], subjects breathe their own tidal volumes. This takes into account that the FRC (residual lung capacity) is different from

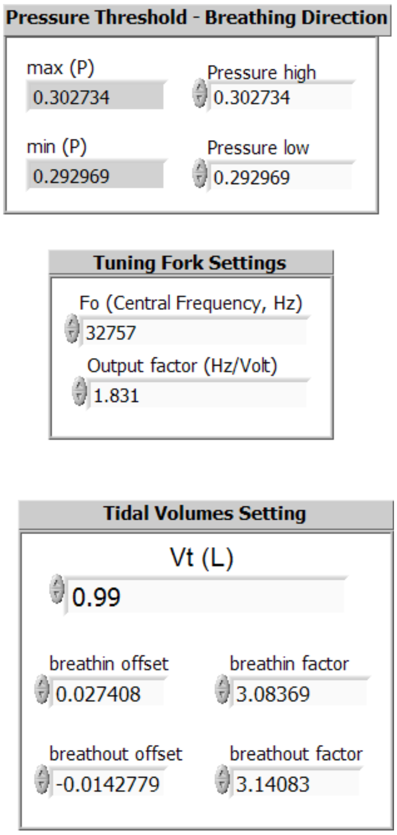

Pressure Threshold - Breathing Direction

max (P) 0.302734

Pressure high 0.302734

min (P) 0.292969

Pressure low 0.292969

Tuning Fork Settings

Fo (Central Frequency, Hz) 32757

Output factor (Hz/Volt) 1.831

Tidal Volumes Setting

Vt (L) 0.99

breathin offset 0.027408

breathin factor 3.08369

breathout offset -0.0142779

breathout factor 3.14083

Figure 4.1: Control programme *DAQmxboth.vi*: parameter settings before helium washout measurement.

person to person. Generally, the tidal volume is about one third of a subject's FRC.

When the subject and system are all ready, it is time to run the control programme and start doing the measurements:

- **Fill The Helium Balloon**: This step is left until just before the measurement starts in oder to avoid the helium gas leaks. The balloon is emptied before refilling it to avoid air remaining in the balloon.
- **Run The Programme**: There are four graphs which display the resonance frequency of the tuning fork, the optical sensor signal, the pressure signal $P2$, and the temperature from two thermistor signals. A bar chart is to display the tidal volume change which helps the subject breathe evenly while doing the measurement.
- **Pre-washout Normal Breathing**: To get the Q_r ratio $(=\frac{\Delta[O_2]}{\Delta[CO_2]})$, four to five breaths are taken before the washout measurements.
- **Helium Wash-in Measurement**: After the pre-washout measurement, helium gas is ready to be washed into lungs. By switching on the full-way handle valve connected to the helium balloon and switching off the other one connected to the air manually, helium gas starts to be breathed in.
- **Helium Washout Measurement**: When the tuning fork signal at each end of the expiration reaches a constant value (it is sometimes hard to tell, but normally after 25 breaths), the full-way valve is opened to the air and the helium supply is closed. The helium gas is ready to be washed out by room air.
- **Measurement Complete**: When the tuning fork signal at each end of the expiration reaches a constant value, the measurement is completed. The washout data will be saved in the text file as `[date Vin Vout P2` F_c `T1 Opt T2]`.
- **Cleaning**: After the measurement each time, the gas analysing system and the flow turbine are dried by flowing air or nitrogen gas. The mouth piece and the

nose clip are cleaned by immersing in the medical usage cleaning liquid overnight. Other tubing and pluming is cleaned by liquid ethanol.

4.2 Analysis Programme

The analysis programme is a LabView programme *MBHW Analysis_02.vi* containing the MatLab scripts. It can be described in three parts. The first part is to separate each breath from the washout data because there is a time delay between the flow signals and the sensors. And the time delay is slightly different breath by breath. It is because the concentration of helium varies, as well as the density and viscosity of the gas mixture, breath by breath. The second part is to calculate the respiratory ratio Q_r from one of the pre-washout normal breaths. This ratio can be given by plotting the $[CO_2]$ versus $[O_2]$ graph and fitting with two linear curves. We have simply made an assumption that the Q_r is fairly constant during the washout measurement since the end-expiration concentration of carbon dioxide from each breath remains fairly constant. The $[O_2]$-$[CO_2]$ curve is separated into two parts considering the respiratory dead space which is about 0.15 to 0.2 litres. The slope of the second fitting curve is the Q_r. The third part of the programme is the main part which gives the normalised phase II and phase III slopes, the mean concentrations and the dead space of four gases (He, N_2, O_2, CO_2). The washout curve from each single breath can also be calculated. The analysis programme diagram is shown in figure 4.2.

4.2.1 Breath Separation

Each breath is separated by examining the flow rates. At the end of each inspiration or expiration, signals from the inspiratory or expiratory flow meter are reset and go down to zero instantaneously. This gives an array of peaks which are the end point of each breath for both inspired and expired tidal volumes. The front panel of this part is shown in figure 4.3. The signals of pressure, temperature, resonance frequency shift from the tuning fork, optical output, and expired tidal volume are displayed in

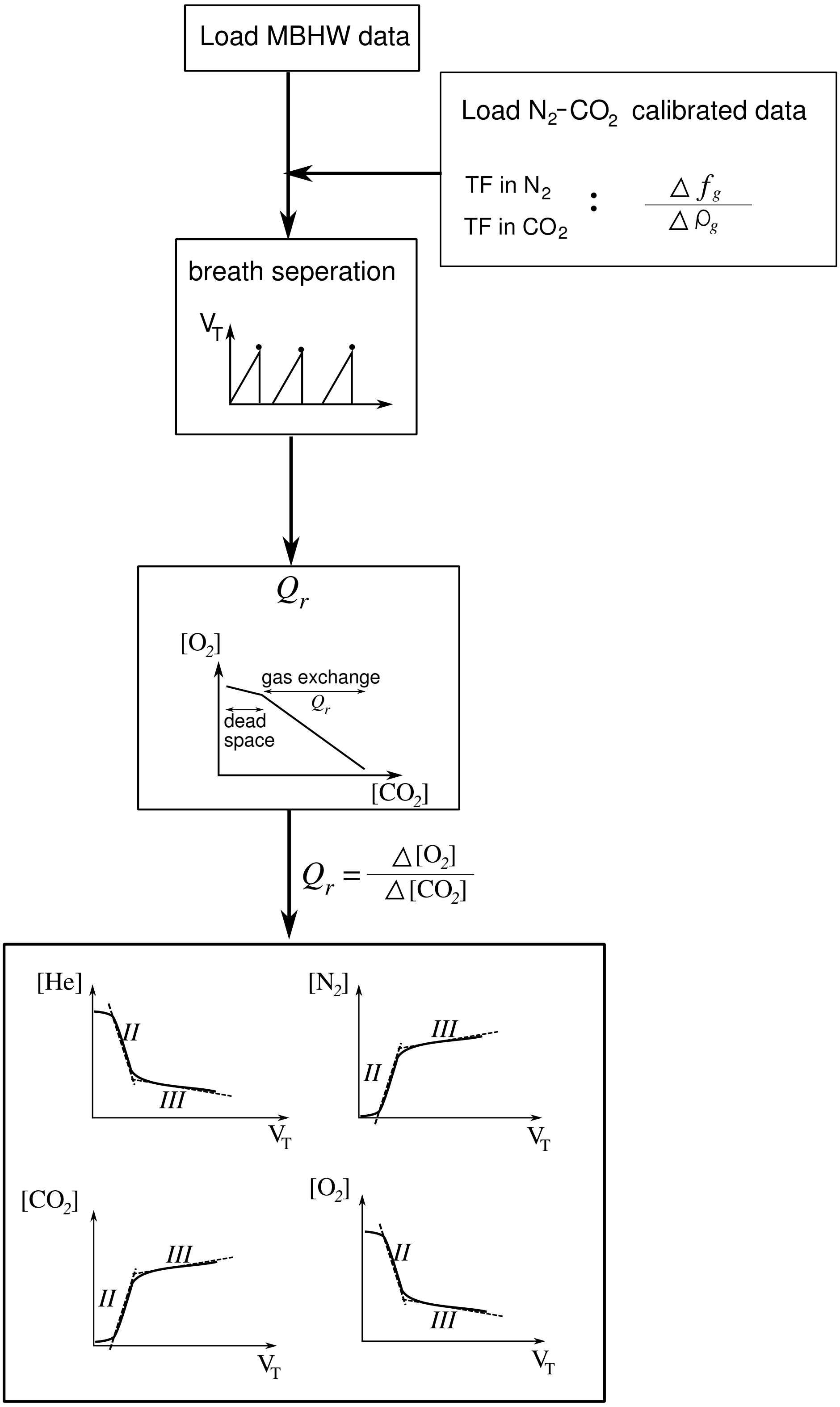

Figure 4.2: Analysis programme *MBHW Analysis_ 02.vi* diagram. Consists of data loading, the frequency shift to gas density change ratio $(\frac{\Delta f_g}{\rho_g})$ calculating, breath separation, respiratory quotient calculating, and phase II phase III slope fitting.

the top panel by choosing a MBHW data text file. Three control icons at the bottom of this panel are for adjusting the time delay (`Opt-TF delay` icon) between the optical signal and the QTF signal which will not change the original data while doing the real analysis. The time delay is slightly different during the wash-in and washout process because the diffusion coefficient of helium is higher than air. Normally, this delay time is about 0.3 sec in air, and 0.25 sec in heliox/air mixture. The `movement` and `factor` icons are to adjust the offset and the signal size of the optical output signal.

The middle panel of figure 4.3 displays the data from a calibration with pure nitrogen and carbon dioxide gas before each MBHW measurement in order to get the ratio of resonance frequency shift (Δf_g) versus density change $\Delta \rho_g$. The density of the gas mixture will be automatically calculated for the next part of the analysis. The concentration of carbon dioxide is calculated by using a linear relation $[CO_2] = -32.959 * \Delta V_{Opt} - 0.1857 + 0.4$ from a calibration results with 5.6% of carbon dioxide, where ΔV_{Opt} is the optical output signal with the subtraction of the offset of the signal with room air only. The bottom panel of figure 4.3 displays the inspired and expired tidal volumes with two separated arrays of end points and total number of breaths. The end of the inspirations and expirationsare determined by the pressure signal $P1$.

4.2.2 Gas Exchange Ratio Q_r

The second part of this analysis programme calculates Q_r which is the consumption of the oxygen ($\Delta[O_2]$) versus the production of the carbon dioxide ($\Delta[CO_2]$). It is taken from one of the normal breaths before the subject starts breathing heliox. The concentration of the oxygen is plotted against the concentration of carbon dioxide (figure 4.4). The $[CO_2] - [O_2]$ curve is separated into two parts by entering a separating carbon dioxide value (`[CO2] fitting`), normally is between 1.5 and 2) and each part is fitted with a linear curve. The first part ($[CO_2]$=0.4:1.5) of the curve represents the system and anatomical dead space. The second part of the curve ($[CO_2]$=1.5:end) is where gas exchange occurs and the slope is the respiratory ratio Q_r. This part of the

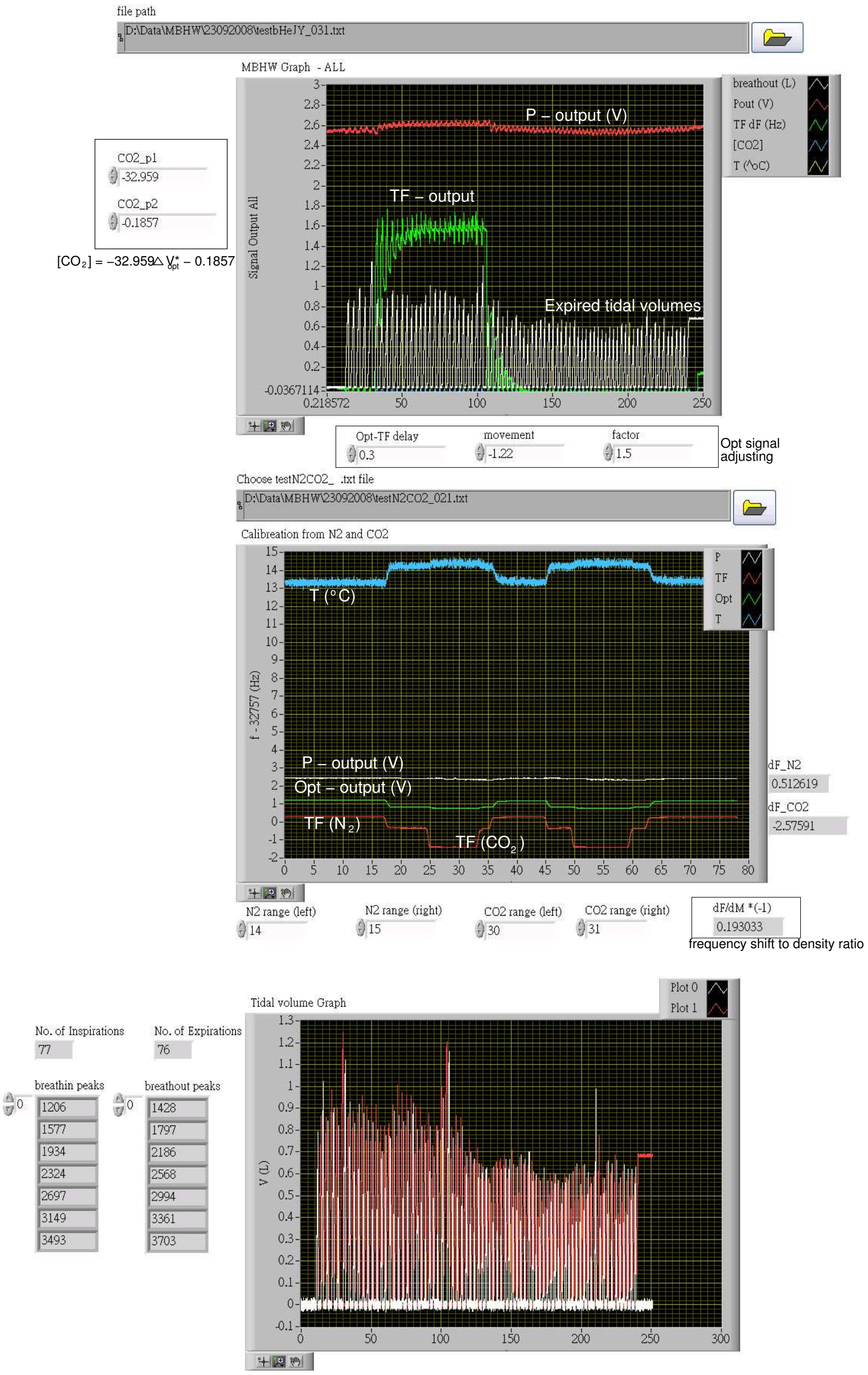

file path: D:\Data\MBHW\23092008\testbHeJY_031.txt

CO2_p1: -32.959

CO2_p2: -0.1857

$[CO_2] = -32.959 \triangle V^{*}_{opt} - 0.1857$

Opt-TF delay: 0.3

movement: -1.22

factor: 1.5

Opt signal adjusting

Choose testN2CO2_ .txt file: D:\Data\MBHW\23092008\testN2CO2_021.txt

dF_N2: 0.512619

dF_CO2: -2.57591

N2 range (left): 14

N2 range (right): 15

CO2 range (left): 30

CO2 range (right): 31

dF/dM *(-1): 0.193033

frequency shift to density ratio

No. of Inspirations: 77

No. of Expirations: 76

breathin peaks	breathout peaks
1206	1428
1577	1797
1934	2186
2324	2568
2697	2994
3149	3361
3493	3703

Figure 4.3: Analysis programme : breath separation part. The top panel displays the signals of pressure, temperature, resonance frequency shift from the tuning fork, optical output, and expired tidal volume. The middle panel shows the calibration data from the pure nitrogen and carbon dioxide to get the frequency shift to density ratio. The bottom panel displays the inspired and expired tidal volumes with two separated arrays of end points and total number of breaths.

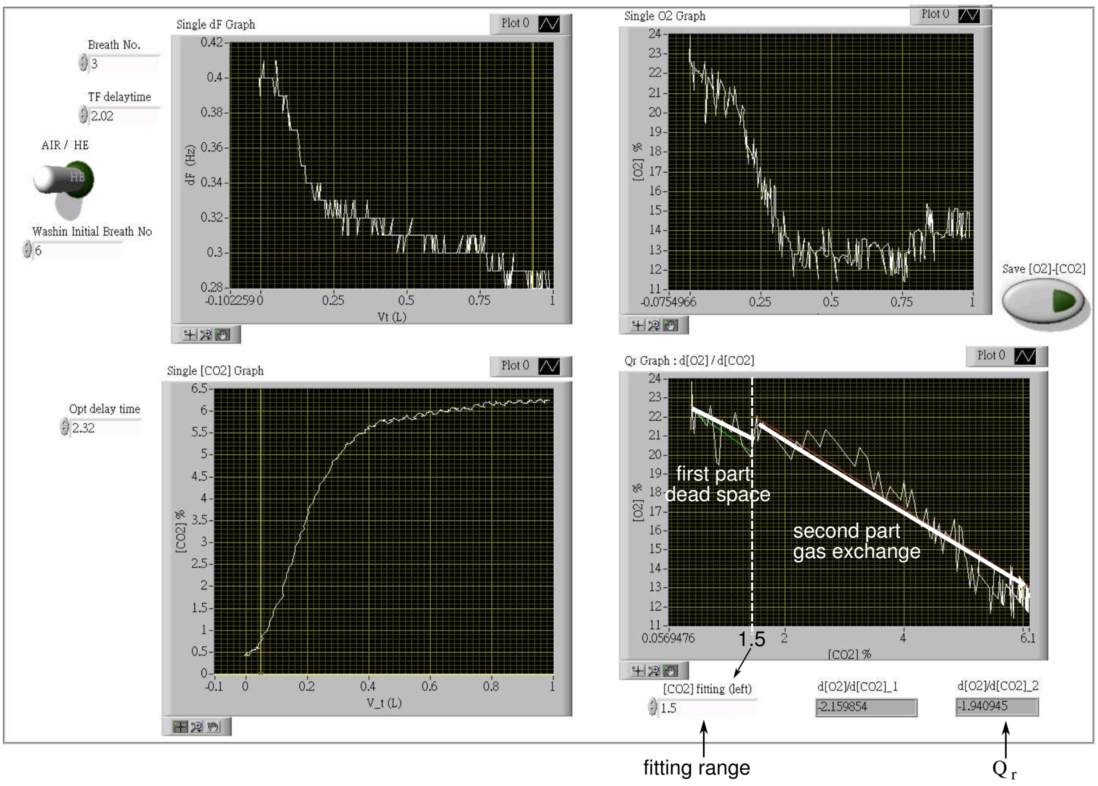
Breath No. 3

TF delaytime 2.02

AIR / HE

Washin Initial Breath No 6

Opt delay time 2.32

[CO2] fitting (left) 1.5

d[O2]/d[CO2]_1 -2.159854

d[O2]/d[CO2]_2 -1.940945

Figure 4.4: Analysis programme : respiratory ratio Q_r. Four panels display the resonance frequency shift, the carbon dioxide concentration, the calculated oxygen concentration, and the oxygen concentration plotted against carbon dioxide concentration from a normal expiration. TF delay time Opt delay time

programme is shown in figure 4.4.

4.2.3 Single Breaths Analysis

The main part of the analysis is to get the normalised phase II and phase III slopes, the mean concentrations of gases and the dead space from each single breath. The breath number can be selected by entering the breath number in the programme. The TF delay time and CO_2 delay time can also be entered. The `washin/washout` LED controller needs to be selected for determining wash-in or washout process which is for determining the initial concentration of oxygen at the start of each expiration. The oxygen concentration is slightly different from the heliox gas to the air. At first, the filled new heliox cylinder contained 79% of He and 21% of O_2. However, initially with a cylinder, there was actually a higher concnetration of helium gas coming out because of the high diffusivity so a lower concentration of oxygen. After using aroud a few hundred litres, there was less helium remaining in the cylinder. Therefore, the oxygen concentration in heliox is increasing gradually as it is used which can then be higher than 21%. Each single breath data (containing expired volume, He, CO_2, N_2, and O_2 concentrations) is saved.

Five panels display the resonance frequency shift (Hz), He, CO_2, N_2, and O_2 concentrations against the expired tidal volume from each single breath (figure 4.5). On the right hand side of each panel, there are six control icons for setting the range of phase II and phase III, and adjusting the phase III slope. `Phase II left` and `Phase II right` are the start and end volume values of phase II. `Phase III left` and `Phase III right` are the start and end volume values of phase III. Bottom two control icons `Phase III slope error` and `Phase III intercept` are for adjusting the value and offset of the phase III linear fitting curve. The mean concentrations are taken as the integral of gas concentration with expired volume. The dead space is simply taken as the middle point of phase II in this programme. The output data containing the normalised phase II and phase III slopes, the dead space, the mean concentration of each breath are saved.

4.3 Error Estimation

Since the biological data is very sensitive to the systematic errors, errors from the systems such as the digital noise or from the analysis are discussed in this section. In this work, two main systematic errors causing the variance in the washout results are estimated. One is the signal noise from the QTF and optical sensor, the other one is from the alignment of the flow signal and signals from QTF and optical sensor which will affect the expired mean concentration of gases.

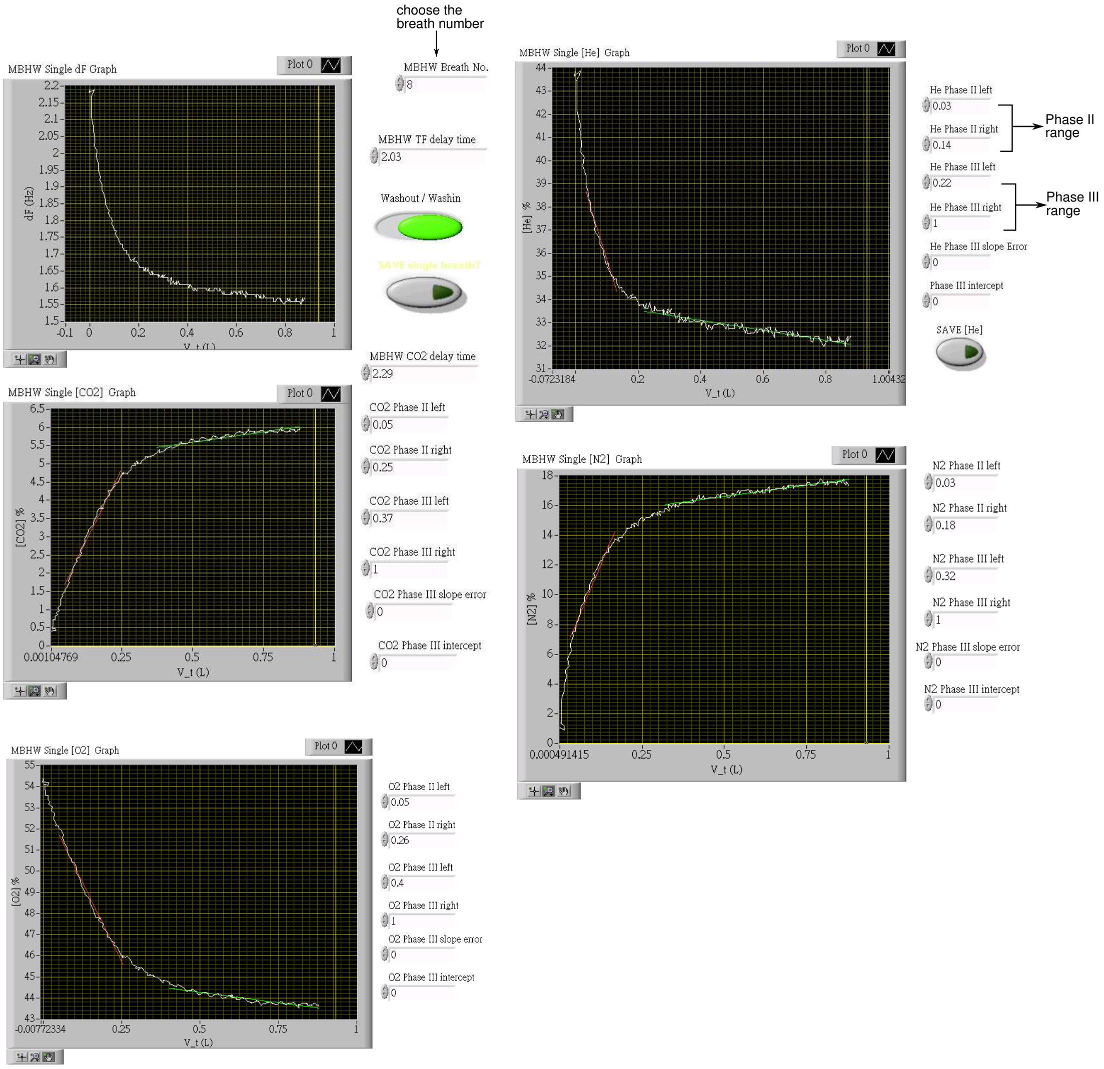

choose the breath number

MBHW Breath No.
8

MBHW TF delay time
2.03

MBHW CO2 delay time
2.29

CO2 Phase II left
0.05

CO2 Phase II right
0.25

CO2 Phase III left
0.37

CO2 Phase III right
1

CO2 Phase III slope error
0

CO2 Phase III intercept
0

O2 Phase II left
0.05

O2 Phase II right
0.26

O2 Phase III left
0.4

O2 Phase III right
1

O2 Phase III slope error
0

O2 Phase III intercept
0

He Phase II left
0.03

He Phase II right
0.14

Phase II range

He Phase III left
0.22

He Phase III right
1

Phase III range

He Phase III slope Error
0

Phase III intercept
0

N2 Phase II left
0.03

N2 Phase II right
0.18

N2 Phase III left
0.32

N2 Phase III right
1

N2 Phase III slope error
0

N2 Phase III intercept
0

Figure 4.5: Analysis programme : single breath analysis. Five panels display the resonance frequency shift, the carbon dioxide concentration, the calculated helium, nitrogen, and oxygen concentrations. TF delay time and Opt delay time are adjusted manually breath by breath. The alignment error will is discussed in the next section.

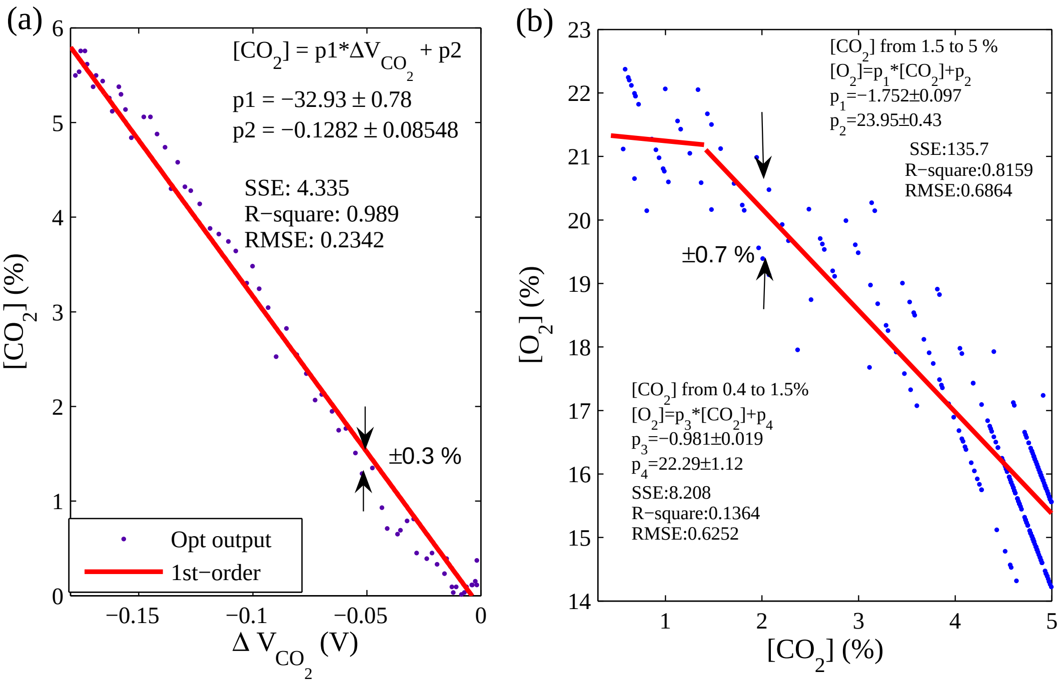

Figure 4.6: Systematic error caused by the sensor signal noise from two main calibrations. (a) is the concentration of carbon dioxide calibrated with the QTF with 0.3% [CO_2] error. (b) is the oxygen concentration calibrated with both QTF and optical sensors with 0.7% [O_2] error.

4.3.1 Signal Noise

In this work, QTF has been used to calibrate the relationship between the optical signal and CO_2 concentration. The highest digital noise from two sensors results in 0.3% [CO_2] of error as shown in figure 4.6(a). The oxygen concentration is given by calibrating the normal breath signal with optical sensor and QTF. The highest signal noise from two sensors results in 0.7% [O_2] error as shown in figure 4.6(b). As described in section 3.5.1, the relationship between the frequency shifts of QTF and gas densities can be given by

$$\frac{\Delta f_g - \Delta f_{N_2}}{\Delta f_{CO_2} - \Delta f_{N_2}} \cong \left(\frac{\rho_g - \rho_{N_2}}{\rho_{CO_2} - \rho_{N_2}} \right), \tag{4.1}$$

where Δf_g is the frequency shift in different gases (Δf_g in gas mixture, Δf_{N_2} in pure nitrogen, Δf_{CO_2} in pure carbon dioxide), and ρ are gas densities (ρ_g is the gas mixture density, ρ_{N_2} is the nitrogen gas density, ρ_{CO_2} is the carbon dioxide gas density). The density of gas mixture ρ_g can be given by

$$\begin{aligned}
\rho_g &\cong \rho_{N_2} + (\rho_{CO_2} - \rho_{N_2}) \cdot \frac{\Delta f_g - \Delta f_{N_2}}{\Delta f_{CO_2} - \Delta f_{N_2}} && (4.2) \\
&\cong \rho_{N_2} + \frac{\Delta f_g - \Delta f_{N_2}}{\zeta}, && (4.3) \\
\rho_g &= \rho_{He}[He] + \rho_{N_2}[N_2] + \rho_{O_2}[O_2] + \rho_{CO_2}[CO_2] + \rho_{H_2O}[H_2O], && (4.4)
\end{aligned}$$

where ρ_{He} is the helium gas density, ρ_{H_2O} is the water vapour density, and

$$\zeta = \frac{\Delta f_{CO_2} - \Delta f_{N_2}}{\rho_{CO_2} - \rho_{N_2}} \qquad (4.5)$$

is given by measuring the frequency shifts in pure nitrogen (Δf_{N_2}) and pure carbon dioxide (Δf_{CO_2}) as described in section 3.10.1 with the QTF digital noise 0.01 Hz. Considering the 0.3% [CO$_2$] error from the [CO$_2$] calibration (figure 4.6(a)) and the 0.7% [O$_2$] error from the [O$_2$]-[CO$_2$] calibration (figure 4.6(b)), the gas concentrations can be related to the gas densities as

$$\rho_{He}[He]+\rho_{N_2}[N_2]+\rho_{O_2}([O_2]\pm0.7)+\rho_{CO_2}([CO_2]\pm0.3)+\rho_{H_2O}[H_2O]-\rho_{N_2} = \frac{\Delta f_g - \Delta f_{N_2}}{\zeta} \qquad (4.6)$$

$$[He] + [N_2] + [O_2] + [CO_2] + [H_2O] = 100\%. \qquad (4.7)$$

The helium gas concentration can thus be given by solving the above equations with the assumption of saturated water vapour concentration [H$_2$O]=0.61,

$$[N_2] = 100 - [He] - [O_2] - [CO_2] - [H_2O] \qquad (4.8)$$

$$\begin{aligned}
[He] &= \frac{(\rho_{O_2} - \rho_{N_2})([O_2] \pm 0.7) + (\rho_{CO_2} - \rho_{N_2})([CO_2] \pm 0.3) + (\rho_{H_2O} - \rho_{N_2})[H_2O]}{\rho_{N_2} - \rho_{He}} \\
&\quad \cdot \left(\frac{\Delta f_g - \Delta f_{N_2}}{\zeta}\right). && (4.9)
\end{aligned}$$

The signal noise from two calibrations thus results in ±0.29% of error in helium concentration and ±1.29% in nitrogen concentration.

4.3.2 Alignment Error

As described in section 3.10.4, the optical signal and QTF signal have almost identical response to the expirations. The delay time between two signals can be determined from the washout data and is fixed during the the wash-in or washout measurement (normally 0.3 sec for washout, 0.25 sec for wash-in) since two sensors are joined in series. However, the time delay between the flow rate signal and QTF (or optical) signal varies breath by breath because of gas diffusion since helium gas has high diffusion coefficient compared to the air. In this work, the alignment of the flow rate and QTF (or optical) signal has been adjusted manually breath by breath. The end of expiration of the QTF signal has been determined as the value reaches the maximum (or minimum) value in each breath. Considering the gas re-breathing from the system dead space 10.405 mL, there is at most ±5.20 mL in the flow rate and QTF alignment which corresponds to less than 0.05 sec time delay error. The mean concentration of helium [He] from each breath can be given by

$$[He] = \frac{\int_{V_T}^{0} [He] dV_T \pm 0.00502 * [He]_{max}}{V_T \pm 0.00502} \tag{4.10}$$

with the corresponding error ±0.00502*$[\mathrm{He}]_{max}/\mathrm{V}_T$, where V_T is the expired tidal volume and $[\mathrm{He}]_{max}$ is the maximum helium concentration of the breath. The error varies breath by breath but the highest value can be estimated from the first breath since its $[\mathrm{He}]_{max}$ value is higher than the rest of the breaths. A typical $[\mathrm{He}]_{max}$ from the first breath is around 55% with the typical tidal volume 1 L, the corresponding error caused by the alighment can thus be calculated as ±0.29% of helium concentraion which decreases exponentially breath by breath.

The highest error caused by the signal noise and the alignment thus results in ±0.58% of helium concentration and ±1.58% of nitrogen concentration.

Chapter 5

MBHW Results

The MBHW results from six normal volunteers (two females, four males), two smokers (one female, one male), and two mild asthmatics (one female, one male) of similar age are described in this chapter. In the first section, the analysis of MBHW is simply described. In the following two sections, the comparison of the results from two asthmatic and two healthy subjects are discussed. In section 5.4, the Fowler dead space is briefly described. In section 5.6, MBHW results from 12 volunteers (seven normal volunteers, three asthmatics, and two smokers) are summarised. MBHW results from a 2.2 litre lung model and the comparison to the results from a real lung are described in section 5.7. Exponential or linear fitting curves have been applied to some of the data. All the fittings have been done by the MatLab curve fitting tool box (v7.0.4) and the goodness of those fittings are represented by SSE (the sum of squares due to error), R-square (the coefficient of multiple determination which represents how successful the fit is, a value closer to 1 indicates a better fit), and RMSE (the root mean square error, a value closer to 0 indicates a better fit)[1].

---

[1] More details about the meaning of those three values can be referred to the user guide of MatLab (v7.0.4).

5.1 A Brief Summary of Analysis

In this section, a brief summary of analysis of the MBHW data is discussed. There has not been any well-defined theories for gas transport in human lungs because of the structural complexity. In this work, all the MBHW curves can be separated into the helium wash-in (nitrogen washout) and helium wash-out (nitrogen wash-in) process. The results will be discussed in three parts derived from both wash-in and washout results. The first part is the lung clearance curves fitted to a sum of two exponential curves based on the two-compartment model [5, 22]. The second part focuses on phase III and the two indices S_{cond} and S_{acin}. The third part focuses on phase II and the Fowler dead space.

5.1.1 Lung Clearance

FRC Calculation

The washout lung clearance curve is taken by plotting the mean concentration of gases (helium or nitrogen) as a function of turnover TO. The mean concentration of gases (c_n from nth breath) have been taken as the expired amount of gas ($\int_0^{V_T} c_n dV$) divided by the expired tidal volume (V_T) from each breath. The turnover TO is the accumulative expired tidal volume ($\sum V_T$) divided by the functional residual capacity (FRC). In the helium or nitrogen washouts, FRC has been simply derived from

$$
\begin{aligned}
c_1 &= \frac{FRC \cdot c_0}{FRC + V_{T,1}}, && (5.1)\\
c_2 &= \frac{FRC \cdot c_1}{FRC + V_{T,2}}, && (5.2)\\
&\vdots && (5.3)\\
c_n &= \frac{FRC \cdot c_{n-1}}{FRC + V_{T,n}}, && (5.4)\\
FRC &= \frac{\sum_{i=1}^{n} c_i \cdot V_{T,i}}{c_0 - c_n}, && (5.5)
\end{aligned}
$$

where $c_{n=0,1,2,\cdots n-1}$ and $V_{T,n(n=0,1,2,\cdots n-1)}$ are the mean concentration of gas and tidal volumes from the initial gas in the lungs, the first, second, and $(n-1)th$ expiration, respectively. This equation is based on the assumption of well-mixed gases in the lungs. Since the FRC has been defined as the lung volume at the end of expiration, it is dependent on the expired tidal volumes and is slightly different breath by breath. In this work, the gas concentrations below 0.1% have been ignored and only gas concentrations above 0.1% have been taken into acount for the FRC calculation. According to the MBHW results from those volunteers, the calculated FRCs from nitrogen washout processes are higher than from the helium washout process since the FRC formula is based on the assumption of well-mixed gas in the lungs but in fact, helium gas mixes faster than nitrogen.

Lung Clearance and Two-Compartment Model

On the basis of the two-compartment model, human lungs can be regarded as two parallel compartments with different ventilations as mentioned in section 2.3.1 [5, 22]. In this section, the washout results from the helium washout process will be discussed. The mean concentration of helium from each breath is plotted as a dual-exponential function (the summation of two exponential functions) of turnover (cumulative expired tidal volumes divided by FRC). It can be expressed as

$$\begin{aligned}
FRC &= FRC_1 + FRC_2, && (5.6)\\
TO_n &= \frac{\sum_1^n V_T}{FRC}, && (5.7)\\
V_T &= V_1 + V_2, && (5.8)\\
c(1+2,n) &= \frac{FRC_1}{FRC_1 + FRC_2} c_{1,n} + \frac{FRC_2}{FRC_1 + FRC_2} c_{2,n}, && (5.9)\\
c_{1,n} &= c_{a0}\left(\frac{FRC_1}{FRC_1 + V_1}\right)^{TO}, && (5.10)\\
c_{2,n} &= c_{a0}\left(\frac{FRC_2}{FRC_2 + V_2}\right)^{TO}, && (5.11)
\end{aligned}$$

where FRC_1 and FRC_2 are the residual capacities of two compartments 1 and 2, $c_{1,n}$ and $c_{2,n}$ are the mean helium concentration from the nth breath, V_1 and V_2 are the expired tidal volumes of two compartments. If compartment 1 represents the better-ventilated compartment compared to the compartment 2, then 1 has a higher washout rate, e.g., $\frac{FRC_1}{FRC_1+V_1} > \frac{FRC_1}{FRC_1+V_1}$. The ratio of $\frac{FRC_1}{FRC}$ represents the proportion of the better-ventilated part of the lung.

In this work, breaths from the first expiration to the end ($> 0.1\%$) of helium gas concentration during helium washout have been taken into account for this two-exponential curve fittings. The intial gas concentraion c_{a0} is thus the mean gas concentration from the first breath. If the initial gas concentration was taken as the gas concentration in the lungs before the washout measurement, the lung clearance washout curve was unable to be fitted well with a sum of two exponential curves. This is likely to result from the imperfect gas mixing such that the mean concentration of the expired gas is smaller than the mean concentration of gas from the whole lungs. FRC_1, FRC_2 are given by Eq. 5.9 and V_1, V_2 are given by Eq. 5.10 and 5.11. The calculated sum of V_1 and V_2 appears to be slightly bigger than the tidal volume V_T which is likely to result from the assumptions of well-mixied gas in the lungs, ignoring the dead space and ignoring gas exchange.

Error Estimation for Lung-Clearance Results

As mentioned in section 4.3, the highest systematic error caused by the signal noise or the analysis alignment results in a variance of 0.58% of helium concentration from a typical case. The error caused by the analysis alignment varies breath by breath since it depends on the highest concentration of each breath. Figure 5.1 shows the lung clearance results from one mild asthmatic and normal subject with the estimated error for each breath. The systematic error is relatively small which has little effect on the curve-fitting of two exponential curves. The error results in the variance of nitrogen concentration is about 2.7 times of helium concentration which can not be ignored in lung-clearance results. Therefore, only the helium washout will be discussed in lung-clearance results.

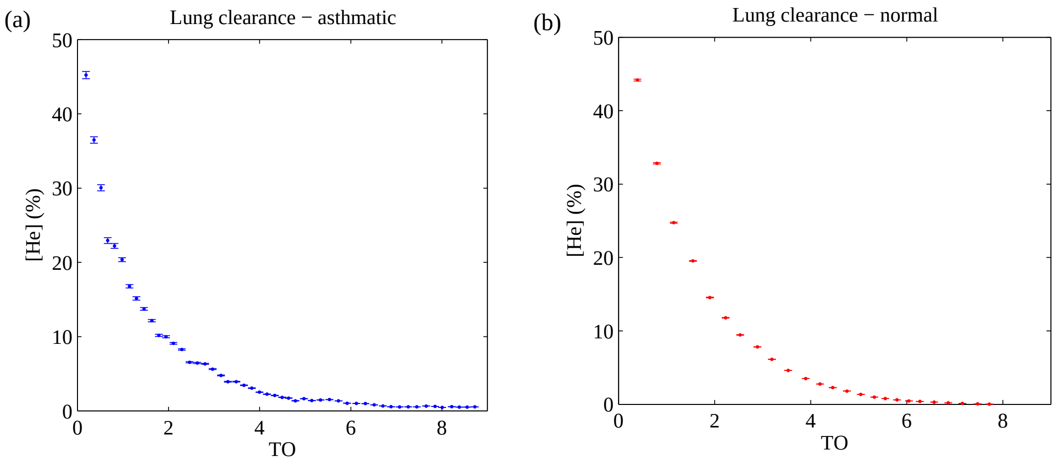

Figure 5.1: (a) Lung clearance result from a mild asthmatic male with estimated systematic errors. (b) Lung clearance result from a normal subject with estimated systematic errors.

5.1.2 Phase III

Phase III from each single breath is fitted by a linear curve with a slightly positive slope. The normalised phase III (S_{NIII}) slope is the slope of the alveolar plateau divided by the mean concentration of gas for each expiration. The range of phase III has been chosen manually and is different breath by breath since phase III appears to be a plateau in a single breath washout curve without any well-defined range [42]. S_{cond} values are given by the increasing rate of S_{NIII} against TO curve from TO=2 to TO=6. The S_{acin} values have been given by the S_{NIII} value from the first breath after subtracting the first TO value multiplied by S_{cond}, *i.e.*, $S_{acin} = S_{NIII}(1) - TO(1) \cdot S_{cond}$. The higher the S_{cond} values, the higher the ventilation inhomogeneity in the conducting airways. The higher the absolute value of S_{acin} value, the higher the ventilation inhomogeneity in the acinar airways. In this work, S_{NIII}-TO washout curves have been plotted from not only washout but also wash-in data. Since there is no well-defined fitting range, the fitting range from $TO = 2$ to 6 has been chosen for consistent comparison from person to person. Also, from our MBHW results, the increasing rate of S_{NIII} generally becomes smaller when $TO \geq 2$ compared to a sharp change from $TO = 0$ to $TO = 2$. In some

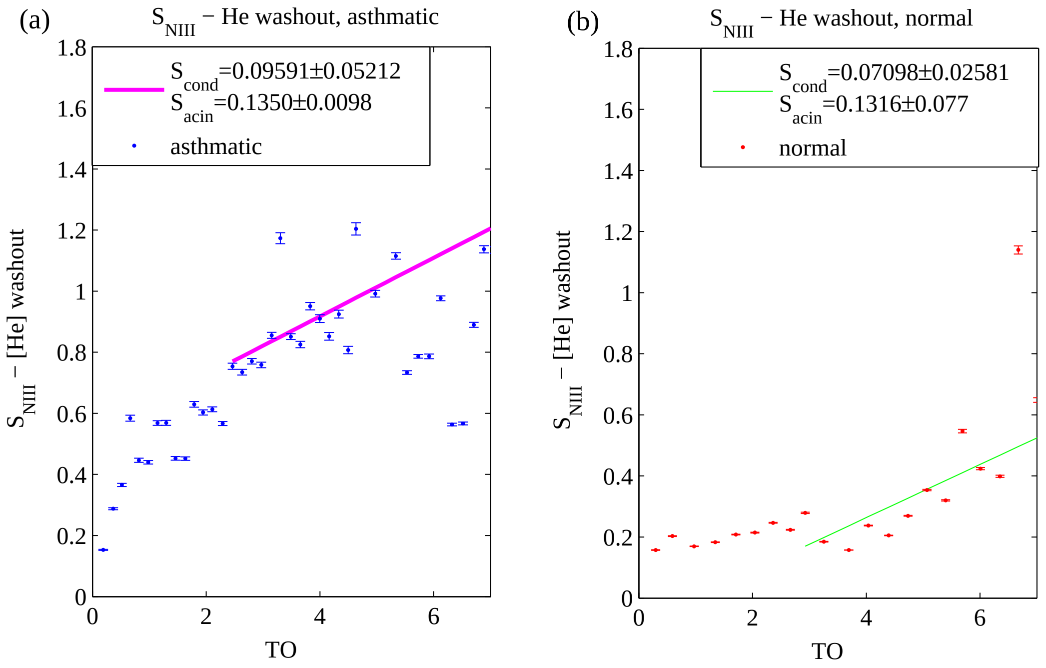

Figure 5.2: (a) Helium washout result from a mild asthmatic with estimated error of normalised phase III slopes. (b) Helium washout result from a normal subject with estimated error of normalised phase III slopes. The systematic error is relatively small compared to the fitting error which results in high variance of S_{cond} and S_{acin} values.

nitrogen washout studies, $TO = 1.5$ to $TO = 6$ has been chosen instead [20, 49, 80].

Error Estimation for Phase III

The normalised phase III slope S_{NIII} is given by the phase III slope divided by the mean concentration of helium gas from each breath. The systematic error will result in the variance of normalised phase III slopes which can be given by

$$\begin{aligned}\Delta S_{NIII} &= \frac{S_{NIII} * ([He] \pm 0.00502 * [He]_{max})}{[He] \pm 0.00502 * [He]_{max}} - S_{NIII} \\ &\cong S_{NIII} \cdot \frac{\pm 0.00502 * [He]_{max}}{[He]}. \end{aligned} \tag{5.12}$$

Figure 5.2 shows the helium washout results from a mild asthmatic and normal subject with the estimated error of normalised phase III slopes. The systematic error is relatively small compared to the fitting errors which results in high variance of S_{cond} and S_{acin} values.

5.1.3 Phase II

Normalised Phase II Slope

The normalised phase II slopes (S_{NII}) slopes have been given by a linear fit to the transition phase which exhibits a sharp increase of gas concentration from a single breath curve. The range of phase II has been chosen manually and is different breath by breath which also depends on the diffusion coefficients of gas mixture since there is no well-defined range [22, 58] for phase II, either.

Fowler Dead Space

As introduced in section 2.2, the Fowler dead space is given from Bohr's equation [4, 22] for anatomic dead space in the respiration system: V_{DB},

$$\frac{V_{DB}}{V_T} = \frac{c_E - c_A}{c_I - c_A} \tag{5.13}$$

where V_T is the tidal volume, c_E, c_I are the mean concentration of expired and inspired gas, and c_A is the mean gas concentration in the alveoli. The Fowler dead space has been defined at the point near the middle point of phase II where two shadowed area are equal as shown in figure 2.4. The Fowler dead space does not seem to be related to lung disease judging from our limited study of MBHW results but depends on the lung capacities and the gas densities. It is briefly described in section 5.4 from six volunteers. The systematic error will cause 5.20 mL variance maximum in Fowler dead space considering the gas re-breathing from the system dead space.

5.2 Asthmatics

Asthma is an obstructive lung disease caused by bronchial tube narrowing. The narrowed bronchial structure results in uneven ventilations from different lung units and

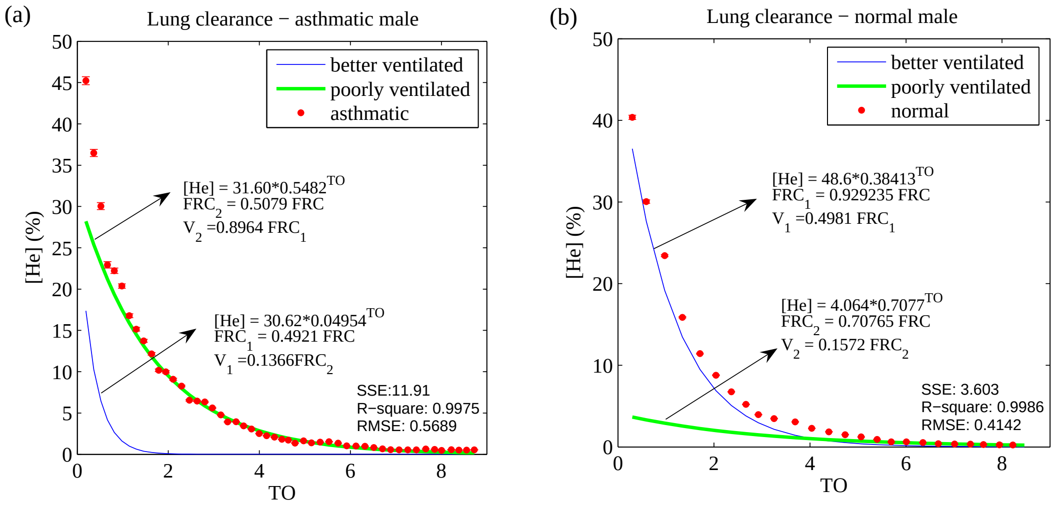

Figure 5.3: (a) Lung clearance result from a mild asthmatic male and two exponential curves (solid lines). The lung is occupied by 49 % of a better-ventilated compartment (FRC_1, thin curve) and 51 % of poorly-ventilated part (FRC_2, thick curve). (b) Lung clearance result from a normal healthy male and two exponential curves. The lung is occupied by 93 % of a better-ventilated compartment (FRC_1, thin curve) and 7 % of poorly-ventilated part (FRC_2, thick curve).

a steeper phase III slope. From the single breath curves, both asthmatic subjects have a steeper phase III compared to normal. From the lung clearance washout curves, both asthmatic results show a larger proportion of poorly-ventilated regions within the lungs. MBHW results from a asthmatic male (29 yrs, 60.2 kg, 165.5 cm, peak flow 450 L/min)) and an asthmatic female (24 yrs, 54.0 kg, 150.0 cm, peak flow 475 L/min) compared to a normal male (25 yrs, 173.0 cm, 100.3 kg, peak flow 575 L/min) and a normal female (26 yrs, 50.0 kg, 166.5 cm, peak flow 420 L/min).

5.2.1 Lung Clearance

Lung Clearance Results from an Asthmatic and Healthy Male

Figure 5.3 shows the lung clearance results from a mild asthmatic male and a normal healthy male of similar age. The mean concentration of helium from each breath is

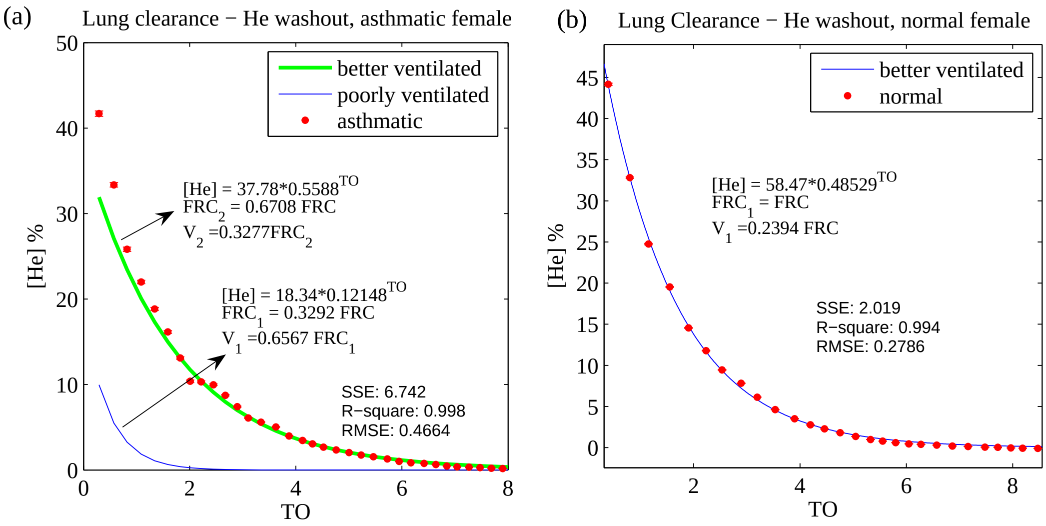

Figure 5.4: (a) Lung clearance result from a mild asthmatic female and two exponential curves. The lung is occupied by 67% of a better-ventilated compartment (FRC_1, thin curve) and 33 % of poorly-ventilated part (FRC_2, thick curve). (b) Lung clearance result from a normal healthy male and two exponential curves. The lung is occupied by only one compartment (FRC_1, thin curve).

plotted against the turnover and fitted to a summation of two exponential curves. The better-ventilated curve decays faster than the poorly-ventilated one. For the asthmatic male (figure 5.3(a)), the poorly-ventilated part ($FRC_2 = 51\% FRC$) occupies nearly half of the whole lungs. The better-ventilated part occupies other half ($FRC_1 = 49\% FRC$) and the helium gas is washed out very quickly in the first two turovers. For the normal healthy male (figure 5.3(b)),the better-ventilated part dominates the whole lung ($FRC_1 = 93\% FRC$). The poorly-ventilated part ($FRC_2 = 7\% FRC$) occupies less than ten percent of the lung. Figure 5.4 shows the lung clearance results from a mild asthmatic female and a normal female at the similar age. For the asthmatic female (figure 5.4(a)), the poorly-ventilated part ($FRC_2 = 33\% FRC$) occupies one third of the whole lungs. The better-ventilated part occupies other two thirds ($FRC_1 = 67\% FRC$) and the helium gas is washed out very quickly in the first two turovers. For the normal healthy female (figure 5.4(b)), the whole lung is like a perfect

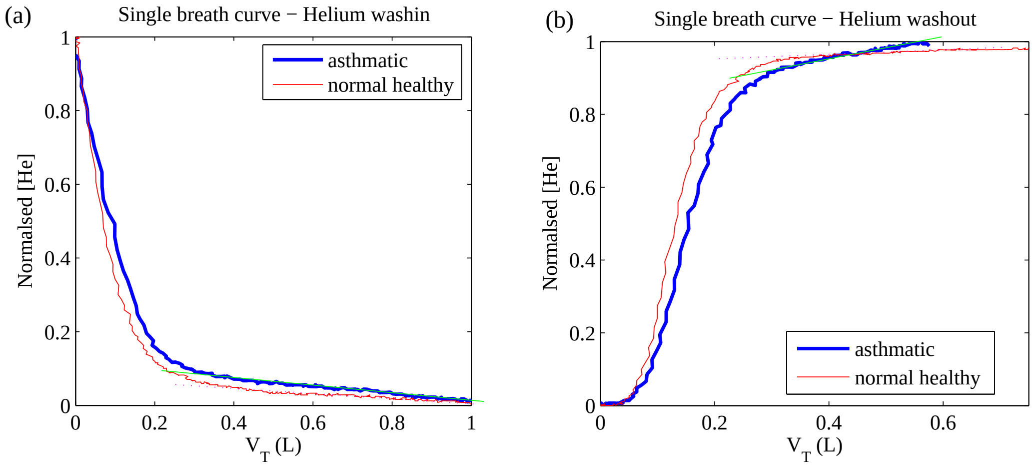

Figure 5.5: (a) A single helium wash-in curve from a mild asthmatic and a normal healthy subject. (b) A single helium washout curve from a mild asthmatic and a normal healthy subject.

compartment. The helium gas is washed out steadily and the clearance data falls on only one exponential curve.

The results from both asthmatics show a bigger proportion of the poorly-ventilated part compared to normal subjects.

5.2.2 Phase III Slopes and Two Indices S_{cond}, S_{acin}

The narrowing bronchial tube for asthmatics normally results in a steeper phase III as shown in figure 5.5.

Washin

Figure 5.6 shows the normalised phase III slopes of helium (a) and nitrogen (b) during helium wash-in and washout process, respectively. The results from the mild asthmatic male shows higher S_{cond} values (0.00739±0.00191, 0.01468±0.00018) than the normal healthy one (0.0020864±0.0017, 0.0032408±0.00068) from both wash-in curves. The higher S_{cond} values from the mild asthmatics reflect the higher inhomogeneity in the conducting airways compared to the normal ones.

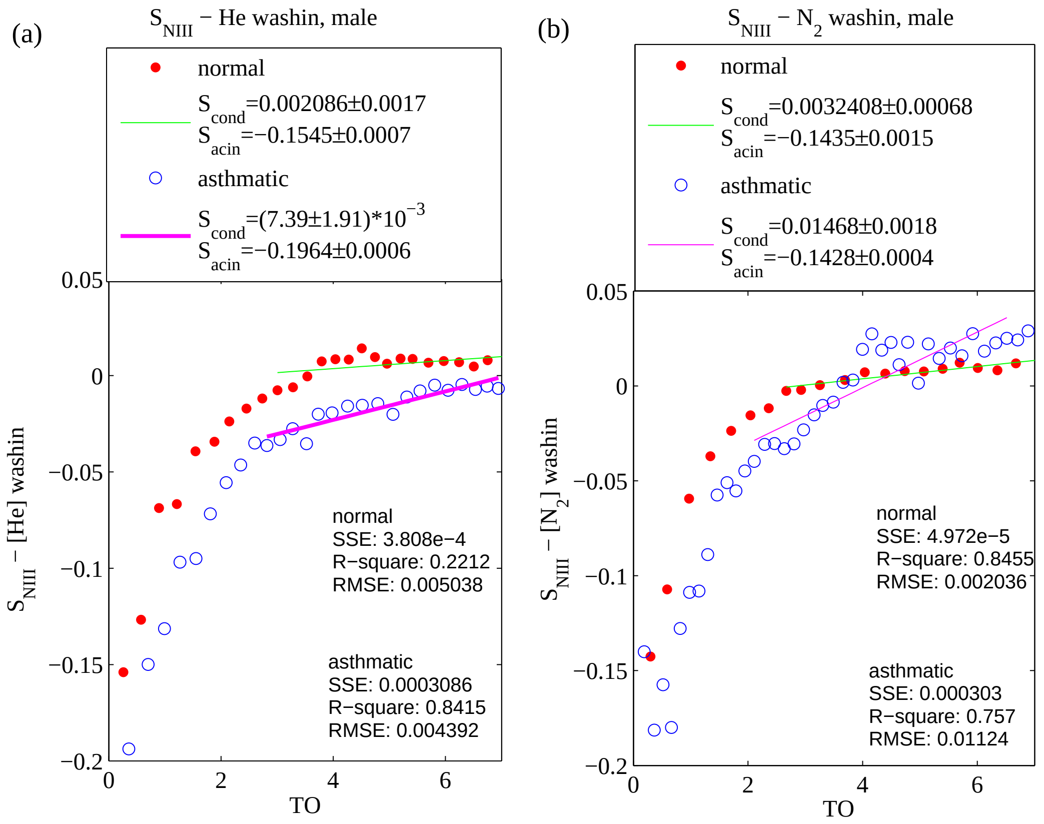

Figure 5.6: (a) The normalised phase III slopes of helium during helium wash-in process from a mild asthmatic male and a normal male. (b) The normalised phase III slopes of nitrogen during helium washout process from a mild asthmatic male and a normal male.

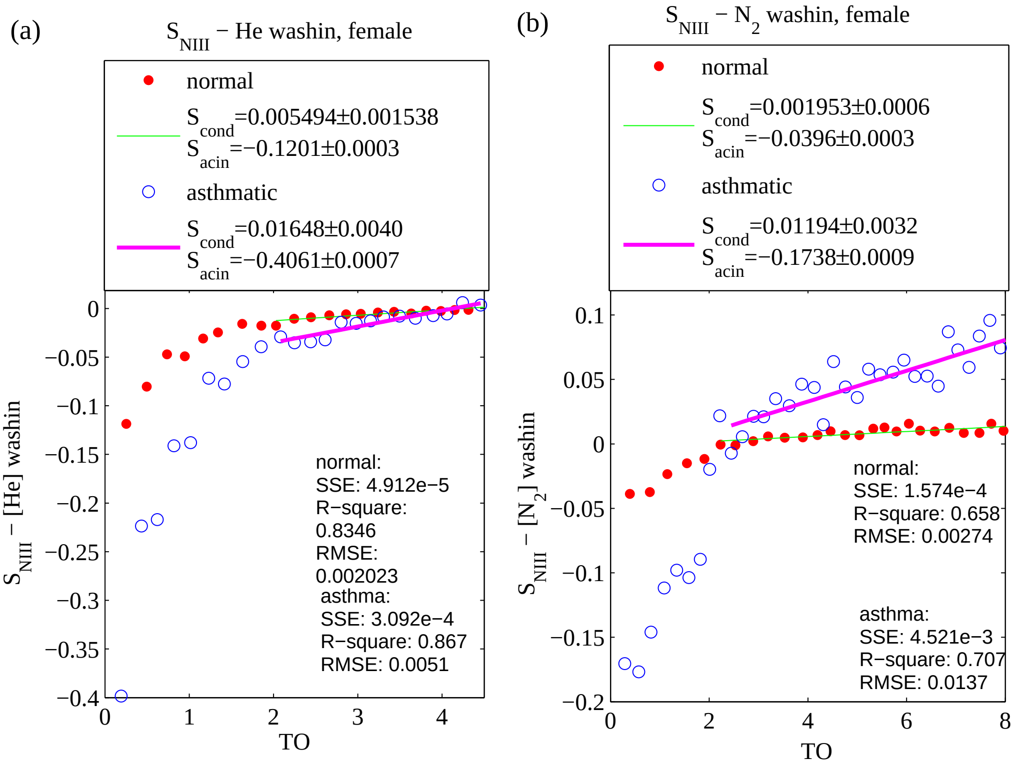

Figure 5.7: (a) The normalised phase III slopes of helium during helium wash-in process from a mild asthmatic female and a normal female. (b) The normalised phase III slopes of nitrogen during nitrogen wash-in process from a mild asthmatic female and a normal female.

The S_{acin} values of the helium wash-in shows asthmatic person has steeper S_{NIII} (S_{acin}=-0.1964±0.0006) than the normal one (S_{acin}=-0.15453±0.0007) with the subtraction of S_{cond} from the first breath. The S_{acin} values of nitrogen wash-in shows both asthmatic and normal person have similar S_{NIII}. The results show that the ventilation in the acinar airways of the mild asthmatics is slightly inhomogeneous than of the normal healthy person and the degree of inhomogeneity can only be revealed in the helium wash-in process.

Figure 5.7 shows the normalised phase III slopes of helium (a) and nitrogen (b) from two females during helium and nitrogen wash-in processes, respectively. The results from the mild asthmatic female shows higher S_{cond} values (0.01648±0.0040, 0.01194±0.0032) compared to the normal healthy one (0.005495±0.001538, 0.001953±0.0006) from both wash-in curves. It shows the ventilation in the conducting airways of the mild asthmatics is more inhomogeneous than of the normal healthy person.

The S_{acin} values from both helium wash-in and nitrogen wash-in show that asthmatic person has steeper S_{NIII} (S_{acin}=-0.4016±0.0006, -0.1738±0.0009) than the normal one (S_{acin}=-0.1201±0.0003, -0.0396±0.0003) with the subtraction of S_{cond} from the first breaths. The higher abolute values of S_{acin} reflect that the ventilation in the acinar airways of the mild asthmatic female is more inhomogeneous than that of the normal healthy person. It implies the asthmatic female may not only have obstructive disease in conducting airways (asthma) but also in the acinar airways (other restrictive diseases such as COPD).

From the wash-in results, both mild asthmatic subjects have higher S_{cond} values than both normal ones. Generally, the normalised phase III slopes are steeper from the nitrogen wash-in (or helium washout) data compared to the helium wash-in data but there is less difference in S_{cond} values from both two groups (asthmatic and normal).

Washout

Figure 5.8 shows the normalised phase III slopes of helium (a) and nitrogen (b) during the helium and nitrogen washout processes, respectively. The results from the mild asthmatic male shows slightly higher S_{cond} values (0.09591±0.05211, 0.09374±0.06434) than the normal healthy one (0.07098±0.0278, 0.03678±0.04993) from both wash-in curves. However, the error of the fitting curve results in a high variance of S_{cond} values which are unable to reflect the ventilation inhomogeneity compared to the wash-in results. The S_{acin} values shows that the asthmatic subject has a similar S_{NIII} (S_{acin}=-0.1350±0.0098, 0.0942±0.0206) compared to the normal one (S_{acin}=0.1316±0.0107, 0.1300±0.0165) with the subtraction of S_{cond} from the first breath.

Figure 5.9 shows the normalised phase III slopes of helium (a) and nitrogen (b) from two females during the helium and nitrogen washout processes, respectively. The high

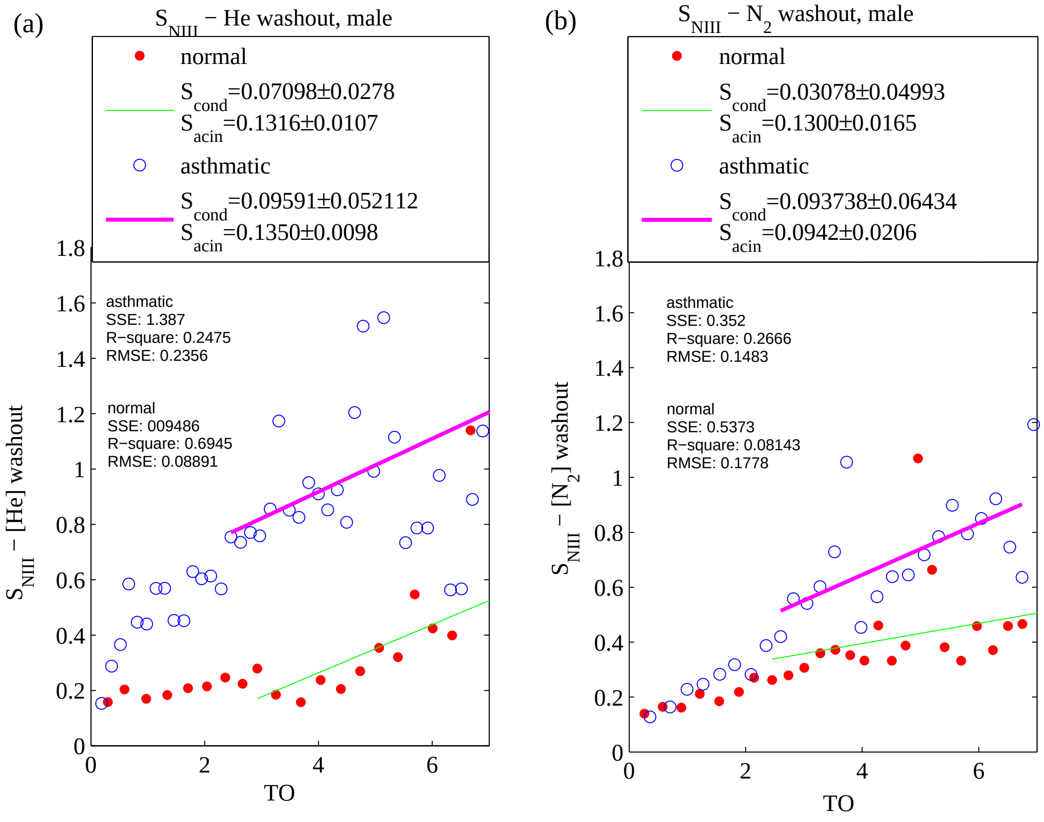

Figure 5.8: (a) The normalised phase III slopes of helium during helium washout process from a mild asthmatic male and a normal male. (b) The normalised phase III slopes of nitrogen during nitrogen washout process from a mild asthmatic male and a normal male.

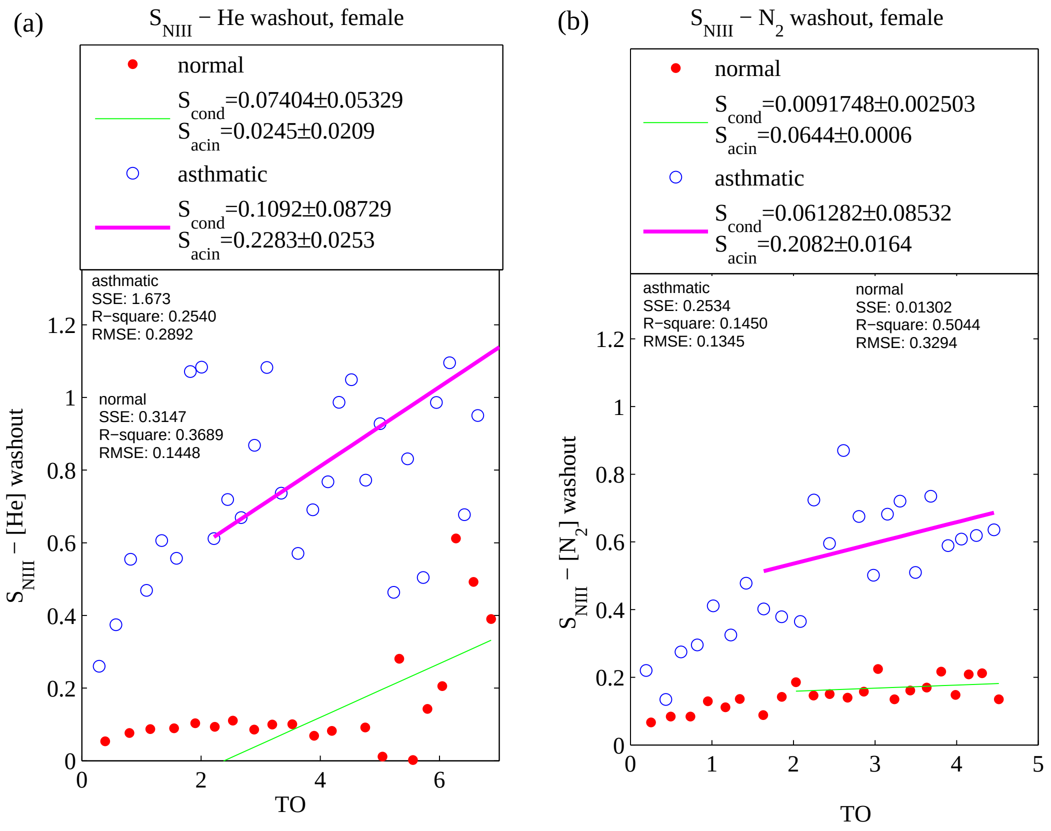

Figure 5.9: (a) The normalised phase III slopes of helium during helium washout process from a mild asthmatic and a normal female. (b) The normalised phase III slopes of nitrogen during nitrogen washout process from a mild asthmatic and a normal female.

variance of S_{cond} and S_{acin} values from both subjects causes the difficulty on reflecting the ventilation inhomogeneity.

Generally, the normalised phase III slopes are steeper from two asthmatics from both wash-in and washout results. However, the high variance of S_{cond} and C_{acin} values from washout results causes the difficulty on reflecting the ventilation inhomogeneity compared to the wash-in results.

5.2.3 Phase II

Figure 5.10 shows the normalised phase II slopes of helium ((a) and (c)) and nitrogen ((b) and (d)) during helium wash-in and nitrogen wash-in processes from males (asthmatic and normal) and females (asthmatic and normal). For both males and females, the results from the asthmatics are almost identical to the normal ones.

Figure 5.11 shows the normalised phase II slopes of helium ((a) and (c)) and nitrogen ((b) and (d)) during the helium washout and nitrogen washout processes from males (asthmatic and normal) and females (asthmatic and normal). For males, the result from the asthmatic subject shows slightly steeper phase II than the normal healthy subject. For females, two normalised phase II curves are identical for both asthmatic and normal subjects. The normalised phase II slopes are decreasing breath by breath during the washout process. The decreasing rate of S_{NII} is identical for both asthmatic and normal males as well as females.

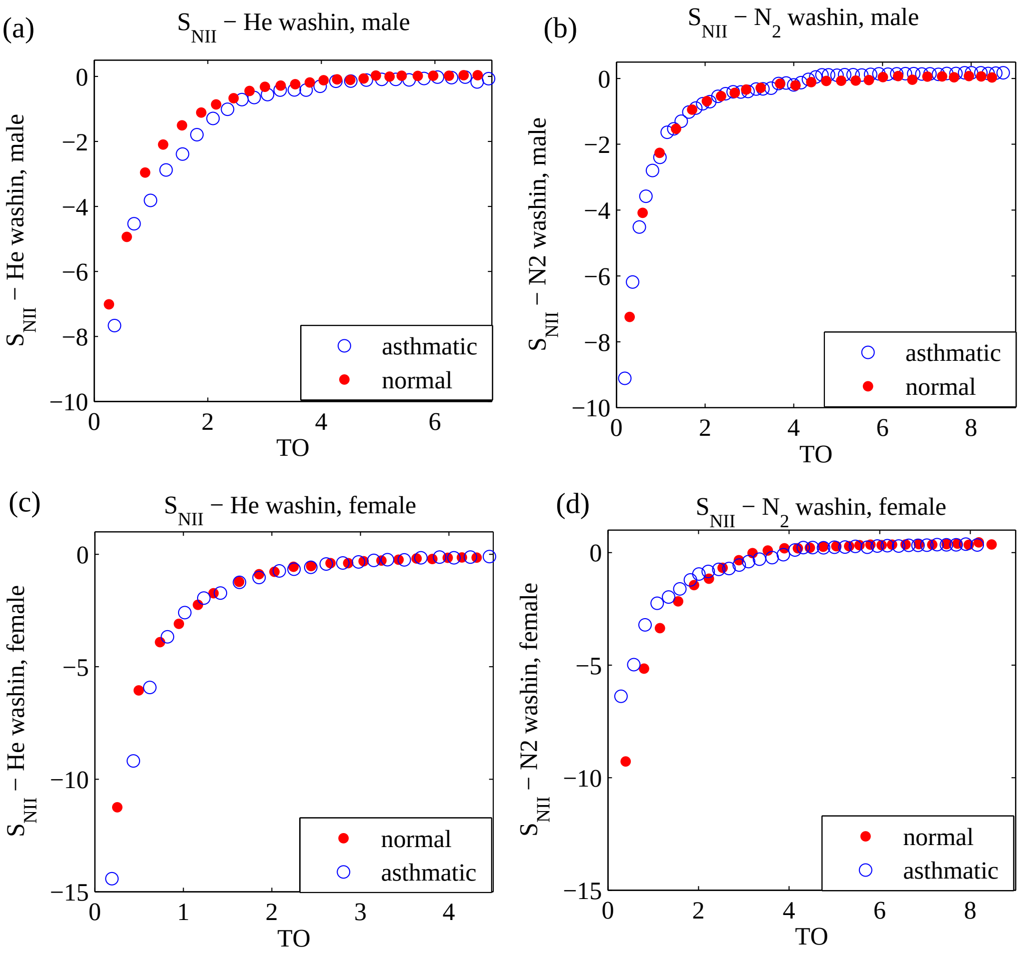

Figure 5.10: (a) The normalised phase II slopes of helium during the helium wash-in process from a mild asthmatic and a normal male. (b) The normalised phase II slopes of helium during nitrogen wash-in process from a mild asthmatic and a normal male. (c) The normalised phase II slopes of nitrogen during helium wash-in process from a mild asthmatic and a normal female. (d) The normalised phase II slopes of nitrogen during nitrogen wash-in process from a mild asthmatic and a normal female.

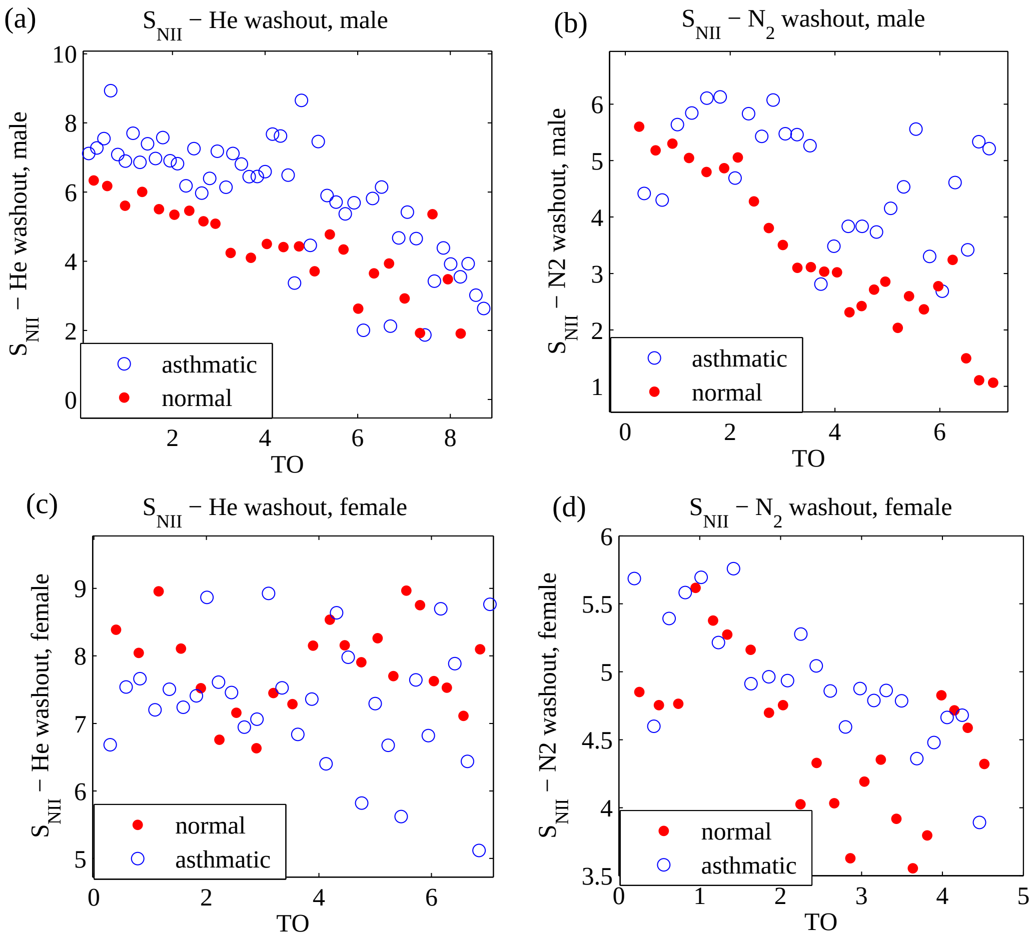

Figure 5.11: (a) The normalised phase II slopes of helium during the helium wash-out process from a mild asthmatic and a normal male. (b) The normalised phase II slopes of helium during nitrogen washout process from a mild asthmatic and a normal male. (c) The normalised phase II slopes of nitrogen during helium washout process from a mild asthmatic and a normal female. (d) The normalised phase II slopes of nitrogen during nitrogen washout process from a mild asthmatic and a normal female.

5.2.4 Carbon Dioxide

During the washout measurement, the concentration of carbon dioxide is almost identical for each single expiration. Figure 5.12 simply displays the normalised phase III slopes of carbon dioxide from both helium wash-in and washout process. Figure 5.12(a) and (b) show the results from two male, one asthmatic and one normal. The bottom two figures (c) and (d) show the results from an asthmatic and a normal female. Two asthmatic subjects have higher normalised phase III slopes than the healthy subjects from both wash-in and washout processes but this difference is more apparent in the helium washout process.

Figure 5.13 shows the normalised phase II slopes of carbon dioxide from both the helium wash-in and washout processes. The above two (figure 5.13(a) and (b)) shows the results from two male, one asthmatic and one normal healthy. The bottom two (figure 5.13(c) and (d)) shows the results from an asthmatic and a normal healthy female. The results show that the normalised phase II slopes of carbon dioxide are identical for the asthmatic and normal males as well as females. It is unable to distinguish the ventilation inhomogeneity from subjects at the same age from the phase II results.

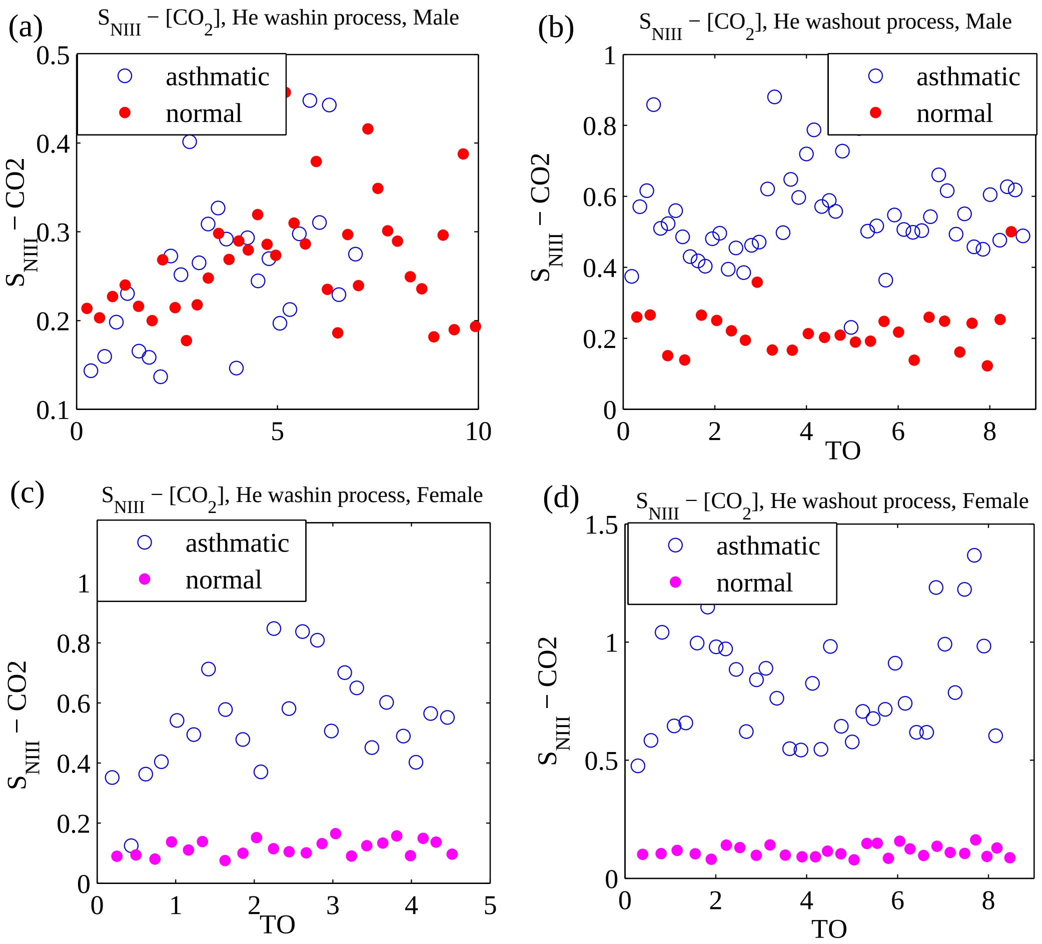

Figure 5.12: (a) The normalised phase III slopes of carbon dioxide during the helium wash-in process from a mild asthmatic and a normal male. (b) The normalised phase III slopes of carbon dioxide during the nitrogen wash-in process from a mild asthmatic and a normal male. (c) The normalised phase III slopes of carbon dioxide during the helium wash-in process from a mild asthmatic and a normal female. (d) The normalised phase III slopes of carbon dioxide during the nitrogen wash-in process from a mild asthmatic and a normal female.

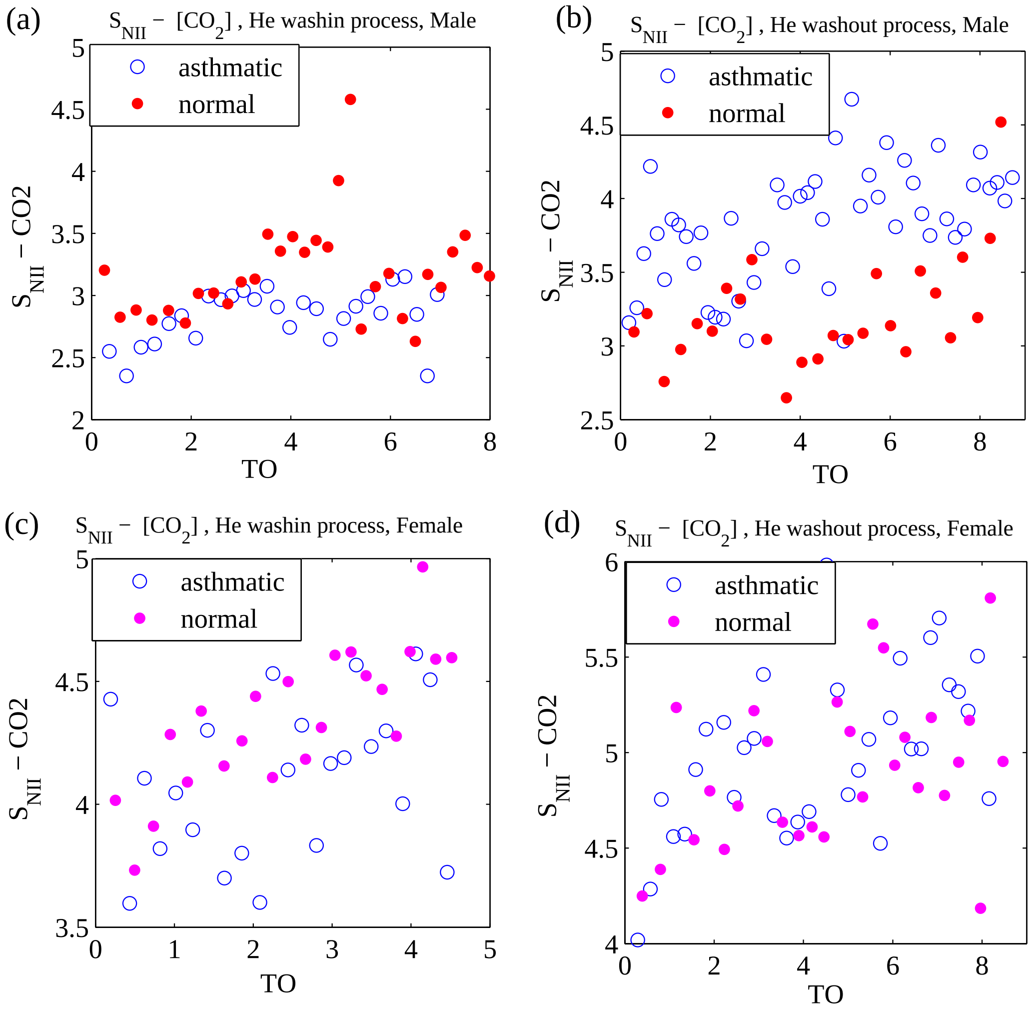

Figure 5.13: (a) The normalised phase II slopes of carbon dioxide during the helium wash-in process from a mild asthmatic and a normal male. (b) The normalised phase II slopes of carbon dioxide during the nitrogen wash-in process from a mild asthmatic and a normal male. (c) The normalised phase II slopes of carbon dioxide during the helium wash-in process from a mild asthmatic and a normal female. (d) The normalised phase II slopes of carbon dioxide during the nitrogen wash-in process from a mild asthmatic and a normal female.

5.3 Smokers

Smoking has well-known negative effects on human health especially leading to lung and heart disease such as emphysema, COPD, stroke, and lung cancer. Helium washout measurements have been performed on a male (5 years smoking history for 0.5 pack/week) and a female (10 years smoking history for 0.75 pack/week, quit for 1.5 years) smoker. Both volunteer smokers have not been diagnosed with any lung disease. Their results are compared to a normal healthy male and a normal healthy female. The MBHW results from both smokers show that they have longer phase II on each single breath curve or there is a feature between phase II and phase III. Also, S_{NIII} of nitrogen from both smokers decreases breath by breath in the helium wash-in process compared to the increasing slopes of the results from normal and asthmatic subjects. However, the number of volunteers in this study is very small.

5.3.1 Lung Clearance

The lung clearance result from the male smoker is shown in figure 5.14 compared to a normal subject. The smoker's lung is occupied by 98.85% of the better-ventilated part which is even higher than the normal subject. While the result from the female smoker as shown in figure 5.15, the smoking lung is occupied by 15.99% of poorly-ventilated portion which is slightly higher than the normal subject. For the male smoker, the lung clearance washout result is no difference from the normal one. For the female smoker with 10-year smoking history, the lung clearance result shows the percentage of the portion occupied by the poorly-ventilated compartment is slightly higher than normal subjects.

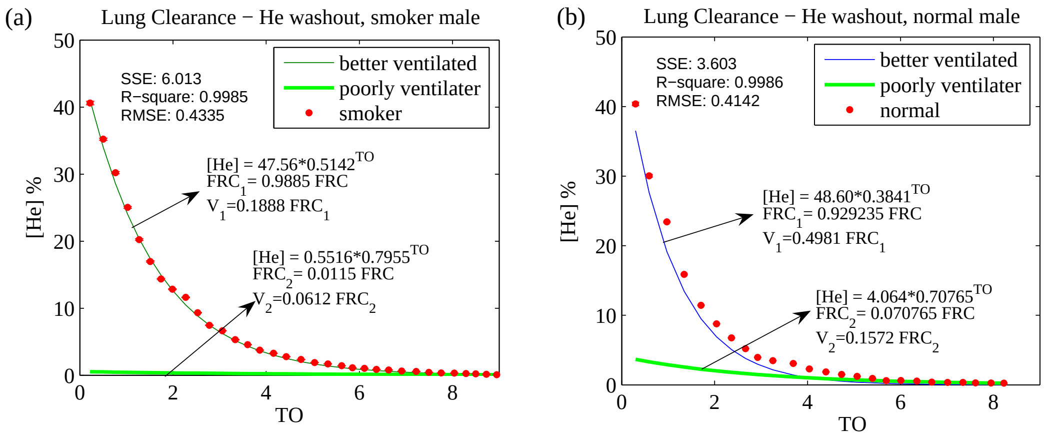

Figure 5.14: (a) Lung clearance result from a male smoker and two exponential curves. The lung is occupied by 98.85 % of a better-ventilated compartment (FRC_1, thin curve) and 1.15 % of poorly-ventilated part (FRC_2, thick curve). (b) Lung clearance result from a normal healthy male and two exponential curves. The lung is occupied by 92.92 % of a better-ventilated compartment (FRC_1, thin curve) and 7.08 % of poorly-ventilated part (FRC_2, thick curve).

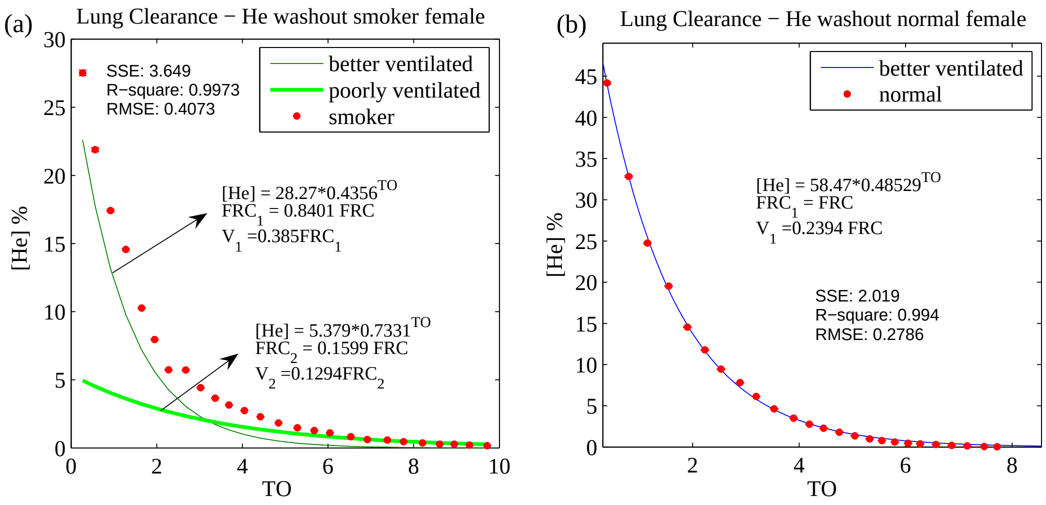

Figure 5.15: (a) Lung clearance result from a female smoker and two exponential curves. The lung is occupied by 84.01% of a better-ventilated compartment (FRC_1, thin curve) and 15.99 % of poorly-ventilated part (FRC_2, thick curve). (b) Lung clearance result from a normal healthy male and two exponential curves. The lung is occupied by only one compartment (FRC_1, thin curve).

5.3.2 Phase II

As mentioned previously, the single breath curves from both smokers reveal a longer phase II or a transition phase between phase II and phase III as shown in figure 5.16 and 5.17. If this transition phase is regarded as a later part of phase II, it shows that the gas concentration goes up more slowly for the smokers and results in a shorter phase III, the alveolar plateau. Also, the existence of this transition feature results in a difficulty in determining the boundary between phase II and phase III. The whole single breath curve looks more 'round' from the results of both smokers compared to the curve from the normal subjects. It reveals more small lung units with different ventilation existing along the smokers' airways. The transition feature may result from the tar coating on the wall of airways which roughens the surface of airways. If we regard the transition phase as a single independent phase not inclusive in phase II or phase III, the resulting alveolar plateaus from the smokers are even flatter while the phase II are still as sharp as the results from the normal subjects.

The two graphs in figure 5.16 shows there is a transition phase between phase II and phase III in a single breath curve from the smokers. This transition phase occupies about 0.15 L volume from the helium wash-in and helium washout results. Figure 5.17 shows the single breath curves of nitrogen carbon dioxide washout. This transition phase is observed in the helium or nitrogen washout but it is not apparent in carbon dioxide single breath curve.

Figure 5.18 shows the normalised phase II slopes of helium and nitrogen in the helium and nitrogen wash-in process. The transition phase between phase II and phase III has not been taken into account in the phase II slopes. The results from the smokers are identical to the normal healthy subjects. Figure 5.19 shows the normalised phase II slopes of helium and nitrogen in helium and nitrogen washout process. Ignoring the long transition phase, the results from the male smoker look identical to the normal healthy one while the results from the female smoker show that normalised phase II slopes decrease more quickly compared to the results from the normal female.

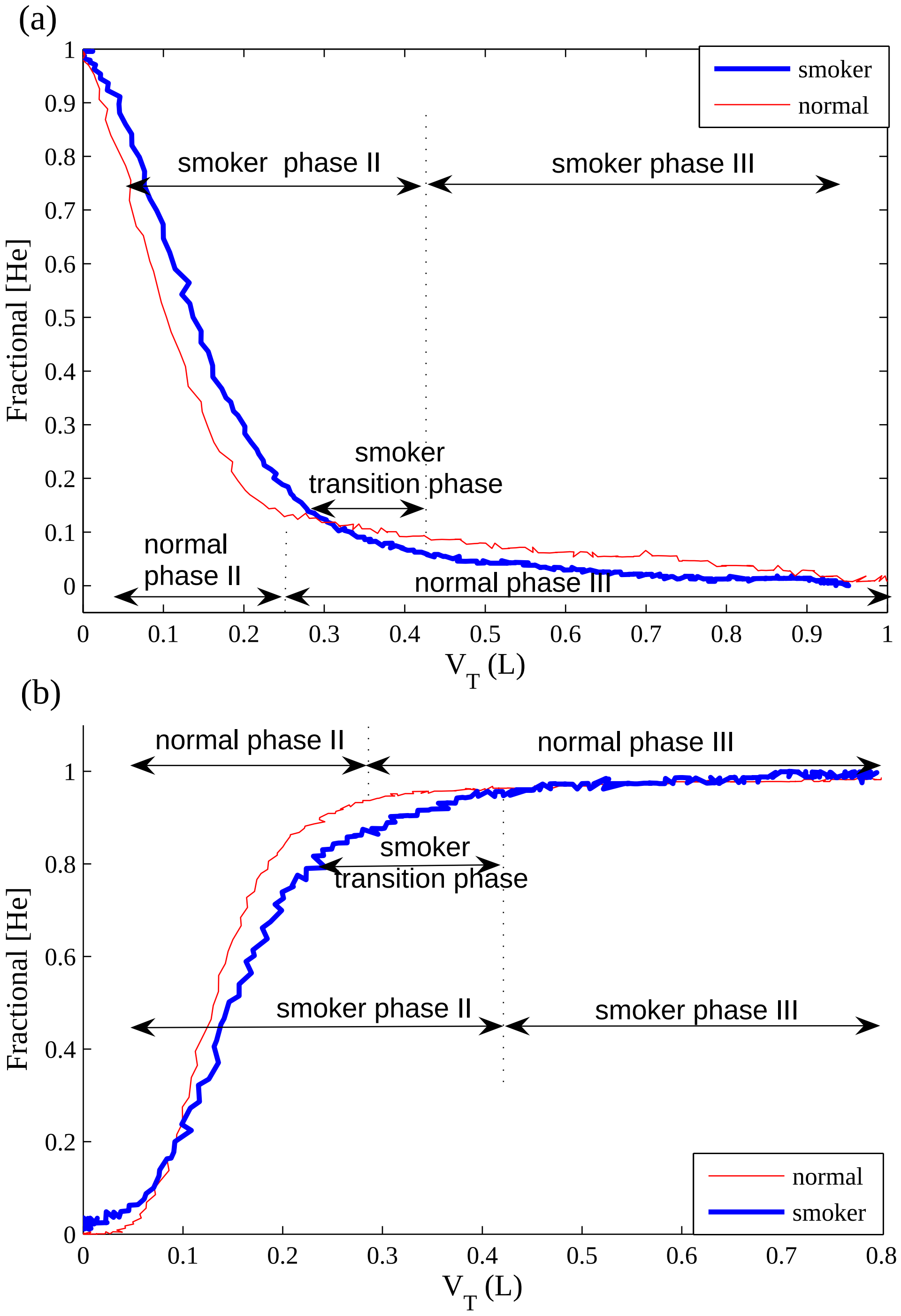

Figure 5.16: (a) A single helium wash-in curve from a male smoker and a normal healthy subject.(b) A single helium washout curve from a male smoker and a normal healthy subject. The phase II from both of the smoking results is longer than from the normal one. There is an transition phase between phase II and phase III.

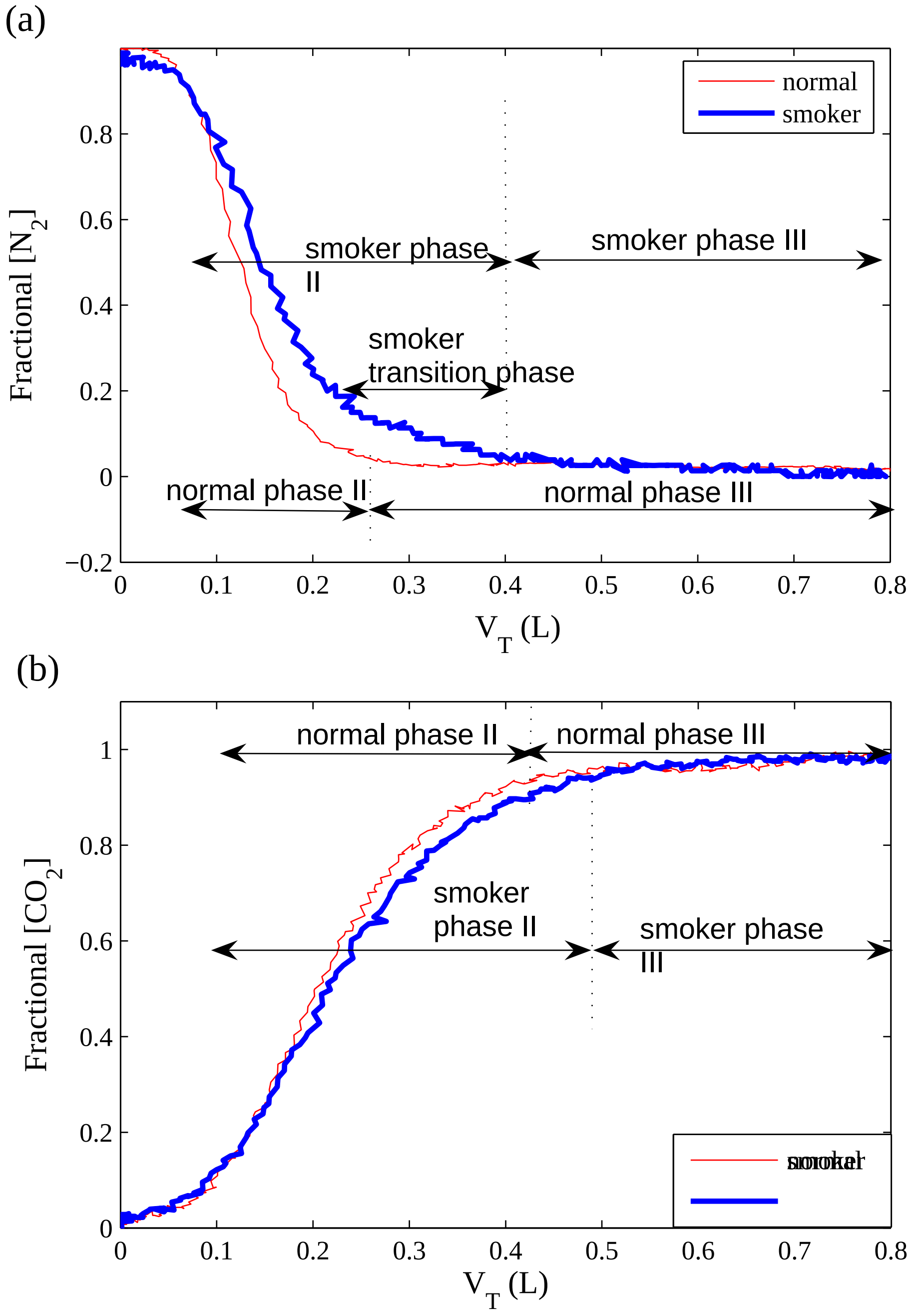

Figure 5.17: (a) A single nitrogen wash-in curve from a male smoker and a normal healthy subject. (b) A single carbon dioxide breath curve from a male smoker and a normal healthy subject.

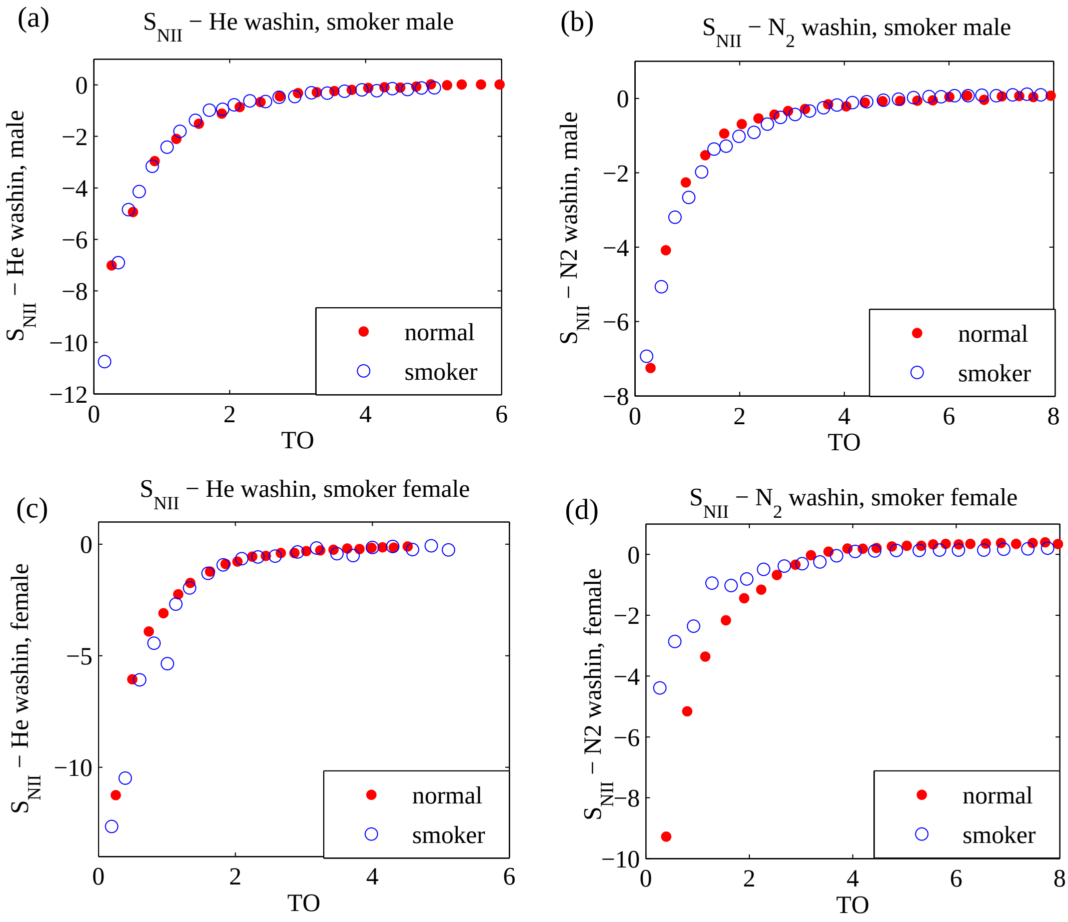

Figure 5.18: (a) The normalised phase II slopes of helium during the helium wash-in process from a male smoker and normal male. (b) The normalised phase II slopes of helium during the nitrogen wash-in process from a male smoker and a normal male. (c) The normalised phase II slopes of nitrogen during the helium wash-in process from a female smoker and a normal female. (d) The normalised phase II slopes of nitrogen during the nitrogen wash-in process from a female smoker and a normal female.

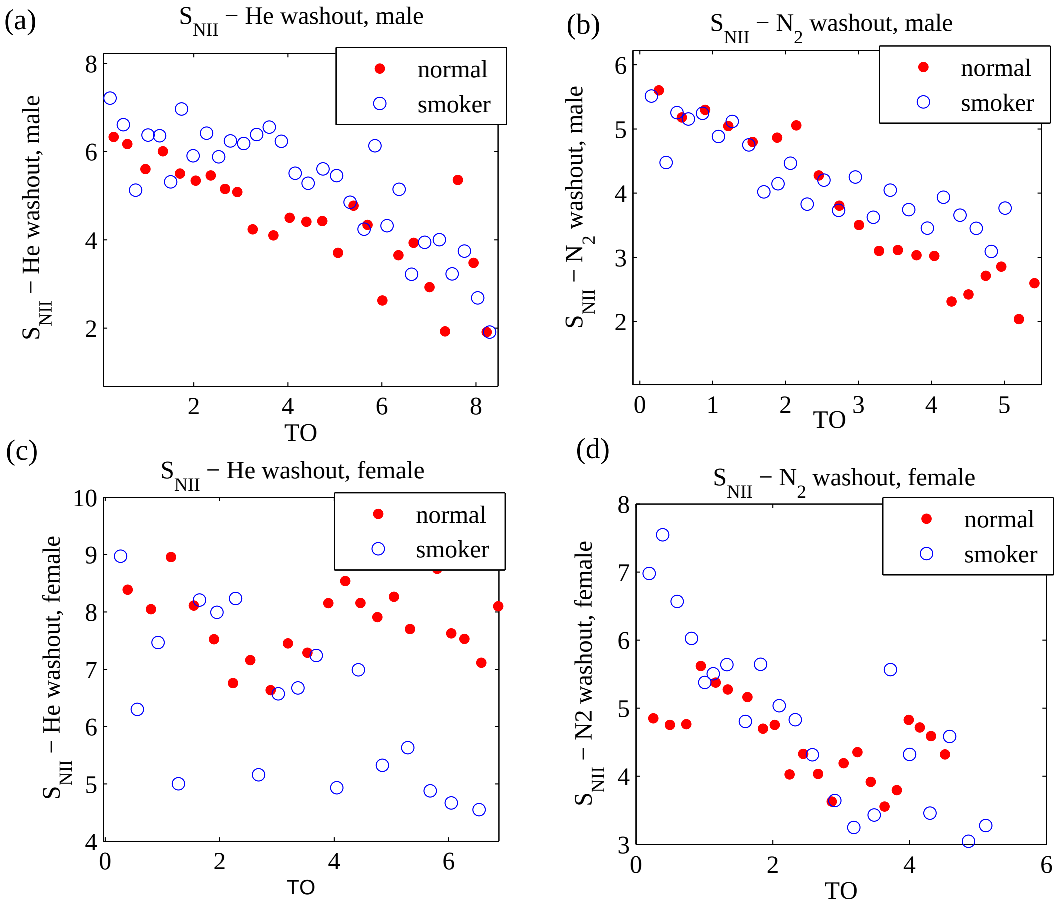

Figure 5.19: (a) The normalised phase II slopes of helium during the helium washout process from a male smoker and a normal male. (b) The normalised phase II slopes of helium during the nitrogen washout process from a male smoker and a normal male. (c) The normalised phase II slopes of nitrogen during the helium washout process from a female smoker and a normal female. (d) The normalised phase II slopes of nitrogen during the nitrogen washout process from a female smoker and a normal female.

5.3.3 Phase III

Wash-in

Figure 5.20 shows the normalised phase III slopes of helium and nitrogen from a smoker and a normal male subject during helium and nitrogen wash-in processes. Figure 5.21 shows the results from a female smoker and a normal female subject. The results from both smokers are similar to the results from normal subjects. The S_{cond} values from both groups are similar while the absolute values of S_{acin} are higher from the smokers than from the normal ones. It indicates that the acinar ventilation is more inhomogeneous in the smokers' lungs compared to the normal lungs.

Washout

Figure 5.22 shows the normalised phase III slopes of helium and nitrogen from a male smoker and a normal male subject during helium and nitrogen washout processes. Figure 5.23 shows the results from a female smoker and a normal female subject. In the nitrogen washout results, both smokers have negative S_{cond} values compared to the normal positive values. However, the high variance of S_{NIII} values results in the big error of S_{cond} and S_{acin} values which is unable to distinguish the results of smokers from the normal ones.

The negative decreasing rates of normalised phase III slopes have rarely been studied or observed previously since washout studies on 'healthy' smoking subjects are rare. The cause of this negative or small S_{cond} may be due to the shorter but flatter phase III in the single breaths from smokers. If the later half part of the long transition phase is considered as an early part of phase III, the phase III will not be a plateau but an exponentially increasing curve and the phase III slopes will be much higher.

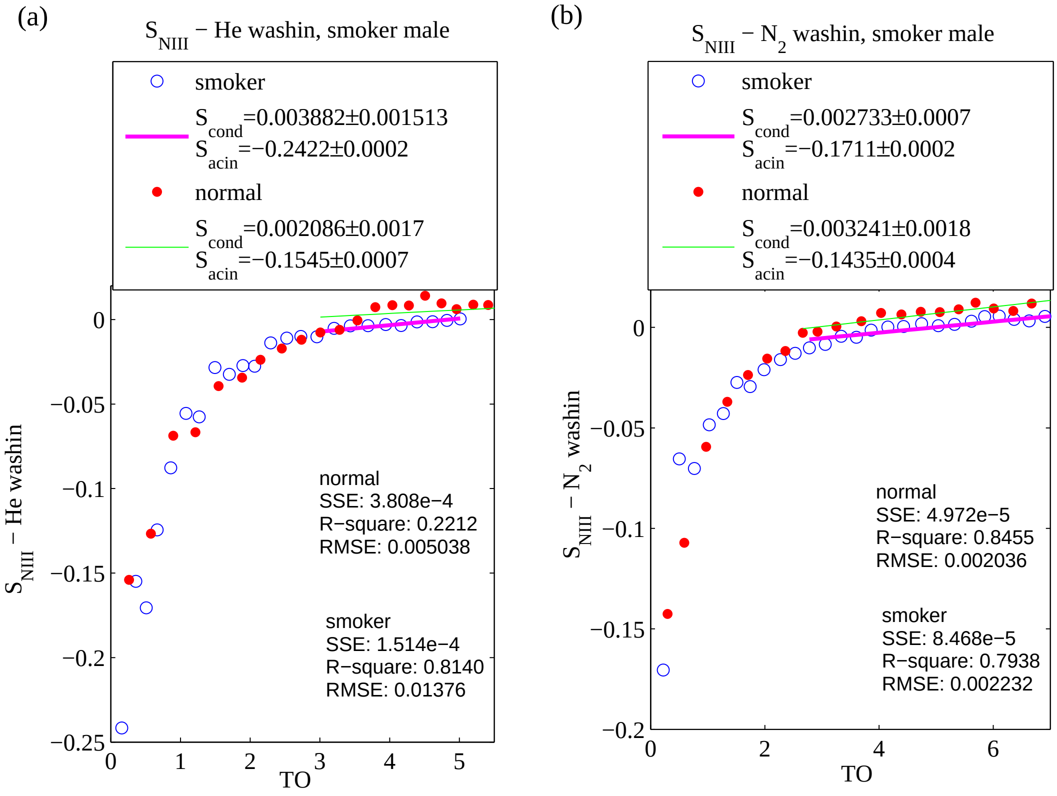

Figure 5.20: (a) The normalised phase III slopes of helium during the helium wash-in process from a male smoker and a normal male. (b) The normalised phase III slopes of nitrogen during the nitrogen wash-in process from a male smoker and a normal male.

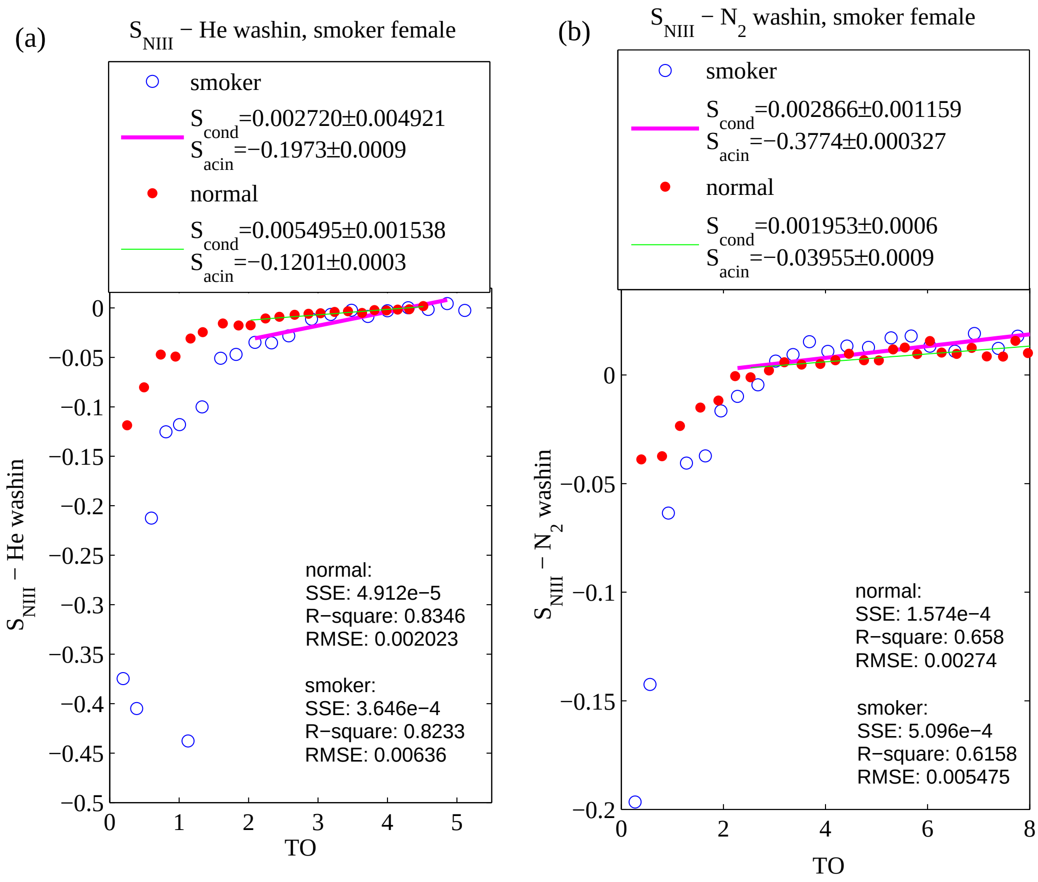

Figure 5.21: (a) The normalised phase III slopes of helium during the helium wash-in process from a female smoker and a normal female. (b) The normalised phase III slopes of nitrogen during the helium washout process from a female smoker and a normal female.

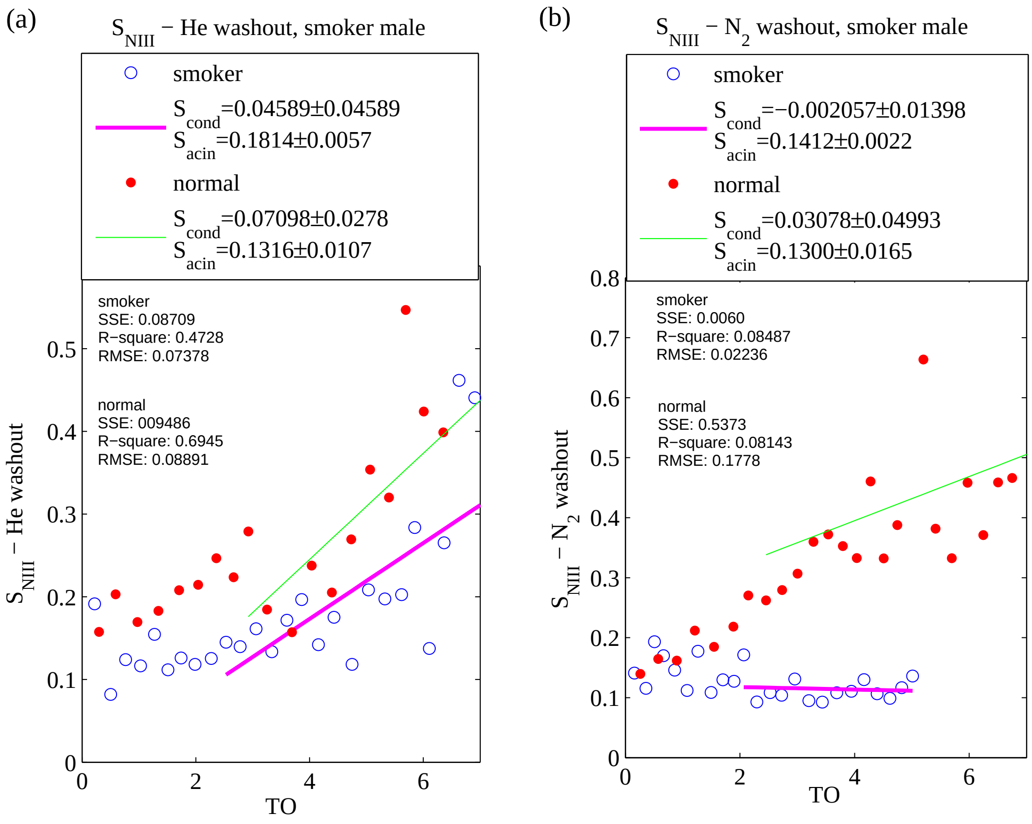

Figure 5.22: (a) The normalised phase III slopes of helium during helium washout process from a male smoker and a normal male. (b) The normalised phase III slopes of nitrogen during nitrogen washout process from a male smoker and a normal male.

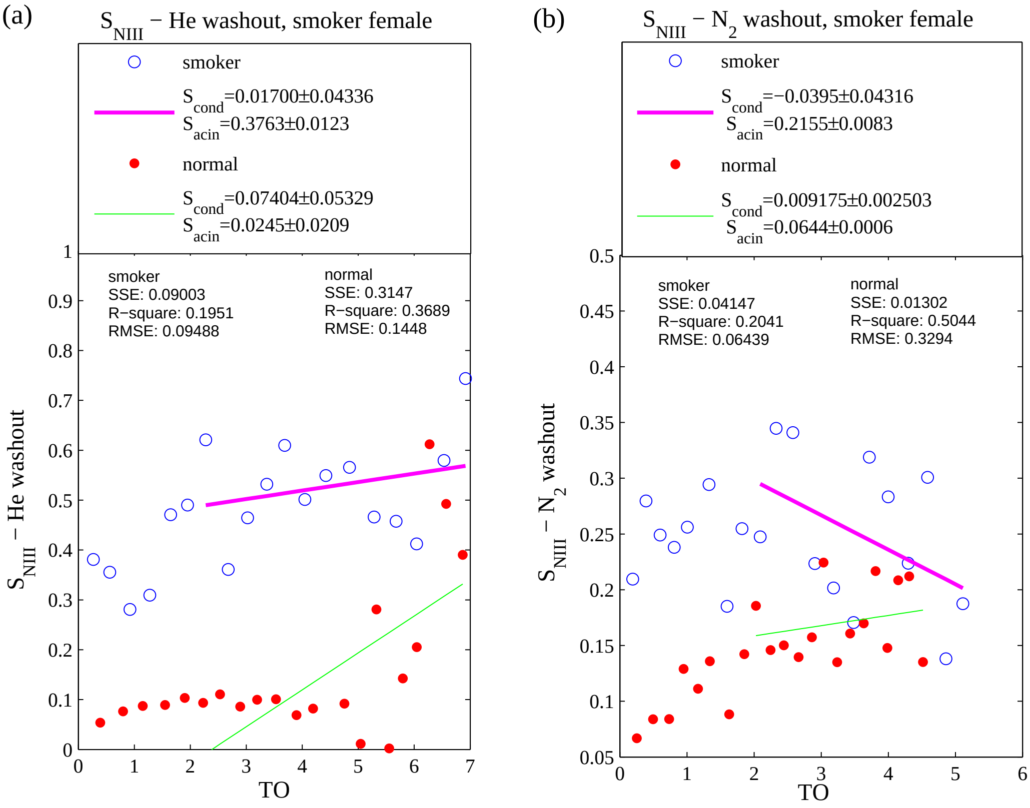

Figure 5.23: (a) The normalised phase III slopes of helium during helium washout process from a female smoker and a normal female. (b) The normalised phase III slopes of nitrogen during nitrogen washout process from a female smoker and a normal female.

5.3.4 Carbon Dioxide

Figure 5.24 shows the normalised phase II slopes of carbon dioxide from the male and female smokers and normal subjects during the helium wash-in and washout processes. The mean concentration of carbon dioxide remains unchanged for all subjects during MBHW measurements. The normalised phase II slopes increases breath by breath for the normal subjects while decreases or remains unchanged for the smokers. This decreasing rate from the female smoker with a ten-year smoking history is higher than the male smoker with a five-year smoking history.

Figure 5.25 shows the normalised phase III slopes of carbon dioxide from the male and female smokers and normal subjects for helium wash-in and washout processes. The normalised phase III slopes increases breath by breath or remains unchanged for the normal subjects while decreases for the smokers. The decreasing rate of S_{NII} from the female smoker is higher compared to the male smoker.

Since there are few washout studies on 'healthy' smokers, the causes of the decreasing rate of normalised phase II and phase III slopes and the extra transition phase between phase II and III will be left for the future work with more volunteer smokers.

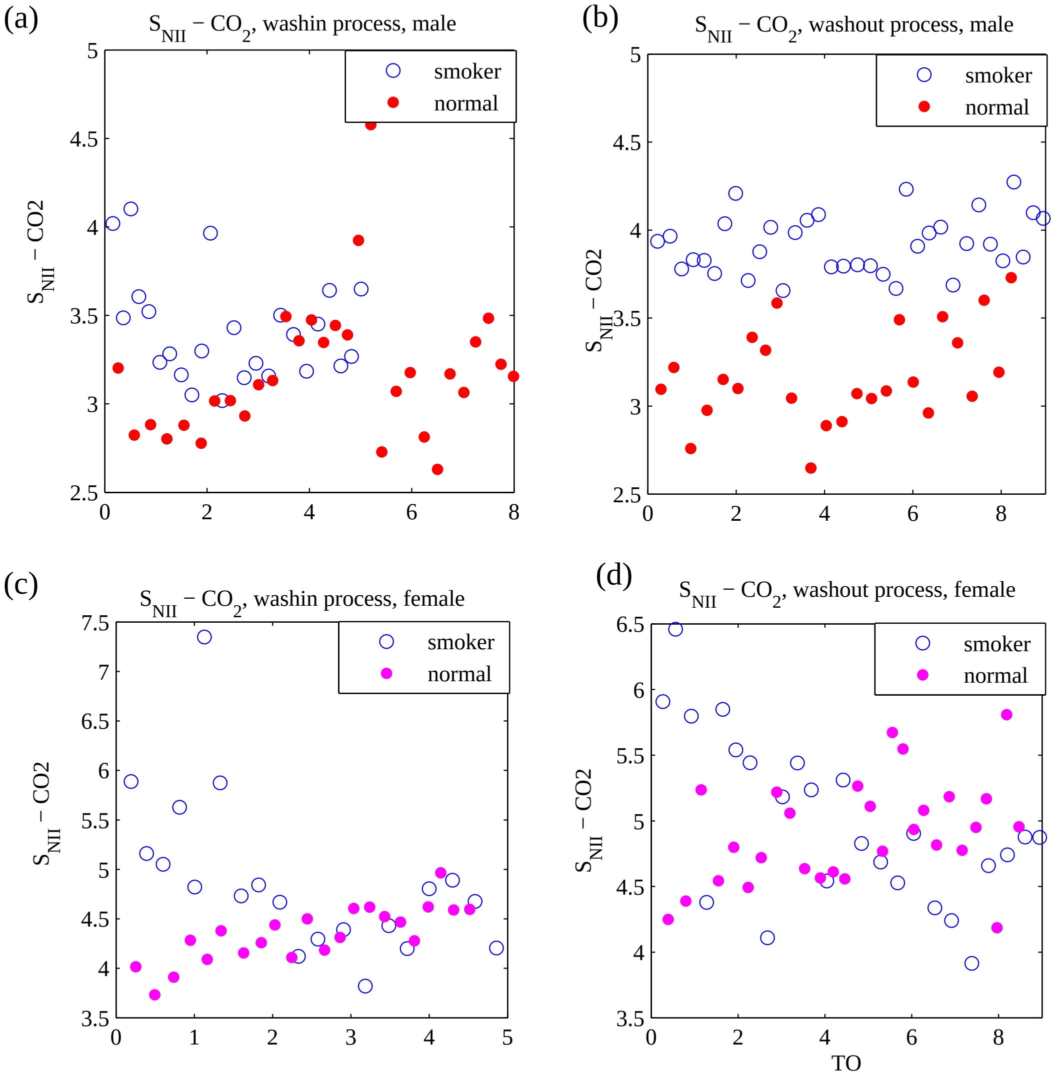

Figure 5.24: (a) The normalised phase II slopes of carbon dioxide during helium wash-in process from a male smoker and a normal male. (b) The normalised phase II slopes of carbon dioxide during helium washout process from a male smoker and a normal male. (c) The normalised phase II slopes of carbon dioxide during helium wash-in process from a female smoker and a normal female. (d) The normalised phase II slopes of carbon dioxide during helium washout process from a female smoker and a normal female.

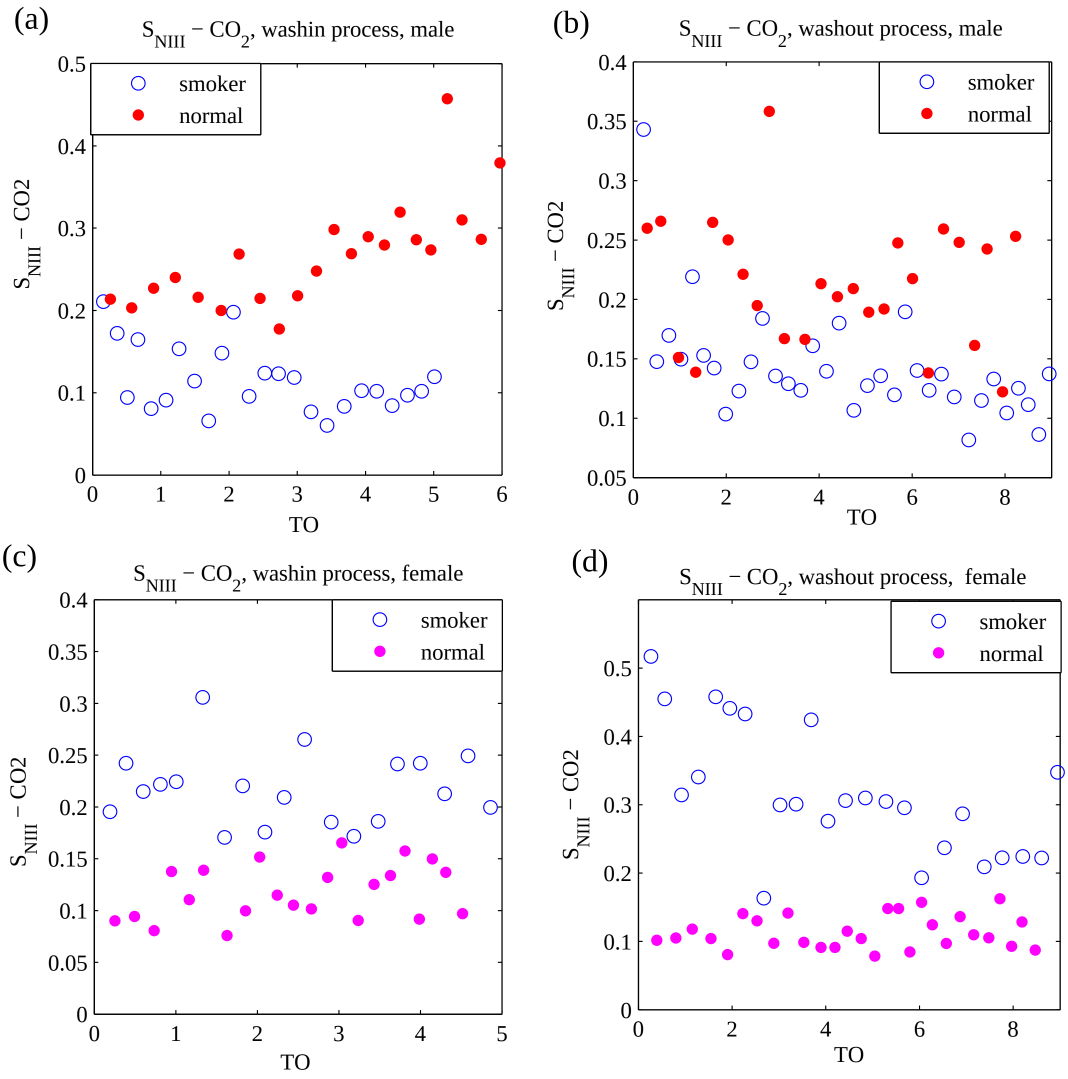

Figure 5.25: (a) The normalised phase III slopes of carbon dioxide during helium wash-in process from a male smoker and a normal male. (b) The normalised phase II slopes of carbon dioxide during nitrogen wash-in process from a male smoker and a normal male. (c) The normalised phase III slopes of carbon dioxide during helium wash-in process from a female smoker and a normal female. (d) The normalised phase III slopes of carbon dioxide during nitrogen wash-in process from a female smoker and a normal female.

5.3.5 Gas Exchange Rate

Since the tar coating on the wall of airways interferes the gas exchange, the gas exchange rate ($Q_r = \Delta[O_2]/\Delta[CO_2]$) of the smokers are compared to the normal healthy subjects. Figure 5.26 shows the oxygen concentration versus the carbon dioxide concentration from two smokers and two normal subjects. A linear curve has been fitted from [CO_2]=1.5 to 6.5% for each dataset. The male smoker has slightly lower Q_r value (1.52±0.06) compared to the normal male (1.65±0.06). The female smoker also has lower Q_r value (1.60±0.07) compared to the normal female (1.90±0.11). Generally, females have higher Q_r values than males and this will be discussed in section 5.5.

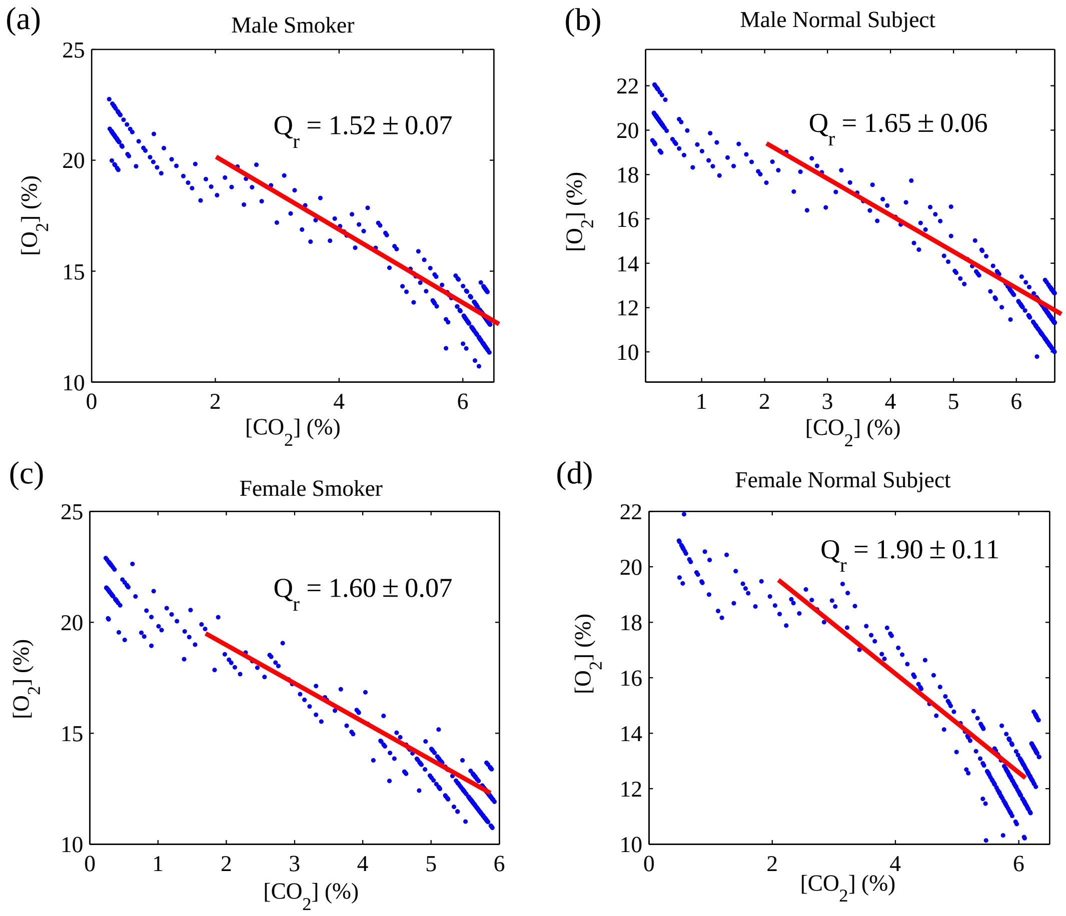

Figure 5.26: Oxygen concentration versus carbon dioxide concentration of a normal breath from (a) a male smoker, (b) a normal male, (c) a female smoker, and (d) a normal female.

5.4 Fowler Dead Space and Gas Density

The Fowler dead space (V_{DF}) from a single breath is located near the middle point of the phase II. In this section, the Fowler dead spaces from two smokers, two asthmatics, and two normal subjects are given for four different gases (He, N_2, O_2, CO_2) during the helium wash-in process as shown in figure 5.27.

For both smokers (5.27(a) and (b)), V_{DF} is smaller for a lighter gas. V_{DF} for helium decreases breath by breath and tends to zero in the helium wash-in process as the helium concentration increases. For the female smoker, V_{DF} is 0.105 L for CO_2, 0.09 L for O_2, 0.06 L for N_2, and 0.02 for He. The ratios of V_{DF} from CO_2, O_2, and N_2 are roughly proportional to the square root of the molecular mass (6.63, 5.66, 5.25, and 2) or the self-diffusion coefficient according to Chapman-Engskon theory [9, 22] as described in section 2.1:

$$D = \frac{1.86 \cdot 10^{-3} T^{3/2} \sqrt{\frac{1}{M_{\mathtt{A}}}}}{P \sigma_{\mathtt{A}}^2 \Omega} \tag{5.14}$$

where T, M_A, P, $\sigma_{\mathtt{A}}$, and Ω are the temperature (K), molecular weights of gases $\mathtt{A}$, ambient pressure (atm), Lennard-Jones force constant for the binary mixture (Å), and the dimensionless integral corresponding to molecular collisions (usually of the order of 1), respectively. The relation is consistent with the results from the male with larger FRC where V_{DS} is 0.165 L for CO_2, 0.14 L for O_2, 0.11 L for N_2, and 0.045 for He. Comparing female to male, the overall V_{DF} is roughly proportional to the FRC.

For asthmatics or normal subjects, V_{DF} for oxygen is the highest even higher than V_{DF} for carbon dioxide. Also, V_{DF} is not necessarily related to the FRC. Generally for non-smokers, V_{DF} for N_2 and He are far below V_{DF} for O_2 and CO_2. The cause of the high V_{DF} for oxygen is unknown and left for the future work with more subjects. The system dead space 10.4 mL will cause 5.2 mL error for the Fowler dead space calculation which can thus only be roughly estimated in this section.

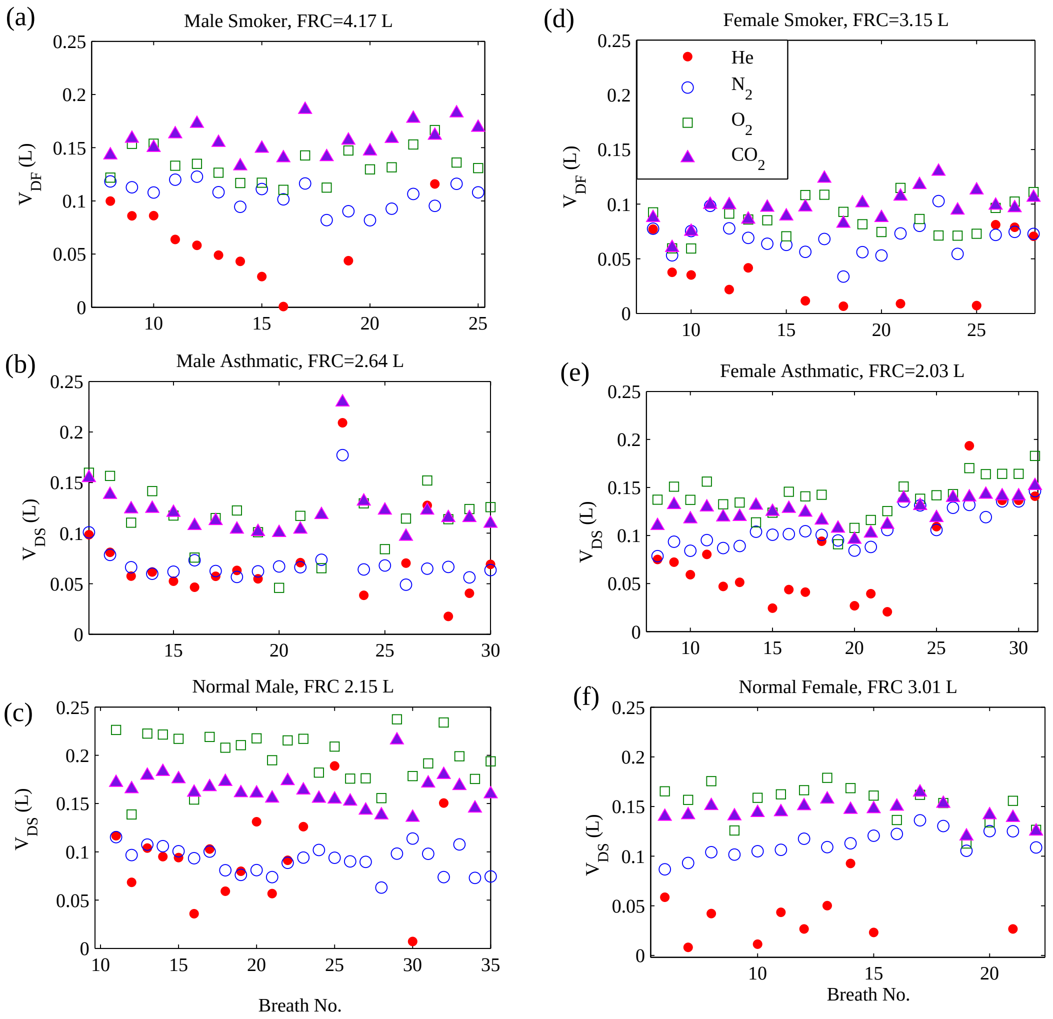

Figure 5.27: Fowler dead space (V_{DF} versus breath number of four different expired gases He (dot), N_2 (circle), O_2 (square), and CO_2 (triangle) from (a) a male smoker, (b) a male asthmatic, (c) a normal male, (d) a female smoker, (e) a female asthmatic, and (f) a normal female. All results are from the helium wash-in measurements.

5.5 MBHW Results from all Volunteers

This section gives a summary of the MBHW results from all volunteers. The peak expiratory flow (PEF) has been measured by a Wright metre (Mini-Wright, Standard Range, EN13826, Clement Clarke International, UK) on all volunteers with the predicted values from the metre data sheet[2]. The PEF measurement has been regarded as a sensitive technique for identifying airflow obstruction [53]. According to the lung clearance MBHW results from male volunteers, subjects with a larger proportion of poorly-ventilated part (FRC_2) have lower PEF values compared to the predicted value as shown in table 5.1.

The lower PEF values are not necessarily related to the lung obstruction. For the female volunteers, PEF values do not simply relate to the lung clearance results. Two normal healthy males with lower PEF also have low gas exchange rate (Q_r). For both male and female smokers, Q_r values are slightly smaller than most of the normal subjects while the high error causes the difficulty to predict the accurate values.

---

[2] This can be found on the website *http://www.peakflow.com/top_nav/normal_values/index.html*

MBHW results from all volunteers

Gender, Age(yrs)	Height (cm)	Weight (kg)	PEF^p (L/min)	PEF^m (L/min)	Q_r	FRC (L)	V$_T$ (L)	$\frac{FRC_1}{FRC}$	$\frac{FRC_2}{FRC}$
M, 25	173	100	608	**485**	1.50±0.13	4.16	1.02	0.41	**0.59**
M, 24	178	66	605	575	1.65±0.06	2.76	0.91	0.93	0.07
M, 25	195	75	637	**425**	1.30±0.11	5.77	2.09	0.24	**0.75**
M$_{ah}$, 27	175	65	618	660	1.64±0.09	3.61	0.92	1	-
M$_{ch}$, 29	185	78	659	605	2.03±0.08	3.58	1.49	0.84	0.16
M$_a$, 29	165	59	595	**450**	1.97±0.11	2.64	0.56	0.49	**0.51**
M$_a$, 47	175	76	625	**570**	1.74±0.09	3.71	1.52	0.68	**0.32**
M$_s$, 27	175	74	620	>800	1.52±0.07	3.40	0.88	0.99	0.01
F, 26	166	50	441	420	2.33±0.08	3.01	0.89	1	-
F, 26	155	57	428	425	1.90±0.11	1.87	0.69	0.98	0.02
F$_a$, 24	155	54	420	450	2.39±0.08	2.03	0.49	0.33	**0.67**
F$_s$, 35	163	53	445	440	1.60±0.07	1.86	0.73	0.84	0.16

Table 5.1: Lung Clearance Results from four male (one with asthma history M$_{ah}$) and two female normal healthy volunteers, two male (M$_a$) and a female (F$_a$) asthmatics, and a female (F$_s$) and male (M$_s$) smoker. The measured PEF values (PEF^m) are compared to the predicted values (PEF^p).

MBHW results from all volunteers

Gender, Age(yrs)	Height (cm)	Weight (kg)	$S_{cond}^{He,in}$ (L^{-1})	$S_{cond}^{N_2,in}$ (L^{-1})	$S_{cond}^{He,out}$ (L^{-1})	$S_{cond}^{N_2,out}$ (L^{-1})
M, 25	173	100	0.0022±0.0017	0.0038±0.0006	0.071±0.028	0.031±0.050
M, 24	178	66	0.0057±0.0010	0.0028±0.0056	0.056±0.015	0.032±0.0007
M, 25	195	75	0.0066±0.0033	0.0005±0.0002	0.023±0.0016	0.007±0.007
M_{ah}, 27	175	75	0.0097±0.0119	0.0033±0.0010	-0.0405±0.0418	0.059±0.129
M_{ch}, 29	193	78	0.0028±0.0008	0.0061±0.0014	0.0162±0.005	0.0164±0.008
M_a, 29	165	59	0.0074±0.0019	0.0147±0.0018	0.096±0.052	0.094±0.064
M_a, 47	175	76	0.0059±0.0020	0.0078±0.0018	0.027±0.006	0.026±0.013
M_s, 27	175	74	0.0039±0.0015	0.0027±0.0007	0.046±0.026	-0.002±0.0140
F, 26	166	50	0.0055±0.0015	0.0019±0.0006	0.074±0.054	0.009±0.002
F, 26	155	57	0.0036±0.0011	0.0007±0.0005	0.076±0.045	0.018±0.016
F_a, 24	155	54	0.0164±0.0041	0.0119±0.0032	0.109±0.087	0.0612±0.0853
F_s, 35	163	53	0.014±0.004	0.0027±0.0011	0.017±0.004	-0.031±0.043

Table 5.2: linespread1.2MBHW Results from all volunteers. S_{cond} values during helium and nitrogen wash-in and washout.

The S_{cond} and S_{acin} values from the all the volunteers have been listed in table 5.2 and 5.3. The results from four groups (normal, normal with asthma and COPD history, smoker, mild asthmatic) are compared and plotted in figure 5.28 and 5.29. The high fitting error results in high variance of both S_{cond} and S_{acin} values. Generally, the mild asthmatic group shows slightly higher S_{cond} and S_{acin} values in wash-in but not much difference in washout measurements compared to the rest of the groups. The S_{cond} and S_{acin} values from nitrogen washout results are similar to the MBNW studies from other group (S_{cond} = 0.033 for normal subjects and 0.032-0.104 for COPD patients, S_{acin} = 0.075 for normal subject and 0.225-0.607 for COPD patients) [79].

MBHW results from all volunteers

Gender, Age(yrs)	Height (cm)	Weight (kg)	$S_{acin}^{He,in}$ (L^{-1})	$S_{acin}^{N_2,in}$ (L^{-1})	$S_{acin}^{He,out}$ (L^{-1})	$S_{acin}^{N_2,out}$ (L^{-1})
M, 25	173	100	-0.154±0.0007	-0.143±0.0015	0.131±0.011	0.130±0.0165
M, 24	178	66	-0.195±0.0002	-0.057±0.0015	0.046±0.004	0.056±0.0001
M, 25	195	75	-0.217±0.0006	-0.054±0.000	0.034±0.007	0.083±0.0015
M_{ah}, 27	175	75	-0.278±0.002	-0.119±0.033	0.139±0.011	0.130±0.021
M_{ch}, 29	193	78	-0.115±0.0002	-0.070±0.0007	0.0823±0.0025	0.0801±0.0024
M_a, 29	175	75	-0.196±0.0006	-0.143±0.0004	0.135±0.0098	0.094±0.021
M_a, 47	165	59	-0.241±0.0005	-0.223±0.0006	0.239±0.002	0.140±0.0036
M_s, 27	175	76	-0.242±0.0002	-0.171±0.0002	0.181±0.005	0.141±0.002
F, 26	166	50	-0.120±0.0003	-0.040±0.0002	0.0245±0.0021	0.060±0.001
F, 26	155	57	-0.119±0.001	-0.026±0.0004	0.128±0.036	0.160±0.074
F_a, 24	155	54	-0.401±0.0008	-0.174±0.001	0.228±0.025	0.208±0.016
F_s, 35	163	53	-0.377±0.001	-0.197±0.0003	0.376±0.0123	0.216±0.008

Table 5.3: linespread1.2MBHW Results from all volunteers. S_{cond} values during helium and nitrogen wash-in and washout.

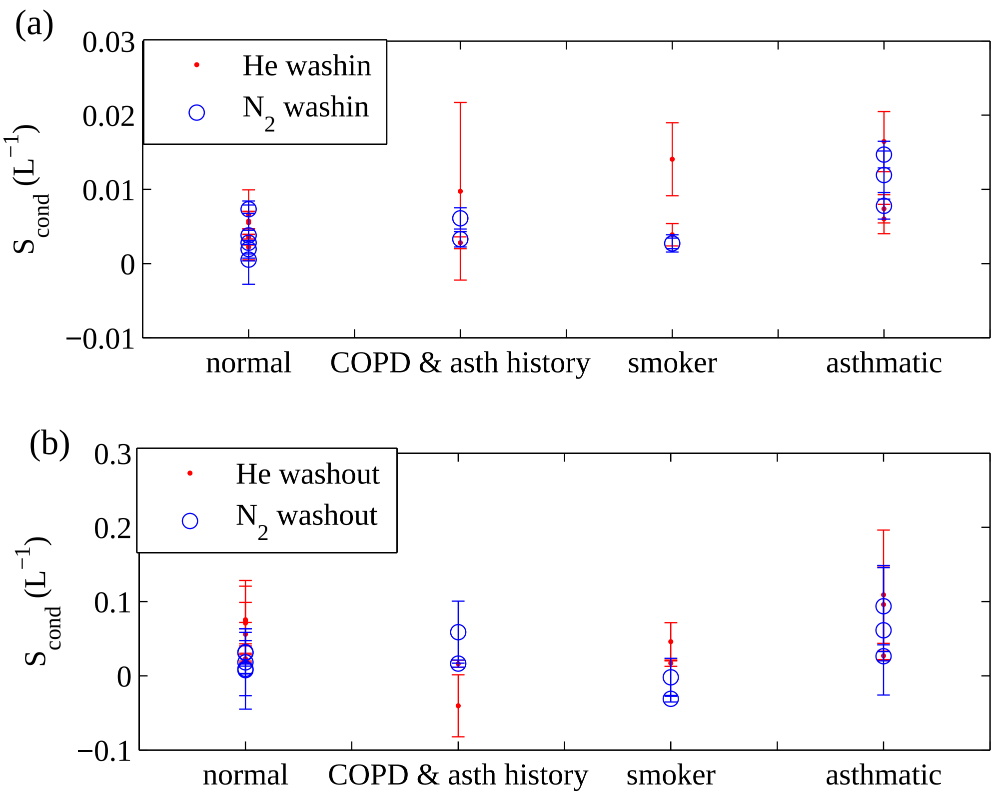

Figure 5.28: MBHW results of S_{cond} values from all volunteers. (a) From the helium and nitrogen wash-in results with systematic errors. (b) From the helium and nitrogen washout results with systematic errors.

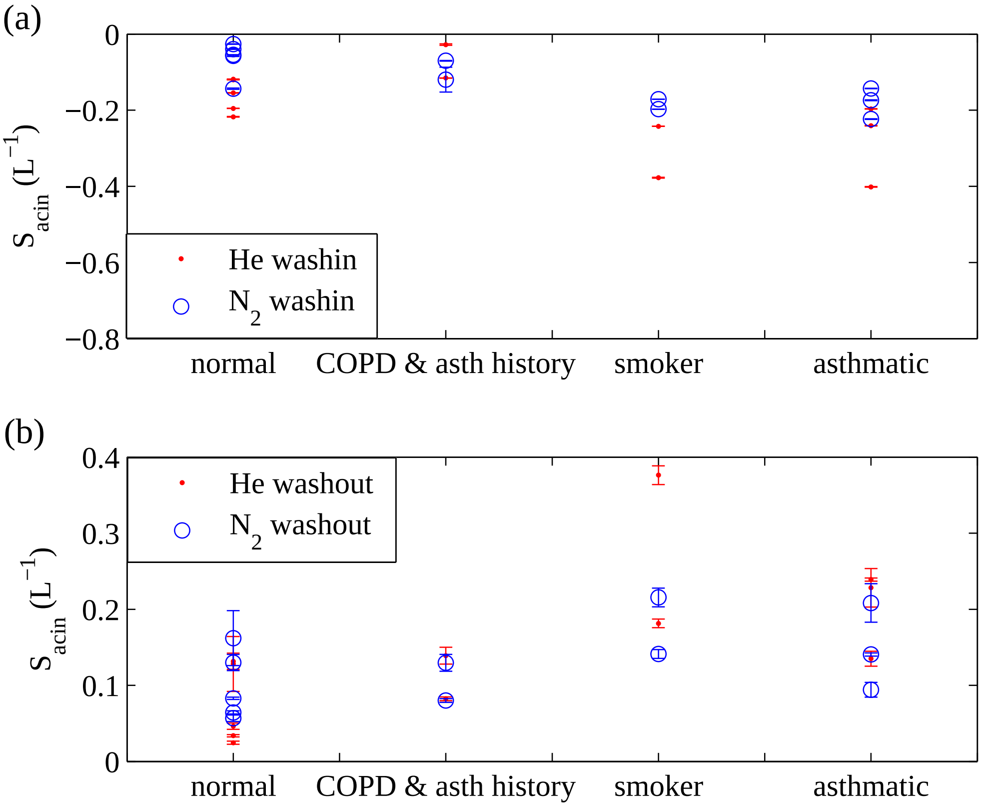

Figure 5.29: MBHW results of S_{acin} values from all volunteers. (a) From the helium and nitrogen wash-in results with systematic errors. (b) From the helium and nitrogen washout results with systematic errors.

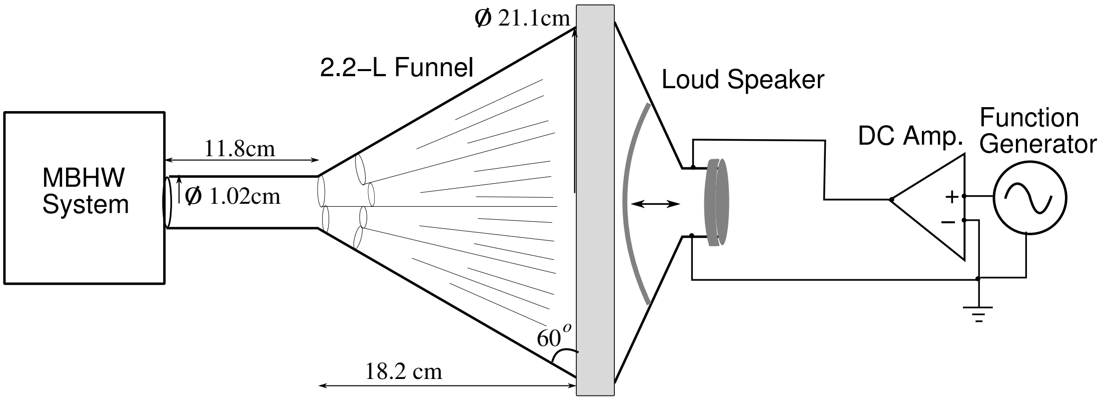

Figure 5.30: A 2.2 litre lung model made of a plastic funnel with $2^1+2^2+2^3+2^4$ small funnels made of transparencies. A loud speaker powered by a function generator and a dc amplifier is connected to the lung model with a 3.5 Vpp triangle wave input to simulate the movement of the diaphragm.

5.6 Lung Model

This section focuses on the MBHW measurements performed on a lung model made of a 2.2 litre funnel with small cones made of plastic foil inside the funnel. MBHW results from the lung model are discussed in the last part of this section.

5.6.1 System Diagram

A 2.2 litre lung model (2.11 litre funnel + 0.12 litre loud speaker) made of a plastic funnel has been built as shown in figure 5.26. 30 small cones with different sizes made of plastic foil have been put inside of the funnel to make a four-generation asymmetric dichotomous structure. A loud speaker (XLS series, Peecless, Denmark) is connected to the funnel and powered by a function generator and a dc amplifier. A 0.25 Hz, 3.5 Vpp triangle wave has been input to the amplifier to simulate the movement of the diaphragm. The corresponding tidal volume is about 0.5 litre. MBHW measurements have been performed on this lung model with 0 to 4 generations, *i.e.*, 1, 1+2, 1+2+4, 1+2+4+8, and 1+2+4+8+16 small compartments.

5.6.2 LCI

Figure 5.31 shows the lung clearance graph from five MBHW measurements on the lung model with 0 to 4 generations. The zero-generation one has been fitted with an exponential curve while others have been fitted with a sum of two exponential curves. Within the two-compartment model [5, 22], the fitted exponential curve with higher decreasing rate represents the better-ventilated compartment while the one with lower decreasing rate is the poorly-ventilated compartment. The proportion of the better-ventilated part or poorly-ventilated part is not necessarily related to the number of generations as displayed in table 5.3. The asymmetric structure and the non-well separated terminals may be the main reason for this result.

Lung Clearance Results from 0- to 4-generation Lung Model

Generation	FRC (L)	V$_T$ (L)	$\frac{FRC_1}{FRC}$	$\frac{FRC_2}{FRC}$	$\frac{V_1}{FRC_1}$	$\frac{V_2}{FRC_2}$
2^0	2.3255	0.5158	1	-	0.2218	-
2^1	1.9624	0.4973	0.3634	0.6366	0.4870	0.1326
2^2	2.0586	0.5101	0.7861	0.2139	0.2459	0.1083
2^3	1.9973	0.5060	0.4807	0.5193	0.3314	0.1174
2^4	2.0559	0.5110	0.3567	0.6433	0.0924	0.1493

Table 5.4: Lung Clearance Results from 0- to 4-generation Lung Model

5.6.3 Phase III

Figure 5.30 shows the normalised phase III slopes (S_{NIII}) from MBHW data on 0- to 4-generation lung model. From the S_{NIII} washout curves, the normalised phase III slopes do not always increase with increasing turnover. The results from the zero-generation lung model show that the S_{NIII} decreases breath by breath in the first 3 turnovers during the helium washout measurement and then increases again. Also, the phase III slopes are not always positive for the zero-generation lung. The results from the zero-generation lung model simply prove that for a trumpet-shape container, the

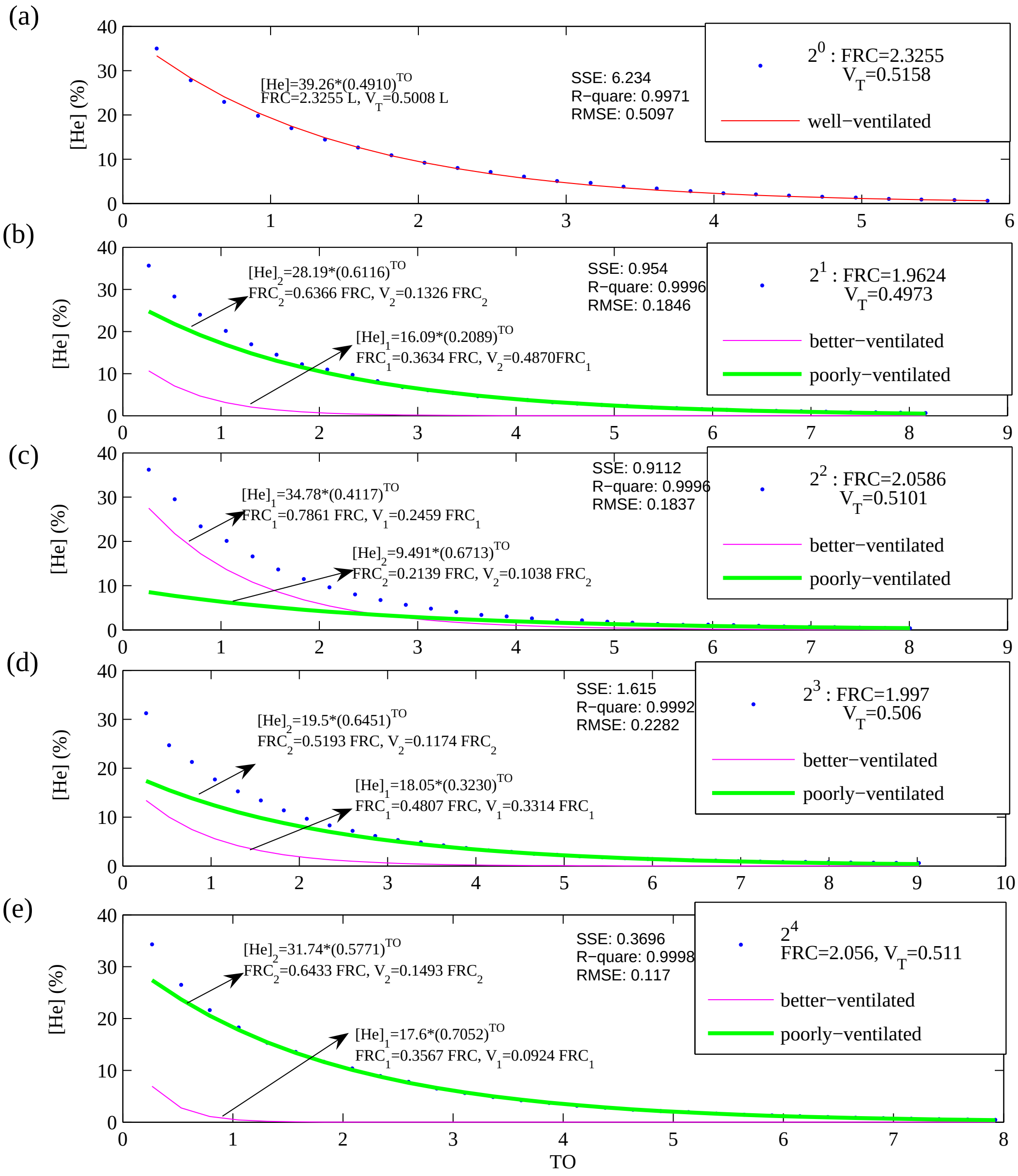

Figure 5.31: Lung clearance washout curves from five MBHW measurements performed on 0- to 4-generation lung model. (a) is from the zero-generation which is the funnel without any small trumpets inside. The result is fitted with an exponential curve. (b), (c), and (d) are from 1-, 2-, and 3-generation lung model and each is fitted with a sum of two exponential curves.

phase III slopes are not always zero or slightly positive but actually negative for most of the breaths. The reason causes the negative phase III slopes may result from the lack of gas exchange from the lung model, the non-instant gas mixing, and the existence of some turbulence.

Compared to the helium washout and nitrogen washout results, the S_{NIII} curves are not consistent with each other from these five lung models. The only particular coincidence is the washout results from 4-generation lung model are similar to the washout results from the asthmatic female as shown in figure 5.31.

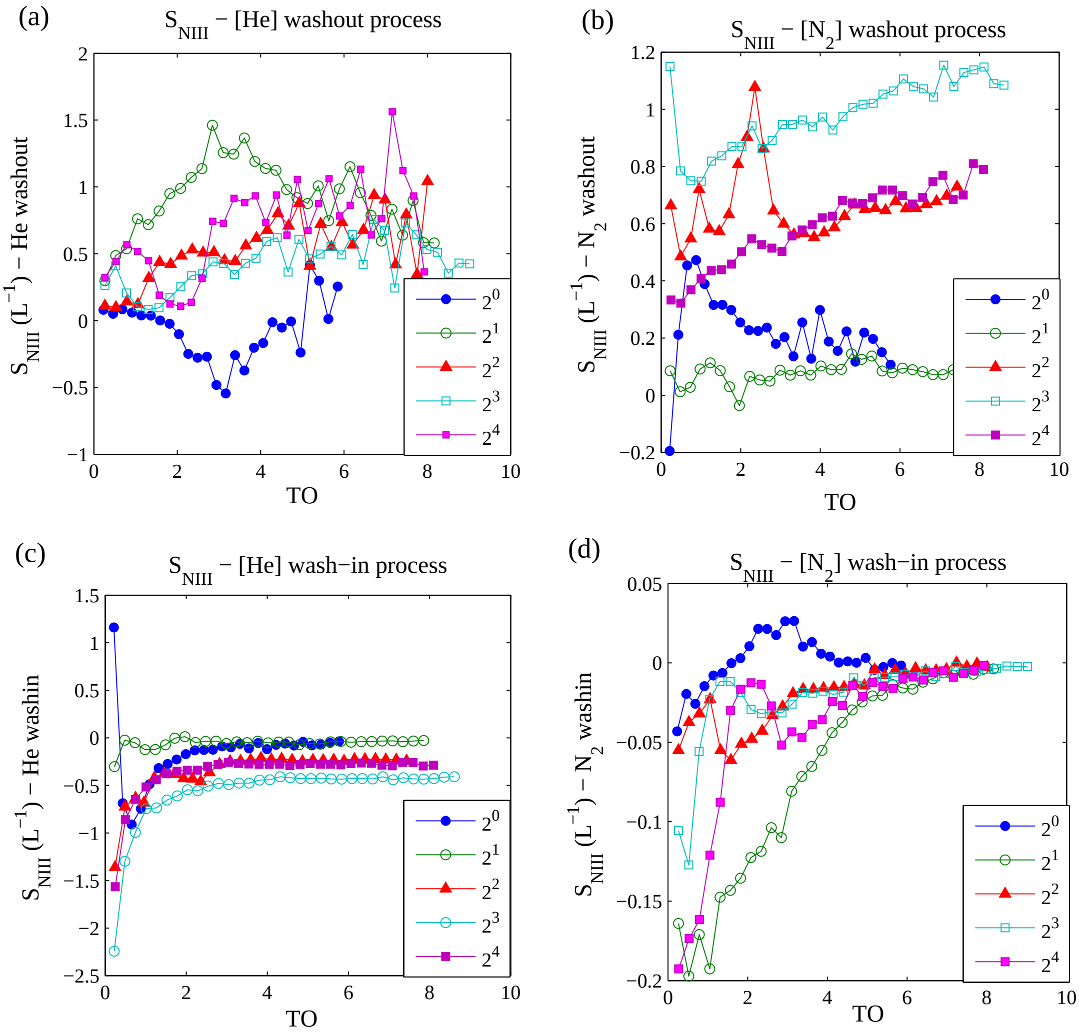

Figure 5.32: Normalised phase III slopes (S_{NIII}) from the MBHW data on 0- to 4-generation (2^0 to 2^4) lung models. (a) is the results from helium during helium washout process. (b) is from nitrogen during nitrogen washout process. (c) is from helium during helium wash-in process. (d) is from nitrogen during nitrogen wash-in process.

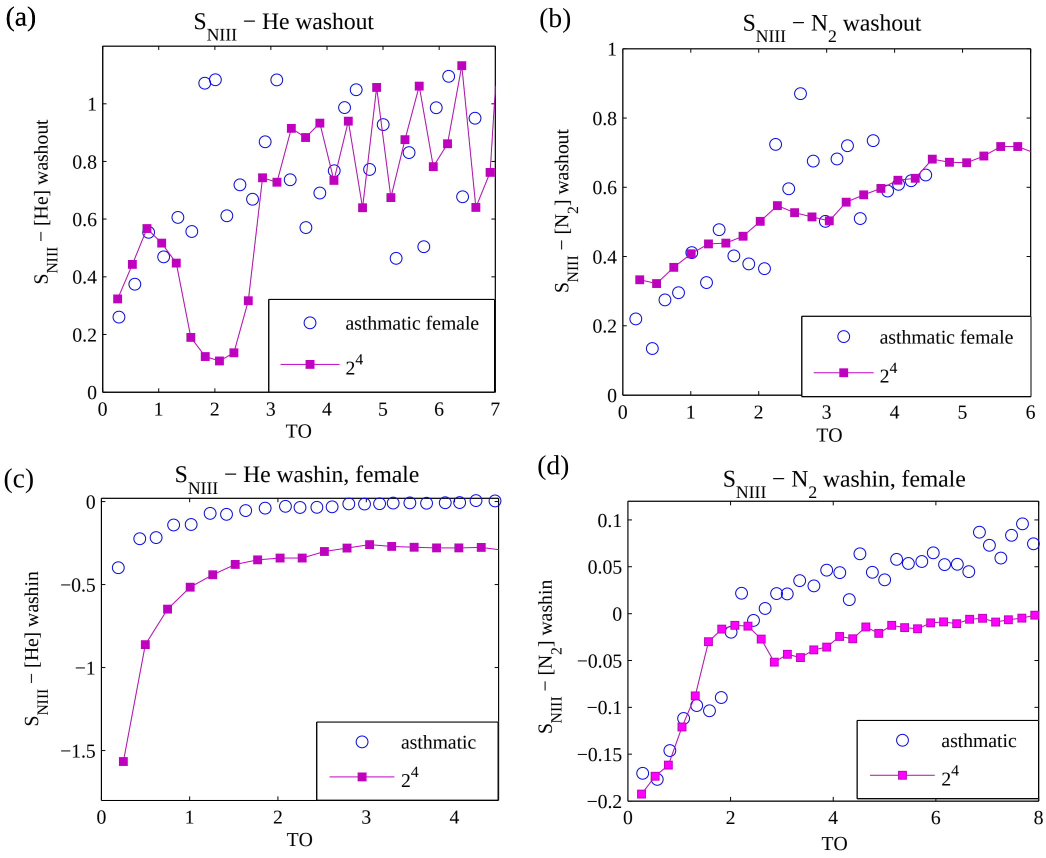

Figure 5.33: Normalised phase III slopes (S_{NIII}) from the MBHW data on 4-generation lung model and a asthmatic female. (a) is the results from helium during helium washout process. (b) is from nitrogen during nitrogen washout process. (c) is from helium during helium wash-in process. (d) is from nitrogen during nitrogen wash-in process.

5.6.4 Phase II

Figure 5.32 shows the normalised phase II slopes (S_{NII}) from MBHW data on the 0- to 4-generation lung model. From the S_{NII} washout curves, the normalised phase II slopes decrease breath by breath during helium washout process but increase during nitrogen washout. Also, during helium washouts, S_{NII} values are absolutely higher for the lower generation lung model. However, there is no relation between S_{NII} and number of generations from the helium wash-in results.

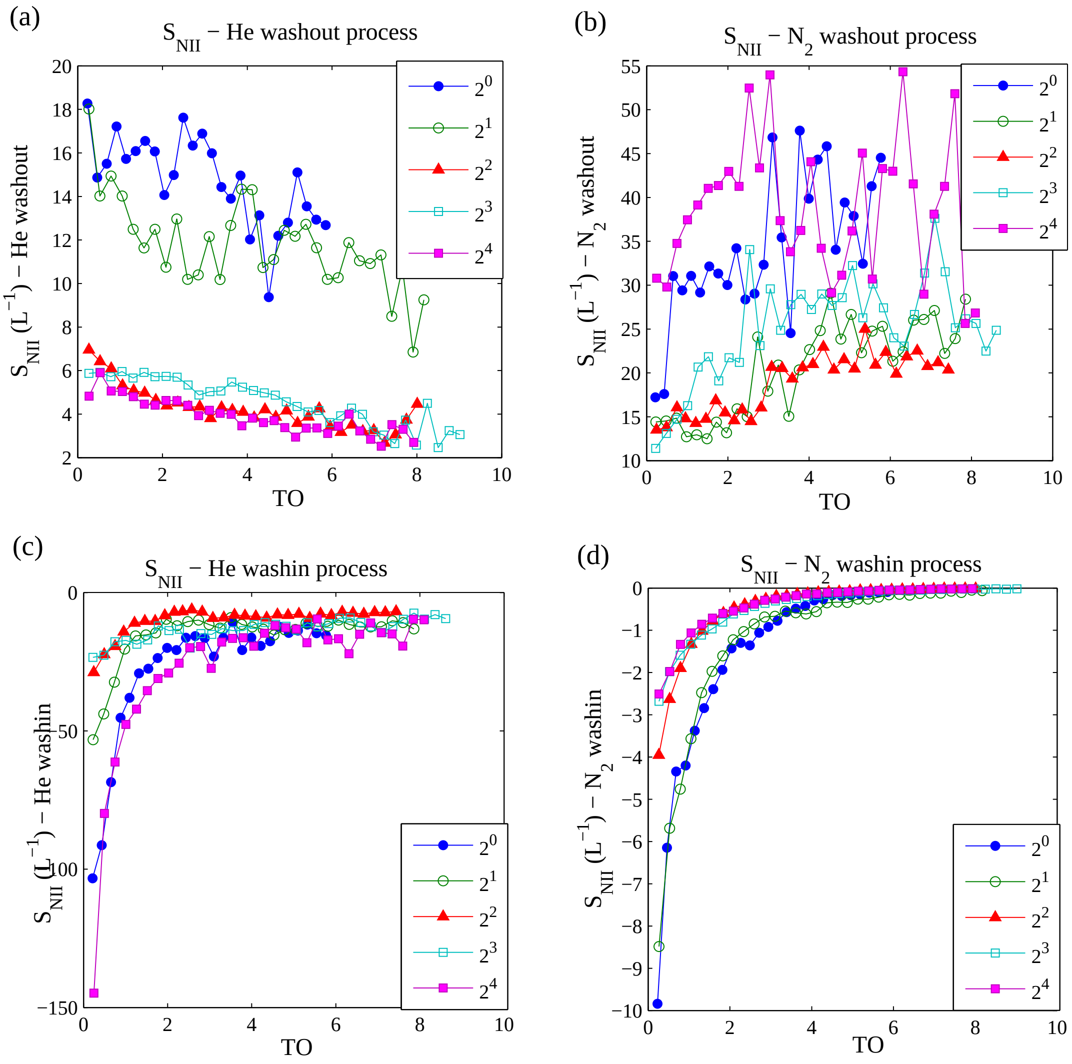

Figure 5.34: Normalised phase II slopes (S_{NII}) from the MBHW data on 0- to 4-generation (2^0 to 2^4) lung models. (a) is the results from helium during helium washout process. (b) is from nitrogen during nitrogen washout process. (c) is from helium during helium wash-in process. (d) is from nitrogen during nitrogen wash-in process.

5.6.5 Discussion

The MBHW results from the lung model with different generations cannot be compared to the MBHW results from real lungs. The reason may result from the lack of gas exchange, the poorly separated compartments at the terminals, irregular sizes of branches, and the very low generation structure. A real lung is a tree-like dichotomous structure which has 23 generations and well-separated tiny aveoli at the terminals. However, the MBHW results from the lung model simply proves that real lungs are unable to be simplified as a two-compartment or four-compartment model.

The following three graphs display the single breaths from the lung models (figure 5.31) and the comparison of the lung model and real lungs (figure 5.34 and 5.35).

Figure 5.33 shows the first five single breaths during helium wash-in and helium washout processes from 0- to 4-generation lung models. Figure 5.33(a) and (f) shows the phase III slopes are not always absolutely positive for the zero-generation lung model. Phase II slopes are smaller for higher generation of lung models.

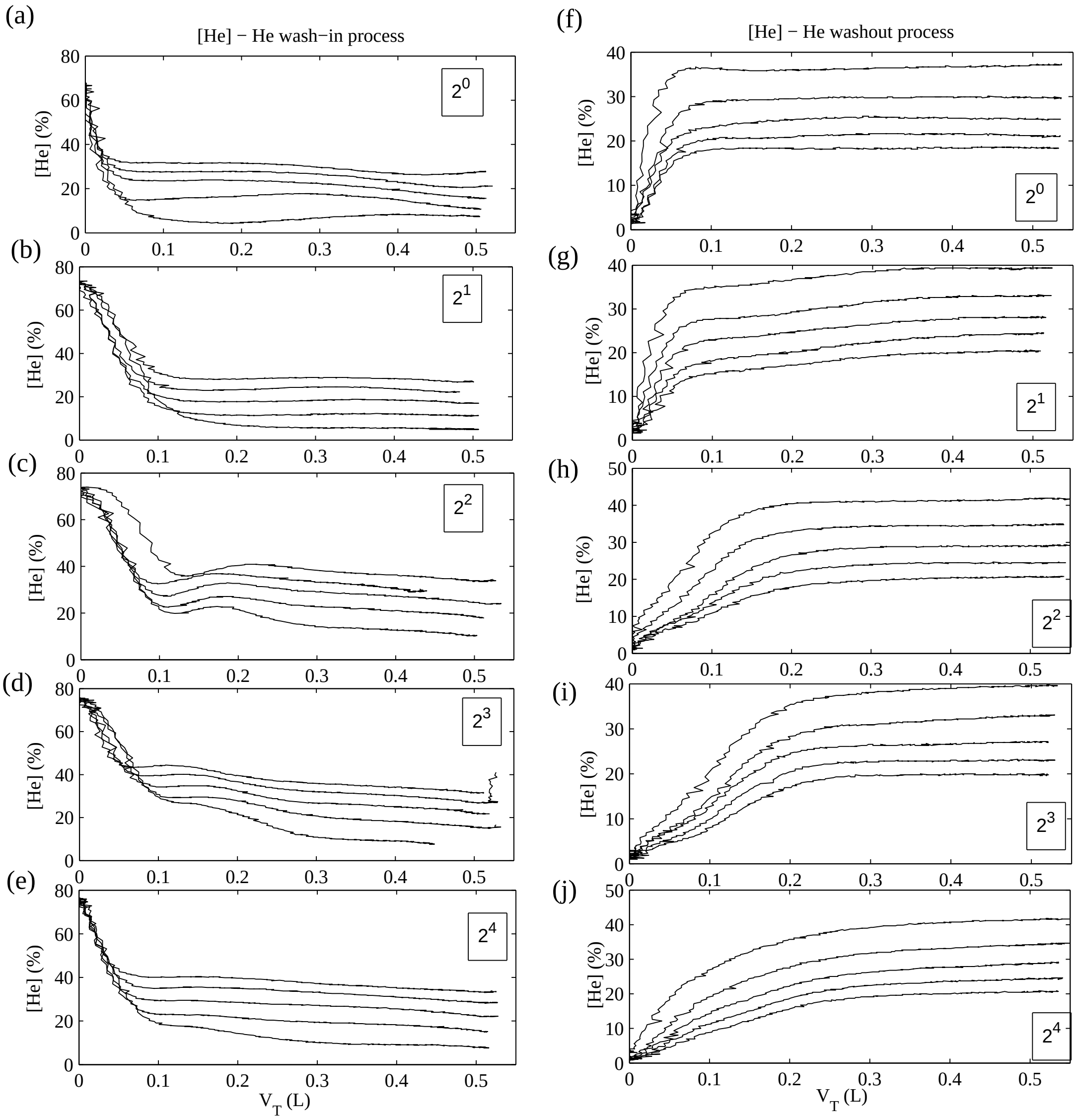

Figure 5.35: The first five breaths of MBHW data during helium wash-in ((a) to (e)) and helium washout ((f) to (j)) processes from 0- to 4-generation lung models.

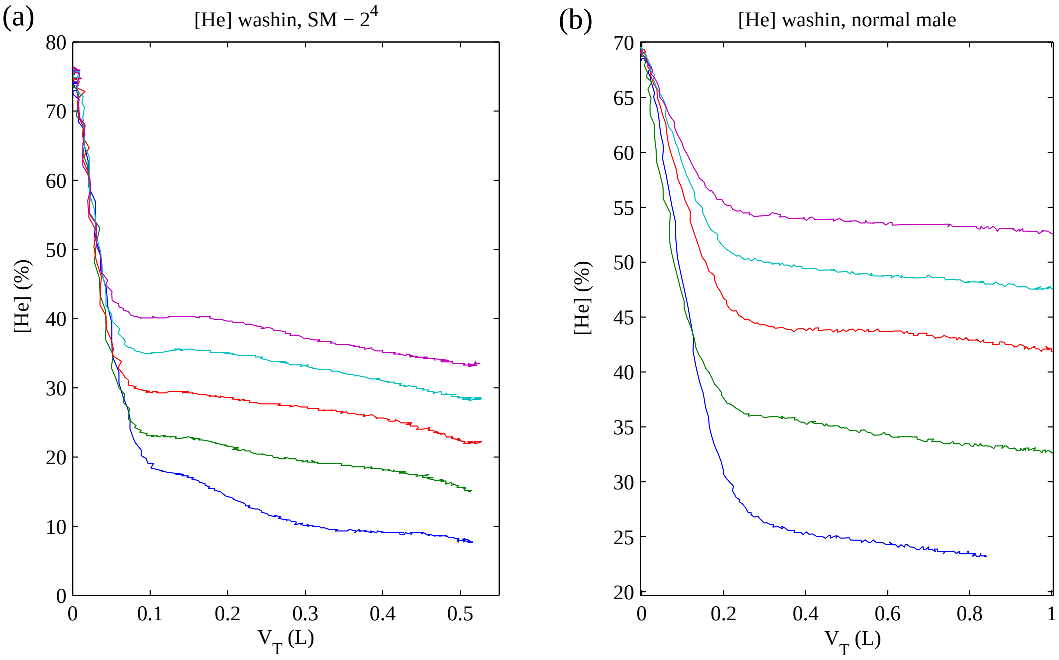

Figure 5.36: The first five breaths of MBHW data during helium wash-in processes from (a) 3-generation lung model and a normal male.

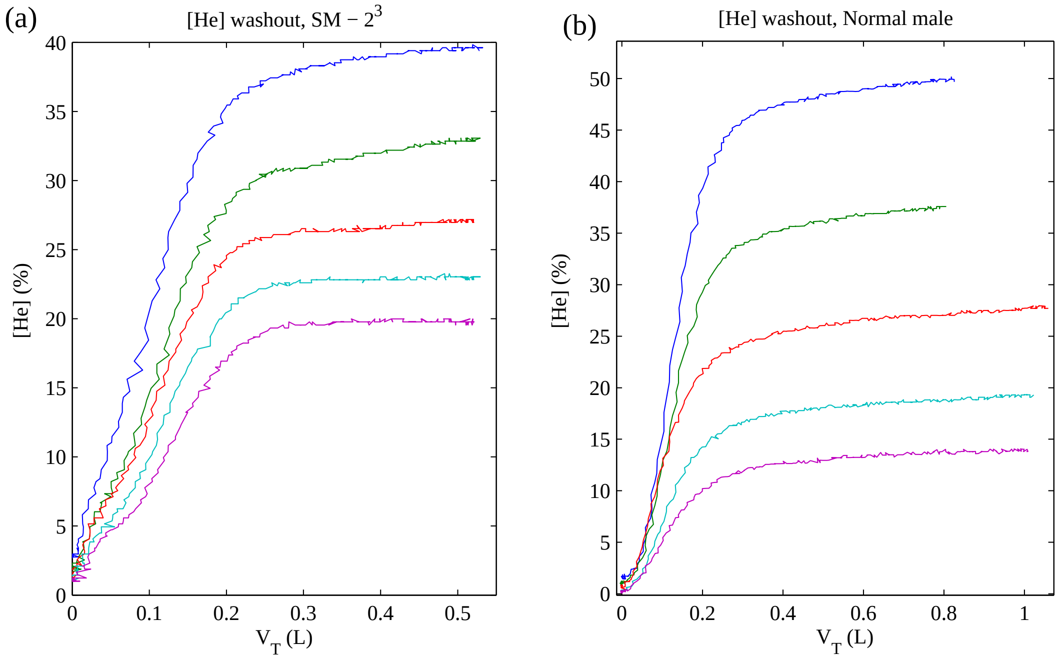

Figure 5.37: The first five breaths of MBHW data during helium washout processes from (a) 4-generation lung model and (b) a male.

5.7 Summary

MBHW measurements have been performed on seven male (four normal, two asthmatic, one smoker) and four female (two normal, one asthmatic, one smoker) volunteers. Peak expiratory flow rates are not necessarily related to the lung obstruction. Subjects with lower PEF values compared to the predicted values have larger proportion of poorly-ventilated part. For asthmatics, their MBHW results show slightly higher S_{cond} values or higher S_{acin} values compared to the normal subjects. For smokers, their respiratory quotient are smaller than normal ones. Generally, female have higher Q_r values than males.

A lung model made of a plastic funnel with 0 to 4 generations has been built. The MBHW results from the lung model cannot simply be compared to the results from real lungs. The phase III slopes from lung model washout results are not always positive especially for the one with less generations. The reason may result from the lack of gas exchange, the unwell separated compartments at the terminals, irregular sizes of branches, and the very low generation structure.

Chapter 6

Other Methods of Helium Gas Concentration Detection

Three trial methods for detecting the helium gas concentration are introduced in this chapter. These methods each have significant drawbacks and thus were found not suitable for MBHW measurements. First method to be considered is the ultrasonic gas density detection. The gas density is given by measuring the group velocity of sound in the gas mixture. However, there is a limitation because for higher concentration of helium gas, the acoustic attenuation is very high which results in an undetectable signal. The ultrasonic method works when the helium concentration is below 52%. It can be used for detecting gases with lower acoustic attenuation.

The second method relies on detecting the thermal conductivity of the gas mixture with two tungsten filament-type thermistors. Two filaments are connected in a Wheatstone Bridge circuit. One is exposed in the air as a reference thermistor, and the other one is put in the sampled gas. The thermal conductivity of the gas mixture is given by comparing those two signals. This thermal-type detector works well for high concentration of helium with a quick response. However, the high signal noise caused by the gas flow reduces the signal to noise ratio (less than 32). The small signal to noise ratio for the lower concentration of helium restricts the detecting limit such that these thermistors are not suitable for the helium washout measurements. Also, those tungsten filaments exposed in the gases are easily be oxidized and normally lasts no more than three days and then needs to be replaced which is also a disadvantage.

The third method is to use a mass spectrometer which is traditionally used in nitrogen washout tests for detecting nitrogen gas [49, 64, 80]. Commercial mass spectrometer systems normally can be used in a helium leak detection scheme [72]. However, the high mobility of helium gas causes a slow response when the mass spectrometer is pumped by a turbo pump. The diffusion pump can pump the helium gas more efficiently and gives a faster response. However, the diffusion oil can pollute the mass spectrometer system and thus shorten its working life. Also, since the mass spectrometer can only operate under a high vacuum environment, the size of the entrance for the sampling gas flowing in is hard to adjust, and the wet gas from our breath can block the orifice easily even after passing through a water trap or heating the system up. Technically, mass spectrometers are not recommended as a method for detecting any wet gas.

6.1 Ultrasonic Gas Density Detector

This detecting method is based on measuring the time of flight of acoustic pulse signals in the gas mixture [27, 75, 83]. The pulse signals are generated by a crystal oscillator through a logic circuit to the 40 kHz ultrasonic transmitter. The ultrasonic receiver signal is then transformed by a second circuit and passed to the input of a lock-in amplifier which gives the a voltage proportional to the time of flight difference between the air and the gas mixture.

6.1.1 Theory

A series of pulse signals are transmitted from an ultrasonic transducer to a receiver through the flowing gas mixture sample. The time of flight of one pulse changes with the gas density since the sound velocity (v_s) is related the gas density (ρ_g) by [27]

$$v_s = \sqrt{\frac{\gamma RT}{\rho_g}} \tag{6.1}$$

where γ is the adiabatic constant (or the isentropic expansion factor), R(=8.3145 J$\cdot$mol$^{-1}\cdot$K^{-1}) is the molar gas constant and T is the gas temperature. The time of flight difference (Δt) between in the air (t_{air}) and in the gas mixture (t_g) is

$$\Delta t = \frac{L}{v_{air}} - \frac{L}{v_g} \tag{6.2}$$

where v_{air} is the sound velocity in air and L is the traveling distance of pulses (or the distance between the ultrasonic transmitter and the receiver in a non-flowing gas). Suppose the flow speed is constant for different gas mixtures, and thus the Doppler effect can be simply ignored. Thus the time of flight difference can be modified as

$$\Delta t = \frac{L}{\sqrt{\gamma RT}}(\sqrt{\rho_{air}} - \sqrt{\rho_g}). \tag{6.3}$$

which is proportional to the change of square root of gas density.

6.1.2 Working Principle

A commercial-supplied circuit (Parking radar K3502, Vellemen Kit, Vellemen Components NV, Belgium) has been modified for this project as shown in figure 6.1. A crystal oscillator with 5.0688 MHz resonance frequency generates a sine wave signal to a 14-stage ripple binary counter (CD4060). The output signal from the sixth stage of the counter has been modified as a series of pulses with frequency 79.2 kHz which goes into another counter (CD4020). The signals from fourth to ninth stages go into a NAND gate (CD4068) which gives a series of 0.156 kHz pulses containing four cycles at 40 kHz. These pulses are converted into mechanical vibrations by a 40 kHz ultrasonic transducer (400PT160, Ultrasonic Transmitter, Prowave, Taiwan) transmitting through a gas mixture and then received by another receiving transducer (400SR160, Ultrasonic Receiver, Prowave, Taiwan). The receiver signal is then amplified and transformed by NAND gates into pulses whose length is dependent on the time of flight. These modified pulses are then integrated so that the amplitude depends on the time of flight. The integrated signal then goes into a lock-in amplifier. The signals from the transmitter, reference, receiver, modified receiver, and integrated receiving signal are

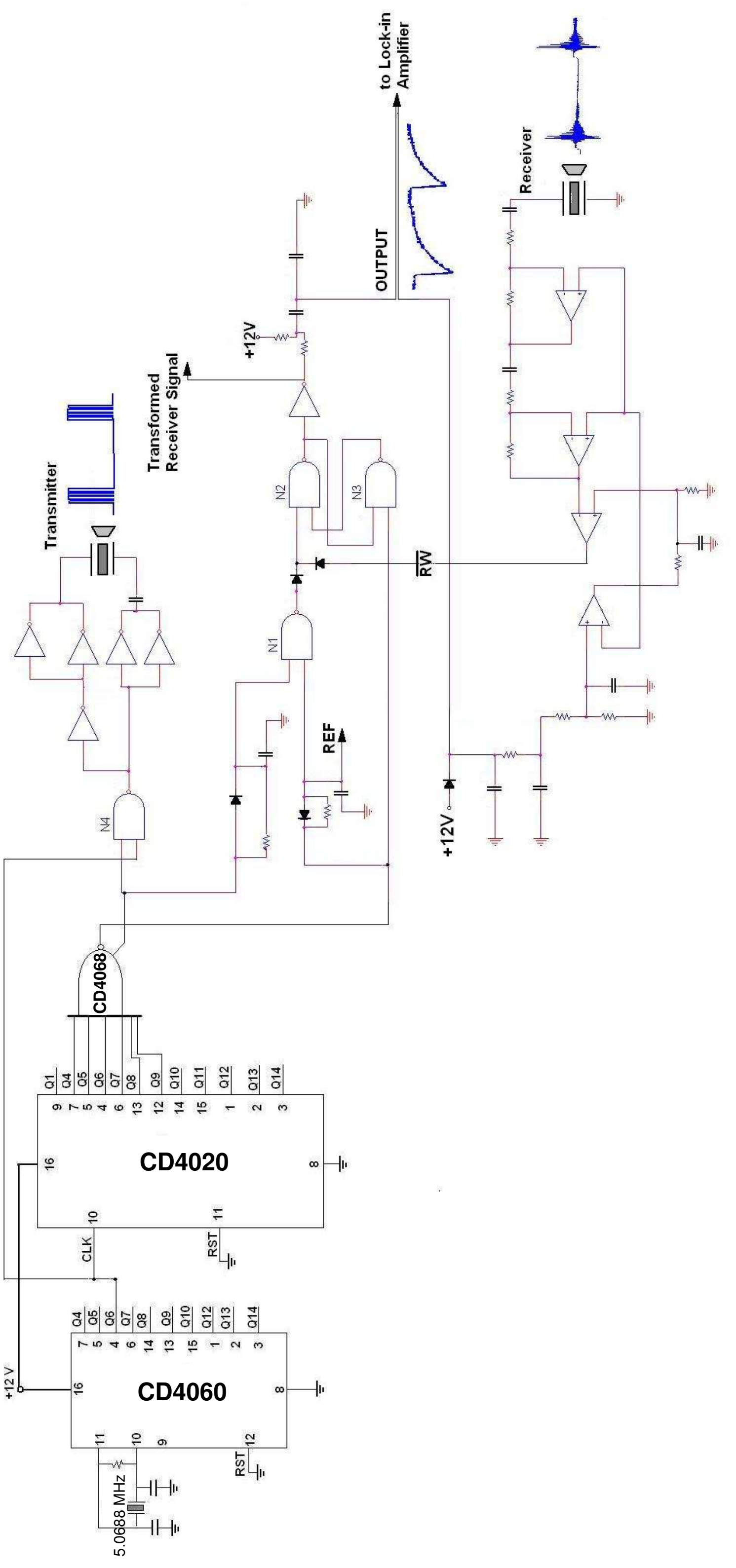

Figure 6.1: The modified ultrasonic circuit from a commercial package.

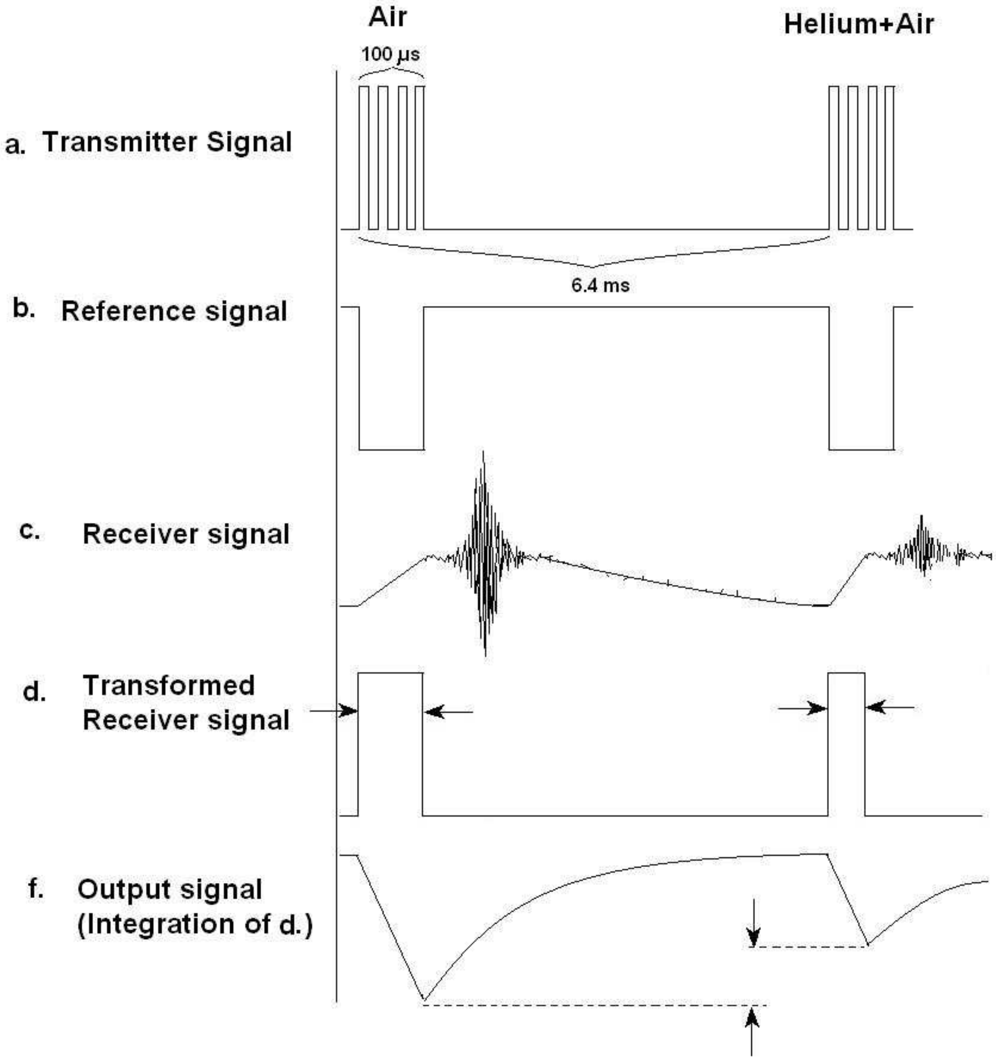

Figure 6.2: The signals from the circuit including transmitting signal, reference signal, receiver signal, transformed receiver signal, and the output signal to the lock-in amplifier.

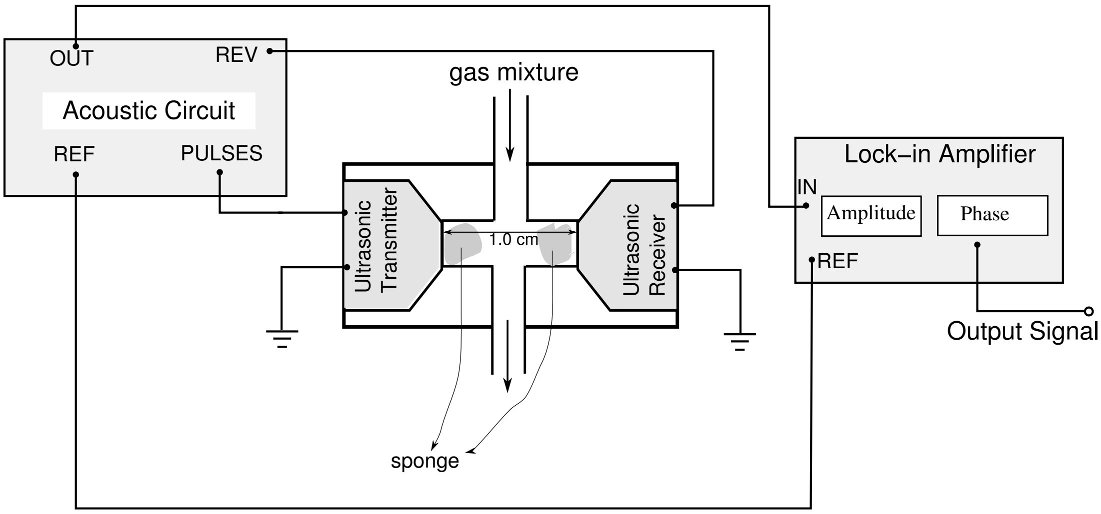

Figure 6.3: The ultrasonic system diagram.

plotted in figure 6.2. Two pulses with different lengths represent different gas mixtures (air and heliox-air mixture) flowing through the acoustic cell as shown in figure 6.3.

6.1.3 System Diagram

Figure 6.3 shows the ultrasonic gas detecting system diagram. Both ultrasonic transducers with a diameter of 16.0 mm are fixed in a acrylic cell with 1.0 cm separation. Two small pieces of sponge are put between two transducers to reduce the reflective pulse signals and other noise. The output signal from the circuit goes into a lock-in amplifier. The output voltage from the lock-in amplifier gives the time of flight difference between in the air and in the gas mixture.

6.1.4 Detection Limitation

The detection limitation comes from the high acoustic attenuation in a helium/air gas mixture which causes the difficulty of identifying the length of the receiving wavelets and thus the length of the modified pulse. Figure 6.4(a) shows the helium concentration in air versus the output voltage from the lock-in amplifier compared to the air signal

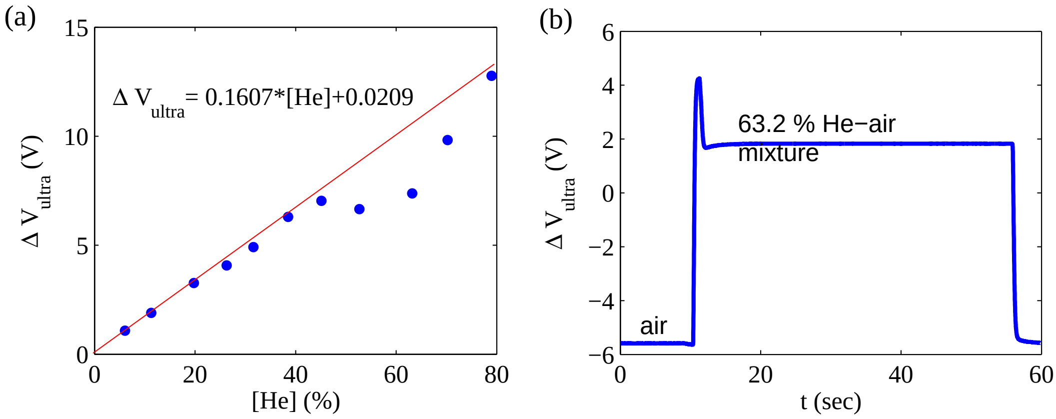

Figure 6.4: (a) The helium concentration in air versus the output voltage from the lock-in amplifier with the subtraction of air signal. The concentrations above 52% fall below the predicted value (line) which makes the ΔV_{ultra} a non-linear function of [He]. (b) The output signal of air and the 64% helium-air mixture. The signal goes up at 4.2 first but decreases very quickly caused by the acoustic attenuation.

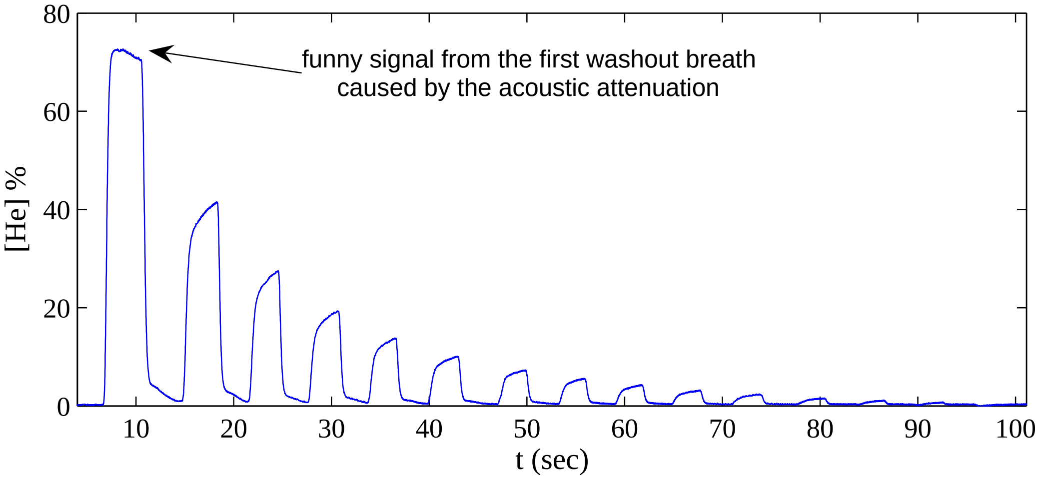

Figure 6.5: The helium washout data from a volunteer. The signal has been converted by a predicted linear equation in figure 6.4(a). The phase III from the first breath shows a negative slope because the high acoustic attenuation restricts the detection.

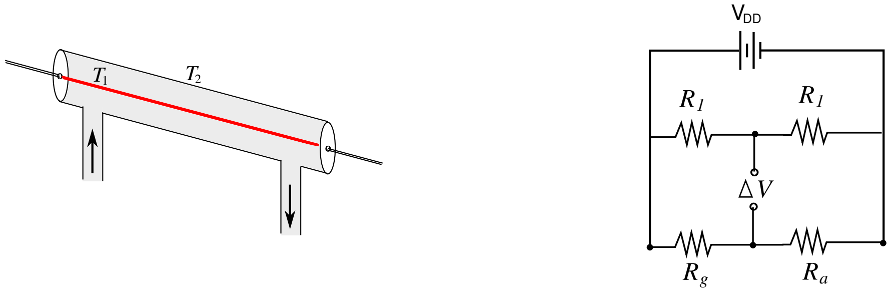

(a) (b)

Figure 6.6: (a) The concentric filament with surface temperature T_1 in a tube with temperature T_2. (b) The Wheatstone Bridge circuit diagram of two filament thermistors with resistance R_g and R_a and connected to two paralleled resistors R_1.

Δ V$_{ultra}$. The concentrations above 52% fall below the predicted value (line) which makes the ΔV_{ultra} is a non-linear function of [He]. In (b), the output signal of air and the 64% helium-air mixture. The signal goes up first but decreases very quickly which is caused by the acoustic attenuation.

6.2 Thermal Conductivity Detector

This type of helium gas sensor is based on detecting the thermal conductivity difference between air and the helium gas mixture [48]. Since helium gas is a better heat conductor than air, when the helium gas flows through the filament, it takes more heat from the filament and thus reduces the filament temperature and the filament resistance compared to the air. By connecting those filaments in a Wheatstone Bridge circuit, the helium concentration can be calculated from the output signal [69].

6.2.1 Working Principle

Heat conduction occurs when there is a temperature gradient in a media. Consider a concentric cylinder made of a homogeneous material with thermal conductivity κ_h and inner and outer diameter r_i and r_o as shown in figure 6.6(a). The inner surface is held at a constant temperature T_1 which is higher than the outer surface temperature T_2. When the length of the cylinder is much longer compared to its radius, the heat flow

$\dot{Q}_h$ from T_1 to T_2 can be given by [48, 69]

$$\dot{Q}_h = \frac{2\pi l \kappa_h (T_1 - T_2)}{ln\frac{r_o}{r_i}} \tag{6.4}$$

where l is the length of the cylinder.

Adapted from the concentric cylinder, a filament-type thermistor consists of a hot tungsten filament in a metal tube. The temperature of the filament T_1 is maintained by an electrical supply V_{DD} while the surface temperature of the metal tube is exposed at room temperature. The heat is conducted by a flowing gas with the thermal conductivity κ_g. The heat flow can be given by

$$\dot{Q}_h = \frac{{V_{DD}}^2}{JR_g} \tag{6.5}$$

where J is the Joule constant (=4.183 W/cal·s). In a certain range of temperature, the filament resistance linearly varies with the temperature, *i.e.*,

$$R_g(T_1 + \Delta T) = R_g(T_1)(1 + \alpha_f \Delta T) \tag{6.6}$$

or

$$\Delta R_g(T_1) = \alpha_f R_g(T_1)\Delta T \tag{6.7}$$

where α_f is the temperature coefficient and ΔT is the temperature change. Suppose the heat is supplied by a constant electric power, then

$$\Delta \dot{Q}_h = \frac{\partial \dot{Q}_h}{\partial T}\Delta T + \frac{\partial \dot{Q}_h}{\partial \kappa_h}\Delta \kappa = 0, \tag{6.8}$$

$$\frac{\Delta T}{T_1} + \frac{\Delta \kappa_h}{\kappa_h} = 0. \tag{6.9}$$

Since

$$\Delta T = \frac{\Delta R_g(T_1)}{\alpha_f R_g(T_1)}, \tag{6.10}$$

the thermal conductivity change can be given by monitoring the change of the resistance, *i.e.*,

$$\Delta R_g(T_1) = -\frac{R_g(T_1)\alpha_f T_1 \Delta \kappa_h}{\kappa_h}. \tag{6.11}$$

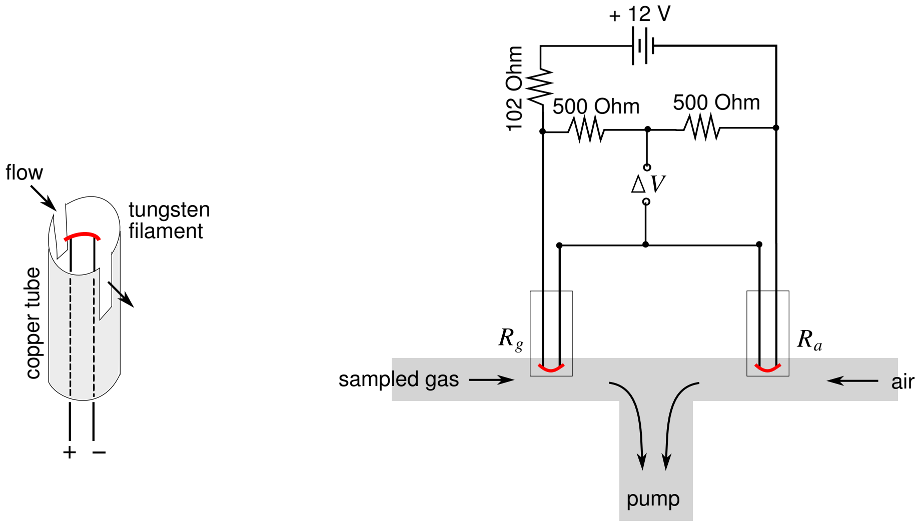

(a) (b)

Figure 6.7: (a) The tungsten filament-type thermistor is fixed in open copper tube. (b) The thermal conductivity detector system diagram.

Two filaments are connected in a Wheatstone Bridge circuit to reduce the noise from the flow and increase the sensitivity as shown in figure 6.6 (b). The output signal ΔV is given by

$$\Delta V = V_{DD}\left(\frac{R_1}{R1+R_2} - \frac{R_a}{R_g+R_a}\right) \tag{6.12}$$

$$= V_{DD}\left(\frac{1}{2} - \frac{1}{1+\frac{R_g}{R_a}}\right). \tag{6.13}$$

The filament resistance in the gas mixture can be given by

$$R_g = R_a - \frac{R_a \alpha_f T_1 \Delta\kappa_h^{gas}}{\kappa_h^{air}} \tag{6.14}$$

and thus the output signal

$$\Delta V_{DD} = V_{DD}\left(\frac{1}{2} - \frac{1}{2 - \frac{\alpha_f T_1 \Delta\kappa_h^{gas}}{\kappa_h^{air}}}\right), \tag{6.15}$$

$$\approx -V_{DD}\frac{\frac{\alpha_f T_1 \Delta\kappa_h^{gas}}{\kappa_h^{air}}}{4}. \tag{6.16}$$

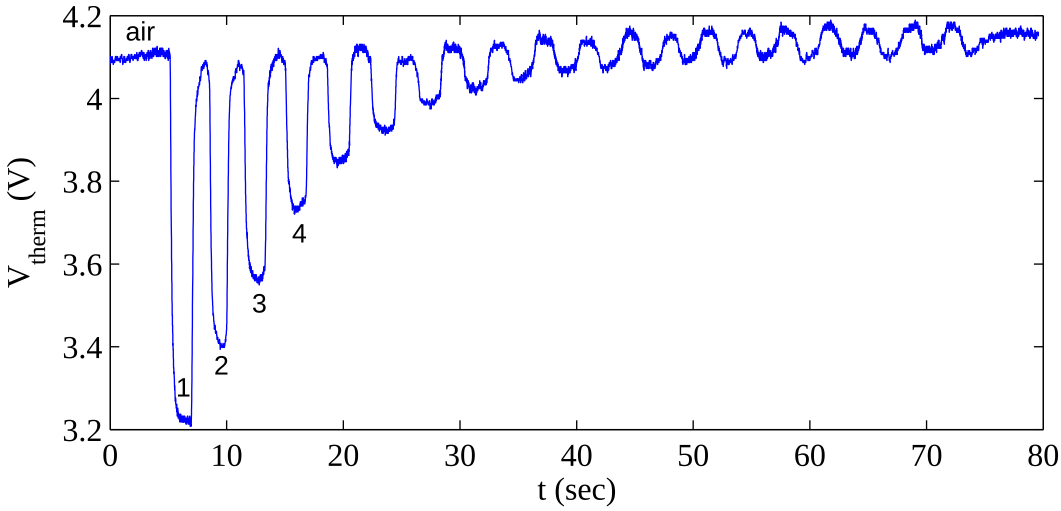

Figure 6.8: The helium washout data measured by the thermal conductivity detecting system.

6.2.2 System Diagram

Two commercial tungsten filament-type thermistors (12V T1 3mm submin wire-ended filament lamp, RoHS, UK) are supplied within their glass bulb. One of them is exposed to the sampled gas and the other one is exposed to the flowing air with their bulb glass removed. Each filament is fixed in a copper tube as shown in figure 6.7(a).

6.2.3 Detection Limitation

The low signal to noise ratio caused by the flow is the main reason that restricts the use of thermistors for the detection. Figure 6.8 shows the helium washout data measured by the thermal conductivity detecting system. After the first few breaths, the helium concentration becomes smaller and smaller while the noise is still high such that the signal-to-noise ratio becomes smaller. The phase III slopes are hard to determine because of the high noise.

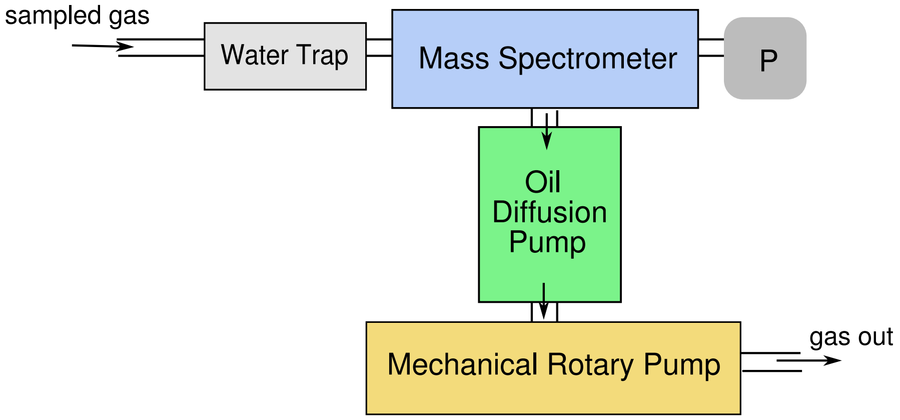

Figure 6.9: The mass spectrometer system diagram. The sampled gas passes through a waster trap and then to the mass spectrometer. An oil-diffusion pump with a mechanical rotary pump is connected to the mass spectrometer for maintaining the high vacuum background ($< 10^{-4}$ mb).

6.3 Mass Spectrometer Gas Analyser

The mass spectrometer tried in this work is a quadrupole-type mass analyser (Anavac-2, VG Gas Analysis Limited, UK). The quadrupole mass analysers are normally considered to be low resolution devices while their sensing parts have smaller size which give faster response than the traditional sector type. Since mass spectrometers need to operate under a high vacuum environment, an oil-diffusion pump (Vapour Pump EO2, Edwards, UK) along with a rotary mechanical pump (High Vacuum Pump E2M5, Edwards, UK) is used in this work. The oil diffusion pump is chosen because it can pump out helium gas more efficiently than a turbo pump. However, its diffusion oil can not be pumped out very efficiently by the mechanical pump and thus pollutes the mass spectrometer system. The pollutant oil renders it unsuitable in the long term for the helium washout measurements. The system diagram is shown in figure 6.9.

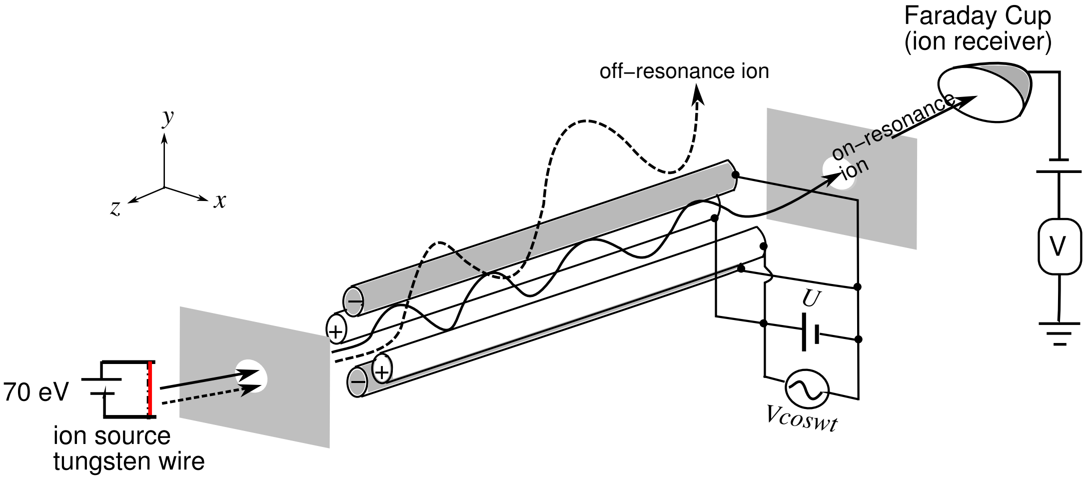

Figure 6.10: The quadrupole mass spectrometer diagram. Ions are ejected by a 70-eV hot tungsten wire through a filter and four parallel electrodes. The applied potential on those electrodes has both dc and rf voltages. On resonance ions which have stable trajectory will be transmitted through the rods and detected by the Faraday cup. Off resonance ions which have unstable trajectory will hit the rods or the walls before being detected. The quadrupole analyser diagram is modified with permission from *http://en.wikipedia.org/wiki/Quadrupole_mass_analyzer.*

6.3.1 Working Principle

Quadrupole Mass Spectrometer

A quadrupole mass spectrometer consists of four parallel electrodes as shown in figure 6.10. Ions are ejected from a 70-eV hot tungsten wire. A dc and rf voltage are applied on those electrodes. On resonance ions which have stable trajectory will be transmitted through the rods and detected by the Faraday cup. Off resonance ions which have unstable trajectory will hit the rods or the wall before being detected. The charge to the mass ratio e/m is determined by the combination of the dc voltage U and rf voltage $V cos\omega t$. A Faraday cup is used as an ion receiver with a volt meter which gives the amount of received charges and thus the partial pressure of the detected gas [18, 21].

Quadrupole Operation

A quadrupole mass analyser consists of four parallel hyperbolic electrodes (two pairs) and a profile of the produced electrical field is shown in figure 6.11. The electrical

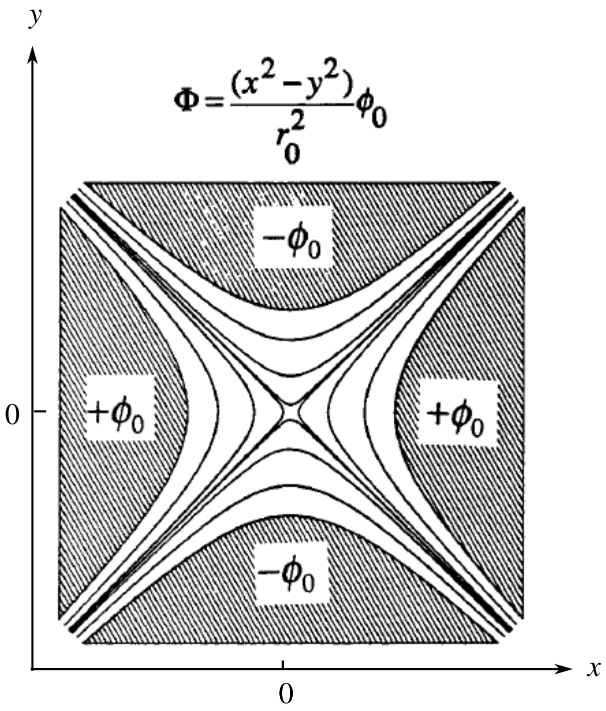

Figure 6.11: The profile of the electrical filed produced by four parallel (two pairs) hyperbolic electrodes. ϕ_0 is the electrical potential applied on an electrode [21].

potential within the rods $\Phi(x, y)$ is given by [21]

$$\Phi(x,y) = \frac{x^2 - y^2}{r_0^2}\phi_0 \tag{6.17}$$

where x and y are the displacements from the centre line, r_0 is the distance from the centre line, and ϕ_0 is the electrical potential applied to an electrode.

Ion motion is determined by Newton's law, $\vec{F} = m\nabla^2 r_0$ (m = ion mass, $\vec{F}$ = electrical force), where the electrical force $\vec{F}$ is related to the electrical field $\vec{E}$ as $\vec{F} = e\vec{E}$ (e = charge on ion). Since the electric field is related to the potential by $\vec{E} = -\nabla\Phi(x, y)$, the equations of ion motion can be given by [21]

$$\begin{aligned} \vec{F} &= -e\nabla\Phi(x,y) = -e\frac{2x}{r_0^2}\phi_0\hat{\imath} + e\frac{2y}{r_0^2}\phi_0\hat{\jmath}, && (6.18)\\ m\frac{d^2x}{dt^2} &= -e\frac{2x}{r_0^2}\phi_0, && (6.19)\\ m\frac{d^2y}{dt^2} &= e\frac{2y}{r_0^2}\phi_0. && (6.20) \end{aligned}$$

The applied electrical potential has both a dc voltage U and a radio-frequency (rf) voltage $Vcos\omega t$, *i.e.*, [21]

$$\phi_0 = U - Vcos\omega t. \tag{6.21}$$

The equations of ion motion thus can be given by

$$\begin{aligned} m\frac{d^2x}{dt^2} &= -e\frac{2x}{r_0^2}(U - Vcos\omega t), & (6.22)\\ m\frac{d^2y}{dt^2} &= e\frac{2y}{r_0^2}(U - Vcos\omega t). & (6.23)\end{aligned}$$

Since the ion motion along the x and y are similar but independent, we consider the differential equation along the x direction and rewrite it as [21]

$$\frac{d^2x}{d\xi^2} + (a_x - 2q_x cos2\xi)x = 0 \tag{6.24}$$

where $\xi = \omega t/2$. This is the Mathieu's equation with two Mathieu parameters a_x and q_x for the x-direction motion

$$\begin{aligned} a_x &= \frac{8eU}{m\omega^2 r_0^2}, & (6.25)\\ q_x &= \frac{4eV}{m\omega^2 r_0^2}. & (6.26)\end{aligned}$$

For the y-direction motion, the Mathieu parameters have the opposite sign of x-direction, *i.e.*, $a_y = -a_x$ and $q_y = -q_x$.

The solutions to the Mathieu's equation can be classified as stable and unstable [21]. An ion trajectory is stable if its oscillation amplitude is always smaller than r_0 that the ion can be transmitted through the rods and be detected. An unstable trajectory occurs when the ion's oscillation amplitude is increasing until the ion hits the rod when the amplitude is larger than r_0 before it is detected. For a given combination of Mathieu's parameters a_x and q_x (or equivalently for a given e/m, dc voltage U, rf voltage V and frequency ω) there are an infinite number of stable solutions. The first three stability regions for both x and y directions (I, II, and III) are shown in figure 6.12(a).

The first stability region is shown in figure 6.12(b) with an operating line which is the mass scanning path. Ions with mass m_2 located at the stability region will pass through the quadrupole rods. Heavier ions m_3 with smaller a_x and q_x values or lighter ions m_1 with bigger a_x and q_x values are located outside of the stability region and will not be transmitted through. Along an operating line which has a fixed a_x/q_x value or equivalently $2U/V$ value, only the ions with the selected e/m value (or located inside the stability region) will be transmitted. By changing the dc and rf voltages together, the selected ions are located near the tip of the stability region to increase the resolution. Therefore, for given stable a_x and q_x values, increasing dc or rf voltage will transmit ions with less e/m values (or heavier ions) [21]. When dc voltage is turned off ($U = 0$), the mases having a e/m $\leq \frac{1}{9}$ are transmitted to the collector thus giving a measure of the total pressure of the system[1].

6.3.2 Detection Limitation

The low efficiency of pumping out helium causes the detection limitation of the mass spectrometer. It results in a unstable background signal as shown in figure 6.13. The output signal from the mass spectrometer gives the partial pressure of helium in the scale of 10^{-6} mb. During the wash-in measurement, the helium failed to come up to the original background value. At the end of the washout, there is a sudden drop of the background signal which may be caused by the accumulation of the water vapour in the mass spectrometer or at the orifice.

---

[1] The working principle is summarised from its user manual.

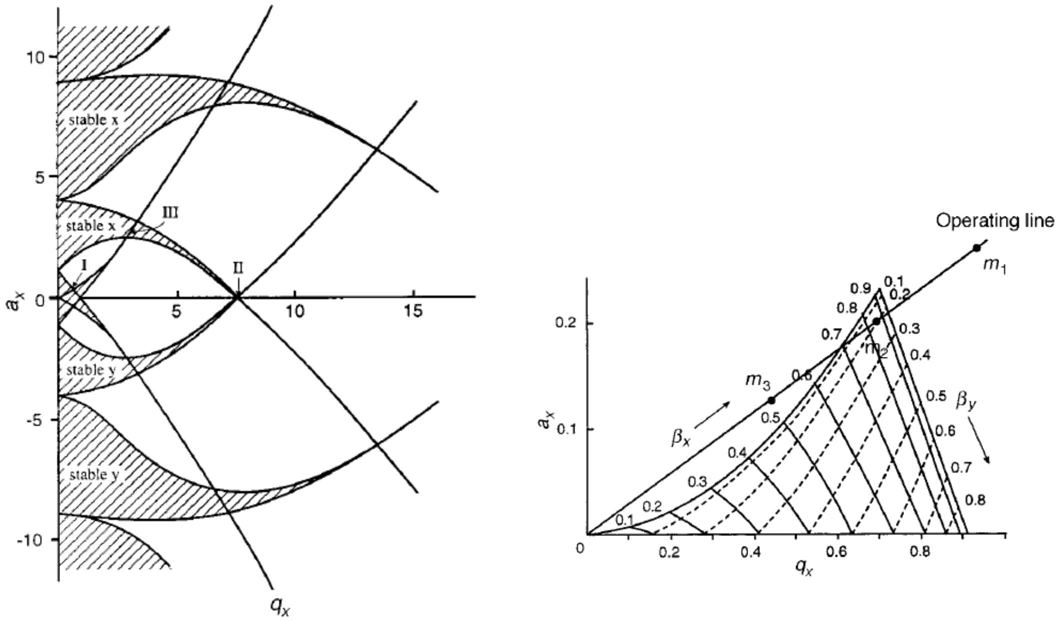

(a) (b)

Figure 6.12: (a) The first three stability regions (I, II, and III) of the solutions to the Mathieu's equation for both x and y directions. (b) The first stability region with an operating line which is the scanning trajectory. Ions with mass m_2 located at the stability region will pass through the quadrupole rods. Heavier ions m_3 or lighter ions m_1 located outside of the stability region will not be transmitted [21].

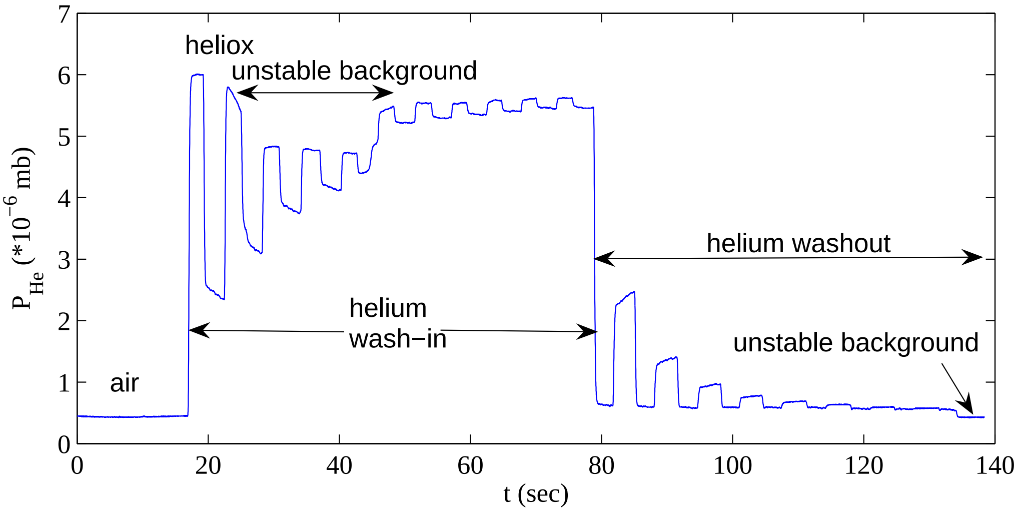

Figure 6.13: MBHW data detected by the mass spectrometer. The output signal is the helium partial pressure in the scale of 10^{-6} mb. The background signal is unstable especially during the helium wash-in measurement.

6.4 Summary

Three methods of measuring helium gas concentration have been described in this chapter. The high acoustic attenuation in helium gas results in a non-linear relation between the helium gas concentration and the time of flight. The ultrasonic detection method only works when the helium concentration is less than 52% which is unsuitable for analysing a higher concnetration of helium gas in MBHW measurements.

The low signal-to-noise ratio of the signal from the thermistor Wheatstone Bridge in a flowing gas restricts the detecting limit especially for low concentration of helium gas. Also, the frequent replacement for the oxidised filament-type thermistor is a disadvantage.

The unstable background caused by low-efficiency on helium gas pumping renders the mass spectrometer unsuitable as a helium gas analyser. Also, the diffusion oil from the diffusion pump pollutes the mass spectrometer system which limits a long term usage. Furthermore, it is difficult to make a small orifice for reducing the inlet pressure that has constant flow and which does not block.

Chapter 7

Conclusions and suggestions for future work

This thesis has discussed the development of a MBHW system for lung function studies. MBHW measurements were performed on 11 volunteers and a lung model. This chapter includes a brief summary of the main areas of the project and some suggestions for future work.

7.1 Summary

7.1.1 Experimental setup

A MBHW system consisting of the gas volume measuring system and gas analysing system has been built. Two flow meters have been used to measure the inspired and expired gas volumes with a pressure sensor to monitor the pressure at the mouth in the gas volume measuring system.

The gas analysing system consists of two gas analysers, the QTF gas density detector and the infrared (IR) CO_2 detector, a pressure sensor, and a temperature sensor. A water trap with an ice bath has been used to filter out the water vapour from the expiration. A pressure sensor and a thermistor have been used to monitor the pressure and temperature signal of the sampled gas. The QTF gas density detector has been used to detect the respiratory gas density. A quartz tuning fork (32768 Hz) with a Pierce crystal oscillator has been built and is placed in the sampled gas. A commercial phase-lock-loop (easyPLL) detector detects the resonance frequency shift which is proportional to the gas density change [89]. The gas density can thus be given by calibrating against the resonance frequency in pure nitrogen and pure carbon dioxide gas.

An infrared CO_2 detector has been used to analyse the concentration of carbon dioxide from the expiratory gas. A temperature-controlled circuit has been built up for keeping the CO_2 detecting system at a constant temperature (about 50 ^oC) and reducing the water vapour condensed in the cell. Infrared absoprtion by carbon dioxide at 4.2 μm is governed by Beer-Lambert's law. A 4.2 μm LED with a PbSe photoconductor have been used as the IR emitter and receiver. A signal balance circuit with a lock-in amplifier was connected to the PbSe photoconductor to amplify the received signal. The output signal from the lock-in amplifier is linearly related to the carbon dioxide concentration (< 6 %).

7.1.2 MBHW measurements on Volunteers

MBHW measurements have been performed on 12 volunteers including six normal subjects, three asthmatics, and two smokers. The peak expiratory flow has also been measured and compared with the predicted values. The lung clearance results from the helium washout data have been fitted with a sum of two exponential curves which represented a better-ventilated and a poorly-ventilated compartment based on the assumption of the two-compartment model [5, 22]. Subjects with larger proportion of poorly-ventilated part have shown a lower PEF compared to their predicted values. The proportion of better- or poorer-ventilated compartment is not necessarily related to lung disease.

The normalised phase III slopes (S_{NIII}) from each breath have been plotted against turnover. Two indices, S_{cond} and S_{acin} have been derived from each MBHW data set. S_{cond} is the increasing rate of S_{NIII} after the first few breaths and a higher S_{cond} value reflects the higher ventilation inhomogeneity in the conducting airways. S_{acin} is the S_{NIII} value from the first breath with the subtraction of S_{cond}. The higher S_{acin} reflects a higher ventilation inhomogeneity in the acinar airways. Results from the asthmatic subjects have shown higher S_{cond} values, or higher S_{acin} values, or both compared to the normal subjects.

The gas exchange rate (Q_r), which is the ratio of oxygen consumption versus carbon dioxide production, has been calculated from the single breaths before each washout measurement. Two smokers have shown slightly lower Q_r values compared to most of the normal subjects.

7.1.3 MBHW Measurements on Lung Model

A lung model made of a 2.2 litre plastic funnel with a loud speaker as a diaphragm has been built. A 0.25 Hz triangular signal was amplified by a dc amplifier and input to the loud speaker to simulate the movement of the diaphragm. A 0- to 4-generation dichotomous structure has been made by putting small cones with different sizes made of plastic foil in the funnel. MBHW measurements have been performed on the lung model. The washout results from the lung model are not easily related to the results from real lungs. The phase III slopes from the lung model washout results were not always positive especially for 0- and 1-generation structure. The reason may result from the lack of gas exchange, the unwell separated compartments at the terminals, irregular sizes of branches, and the very low generation structure.

7.1.4 Other Methods of Helium Gas Concentration Detection

Three methods of detecting helium gas concentration (ultrasonic gas density detector, thermal conductivity detector, and mass spectrometer detection) have been used but they were found to be unsuitable for MBHW measurement.

The ultrasonic gas density detector measures the difference of acoustic group velocity in various concentration of helium gas media compared to air. The high acoustic attenuation in helium gas results in a non-linear relation of the helium gas concentration and the time of flight. This ultrasonic detection method only works when the helium concentration is less than 52% which is unsuitable for analysing a higher concnetration of helium gas in MBHW measurements where up to 78 % of helium gas is used.

The thermal conductivity gas detector with a thermistor Wheatstone Bridge senses the thermal conductivity of the flowing gas. The low signal-to-noise ratio in a flowing gas restricts the detection limitation especially for low concentration of helium gas. Also, the frequent replacement of the oxidised filament-type thermistor is a disadvantage.

The quadrupole mass spectrometer requires a high vacuum working background. The unstable background caused by low-efficiency of helium gas pumping renders the mass spectrometer unsuitable for helium gas analyser. Also, the diffusion oil from the diffusion pump pollutes the mass spectrometer system which restricts it for a long term usage.

7.2 Suggestions for future work

Some suggestions for improvements to the MBHW system and the measurements that could be made are outlined in this section.

7.2.1 MBHW System

- The gas exchange Q_r has been assumed to be fixed during the washout measurement. The expiratory concentration of oxygen from each single washout breath is thus given by the carbon concentration multiplied by Q_r. To get a more accurate oxygen concentration would require a fast oxygen sensor such as the oxygen optode.

- A commercial phase-lock-loop (easyPLL detector) has been used for detecting the resonance frequency shift of the QTF. The signal-to-noise ratio is lower for lower concentration of sampled gases compared to air. To get a higher signal-to-noise ratio would require a QTF with higher resonance frequency (such as a few MHz) and a suitable PLL detector.

- A variety of rubber and copper tubes have been used to join the sensors to the gas flow and each other. To make a stronger and more stable system would require an improved gas handling system securely fixed in place.
- The MBHW system has been built up for development purposes rather than clinical usage. A better testing environment and an improved construction would be required if applying the MBHW system to clinical studies.

7.2.2 Measurements

- The MBHW has only been performed on 11 volunteers from the department. To get more reliable conclusions, such as the relation between the proportion of poorly-ventilated compartment and PEF values, requires more washout measurements on volunteers with lung diseases.
- The MBHW results have not been compared with the clinical lung function results such as the spirometry results. A more complete study with a clinical reference for subjects that have been diagnosed with lung diseases would require the spirometry results from all volunteers.
- The limited number of smokers in this work have been found to have a lower respiratory quotient values. To get a more reliable conclusion would require more volunteers.
- For non-smokers, the Fowler dead space (V_{DF}) for oxygen gas has been found higher than other gases (CO_2, N_2, He). Also, V_{DF} is not necessarily related to FRC in non-smokers. However, for those two smokers, V_{DF} for different gases is proportional to the self-diffusion coefficient as well as to the FRC. To get a reliable conclusion about how V_{DF} relates to smoking disease would require more volunteer smokers and further studies.

- This study has been focused on young adults, to study the relation between the age and the respiratory ventilation would require various ages of subjects.

7.2.3 Lung Model

- The results from the lung model made of one 2.2 litre funnel cannot be compared directly to the real lungs due to the poorly separated compartments at the terminals. To separate compartments, a better method would be to construct a model made of two funnels with different sizes and tidal volumes. To more closely approach real lungs, a tree-like structure made of different sizes of tubes with small balloons at the end is required.

- A longer phase II (or a transition feature) has been found in some single breath washout curves from smokers' MBHW data. It may result from a higher resistance of the airway caused by the tar coating. To simply prove the relation between the airway resistance and the single breath washout curve, a lung model with different surface resistance needs to be constructed.

Bibliography

[1] L. G. Baker, J. S. Ultman, and R. A. Rhodes. Simultaneous flow and diffusion in a symmetric airway system: a mathematical model. *Respir. Physiol.*, 21:119–138, 1974.

[2] G. K. Batchelor. *An Introduction to Fluid Dynamics.* Cambridge University Press, 2nd edition, 2006.

[3] R. Blaauwgeers, M. Blazkova, M. Človečko, V. B. Eltsov, R. Graaf, J. Hosio, m. Krusius, D. Schmoranzer, W. Schoepe, L. Skrbek, P. Skyba, R. E. Solntsev, and D. E. Zmeev. Quartz tuning fork: Thermometer, pressure- and visometer for helium liquids. *J. Low Temp. Physics*, 146:537–562, 2007.

[4] C. Bohr. Ueber die lungenatmung. *Skand. Arch. Physiol.*, 2:236–268, 1891.

[5] A. Bouhuys, K. E. Hagstam, and G. Lundin. Efficiency of pulmonary ventilation during rest and light exercise. *Acta. Physiol. Scand.*, 35:289–304, 1956.

[6] A. Bouhuys and H. J. Van Lennep. Effect of body posture on gas distribution in the lungs. *J. Appl. Physiol.*, 17(1):38–42, 1962.

[7] R. H. Bube. *Photoconductivity of solids.* Wiley, 1st edition, 1960.

[8] A. Sonia Buist. Early Detection of Airways Obstruction by the Closing Volume Technique. *Chest*, 64(4):495–499, 1973.

[9] S. Chapman and T. G. Cowling. *The Mathematical Theory of Nonuniform Gases.* Cambridge University Press, 3rd edition, 1970.

[10] W. H. Chu. Dtmb contract nobs-86396. *Southwest Research Institute Technical Report No. 2*, X:NObs86396, 1963 (unpublished).

[11] J. P. Cleveland, S. Manne, D. Bocek, and P.K. Hansma. A nondestructive method for determining the spring constant of cantilevers for scanning force microscopy. *Rev. Sci. Instrum.*, 64(2):403, 1993.

[12] J. E. Cotes. *Lung Function: Chapter 15.* Blackwell Scientific Publications, 3rd edition, 1975.

[13] A. B. H. Crawford, M. Makowska, and L A. Engel. Effect of bronchomotor tone on static mechanical properties of lung and ventilation distribution. *J. Appl. Physiol.*, 62(6):2278–2285, 1987.

[14] A. B. H. Crawford, M. Makowska, M. Paiva, and L. A. Engel. Convection- and diffusion-dependent ventilation maldistribution in normal subjects. *J. Appl. Physiol.*, 59(3):838–846, 1985.

[15] G. Cumming. Gas mixing efficiency in the human lung. *Respir. Physiol.*, 2:213–224, 1967.

[16] A. Cutillo, E. Omboni, and S. Delgrossi. Effects of respiratory frequency on distribution of inspired gas in normal subjects and in patients with chronic obstructive lung disease. *Am. Rev. Respir. Dis.*, 105:756–767, 1972.

[17] A. Cutillo, R. Perondi, M. Turiel, J. Egger, S. Watanabe, and A. Renzetti. Reprodusibility of multibreath nitrogen washout measurements. *Am. Rev. Respir. Dis.*, 124:505–507, 1981.

[18] P. H. Dawson. Quadrupole mass analyaer: Performance, design, and some recent applications. *Mass Spectrometry Rev.*, 5:1–37, 1986.

[19] S. R. Downie, C. M. Salome, S Verbanck, B. Thompson, N. Berend, and G. King. Ventilation heterogeneity is a major determinant of airway hyperresponsiveness in asthma, independent of airway inflammation. *Throax*, 62:684–689, 2007.

[20] S. R. Downie, S Verbanck, U. Gunnar, G. King, C. Salome, and N. Berend. Detection of small and large airway heterogeneity in asthma by the multiple breath nitrogen washout test. *Respirology*, 9S:2:A31, 2004.

[21] Z. Du, D. J. Douglas, and N. Konenkov. Elemental analysis with quadrupole mass filters operated in higher stability regions. *J. Anal. At. Spectrom.*, 14:1111–1119, 1999.

[22] L. A. Engel and M. Paiva. *Gas mixing and distribution in the lung (Lung biology in health and disease) : Chapter 7.* Marcel Dekker, New York, 1st edition, 1985.

[23] W. S. Fowler. Lung function studies. ii. the respiratory dead space. *Am. J. Physiol.*, 154:405–416, 1948.

[24] W. S. Fowler. Lung function studies. iii. uneven pulmonary ventilation in normal subjects and in patients with pulmonary disease. *J. Appl. Physiol.*, 2:283–299, 1949.

[25] W. S. Fowler, E. R. Cornish, and S. K. Seymour. Lung Function Studies VIII. Analysis of Alveolar Ventilation by Pulmonary N2 Clearance Curves. *J. Clin. Invest.*, 31(1):40–50, 1952.

[26] D. J. Gavaghan and C. E. W. Hahn. A tidal breathing model of the forced inspired inert gas sinewave technique. *Respir. Physiol.*, 106:209–221, 1996.

[27] F. W. Giacobbe. Precision measurement of acoustic velocities in pure gases and gas mixtures. *J. Acoust. Soc. Am.*, 694(3):1200–1210, 1993.

[28] F. J. Giessibl. Atomic resolution on si(111)-(7x7) by noncontact atomic force microscopy with a force sensor based on a quartz tuning fork. *Appl. Phys. Lett.*, 76:1470–1472, 2000.

[29] E H Gluck, D J Onorato, and R Castriotta. Helium-oxygen mixtures in intubated patients with status asthmaticus and respiratory acidosis. *Chest*, 98(3):693–698, 1990.

[30] S. M. Han, H. Benaroya, and T. Wei. Dynamics of transversely vibrating beams using four engineering theories. *Journal of Sound and Vibration*, 225:935–988, 1999.

[31] R. H. Harada and H. T. Minden. Photosensitization of pbs films. *Phys. Rev.*, 102(5):1258–1262, 1956.

[32] Y. Hasegawa and T. Eguchi. Potential profile around step edges of si surface measured by nc-afm. *Appl. Surf. Sci.*, 188(3-4):386–390, 2002.

[33] C Herring and E. Vogt. Transport and defromation-potential theory for many-valley semiconductors with anisotropic scattering. *Phys. Rev.*, 101(3):944, 1956.

[34] J. N. Humphery. Photoconductivity in lead selenide. experimental. *Phys. Rev.*, 105(2):469, 1957.

[35] J. N. Humphery. Photoconductivity in lead selenide. theory of the mechanism of sensitization. *Phys. Rev.*, 105(6):1736, 1957.

[36] James N. Humphrey and Richard L. Petritz. Photoconductivity in lead selenide: Theory of the dependence of sensitivity on film thickness and absorption coefficients. *Phys. Rev.*, 105(4):1192–1197, 1957.

[37] D. P. Johns and R. Pierce. *Spirometry: the measurement and interpretatioon of ventilatory function in clinical practice.* National Asthma Council, Melbourne, 6th edition, 2004.

[38] N. V. Joshi. *Photoconductivity: Art, Science and Technology (Optical Engineering).* CRC Press, 1st edition, 1990.

[39] A. H. Kars, J. M. Bogaard, T. Stijnen, J. de Vries, A. F. Verbaak, and C. Hilvering. Deadspace and slope indices from the expiratory carbon dioxide-tension volume curve. *Eur. Respir. J.*, 10:1829–1836, 1997.

[40] T. Kunstmann, M. Fendrich, D. Paulkowski, Th. Wagner, and R. Möller. Combined normal and torsional mode in frequency-modulation atomic force microscopy for lateral dissipation measurement. *Appl. Phys. Lett.*, 88(15):153112, 2006.

[41] E. W. Lemmon and R. T. Jacobsen. Viscosity and thermal conductivity equation for nitrogen, oxygen, argon, and air. *Int. J. Thermophys.*, 25(1):21–65, 2004.

[42] M. G. Levitzky. *Pulmonary Physiology.* McGraw-Hill, 6th edition, 2002.

[43] S. M. Lewis. Emptying patterns of the lung studied by multiple-breath n_2 washout. *J. Appl. Physiol.*, 44:424–430, 1978.

[44] S. M. Lewis, J. W. Evans, and A. A. Jalowayski. Continuous distributions of specific ventilation recovered from inert gas washout. *J. Appl. Physiol.*, 44:416–423, 1978.

[45] K. R. Lutchen, R. H. Habib, H. L. Dorkin, and M. A. Wall. Respiratory impedence and multiplebreah n2 washout in healthy, asthmatic, and cystic fibrosis subjects. *J. Appl. Physiol.*, 68:2139–2149, 1990.

[46] A. Mansell, C. Bryan, and H. Levison. Airway closure in children. *J Appl Physiol*, 33(6):711–714, 1972.

[47] P. E. Martin and E. F. Barker. The infrared absorption spectrum of carbon dioxide. *Phys. Rev.*, 41:291–303, 1932.

[48] W. Mohlenhoff. *PhD Thesis: Experimental Study of Helium dilution in the wale of a circular cylinder at M=5.8.* California Institute of technology, USA, 1960.

[49] A. V. Muylem, S. Verbanck, and M. Estenne. Monitoring the lung periphery of transplanted lungs. *Repiratory Physiology and Neurobiology*, 148:141–151, 2005.

[50] K. K. Nanda and S. N. Sarangi. Electrical properties of 1n4007 silicon diode. *Rev. Sci. Instrum.*, 68(7):2904, 1997.

[51] C. J. Newth, P. Enright, and R. L. Johnson. Multiple-breath nitrogen washout techniques including measurements with patients on ventilators. *Eur. Respir. J.*, 10(10):2174–2185, 1997.

[52] J. R. Nielsen, V. Thornton, and E. B. Dale. The absorption laws for gases in the infra-red. *Rev. Mod. Physics*, 16(3):307, 1944.

[53] A. J. Nunn and I. Gregg. New regression equations for predicting peak expiratory flow in adults. *BMJ*, 298(1):1068–1070, 1989.

[54] M. Paiva. Gas transport in the humna lung. *J. Appl. Physiol.*, 35:401–410, 1973.

[55] M. Paiva. Two new pulmonary functional indexes suggested by a simple mathematical model. *Respir. Physiol.*, 32:389–403, 1975.

[56] M. Paiva and L. A. Engel. Pulmonary interdependence of gas transport. *J. Appl. Physiol.*, 47:296–305, 1979.

[57] M. Paiva and L. A. Engel. Model analysis of gas distribution within human acinus. *J. Appl. Physiol.*, 56:418–425, 1984.

[58] M. Paiva and L. A. Engel. Theoretical studies of gas mixing and ventilation distribution in the lung. *Physiological Reviews*, 67:751–797, 1987.

[59] M. Paiva and V. Paiva. Stochastic simulation of the gas diffusion in the air phase of the human lung. *Bell. Math. Biophys.*, 34:457–466, 1972.

[60] M. Paiva, A. Van Muylem, and L. A. Engel. The slope of phase iii in multibreath nitrogen washout and washin. *Bull. Eur. Physiopathol. Respir.*, 18:273–280, 1982.

[61] R. L. Petritz. Theory of photoconductivity in semiconductor films. *Phys. Rev.*, 104:1508–1516, 1956.

[62] H. P. Pinto, G. H. Enevoldsen, F. Besenbacher, J. V. Lauritsen, and A. S. Foster. The role of tip size and orientation tip-surface relaxations and surface impuries in simultaneous afm and stm. *Nanotechnology*, 20(9pp):264020, 2009.

[63] G. K. Prisk, H. J. Guy, A. R. Elliott, M. Paiva, and J. B. West. Ventilatory inhomogeneity determined from multiple-breath washouts during sustained microgravity on Spacelab SLS-1. *J. Appl. Physiol.*, 78(2):597–607, 1995.

[64] G. K. Prisk, H. J. Guy, A. R. Elliott, M. Paiva, and J. B. West. Ventilatory inhomogeneity determined from multiple-breath washouts during sustained microgravity on Spacelab SLS-1. *J. Appl. Physiol.*, 78(2):597–607, 1995.

[65] J. S. Robertson, W. E. Siri, and H. B. Jones. Lung ventilation patterns determined by analysis of nitrogen elimination rates; use of the mass spectrometer as a continuous gas analyzer. *J. Clin. Invest.*, 29:577–590, 1950.

[66] A. Roos, H. Dahlstrom, and J. P. Murphy. Distribution of inspired air in the lungs. *J. Appl. Physiol.*, 7:645–659, 1954.

[67] J. E. Sader. Frequency response of cantilever beams immersed in viscous fluids with application to the atomic microscope. *J. Appl. Physics*, 84(1), 1998.

[68] K. Saitoh, K. , Hayashi, Y. Shibayama, and K. Shirahama. A low temperature scanning probe microscope using a quartz tuning fork. *J. Physics: Conference Series*, 150(012039), 2009.

[69] V. K. Saxena and S. C. Saxena. Measurement of the thermal conductivity of helium using a hot-wire type of thermal diffusion column. *Brit. J. Appl. Phys.*, 1:1341–1351, 1968.

[70] A. S. Sedra and K. C. Smith. *Microelectronic Circuits.* Oxford University Press, 5th edition, 2004.

[71] R. S. Sikand, H. Magnussen, P. Scheid, and J. Piiper. Convective and diffusive gas mixing in human lungs: experiments and model analysis. *J. Appl. Physiol.*, 40:362–371, 1976.

[72] N. Sillon and R. Baptist. Micromachined mass spectrometer. *Sens. and Actuat. B*, 83(1-3):129–137, 2002.

[73] C. S. Smith. Piezoresistance effect in germanium and silicon. *Phys. Rev.*, 94(1):42, 1954.

[74] Yoshiaki Sugimoto, Seiji Innami, Masayuki Abe, Oscar Custance, and Seizo Morita. Dynamic force spectroscopy using cantilever higher flexural modes. *Appl. Phys. Lett.*, 91(9):093120, 2007.

[75] J. T. Tinge, K. Mencke, Bosgra, and A. A. H. Drinkenburg. Ultrasonic gas analyzer for high resolution determination of binary-gas composition. *J. Phys. E: Sci. Instum.*, 19:953–956, 1986.

[76] O. N. Tufte, P. W. Chapman, and D. Long. Silicon diffused-element piezoresistive diaphragms. *J. Appl. Physics*, 33(11):3322, 1962.

[77] G. Tusman, M. Areta, C. Climente, R. Plit, F. Suarez-Sipmann, M. J. Rodríguez-Nieto, G. Peces-arba, E. Turchetto, and S. H. Böhm. Effect of pulmonary perfusion on the slopes of single-breath test of co$_2$. *J. Appl. Physiol.*, 99:650–655, 2005.

[78] C. A. Van Eysden and J. E. Sader. Resonant frequencies of a rectangular cantilever beam immersed in a fluid. *J. Appl. Physics*, 100:114916, 2006.

[79] S. Verbanck, D. Schuermans, A Van Muylem, C. Melot, M. Noppen, W. Vincken, and M. Paiva. Conductive and acinar lung-zone contributions to ventialtion inhomogeneity in copd. *Am. J. Respir. Crit. Care Med.*, 157:1573–1577, 1998.

[80] S. Verbanck, D. Schuermans, A. Van Muylem, M. Paiva, M. Noppen, and W. Vicken. Ventilation distribution during histamine provocation. *J. Appl. Physiol.*, 83:1907–1916, 1997.

[81] E. R. Weibel. Fractal geometry: a design principle for living organisms. *Am. J. Physiol. Lung Cell Mol. Physiol.*, 261:L361–L369, 1991.

[82] E. R. Weibel, B. Sapoval, and M. Filoche. Design of peripheral airways for efficient gas exchange. *Respiratory Physiology and Neurobiology*, 148:3–21, 2005.

[83] D. E. Weston. The theory of propagation plane sound waves in tubes. *Proc. Phys. Soc. B*, 66:695–709, 1953.

[84] J. P. Whiteley, D. J. Gavaghan, and C. E. W. Hahn. A tidal breathing model for the multiple inert gas elimination technique. *J. Appl. Physiol.*, 87:161–169, 1999.

[85] J. Y. Wong. Self-calibrating carbon dioxide analyzer. *US Patents*, (4578762), 1986.

[86] H. Wrigge, M. Sydow, J. Zinserling, P. Neumann, J. Hinz, and H. Burchardi. Early Detection of Airways Obstruction by the Closing Volume Technique. *Intensive Care Medicine*, 24(5):487–493, 1998.

[87] D. A. Wright. Photoconductivity. *British J. Appl. Phys.*, 9:205, 1958.

[88] S. Yamamori and H. Dainobu. Infrared detector and gas analyzer. *US Patents*, (6218665), 2001.

[89] D. Zeisel, H. Menzi, and L. Ullrich. A precise and robust quartz sensor based on tuning fork technology for (sf_6)-gas density control. *Sensors and Actuators*, 80:233–236, 2000.

[90] J. Zhang and S. O'Shea. Tuning forks as micromechanical mass sensitive sensors for bio- or liquid detection. *Sensors and Actuators B*, 94:65–72, 2003.